

# **SANDIA REPORT**

SAND2007-6179

Unlimited Release

Printed October 2007

## **A Mathematical Framework for Multiscale Science and Engineering: the Variational Multiscale Method and Interscale Transfer Operators**

Pavel B. Bochev, S. Scott Collis, Reese E. Jones, Richard B. Lehoucq, Michael L. Parks, Guglielmo Scovazzi, Stewart A. Silling, Jeremy A. Templeton, and Gregory J. Wagner

Prepared by  
Sandia National Laboratories  
Albuquerque, New Mexico 87185 and Livermore, California 94550

Sandia is a multiprogram laboratory operated by Sandia Corporation,  
a Lockheed Martin Company, for the United States Department of Energy's  
National Nuclear Security Administration under Contract DE-AC04-94-AL85000.

Approved for public release; further dissemination unlimited.



**Sandia National Laboratories**

Issued by Sandia National Laboratories, operated for the United States Department of Energy by Sandia Corporation.

**NOTICE:** This report was prepared as an account of work sponsored by an agency of the United States Government. Neither the United States Government, nor any agency thereof, nor any of their employees, nor any of their contractors, subcontractors, or their employees, make any warranty, express or implied, or assume any legal liability or responsibility for the accuracy, completeness, or usefulness of any information, apparatus, product, or process disclosed, or represent that its use would not infringe privately owned rights. Reference herein to any specific commercial product, process, or service by trade name, trademark, manufacturer, or otherwise, does not necessarily constitute or imply its endorsement, recommendation, or favoring by the United States Government, any agency thereof, or any of their contractors or subcontractors. The views and opinions expressed herein do not necessarily state or reflect those of the United States Government, any agency thereof, or any of their contractors.

Printed in the United States of America. This report has been reproduced directly from the best available copy.

Available to DOE and DOE contractors from  
U.S. Department of Energy  
Office of Scientific and Technical Information  
P.O. Box 62  
Oak Ridge, TN 37831

Telephone: (865) 576-8401  
Facsimile: (865) 576-5728  
E-Mail: [reports@adonis.osti.gov](mailto:reports@adonis.osti.gov)  
Online ordering: <http://www.osti.gov/bridge>

Available to the public from  
U.S. Department of Commerce  
National Technical Information Service  
5285 Port Royal Rd  
Springfield, VA 22161

Telephone: (800) 553-6847  
Facsimile: (703) 605-6900  
E-Mail: [orders@ntis.fedworld.gov](mailto:orders@ntis.fedworld.gov)  
Online ordering: <http://www.ntis.gov/help/ordermethods.asp?loc=7-4-0#online>



# A Mathematical Framework for Multiscale Science and Engineering: the Variational Multiscale Method and Interscale Transfer Operators

Pavel B. Bochev<sup>1</sup>   S. Scott Collis<sup>1</sup>   Reese E. Jones<sup>2</sup>  
Richard B. Lehoucq<sup>1</sup>   Michael L. Parks<sup>1</sup>   Guglielmo Scovazzi<sup>3</sup>  
Stewart A. Silling<sup>4</sup>   Jeremy A. Templeton<sup>5</sup>   Gregory J. Wagner<sup>5</sup>

<sup>1</sup>Computational Mathematics and Algorithms

<sup>3</sup>Computational Shock and Multiphysics

<sup>4</sup>Multiscale Dynamic Material Modeling

Sandia National Laboratories

P.O. Box 5800

Albuquerque, NM 87185-1320

<sup>2</sup>Mechanics of Materials

<sup>5</sup>Thermal/Fluid Science and Engineering

Sandia National Laboratories

P.O. Box 969

Livermore, CA 94551

## Abstract

This report is a collection of documents written as part of the Laboratory Directed Research and Development (LDRD) project *A Mathematical Framework for Multiscale Science and Engineering: The Variational Multiscale Method and Interscale Transfer Operators*. We present developments in two categories of multiscale mathematics and analysis. The first, continuum-to-continuum (CtC) multiscale, includes problems that allow application of the same continuum model at all scales with the primary barrier to simulation being computing resources. The second, atomistic-to-continuum (AtC) multiscale, represents applications where detailed physics at the atomistic or molecular level must be simulated to resolve the small scales, but the effect on and coupling to the continuum level is frequently unclear.



# Contents

<b>1</b>	<b>Introduction</b>	<b>15</b>
<b>2</b>	<b>The Local Variational Multiscale Method: Applications to Wall-bounded Turbulence</b>	<b>19</b>
2.1	Introduction	19
2.2	Local Variational Multi-Scale ( $\ell$ VMS) Method	21
2.3	$\ell$ VMS Formulation	24
2.4	VMS Model Description	28
2.5	Discretization and Implementation	28
2.6	$\ell$ VMS Advantages and Potential	29
2.7	Numerical Results – Effects of Spatial Resolution	30
2.7.1	DG Spatial Discretization	31
2.8	Dealiasing Strategies	35
2.8.1	Polynomial Dealiasing (PD)	35
2.8.2	Spectral Filtering (SF)	36
2.8.3	Numerical Results: Dealiasing Strategies	37
2.9	Multi-Scale Modeling Using $\ell$ VMS	38
2.9.1	Parameter Selection	38
2.9.2	Low Reynolds Number: $Re_\tau = 100$	39
2.9.3	Moderate Reynolds Number: $Re_\tau = 395$	41
2.10	Conclusions	43
2.11	Acknowledgements	43
<b>3</b>	<b>A Multiscale Discontinuous Galerkin Method with the Computational Structure of a Continuous Galerkin Method</b>	<b>57</b>
3.1	Introduction	57

3.2	Advection-Diffusion Equation	59
3.2.1	Strong form of the problem	59
3.2.2	Definitions and notations for the discontinuous Galerkin method	60
3.3	Global Weak Formulation	63
3.3.1	Conservative formulation	63
3.3.1.1	Conservation properties	64
3.3.1.2	Euler-Lagrange equations	66
3.4	Local Weak Formulations	67
3.4.1	Local problem for the trial solution	67
3.4.1.1	Multiscale interpretation	70
3.4.2	Local problem for the weighting function	71
3.5	Numerical Results	72
3.5.1	One-dimensional advection-diffusion	72
3.5.1.1	Weak formulation	72
3.5.1.2	Local problem for the trial solution	72
3.5.1.3	Limit behavior	75
3.5.1.4	Local problem for the weighting function	75
3.5.1.5	Numerical results	78
3.5.2	Two-dimensional advection equation	89
3.5.2.1	Advection skew to the mesh	89
3.5.2.2	Rotating flow	89
3.6	Conclusions and Future Directions	97
<b>4</b>	<b>A Multiscale Discontinuous Galerkin Method</b>	<b>99</b>
4.1	Introduction	99
4.2	Notation	100
4.3	Multiscale Discontinuous Galerkin Method	102
4.3.1	Definition of the interscale operator	102

4.4	Multiscale DG for a scalar advection-diffusion problem . . . . .	104
4.4.1	A donor DG method for the model problem . . . . .	104
4.4.2	The interscale operator . . . . .	106
4.4.2.1	Local problem for DG-A . . . . .	106
4.4.2.2	Local problem for DG-B . . . . .	107
4.5	Conclusions . . . . .	107
<b>5</b>	<b>Force Flux and the Peridynamic Stress Tensor</b>	<b>109</b>
5.1	Introduction . . . . .	109
5.2	Peridynamic Stress Tensor . . . . .	110
5.3	Behavior of the Peridynamic Stress Tensor on a Boundary . . . . .	113
5.4	Variational Interpretation of the Peridynamic Stress Tensor . . . . .	115
5.5	Peridynamic Force Flux . . . . .	118
5.6	Mechanical Interpretation of the Force Flux . . . . .	118
5.7	An example . . . . .	120
<b>6</b>	<b>Statistical Coarse-graining of Molecular Dynamics into Peridynamics</b>	<b>123</b>
6.1	Introduction . . . . .	123
6.2	Peridynamics (PD) . . . . .	124
6.3	PD Probabilistic Distribution . . . . .	125
6.4	Homogenization . . . . .	127
6.5	Rescaling . . . . .	129
<b>7</b>	<b>An Atomistic-to-Continuum Coupling Method for Heat Transfer in Solids</b>	<b>131</b>
7.1	Introduction . . . . .	131
7.2	Problem Definition . . . . .	133
7.3	The Atomistic Temperature Field . . . . .	135
7.3.1	Nodes-to-atoms reduction operation . . . . .	135
7.3.2	Augmented molecular dynamics force . . . . .	137

7.3.3	Total energy conservation .....	137
7.4	The Finite Element Heat Equations .....	139
7.5	Time-Filtered Coupling .....	141
7.6	Numerical Implementation Details .....	142
7.6.1	Computation of interatomic forces .....	142
7.6.2	Surface integrals on the MD interface .....	143
7.6.3	Time Integration .....	144
7.6.4	Initial Conditions and the Rescaling Thermostat .....	146
7.7	Examples .....	147
7.7.1	One Dimensional Heat Conduction .....	148
7.7.2	Diffusion of an Initial Gaussian Temperature Field .....	149
7.7.3	Thermal Transport Across an Acoustic Mismatch .....	151
7.8	Discussion and Conclusions .....	151
<b>References</b>		<b>159</b>



# List of Figures

2.1	Schematic of DGM discretization [44]. . . . .	21
2.2	Illustration of $\ell$ VMS modeling capabilities for flows in complex geometries . . . . .	30
2.3	Profiles of turbulence quantities for $Re_\tau = 100$ computed with different mesh topologies using $p = 3$ . . . . .	46
2.4	$Re_\tau = 100$ using $p = 3$ with different mesh topologies – mean velocity and turbulence intensity profiles . . . . .	47
2.5	Profiles of meanflow and one-dimensional streamwise energy spectra, respectively, for different mesh topologies using various polynomial orders . . . . .	48
2.6	Wall shear stress and average streamwise velocity slip at the wall. . . . .	49
2.7	Spectral filter transfer function for various polynomial orders. . . . .	50
2.8	Non-linear stability strategies evaluation at $Re_\tau = 100$ – Meanflow and rms profiles. . . . .	51
2.9	Important length scales for partition selection in $\ell$ VMS. . . . .	52
2.10	Turbulence statistics for $Re_\tau = 100$ computed with a $4 \times 4 \times 4$ mesh with different polynomial distributions and models. . . . .	53
2.11	Turbulence statistics for $Re_\tau = 100$ computed with a $6 \times 4 \times 4$ mesh using $p = \{6, 5, 5, 6\}$ . . . . .	54
2.12	Turbulence statistics for $Re_\tau = 395$ computed with a $6 \times 8 \times 6$ variable-order mesh. . . . .	55
3.1	Boundary partitions. . . . .	60
3.2	Schematic of the inflow and outflow boundaries for an element with respect to the convective field $\mathbf{a}$ . . . . .	60
3.3	Schematic of the normals and $+/-$ regions with respect to an edge. . . . .	62
3.4	Definition of $h_\perp$ for two adjacent triangular elements. . . . .	64
3.5	Local conservation of flux: inflow fluxes from the contiguous upwind elements (blue) are balanced by the outflow flux on the outflow boundary of the element (red). . . . .	65

3.6	Schematic illustration of the basis functions in the local problem. On the left is a 16-node bicubic quadrilateral element. Its boundary nodes are identified on the right. The corresponding basis functions satisfy $\bar{\psi}_j = \psi_j$ , $j = 1, 2, \dots, 12$ . The internal degrees-of-freedom, corresponding to $\psi_{13}, \psi_{14}, \psi_{15}, \psi_{16}$ , are eliminated by the solution of the local problem. Only the unique, shared, boundary degrees-of-freedom are retained in the global problem. ....	69
3.7	Locus of $\Delta = 0$ for $s = -1$ and $\delta = 0$ on the $Pe_h, \epsilon$ -plane (left) and on an elevation plot of the function $\Delta$ . It is seen that $\epsilon > 2$ prevents the determinant from vanishing for all Péclet numbers. ....	74
3.8	Schematic of the behavior of the new method. In the advective limit, the solution exhibits upwind influence, whereas in the diffusive limit the solution behaves like the continuous solution although it is not identical to it in the case $f \neq 0$ . ....	76
3.9	In the advective limit, outflow and sink nodes are stabilized by the $\delta$ -term. Strictly speaking, the sink-node cases are precluded by our assumption that $\mathbf{a}$ is solenoidal. Nevertheless, in numerical calculations $\mathbf{a}$ will also be a discrete approximation and therefore it will typically not be exactly solenoidal. See Hughes and Wells [91] for a discussion of this issue. ....	77
3.10	Solution plots in terms of varying Péclet number, on a uniform mesh of 4 elements, with $f = 0$ . Red, exact solution; blue, MDG $\bar{\phi}_h$ ; light blue, MDG $\phi_h$ ; magenta, global DG solution without local condensation. ....	79
3.11	Solution plots in terms of varying Péclet number, on a uniform mesh of 4 elements, with $f = 1$ . Red, exact solution; blue, MDG $\bar{\phi}_h$ ; light blue, MDG $\phi_h$ ; magenta, global DG solution without local condensation. ....	80
3.12	Solution plots in terms of varying mesh size, on uniform meshes of 2, 8, and 32 elements, $Pe_L = 24$ , with $f = 0$ . Red, exact solution; blue, MDG $\bar{\phi}_h$ ; light blue, MDG $\phi_h$ ; magenta, global DG solution without local condensation. ....	81
3.13	Solution plots in terms of varying mesh size, on uniform meshes of 2, 8, and 32 elements, $Pe_L = 24$ , with $f = 1$ . Red, exact solution; blue, MDG $\bar{\phi}_h$ ; light blue, MDG $\phi_h$ ; magenta, global DG solution without local condensation. ....	82
3.14	Convergence rates, skew ( $s = +1$ ) version, with $f = 0$ . Blue, MDG $\bar{\phi}_h$ ; light blue, MDG $\phi_h$ ; magenta, global DG solution without local condensation; red, $(Pe_h)^2$ slope. ....	83
3.15	Convergence rates, neutral ( $s = 0$ ) version, with $f = 0$ . Blue, MDG $\bar{\phi}_h$ ; light blue, MDG $\phi_h$ ; magenta, global DG solution without local condensation; red, $(Pe_h)^2$ slope. ....	84
3.16	Convergence rates, symmetric ( $s = -1$ ) version, with $f = 0$ . Blue, MDG $\bar{\phi}_h$ ; light blue, MDG $\phi_h$ ; magenta, global DG solution without local condensation; red, $(Pe_h)^2$ slope. ....	85
3.17	Convergence rates in the $L^2$ -norm of the error, symmetric ( $s = -1$ ) version, with $f = 1$ . Blue, MDG $\bar{\phi}_h$ ; light blue, MDG $\phi_h$ ; magenta, global DG solution without local condensation; red, $(Pe_h)^2$ slope. ....	86

3.18	Convergence rates in the $H^1$ broken seminorm of the error, symmetric ( $s = -1$ ) version, with $f = 1$ . Blue, MDG $\bar{\phi}_h$ ; light blue, MDG $\phi_h$ ; magenta, global DG solution without local condensation; red, $(Pe_h)^1$ slope. ....	87
3.19	Convergence rates in the $L^1$ -norm of the error, symmetric ( $s = -1$ ) version, with $f = 1$ . Blue, MDG $\bar{\phi}_h$ ; light blue, MDG $\phi_h$ ; magenta, global DG solution without local condensation; red, $(Pe_h)^2$ slope. ....	88
3.20	Advection skew to the mesh, $\theta = 30^\circ$ . Left, continuous representation of the MDG solution, $\bar{\phi}_h$ ; center, discontinuous representation, $\phi_h$ ; right, solution of the global DG method without local condensation. ....	90
3.21	Advection skew to the mesh, $\theta = 30^\circ$ . Left, solution at $y/L = .5$ ; right, solution at $x/L = 0$ . Blue, MDG $\bar{\phi}_h$ ; light blue, MDG $\phi_h$ ; magenta, global DG solution without local condensation. ....	91
3.22	Advection skew to the mesh, $\theta = 45^\circ$ . Left, continuous representation of the MDG solution, $\bar{\phi}_h$ ; center, discontinuous representation, $\phi_h$ ; right, solution of the global DG method without local condensation. ....	92
3.23	Advection skew to the mesh, $\theta = 45^\circ$ . Left, solution at $y/L = .5$ ; right, solution at $x/L = 0$ . Blue, MDG $\bar{\phi}_h$ ; light blue, MDG $\phi_h$ ; magenta, global DG solution without local condensation. ....	93
3.24	Advection skew to the mesh, $\theta = 60^\circ$ . Left, continuous representation of the MDG solution, $\bar{\phi}_h$ ; center, discontinuous representation, $\phi_h$ ; right, solution of the global DG method without local condensation. ....	94
3.25	Advection skew to the mesh, $\theta = 60^\circ$ . Left, solution at $y/L = .5$ ; right, solution at $x/L = 0$ . Blue, MDG $\bar{\phi}_h$ ; light blue, MDG $\phi_h$ ; magenta, global DG solution without local condensation. ....	95
3.26	Rotating flow. Left, continuous representation of the MDG solution, $\bar{\phi}_h$ ; center, discontinuous representation $\phi_h$ ; right, solution at $y/L = .5$ , in which the continuous and discontinuous solutions are seen to overlap. ....	96
4.1	The space $\Phi_h(\Omega)$ (left) and the corresponding minimal $C^0$ space $\bar{\Phi}_h(\Omega)$ (right). ...	101
4.2	Orientation of internal edges in $\mathcal{T}_h$ and $+/-$ elements with respect to an edge (left). Partition of element boundary into $\partial^+ K$ and $\partial^- K$ (right). ....	101
5.1	Interpretation of the force flux at $\mathbf{x}$ across a plane with unit normal $\mathbf{n}$ . ....	119
5.2	Peridynamic stress components in a body occupying the upper half-space (Example 1). 121	
7.1	Coupled domain geometry ....	134
7.2	Ghost atoms (empty circles) near $\Gamma_{md}$ used to compute interatomic forces. ....	143

7.3	One dimensional heat conduction: mesh and atomic positions for $h = 4\ell$ . . . . .	149
7.4	Temperature profiles for $h = 2\ell$ and $\tau = 25\text{ ps}$ at $t = 0.0, 12.5, 1000.0\text{ ps}$ . . . . .	150
7.5	Root mean square fluctuations of temperature at center of the domain as a function of $\tau$ for various $h$ . . . . .	151
7.6	Mesh and atomic positions for the coupled simulation of the diffusion of an initial Gaussian temperature field . . . . .	152
7.7	Comparison of a sequence of temperature contours for the coupled simulation (left) and the reference simulation (right): (a) initial $t = 0.0\text{ ps}$ , (b) $t = 30.0\text{ ps}$ , and (c) $t = 70.0\text{ ps}$ . . . . .	154
7.8	Comparison of integrated temperature evolution for the diffusion of a Gaussian temperature field . . . . .	155
7.9	Mesh and atomic positions for $a = 8$ showing regions of different atomic mass . . . .	156
7.10	Temperature profiles for various atomic domain sizes $a$ . . . . .	157

# List of Tables

2.1	Simulation parameters and results for spatial resolution study at $Re_\tau = 100$ . . . . .	44
2.2	Simulation parameters and results for $4 \times 4 \times 4$ mesh using $p = 5$ to compare spectral filtering against dealiasing $Re_\tau = 100$ . . . . .	44
2.3	Simulation parameters and results for $6 \times 4 \times 4$ mesh using $p = \{6, 5, 5, 6\}$ at $Re_\tau = 100$ to evaluate the effectiveness of the $\ell$ VMS model. . . . .	45
2.4	Simulation parameters and results for $6 \times 8 \times 6$ mesh using $p = \{6, 6, 5, 5, 5, 5, 6, 6\}$ at $Re_\tau = 395$ to evaluate the effectiveness of the $\ell$ VMS model. . . . .	45
3.1	Analysis of the sign of the determinant $\Delta$ for $\delta = 0$ . . . . .	74
4.1	Specialization of fluxes and weight function for the donor DG methods. . . . .	105
4.2	Specialization of fluxes for the local problem. . . . .	106

This page intentionally left blank.

# Chapter 1

## Introduction

An emerging consensus within the computational sciences is that simulation over a broad range of scales is needed for tomorrow's efforts in science and engineering. Multiscale modeling and simulation has emerged as an important new discipline, and today entire journals, conferences and workshops are devoted to the subject. There is much to be done in developing methods to bridge length and time scales, as most classical modeling methods are either invalid or computationally infeasible outside their native spatial and temporal scales. Multiscale mathematics is a systematic approach for analyzing the integration of heterogeneous models and data over a broad range of scales.

We separate the accomplishments of this LDRD project into two categories of multiscale. The first, continuum-to-continuum (CtC), includes problems that allow application of the same continuum model at all scales with the primary barrier to simulation being computing resources. The second, atomistic-to-continuum (AtC), represents applications where detailed physics at the atomistic or molecular level must be simulated to resolve the small scales, but the effect on and coupling to the continuum level is frequently unclear.

### **Continuum-to-Continuum Multiscale**

We have explored two approaches for continuum-to-continuum (CtC) multiscale modeling that leverage the flexibility of discontinuous Galerkin methods with the variational multiscale method: local variational multiscale and hybrid continuous/discontinuous Galerkin methods.

In Chapter 2 we present the local variational multiscale ( $\ell$ VMS) method for large eddy simulation in which high-order DG representations are used on each element with a VMS decomposition performed locally on each element. This method enables a surgical approach to subgrid-scale modeling that allows multiscale models and model parameters to be varied on an element-by-element manner. In general, distinct multiscale representations can be used on neighboring elements and numerical fluxes are devised that play the role of inter-scale transfer operators between different multiscale representations on each element. The capabilities of  $\ell$ VMS are explored in the context of wall-bounded turbulence for planar, compressible turbulent channel flow. In so doing, we address resolution requirements, numerical dissipation, and aliasing errors as well as the important issue of scale separation that is specific to the VMS approach. Through detailed results, the flexibility of  $\ell$ VMS is demonstrated for efficient and accurate simulation of wall-bounded turbulence and this work lays the foundation for extensions of this method to more complex flows.

The second approach we have considered is a hybrid continuous-discontinuous Galerkin multiscale formulation. The  $\ell$ VMS method discussed above provides explicit support for rich, hierarchical multiscale representations. However, there is also need for multiscale representations that can be directly utilized by second-order finite element and finite volume codes that are commonly used

within DOE applications. In Chapters 3 and 4 we discuss the second aspect of our CtC multiscale research, which develops new methods that either extend or extract multiscale representations from more traditional discretizations.

We have developed a new class of Discontinuous Galerkin (DG) methods based on variational multiscale ideas. Our approach combines the advantages of DG methods with the attractive and more efficient computational structure of a continuous Galerkin method. We begin with an additive decomposition of the discontinuous finite element space into continuous (coarse) and discontinuous (fine) components. The continuous space represents the coarse-scale approximation and the difference with the discontinuous space is the fine-scale approximation. A standard global discontinuous Galerkin method may be applied to the discontinuous space. The unique feature of the formulation is the use of local, element-wise problems, to define the discontinuous field in terms of the degrees of freedom of the continuous field. The local problems employ weakly imposed boundary conditions and the solutions remain discontinuous but they are parameterized by the degrees of freedom of the smaller (in dimension) continuous space. The global problem has the equation size and structure of a continuous Galerkin method but is indeed a discontinuous Galerkin method. The local problems serve to project the solution into a reduced-dimensional subspace that expresses the PDE structure of the problem considered. This aspect is related to methods used in wave propagation problems, relying on numerical fluxes inspired by local Riemann solutions, but here the local problems are solved numerically using the local basis functions. Effectively, the local problems give rise to interscale transfer operators and can be interpreted as providing constitutive relations that express fine-scales in terms of the coarse scales. We illustrate the new class of DG methods for a scalar advection-diffusion problem.

### **Atomistic-to-Continuum Multiscale**

Atomistic-to-continuum multiscale research addresses the fundamental problems in multiscale modeling that cannot be solved merely by building bigger and faster computers but instead require the development of new computational mathematics, as the governing physics and thus the governing partial differential equations often also change with the scale. Our work in this area is in consort with the DOE program “A Mathematical Analysis of Atomistic to Continuum Coupling Methods” DE-FG01-05ER05-16. We have pursued two different avenues of investigation.

In the first, we consider the Silling’s peridynamic (PD) model. The well-documented local/nonlocal interface issue arising when coupling an atomistic model to a local linear elastic model is a fundamental difficulty that cannot be completely overcome by any coupling scheme. We seek to avoid this issue altogether with the peridynamic model, which is a fundamentally nonlocal continuum mechanics model based on the idea that pairs of particles exert forces on each other across a finite distance. In Chapter 5, a notion of a peridynamic stress tensor derived from nonlocal interactions is defined. At any point in the body, this stress tensor is obtained from the forces within peridynamic bonds that geometrically go through the point. The peridynamic equation of motion can be expressed in terms of this stress tensor, and the result is formally identical to the Cauchy equation of motion in the classical model, even though the classical model is a local theory. We also establish that this stress tensor field is unique in a certain function space compatible with finite element approximations.

The local/nonlocal AtC interface issue also complicates any practical scheme for coarse-graining molecular dynamics into classical continuum mechanics (CM), for instance when the finite element method is used for the classical CM discretization. In Chapter 6 we describe a method for representing a collection of atoms at finite temperature as a peridynamic body. The PD representation



is homogenized and rescaled to enable a statistical coarse-graining of molecular dynamics. This coarse-graining avoids the use of a unit cell and the Cauchy-Born rule. In contrast with classical CM, the PD homogenized system of linear springs and masses is shown to have the same dispersion relation as the original spring-mass system.

In the second avenue investigated, we address the issue of AtC bidirectional heat transfer. This is a difficult problem, as temperature is an aggregate property of a collection of atoms, while it is a scalar field variable of a continuum domain. In Chapter 7 we present a seamless, energy-conserving method to thermally couple atomistic and continuum representations of material. This technique allows a molecular dynamics simulation to be used in localized regions of the computational domain, surrounded and overlaid by a continuum finite element representation. Thermal energy can pass between the two regions in either direction, making larger simulations of nanoscale thermal processes possible. We discuss theoretical developments and numerical implementation details. In addition, we present and analyze a set of representative simulations.

For the work we have elected to showcase in this report, Chapter 3 appeared in *Computer Methods in Applied Mechanics and Engineering* [80], Chapter 4 appeared as a proceedings article for the 2005 International Conference in Large Scale Scientific Computing in Sozopol, Bulgaria [19], Chapter 5 was accepted for publication in *the Journal of Mechanics and Physics of Solids* [107], Chapter 6 was submitted to *Physical Review Letters* [108], and Chapter 7 was submitted to a special issue of *Computer Methods in Applied Mechanics and Engineering* [154]. For completeness, we also provide a listing of other publications have been produced as a result of the work for this project, and have either been published or are awaiting publication:

1. P. BOCHEV, T. HUGHES, AND G. SCOVAZZI, *Variational multiscale framework for DG*, ASME paper IMECE2005-80894, Proceedings of 2005 ASME International Mechanical Engineering Congress and Exposition, Orlando Florida, 2005.
2. S. RAMAKRISHNAN AND S. COLLIS, *The Local Variational Multi-Scale Method for Turbulence Simulation*, Sandia Report, SAND2005-2733, May, 2005.
3. S. COLLIS AND S. RAMAKRISHNAN, *The local variational multiscale method*, In Computational Fluid and Solid Mechanics, K.J. Bathe (Ed), Elsevier Science Ltd., p. 623-627, 2005.
4. S. RAMAKRISHNAN AND S. COLLIS, *Partition Selection in Multi-Scale Turbulence Modeling*, Physics of Fluids, Volume 18, Issue 7, pp. 075105-075105-16, 2006.
5. T. HUGHES, G. SCOVAZZI, P. BOCHEV, AND A. BUFFA, *A multiscale Discontinuous Galerkin method with the computational structure of a continuous Galerkin method*, Computer Methods in Applied Mechanics and Engineering, Vol. 195, pp.2761-2787, 2006.
6. P. BOCHEV, T. HUGHES, AND G. SCOVAZZI, *A multiscale Discontinuous Galerkin method*, Proceedings of LSSC 2005, I. Lirkov, S. Margenov and J. Wasniewski (Eds.), Springer Lecture Notes in Computer Science 3743, pp. 84-93, 2006.
7. R. LEHOUCQ, S. SILLING, *Force Flux and the Peridynamic Stress Tensor*, Accepted for publication in the Journal of Mechanics and Physics of Solids, June, 2007.
8. R. LEHOUCQ, S. SILLING, *Statistical Coarse-graining of Molecular Dynamics into Peridynamics*, Submitted to Physical Review Letters, September, 2007.

9. G. WAGNER, R. JONES, J. TEMPLETON, AND M. PARKS, *An Atomistic-to-Continuum Coupling Method for Heat Transfer in Solids*, Submitted to Computer Methods in Applied Mechanics and Engineering, July, 2007.

Additionally, the following presentations have been given by group members on work for this project:

1. P. BOCHEV, Invited presentation, *A Multiscale Discontinuous Galerkin Method*, 5th International Conference on Large-Scale Scientific Computations, Sozopol, Bulgaria, June 2005.
2. G. WAGNER, *The Bridging Scale Decomposition Method with Time Filtering for Finite Temperature Simulations*, 8th US National Congress on Computational Mechanics, Austin, TX., July 25-27, 2005.
3. P. BOCHEV, *Variational Multiscale Framework for Discontinuous Galerkin Methods*, 7th World Congress on Computational Mechanics, Los Angeles, CA., July 16-22, 2006.
4. G. WAGNER<sup>1</sup>, *Atomistic-to-Continuum Coupling for Heat Transfer in Solids*, 7th World Congress on Computational Mechanics, Los Angeles, CA., July 16-22, 2006.
5. G. WAGNER, Invited Presentation, *Atomistic-to-Continuum Coupling for Multiscale Solid Materials Simulation*, Center for Advanced Vehicular Systems, Mississippi State University, Starkville, MS., Sept. 2006.
6. G. WAGNER, Invited Presentation, *An Atomistic-to-Continuum Coupling Method for Non-Equilibrium Heat Transfer in Solids*, 2nd Workshop on Atomistic-to-Continuum Coupling Methods, Austin, TX., April 2-3, 2007.
7. J. TEMPLETON, *An Atomistic-to-Continuum Coupling Method for Non-Equilibrium Heat Transfer in Solids*, Seventh Biennial Tri-Laboratory Engineering Conference, Albuquerque, NM., May 7-10, 2007.
8. G. WAGNER, Invited Presentation, *An Atomistic-to-Continuum Coupling Method for Non-Equilibrium Heat Transfer in Solids*, 9th US National Congress on Computational Mechanics, San Francisco, CA., July 23-26, 2007.

---

<sup>1</sup>Canceled due to family illness.

## Chapter 2

# The Local Variational Multiscale Method: Applications to Wall-bounded Turbulence

**Principle Authors: Srinivas Ramakrishnan<sup>1</sup> and S. Scott Collis**

This paper presents the Local Variational Multiscale Method,  $\ell$ VMS, for large eddy simulation that combines a Discontinuous Galerkin (DG) spatial discretization with a Variational Multi-Scale (VMS) approach to subgrid-scale modeling. The resulting method enables a surgical approach to subgrid-scale modeling that allows multiscale models and model parameters to be varied on an element-by-element manner. The capabilities of  $\ell$ VMS are explored in the context of wall-bounded turbulence for planar, compressible turbulent channel flow. In so doing, we address resolution requirements, numerical dissipation, and aliasing errors as well as the important issue of scale separation that is specific to the VMS approach. Through detailed results, the flexibility of  $\ell$ VMS is demonstrated for effective simulation of wall-bounded turbulence and this work lays the foundation for extensions of this method to more complex flows.

## 2.1 Introduction

Accurate and efficient turbulence simulation in complex geometries is a formidable challenge. The high fidelity of Direct Numerical Simulation (DNS) makes it an ideal tool for research [118]. However, the prohibitive cost of DNS makes it unsuitable as a tool for the working engineer in the foreseeable future. Furthermore, the restrictions of high-order methods, such as global spectral methods that are commonly used for DNS, to structured grids is not practical, in general, for realistic flow configurations. Meanwhile, the overwhelming need for computational efficiency led to the adoption of Reynolds Averaged Navier-Stokes (RANS) simulations as the industry standard for turbulence prediction.

Fortunately, crucial advances in the development of Large Eddy Simulation (LES), such as the dynamic procedure for tuning the model coefficient [66], led to successful applications in a variety of flows. Moreover, the ever increasing growth of computational power and the need to represent and study the unsteady dynamics in complex flows with greater fidelity than afforded by RANS has led to concerted efforts in improving LES for such flows. Simultaneously, hybrid methods are proposed that attempt to build on the experience gleaned

---

<sup>1</sup>Mechanical Engineering and Materials Science, Rice University, Houston, TX 77005-1892

in the development and application of LES and RANS (see, e.g., [8, 105, 142, 149]).

While these approaches show some advantages in the interim, their long term success is limited, for a number of well-known reasons:

1. Models are often tuned to match mean flow quantities;
2. They use ad hoc blending functions to couple LES and RANS regions and/or wall functions;
3. The methods often do not converge to the exact solution (DNS);
4. Spatial filters (LES) are used that have known difficulties in unstructured grids and near physical boundaries;
5. Models are often developed without regard for discretization; and
6. Low-order numerical methods are employed that are unsuitable for accurate prediction in unsteady flows and are known to interact adversely with subgrid scale models.

Recently, the development of the Variational Multi-Scale (VMS) [42, 88] method as a paradigm for LES has yielded promising results for a variety of applications [89, 90, 103, 133]. VMS is attractive for LES as it addresses many of the limitations enumerated above. In addition, the use of variational projection to effect scale separation in lieu of spatial filtering makes the extension to complex geometries particularly straightforward.

Therefore, Collis [43] proposed a framework, building on the promise of VMS, suitable for LES in complex geometries. This involves a merger of a Discontinuous Galerkin (DG) spatial discretization with Variational Multi-Scale (VMS) that was termed Local VMS ( $\ell$ VMS). This framework has many desirable features while, simultaneously, addressing the limitations of traditional approaches outlined above.

Overall, the DG/VMS [43] combination is particularly synergistic, since high-order hierarchical representations at the element-level are a natural framework for *a priori* scale identification crucial for multi-scale modeling. The flexibility engendered by  $\ell$ VMS relates to the inherent features of the individual components. The locality introduced by DG in *physical space* allows for a natural coupling of different fidelity models in adjacent regions in the physical domain through numerical fluxes. And, VMS introduces locality in *spectral space* that allows a natural coupling of a range of traditional approaches such as DNS and LES on adjacent range of scales. Thus, we obtain a method that is flexible both from a modeling and computational efficiency perspective while offering mathematical consistency [88], and high-order accuracy [12]. Importantly,  $\ell$ VMS is also compatible with unstructured meshes for complex geometries making it particularly attractive for application to engineering flows.

The current article updates our latest progress in the development of the DG/VMS framework [43], building on our prior efforts [44, 131]. The organization of the paper is as follows. We begin with a brief description of the DG method for the Navier–Stokes equations of motion followed by an introduction to VMS modeling to arrive at the  $\ell$ VMS model

equations. Next, we present strategies that address the non-linear stability of simulations. Then, we present numerical results starting with a detailed resolution study to record the effects of the DG spatial discretization on turbulence using a planar turbulent channel flow. Before introducing multi-scale modeling, we test the strategies introduced for improving the non-linear stability of simulations. Selecting a suitable strategy for dealiasing, we introduce a VMS model to account for the SGS effects. Finally, we conclude with a summary of our findings.

## 2.2 Local Variational Multi-Scale ( $\ell$ VMS) Method

We present the description of the Discontinuous Galerkin method following the discussion of Collis [43]. We begin with the strong form of the compressible Navier–Stokes equations of motion.

$$\mathbf{U}_{,t} + \mathbf{F}_{i,i} - \mathbf{F}_{i,i}^v = \mathbf{S} \quad \text{in } \Omega, \quad (2.1a)$$

$$\mathbf{U}(\mathbf{x}, 0) = \mathbf{U}_0(\mathbf{x}), \quad (2.1b)$$

where  $\mathbf{U} = \{\rho, \rho \mathbf{u}, \rho e\}^T$  is the vector of conserved variables,  $\rho$  is the fluid density,  $\mathbf{u} = \{u, v, w\}^T$  is the fluid velocity vector, and  $e = e_{int} + \frac{u_i u_i}{2}$  is the total energy per unit mass ( $e_{int}$  is the internal energy). The inviscid and viscous flux vectors in the  $i$ th coordinate direction are  $\mathbf{F}_i(\mathbf{U})$  and  $\mathbf{F}_i^v(\mathbf{U})$  defined as

$$\mathbf{F}_i(\mathbf{U}) = u_i \mathbf{U} + p \begin{Bmatrix} 0 \\ \delta_{1i} \\ \delta_{2i} \\ \delta_{3i} \\ u_i \end{Bmatrix}, \quad \mathbf{F}_i^v(\mathbf{U}) = \begin{Bmatrix} 0 \\ \tau_{1i} \\ \tau_{2i} \\ \tau_{3i} \\ \tau_{ij} u_j - q_i \end{Bmatrix}, \quad (2.2)$$

where  $p$  is the thermodynamic pressure,  $\tau_{ij} = 2\mu S_{ij} + \lambda u_{k,k} \delta_{ij}$ , the strain rate tensor  $S_{ij} = \frac{1}{2}(u_{i,j} + u_{j,i})$  and  $\lambda$  is the bulk viscosity. Also, the heat flux,  $q_i = -\kappa T_{,i}$  where  $\kappa$  is the molecular conductivity and  $T$  is the temperature. Any source terms present are included in  $\mathbf{S}$ .

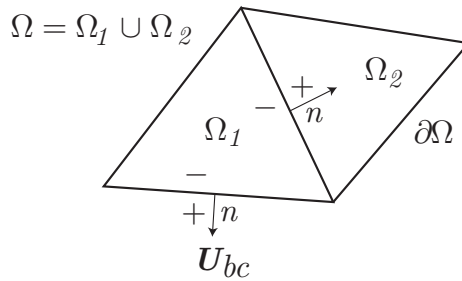


**Figure 2.1.** Schematic of DGM discretization [44].

We solve (2.1a) subject to the appropriate boundary conditions specific to the problem of interest. Also, a state equation, such as the ideal gas law to relate the thermodynamic

variables and constitutive laws to define the physical properties such as viscosity and thermal conductivity as functions of the conserved variables provide closure to the system of equations [73].

The fixed spatial domain for the problem is denoted by  $\Omega$ , which is an open, connected, bounded subset of  $\mathbb{R}^3$ , with boundary  $\partial\Omega$ . Let  $\mathcal{P}_h$  be a partition of the domain  $\Omega$  into  $N$  subdomains  $\Omega_e$  where

$$\bar{\Omega} = \bigcup_{e=1}^N \bar{\Omega}_e \quad \text{and} \quad \Omega_e \cap \Omega_f = \emptyset \quad \text{for} \quad e \neq f. \quad (2.3)$$

Now, we construct the weak form of the equations starting with the strong form of the compressible Navier–Stokes equations (2.1a). Consider a single subdomain,  $\Omega_e$ , we multiply (2.1a) by a weighting function,  $\mathbf{W}$ , that is continuous in  $\Omega_e$  and integrate the flux terms by parts

$$\int_{\Omega_e} (\mathbf{W}^T \mathbf{U}_{,t} + \mathbf{W}_{,i}^T (\mathbf{F}_i^v - \mathbf{F}_i)) d\mathbf{x} + \int_{\partial\Omega_e} \mathbf{W}^T (\mathbf{F}_n - \mathbf{F}_n^v) ds = \int_{\Omega_e} \mathbf{W}^T \mathbf{S} ds, \quad (2.4)$$

where  $\mathbf{F}_n = \mathbf{F}_i n_i$ . In the standard Galerkin formulation, where the solution is continuous across the elements, the summation over all the elements in the domain would lead to the flux terms telescoping to the boundary of the spatial domain  $\partial\Omega$ .

However, discontinuous Galerkin allows the solution and weighting functions to be discontinuous across element interfaces (see Fig. 2.1) and the coupling of the solution between adjacent elements is achieved through suitably defined numerical fluxes for both the inviscid flux ( $F_i$ ) and the viscous flux ( $F_i^v$ ). Since the solution is not single-valued at the element interface the numerical fluxes for the inviscid and viscous flux terms generally assume the following forms ( $F_i \rightarrow \hat{\mathbf{F}}_n(\mathbf{U}^-, \mathbf{U}^+)$ ) and ( $F_i^v \rightarrow \hat{\mathbf{F}}_i^v(\mathbf{U}^-, \mathbf{U}_{,j}^-, \mathbf{U}^+, \mathbf{U}_{,j}^+)$ ), respectively.

Now, summing over the domain and introducing the numerical fluxes, we obtain

$$\begin{aligned} B_{DG}(\mathbf{W}, \mathbf{U}) &= \sum_{e=1}^N \int_{\Omega_e} (\mathbf{W}^T \mathbf{U}_{,t} + \mathbf{W}_{,i}^T (\mathbf{F}_i^v - \mathbf{F}_i)) d\mathbf{x} \\ &+ \sum_{e=1}^N \int_{\partial\Omega_e} \mathbf{W}^T (\hat{\mathbf{F}}_n(\mathbf{U}^-, \mathbf{U}^+)) ds \\ &- \sum_{e=1}^N \int_{\partial\Omega_e} \mathbf{W}^T (\hat{\mathbf{F}}_i^v(\mathbf{U}^-, \mathbf{U}_{,j}^-, \mathbf{U}^+, \mathbf{U}_{,j}^+)) ds \\ &= \sum_{e=1}^N \int_{\Omega_e} \mathbf{W}^T \mathbf{S} ds, \end{aligned} \quad (2.5)$$

where the  $\mathbf{U}^+$  and  $\mathbf{U}^-$  states are illustrated in Fig. 2.1. For a particular element on the physical boundary,  $\partial\Omega$ ,  $\mathbf{U}^+ = \mathbf{U}_{bc}$ . Meanwhile, for the inter-element boundaries,  $\mathbf{U}^+$  is obtained from the neighboring element. Thus, all boundary conditions and interface conditions are set through the numerical fluxes.

While there are a wide range of choices for both the inviscid and viscous numerical fluxes [38], we have chosen to use a Lax–Friedrichs method for the Euler flux

$$\hat{\mathbf{F}}_n(\mathbf{U}^-, \mathbf{U}^+) = \frac{1}{2} (\mathbf{F}_n(\mathbf{U}^-) + \mathbf{F}_n(\mathbf{U}^+)) + \frac{1}{2} [\lambda_m (\mathbf{U}^- - \mathbf{U}^+)] , \quad (2.6)$$

where  $\lambda_m$  is the maximum, in absolute value, of the eigenvalues of the Euler Jacobian  $\mathbf{A}_n = \partial \mathbf{F}_n / \partial \mathbf{U}$ .

For the numerical viscous flux, we use the method of Bassi and Rebay [11], that we shall refer to hereafter as the Bassi-Rebay (BR) flux. First, a “jump savvy” gradient of the state,  $\sigma_j \sim \mathbf{U}_{,j}$  is computed by solving

$$\sum_{e=1}^N \int_{\Omega_e} \mathbf{W}^T \sigma_j d\mathbf{x} = - \sum_{e=1}^N \int_{\Omega_e} \mathbf{W}_{,j}^T \mathbf{U} d\mathbf{x} + \sum_{e=1}^N \int_{\partial\Omega_e} \mathbf{W}^T \hat{\mathbf{U}}_{n_j} ds \quad (2.7)$$

$\forall \mathbf{W} \in \mathcal{V}(\mathcal{P}_h)$  and for each direction,  $j$ , where

$$\hat{\mathbf{U}} \equiv \frac{1}{2} (\mathbf{U}^- + \mathbf{U}^+) . \quad (2.8)$$

The BR [11] viscous flux is then computed using

$$\hat{\mathbf{F}}_n^v(\mathbf{U}^-, \sigma_j^-, \mathbf{U}^+, \sigma_j^+) = \frac{1}{2} (\mathbf{F}_n^v(\mathbf{U}^-, \sigma_j^-) + \mathbf{F}_n^v(\mathbf{U}^+, \sigma_j^+)) . \quad (2.9)$$

While this method is known to be only “weakly stable” [7], we have not encountered any difficulties for the problems considered here and this method has been used successfully in prior studies [11]. The above flux definition (2.8) is central to the current work. Essentially, this numerical flux is responsible for enforcing the Dirichlet (wall) boundary conditions. Also, the VMS model, to be introduced shortly, that is an eddy viscosity model that resembles the physical diffusion term is implemented in similar fashion, with appropriate modifications consistent with a multi-scale model.

In setting boundary conditions weakly through the numerical fluxes, one must construct a state,  $\mathbf{U}_{bc}$ , that enforces the appropriate boundary conditions and Atkins [9] provides a discussion of the important issues involved in selecting  $\mathbf{U}_{bc}$ . For the Navier–Stokes calculations reported here, we use the following approach at the isothermal wall boundaries. We evaluate  $\mathbf{U}_{bc}$  separately for the convective and viscous fluxes.

Let  $m_i$  be the suitable conditions on the momentum for the Euler flux that are commonly used [9, 44]. Then the reconstructed state at a wall for the convective flux is

$$\mathbf{U}_{bc} = \left\{ \begin{array}{c} \rho^- \\ \rho^- m_1 \\ \rho^- m_2 \\ \rho^- m_3 \\ \rho^- e^- + 0.5 \rho^- (m_1^2 + m_2^2 + m_3^2) \end{array} \right\} . \quad (2.10)$$

This state enforces the no-penetration condition which is appropriate for both inviscid and viscous calculations. For the viscous flux, the no-slip condition is enforced using

$$\mathbf{U}_{bc} = \left\{ \begin{array}{c} \rho^- \\ 0 \\ 0 \\ 0 \\ \rho^- T_w / (\gamma(\gamma - 1)M^2) \end{array} \right\}, \quad (2.11)$$

where  $T_w$  is the prescribed wall temperature,  $\gamma$  is the ratio of specific heats, and  $M$  is the reference Mach number. Now, the discontinuous Galerkin problem statement can be compactly stated using (2.5), (2.6), and (2.9) as: Given  $\mathbf{U}_0 = \mathbf{U}_0(\mathbf{x})$ , for  $t \in (0, T)$ , find  $\mathbf{U}(\mathbf{x}, t) \in \mathcal{V}(\mathcal{P}_h) \times H^1(0, T)$  such that  $\mathbf{U}(\mathbf{x}, 0) = \mathbf{U}_0(\mathbf{x})$  and

$$B_{DG}(\mathbf{W}, \mathbf{U}) = (\mathbf{W}, \mathbf{S}) \quad \forall \mathbf{W} \in \mathcal{V}(\mathcal{P}_h), \quad (2.12)$$

where  $\mathcal{V}(\mathcal{P}_h)$  is a so-called broken space [14]. If  $\mathcal{V}(\mathcal{P}_h)$  is restricted to a space of continuous functions, then one recovers the classical continuous Galerkin approximation upon using the consistency properties of the numerical fluxes [38].

The DG method described above can be considered a hybrid between finite-element and finite-volume methods that has the following salient features that make it a promising method for turbulence simulation.

1. High order (spectral) accuracy on arbitrary grids.
2. Local  $hp$ - refinement capability.
3. Local conservation allows the use of different models in adjoining elements.
4. Highly parallelizable for computational efficiency.
5. Boundary and interface conditions are set weakly through numerical fluxes.
6. The orthonormal hierarchical basis on each element is a natural framework for scale separation that is crucial for multi-scale turbulence models (see below).

Importantly, since DG methods are ideal for hyperbolic systems or nearly hyperbolic systems, it holds great potential for high Reynolds number turbulent flows.

## 2.3 $\ell$ VMS Formulation

Now, we provide a brief overview of the VMS method before we merge it with the DG spatial discretization presented above. For a detailed exposition on the VMS method, the reader is requested to consult the articles by Hughes *et al.* [88] and Collis [42]. In VMS, the projection operation partitions the solution as  $\mathbf{U} = \bar{\mathbf{U}} + \tilde{\mathbf{U}} + \mathbf{U}'$  where  $\bar{\mathbf{U}}$  are the large scales,  $\tilde{\mathbf{U}}$  are the small scales and  $\mathbf{U}'$  are the unresolved scales. Introducing the scale



decomposition for the test functions, the discrete, modeled Navier–Stokes equations for the *resolved scales* in the domain  $\Omega$  can be written formally as

$$B(\widetilde{\mathbf{W}}, \widetilde{\mathbf{U}}) = (\widetilde{\mathbf{W}}, \mathbf{F})_{\mathbf{Q}} + \overline{M}(\overline{\mathbf{W}}, \overline{\mathbf{U}})_{\mathbf{Q}} + \widetilde{M}(\widetilde{\mathbf{W}}, \widetilde{\mathbf{U}})_{\mathbf{Q}}, \quad (2.13)$$

where  $B(\widetilde{\mathbf{W}})_{\Omega}$  denotes a variational form of the Navier–Stokes equations with weighting functions  $\widetilde{\mathbf{W}} = \overline{\mathbf{W}} + \widetilde{\mathbf{W}}$  that correspond to the resolved scales (see Collis [42] for details) and  $\overline{M}$ ,  $\widetilde{M}$  denote the model terms acting on the large and small scales, respectively. It is desirable that there be no direct modeling in the large scale equations ( $\overline{M} = 0$ ), while the small scales may have models such as a simple Smagorinsky closure, similar to classical LES. By changing the partitioning between large- and small-scales and/or by changing the form of the model terms, one can alter the formulation from DNS to LES thereby providing a true hybrid approach and this is a direction of research that we are currently considering [43]. Additionally, the VMS approach to Sub-Grid Scales (SGS) modeling is desirable for the reasons given below.

1. The variational formulation provides a solid mathematical foundation for turbulence modeling [42, 88].
2. Variational projection is used for scales separation allowing the extension to complex geometries straightforward – there are no commutativity or homogeneity issues like those that arise when using spatial filters (see e.g. [67, 88]).
3. The large scales have no direct model terms. Therefore, the exact solution satisfies the large-scale equations leading to a consistent method i.e. the solution converges to DNS in the limit of high resolution. This feature is missing from classical LES and RANS methods.
4. *A priori* scale separation allows for different modeling approximations on different scale ranges.
5. A simple constant coefficient Smagorinsky type model acting only on the smallest *resolved* scales has been shown to be effective for both the decay of homogeneous isotropic turbulence [89] and wall bounded flows [90, 123]. Also, the modeled equations are considerably simpler than the dynamic subgrid-scale model [66, 111] making calculations potentially more efficient.

Now, introducing the DG discretization and VMS modeling assumptions in equation (2.13), we obtain the  $\ell$ VMS equations as

$$B_{DG}(\widetilde{\mathbf{W}}, \widetilde{\mathbf{U}}) = (\widetilde{\mathbf{W}}, \mathbf{F})_{\mathbf{Q}} + \widetilde{M}_{DG}(\widetilde{\mathbf{W}}, \widetilde{\mathbf{U}})_{\mathbf{Q}}, \quad (2.14)$$

where  $\widetilde{M}_{DG}(\widetilde{\mathbf{W}}, \widetilde{\mathbf{U}})_{\mathbf{Q}}$  is the model flux, that is treated in the same manner as the viscous flux (see equations (2.7), (2.8) and (2.9)) with suitable modifications consistent with the multi-scale decomposition. To be more explicit, the flux is computed using just the small scales ( $\widetilde{\mathbf{U}}$ ), and therefore, the BR flux recast for the VMS model can be written as

$$\sum_{e=1}^N \int_{\Omega_e} \widetilde{\mathbf{W}}^T \widetilde{\sigma}_j d\mathbf{x} = - \sum_{e=1}^N \int_{\Omega_e} \widetilde{\mathbf{W}}_{,j}^T \widetilde{\mathbf{U}} d\mathbf{x} + \sum_{e=1}^N \int_{\partial\Omega_e} \widetilde{\mathbf{W}}^T \widehat{\mathbf{U}} n_j ds \quad (2.15)$$

$\forall \mathbf{W} \in \mathcal{V}(\mathcal{P}_h)$  for each direction,  $j$ , where

$$\hat{\mathbf{U}} \equiv \frac{1}{2} \left( \tilde{\mathbf{U}}^- + \tilde{\mathbf{U}}^+ \right). \quad (2.16)$$

The BR [11] viscous flux, for the VMS model, is then computed using

$$\hat{\mathbf{F}}_n^m(\tilde{\mathbf{U}}^-, \tilde{\sigma}_j^-, \tilde{\mathbf{U}}^+, \tilde{\sigma}_j^+) = \frac{1}{2} \left( \tilde{\mathbf{F}}_n^m(\tilde{\mathbf{U}}^-, \tilde{\sigma}_j^-) + \tilde{\mathbf{F}}_n^m(\tilde{\mathbf{U}}^+, \tilde{\sigma}_j^+) \right). \quad (2.17)$$

It remains to define the the model term  $\widetilde{M}_{DG}(\widetilde{\mathbf{W}}, \widetilde{\mathbf{U}})$  appearing the (2.14). Since we have assumed an orthogonal basis, the model represents the projection of the generalized Reynolds and cross stresses onto the small scales. For incompressible flows, this simplifies directly to the Reynolds and cross stresses. For compressible flows, there are additional terms arising from the variable density in the Reynolds stresses as well as from terms in the energy equation. For a thorough discussion of LES modeling issues in compressible flows, the interested reader is directed to the article by Martinelli *et al.* [116] that present results of *a priori* evaluation of the models developed for compressible flows.

With this background, we now merge the variational multi-scale method described above with the DG method described earlier and present the primal formulation. We denote the boundary of the domain  $\Omega$  as  $\partial\Omega = \Gamma_D \cup \Gamma_N$  where  $\Gamma_D$  is the portion of the boundary where Dirichlet conditions are specified and  $\Gamma_N$  is the portion of the boundary where Neumann conditions are set. The element boundary is denoted as  $\Gamma = \{\Gamma_D, \Gamma_N, \Gamma_0\}$  where  $\Gamma_0$  are the inter-element boundaries. Let  $\Omega_1$  and  $\Omega_2$  be two adjacent elements; let  $\Gamma_{12} = \partial\Omega_1 \cap \partial\Omega_2$ ; and let  $\mathbf{n}^{(1)}$  and  $\mathbf{n}^{(2)}$  be the corresponding outward unit normal vectors at that point. Let  $\mathbf{U}^{(e)}$  and  $\mathbf{F}_i^{(e)}$  be the trace of a state vector  $\mathbf{U}$  and flux vectors  $\mathbf{F}_i$ , respectively, on  $\Gamma_{12}$  from the interior of subdomain  $\Omega_e$ . Then, we define the average  $\langle \cdot \rangle$  and jump  $[\cdot]$  operators on  $\Gamma_{12}$  as

$$[\mathbf{U}n_i] = \mathbf{U}^{(1)}n_i^{(1)} + \mathbf{U}^{(2)}n_i^{(2)}, \quad (2.18a)$$

$$[\mathbf{F}_n] = \mathbf{F}_i^{(1)}n_i^{(1)} + \mathbf{F}_i^{(2)}n_i^{(2)}, \quad (2.18b)$$

$$\langle \mathbf{U} \rangle = \frac{1}{2} \left( \mathbf{U}^{(1)} + \mathbf{U}^{(2)} \right), \quad (2.18c)$$

$$\langle \mathbf{F}_i \rangle = \frac{1}{2} \left( \mathbf{F}_i^{(1)} + \mathbf{F}_i^{(2)} \right), \quad (2.18d)$$

where  $\mathbf{F}_n = \mathbf{F}_i n_i$ .

Here, the  $\ell$ VMS model takes the form of a generalized eddy diffusivity that on each subdomain,  $\Omega_e$ , is given as

$$M(\widetilde{\mathbf{W}}, \widetilde{\mathbf{U}}) = \int_{\partial\Omega_e} \widetilde{\mathbf{W}}^T \mathbf{F}_{n_e}^m(\widetilde{\mathbf{U}}) ds - \int_{\Omega_e} \widetilde{\mathbf{W}}_{,i}^T \mathbf{F}_i^m(\widetilde{\mathbf{U}}) d\mathbf{x}, \quad (2.19)$$

where the model flux  $\mathbf{F}_i^m(\widetilde{\mathbf{U}})$  is of the form  $\mathbf{F}_i^m(\widetilde{\mathbf{U}}) = \mathbf{D}_i^m(\widetilde{\mathbf{U}})\widetilde{\mathbf{U}}$  and the matrix  $\mathbf{D}_i^m(\widetilde{\mathbf{U}})$  is possibly a nonlinear differential operator.

Extending equation (2.19) to a form compatible with discontinuous Galerkin leads to

$$\begin{aligned}
M_{DG}(\tilde{\mathbf{W}}, \tilde{\mathbf{U}}) &= \int_{\Gamma_0} \left( [\tilde{\mathbf{W}}^T] \langle \mathbf{F}_n^m(\tilde{\mathbf{U}}) \rangle \right) + \int_{\partial\Omega} \left( \tilde{\mathbf{W}}^T \mathbf{F}_n^m(\tilde{\mathbf{U}}) \right) \\
&\quad - \sum_{\Omega_e \in \mathcal{P}_h} \int_{\Omega_e} \tilde{\mathbf{W}}_{,i}^T \mathbf{F}_i^m(\tilde{\mathbf{U}}) d\mathbf{x}
\end{aligned} \tag{2.20}$$

which clearly simplifies to a classical weak Galerkin approximation for continuous functions. On inter-element boundaries, an averaged flux is used while on the domain boundary one obtains a weighted integral of the modeled turbulent flux across the boundary. This last integral marks a dramatic difference between discontinuous Galerkin and standard Galerkin approximations [42, 88] on solid surfaces.

In general, the weighting functions for velocity at wall boundaries using traditional Galerkin forms are set to zero since they are assumed to satisfy the Dirichlet conditions exactly. This precludes a means to enforce the flux of modeled turbulent stresses to be zero at solid walls. However, in discontinuous Galerkin, since all interface and boundary conditions are set through numerical fluxes, specifically boundary flux integrals, it allows the weak enforcement of zero turbulent flux at solid walls by setting the second integral in (2.20) to zero on solid surfaces. Moreover, this integral can be set to particular values on inflow domains to represent the inflow of unresolved turbulent stress if desired.

From (2.20) we see that one can easily vary the partition between large and small scales on different subdomains. Likewise, the particular model for the turbulent flux can be altered on each domain. Thus, the model term can be written as

$$\begin{aligned}
M_{DG}(\tilde{\mathbf{W}}, \tilde{\mathbf{U}}) &= \int_{\Gamma_0} \left( [\tilde{\mathbf{W}}_e^T] \langle \mathbf{F}_n^{m_e}(\tilde{\mathbf{U}}_e) \rangle \right) + \int_{\partial\Omega} \left( \tilde{\mathbf{W}}_e^T \mathbf{F}_n^{m_e}(\tilde{\mathbf{U}}_e) \right) \\
&\quad - \sum_{\Omega_e \in \mathcal{P}_h} \int_{\Omega_e} \frac{\partial \tilde{\mathbf{W}}_e}{\partial x_i} \mathbf{F}_i^{m_e}(\tilde{\mathbf{U}}_e) d\mathbf{x},
\end{aligned} \tag{2.21}$$

where the modeled turbulent flux and the solution space partitioning are dependent on the element index  $e$ . Across element boundaries, the first integral communicates the unresolved turbulent flux between neighboring elements thereby automatically converting from one partitioning to another and from one turbulent flux model to another. It is this novel capability of the  $\ell$ VMS that makes it particularly attractive for turbulence modeling in complex flows (see Figure 2.2).

## 2.4 VMS Model Description

Now, we present specific choices for the models used in this work. The standard eddy diffusivity model from (2.19) can be put in the form given below

$$\mathbf{F}_i^m(\tilde{\mathbf{U}}) = 2\tilde{\nu}_T \begin{bmatrix} 0 \\ (\nabla^s \tilde{\mathbf{u}})_{:i} \\ \tilde{T}_{,i}/Pr_t \end{bmatrix}, \quad (2.22)$$

where  $\nabla^s \mathbf{u}$  is the symmetric part of the gradient tensor [i.e.  $(\nabla^s \mathbf{u})_{ji} = (\mathbf{u}_{i,j} + \mathbf{u}_{j,i})/2$ ] and  $(\nabla^s \mathbf{u})_{:i}$  is the  $i$ th column of this tensor. The Smagorinsky eddy diffusivity, based on the “small-small” VMS model of Hughes *et al.* [89, 90], defined on the small-scales is

$$\tilde{\nu}_T = (C_S \tilde{\Delta})^2 |\nabla^s \tilde{\mathbf{u}}| \quad (2.23)$$

where  $C_S$  is the Smagorinsky coefficient that is 0.1 unless otherwise stated,  $\tilde{\Delta}$  is a length scale representative of both the mesh ( $h$ ) and local polynomial order ( $p$ ) for the small scales defined as

$$\tilde{\Delta}^2 = (L_x L_z)/(N_x N_z (p+1)^2), \quad (2.24)$$

where  $L_x$  and  $L_z$  are the domain sizes in the streamwise ( $x$ ) and spanwise ( $z$ ) directions, respectively. Similarly,  $N_x$  and  $N_z$  are the number of elements in the streamwise and spanwise directions, respectively. We note in passing that we use a Van Driest wall damping function [61] to mitigate possible timestep restrictions arising from the use of a explicit time advancement. Next,  $Pr_t$  is the turbulent Prandtl number that is set to a value of 1.0 for all the cases considered here. Finally,  $\tilde{T}_{,i}$  is the gradient of the small-scale temperature field used to form the eddy diffusivity term to model SGS heat flux in the energy equation. In practice, scale-similar and mixed-models appear advantageous for compressible flows [116] and VMS versions of these models can also be devised.

In order to complete the description of any VMS model, we need to specify a partition of the resolved scales. In the current work, we use a two-level partition that divides the resolved scales into large- and small-scales that is specified by a modal cutoff  $L_e$  on each element. For a given polynomial order on a element  $p_e > 0$ , the partition bifurcates the polynomial space, in each direction, as  $P_{p_e}(\Omega_e) = \{0, \dots, L_e, \dots, p_e\}$ , where the modes less than  $L_e$  are considered large scales while the remaining modes including  $L_e$  form the small scales. In general, we can specify the parameter  $L_e$  independently within each element as  $L_{e_x}$ ,  $L_{e_y}$ , and  $L_{e_z}$  in the streamwise, wall-normal, and spanwise directions, respectively (Note: unless otherwise stated,  $L_e = L_{e_x} = L_{e_y} = L_{e_z}$ ).

## 2.5 Discretization and Implementation

For every element  $\Omega_e \in \mathcal{P}_h$  we define the finite-dimensional space  $P_{p_e}(\hat{\Omega})$  of polynomials of degree  $\leq p_e$  defined on a master element  $\hat{\Omega}$ . Then

$$P_{p_e}(\Omega_e) = \left\{ \phi | \phi = \hat{\phi} \mathbf{J}_{\Omega_e}^{-1}, \hat{\phi} \in P_{p_e}(\hat{\Omega}) \right\}, \quad (2.25)$$

where  $\mathbf{J}_{\Omega_e}$  is the Jacobian of the transformation of element  $\Omega_e$  to the master element and

$$\mathbf{V}_p(\mathcal{P}_h) = \left( \prod_{e=1}^N P_{p_e}(\Omega_e) \right)^m \subset \mathbf{V}(\mathcal{P}_h), \quad (2.26)$$

where  $m$  is the number of conserved variables,  $m = 5$ .

Thus, the semi-discrete discontinuous Galerkin method is: Given  $\mathbf{U}_0 = \mathbf{U}_0(\mathbf{x})$ , for  $t \in (0, T)$ , find  $\mathbf{U}_h(\mathbf{x}, t) \in \mathbf{V}_p(\mathcal{P}_h) \times H^1(0, T)$  such that

$$B_{DG}(\mathbf{W}_h, \mathbf{U}_h) = M_{DG}(\widetilde{\mathbf{W}}_h, \widetilde{\mathbf{U}}_h) + (\mathbf{W}_h, \mathbf{S}), \quad \forall \mathbf{W}_h \in \mathbf{V}_p(\mathcal{P}_h). \quad (2.27)$$

In practice, one can use a variety of polynomial bases to approximate the functions in (2.27) which offer different advantages and disadvantages. A number of options are presented in Atkins [112] including monomials, tensor products of Legendre polynomials, and warped product bases introduced by Dubiner [56]. For the VMS method, the use of orthogonal bases greatly simplifies the form of the unclosed terms in the equations. Therefore we utilize the family of orthogonal, hierarchical bases formed from tensor products of Jacobi polynomials as described in Karniadakis and Sherwin [98] which are supported in a wide range of elements types in two- and three-dimensions.

## 2.6 $\ell$ VMS Advantages and Potential

The promise of the merger of VMS and DG spatial discretization that we term Local VMS ( $\ell$ VMS) can be attributed to the locality introduced in spectral and physical space by the former and the latter, respectively. To be more explicit, the VMS approach to LES introduces no explicit modeling on the largest resolved scales, a feature attributed to its success [89, 90, 123, 129, 133], while a SGS scale model is active on the smallest resolved scales. This can be thought of as coupling of “DNS” or no-model on the large scales with a SGS model on the small scales. Now, using DG, we extend this concept in physical space.

As an illustration of the the potential of  $\ell$ VMS, consider the case of a airfoil in crossflow at sufficiently high Reynolds number (see Figure 2.2). With the current framework, we can use  $hp$ -refinement to reduce the degrees of freedom away from the surface of the airfoil and wake. Next, one can employ  $\ell$ VMS in the region near the surface of the airfoil to represent the boundary layer and turbulent wake ( $\ell$ VMS<sub>*b*</sub> and  $\ell$ VMS<sub>*w*</sub> in Figure 2.2). Further, in regions where turbulence is not active, the model can be turned “off” to recover DNS ( $\ell$ VMS<sub>*l*</sub> and  $\ell$ VMS<sub>*f*</sub> in Figure 2.2). This can be accomplished in VMS simply by selecting the partition ( $L_e$ ) to have all the resolved scales in the large scale space.

Moreover, it is likely that the large scales for the boundary layer are different from that in the wake region [27, 45]. First, using the local refinement capabilities, we select a mesh and polynomial order to sufficiently represent the features of the boundary layer and wakes. Then,  $\ell$ VMS allows the parameters such as the modal partition  $L_e$  to separate the large and small scale spaces to be specified individually on each element.

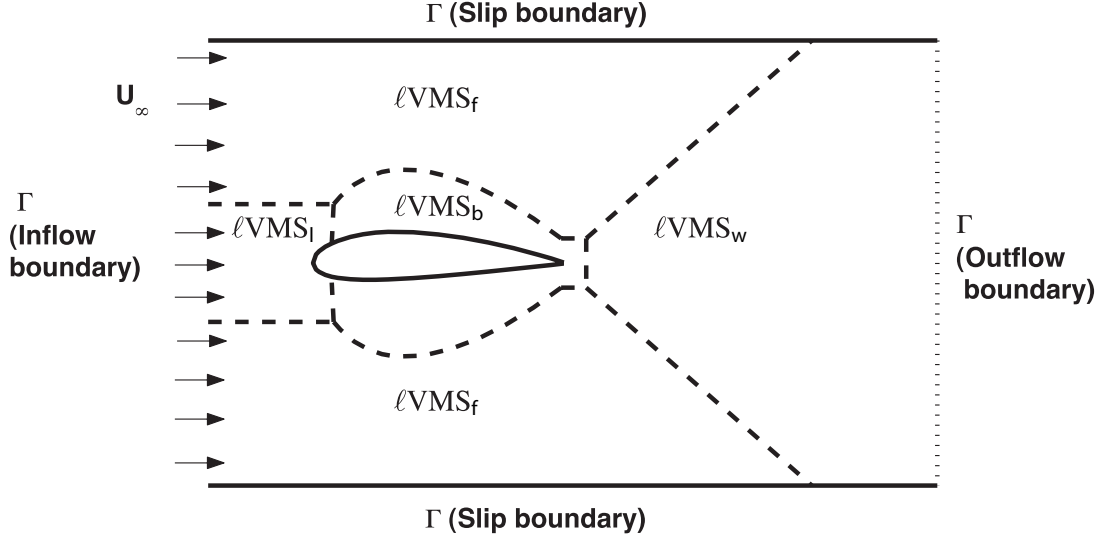


**Figure 2.2.** Illustration of  $\ell$ VMS modeling capabilities for flows in complex geometries:  $U_\infty$  freestream velocity;  $\ell$ VMS<sub>l</sub>, model for laminar boundary layer;  $\ell$ VMS<sub>b</sub>, model for a turbulent boundary layer;  $\ell$ VMS<sub>f</sub>, model for region outside the boundary layer;  $\ell$ VMS<sub>w</sub>, model for a turbulent wake; ---- Boundary separating different  $\ell$ VMS modeling zones.

For many flows, the large scales in different regions of the flow are vastly different in character. Allowing the specification of the model parameters locally based on the knowledge of physical structures in the flow, if available, can potentially lead to improved modeling of the flow. In fact, conceptually, one can even change the model in different regions in the flow. Overall, fully exploiting  $\ell$ VMS offers the flexibility needed to accurately model flows in a efficient manner even in complex geometries. As a first step towards simulations just described, we test the capabilities of the method on a simple but canonical turbulent flow — fully-developed turbulence in a planar channel.

## 2.7 Numerical Results – Effects of Spatial Resolution

Consider the fully-developed turbulent flow in a planar channel with coordinates  $x = x_1$  in the streamwise direction,  $y = x_2$  in the wall-normal direction, and  $z = x_3$  in the spanwise direction. The reference length scale is the channel half-height  $\delta$  and the reference velocity is the friction-velocity  $u_\tau \equiv \sqrt{\tau_w/\rho}$  in the initial condition, where  $\nu$  is the kinematic viscosity,  $\tau_w$  is the shear stress at the wall (drag at the wall), and  $\rho$  is the fluid density. Thus, the reference Reynolds number is  $Re_\tau \equiv u_\tau \delta / \nu$ . In reporting our results, we frequently present flow quantities in wall units (or inner scaling) with  $t^+ = tu_\tau^2/\nu$ ,  $x_i^+ = x_i u_\tau / \nu$  and  $u_i^+ = u_i / u_\tau$ . The flow is assumed to be periodic in the streamwise and spanwise directions where the box size is selected so that the turbulence is adequately decorrelated in both di-

rections. As a first step towards utilizing DG for turbulent flows, we have performed coarse grid DNS at  $Re_\tau = 100$  with a centerline Mach number of  $M_c = 0.3$  so that comparisons can be made directly to prior incompressible results (see, e.g., [99, 119]). Following Coleman *et al.* [41], we use a cold, isothermal wall so that internal energy created by molecular dissipation is removed from the domain via heat transfer across the walls, allowing a statistically steady state to be achieved. While using moderate resolutions, the bulk mass flow is held constant by the addition of an  $x_1$ -momentum source. However, at coarse resolutions additional source terms are required in both the continuity and energy equations to hold the bulk density and the average total energy constant.

### 2.7.1 DG Spatial Discretization

First, we undertake a detailed resolution study at  $Re_\tau = 100$  with different polynomial orders ( $p$ ) using the following mesh topologies:  $4 \times 4 \times 8$ ,  $8 \times 4 \times 8$ ,  $4 \times 8 \times 8$ , and  $8 \times 8 \times 8$  ( $N_x \times N_y \times N_z$ ) where  $N_x$ ,  $N_y$ , and  $N_z$  are the number of elements in the streamwise, wall-normal, and spanwise directions, respectively. The meshes are stretched in the wall-normal direction unless otherwise stated. For the stretched mesh, the grid points are given by

$$y_j = \frac{\tanh(c_s(2j/N_y - 1))}{\tanh c_s} + 1, \quad j = 0, 1, \dots, N_y \quad (2.28)$$

where  $N_y$  is the number of elements in the wall-normal direction and  $c_s$  is the stretching factor in the range  $1.0 < c_s < 2.0$ . Unless explicitly stated, we use the stretched mesh. The choice of the meshes used in this study is to highlight the effects of resolution in the planar and wall-normal directions as well as the interaction between the two.

For convenience in presenting the results at  $Re_\tau = 100$ , we refer to the following meshes,  $4 \times 4 \times 8$ ,  $8 \times 4 \times 8$ ,  $4 \times 8 \times 8$ ,  $8 \times 8 \times 8$ , and  $8 \times 8 \times 8$  uniform  $y$ -direction, as A, B, C, D, and E, respectively. Also, since we consider different polynomial orders on each of the meshes above, in referring to a particular combination of a mesh using a polynomial order  $p$ , we employ the following notation that we illustrate by example – a mesh using  $4 \times 4 \times 8$  (A) with  $p = 3$  will be referred to as A3 and so on.

In all the cases, we use third-order TVD-RK time advancement with  $0.000025 \leq \Delta t \leq 0.0001$ . The upper bound on  $\Delta t$  is used with  $Re_\tau = 100$  while the lower bound corresponds to simulations at  $Re_\tau = 395$  (refer to Section 2.9.3). The timesteps used here are typically smaller by a order of magnitude compared to other incompressible codes that treat the diffusion terms implicitly [34]. We plan to incorporate implicit time-advancement with  $\ell$ VMS in the future.

Let us begin with a study using  $p = 3$  for the meshes A-E at  $Re_\tau = 100$ . The simulation parameters and results summary for each individual mesh using different polynomial orders are reported in Table 2.1. It is important to point out the salient features of the meshes selected that may be useful in interpreting the results presented below.

1. Cases A3, B3, and E3 share a similar near-wall resolution  $\Delta y_w^+ \approx 4.3$  ( $\Delta y_m^+ \approx 25$ ).

2. Cases A3 and C3 share the same planar resolution ( $x - z$  plane).
3. Cases B3, D3, and E3 share the same planar resolution ( $x - z$  plane).
4. Finally, Cases C3 and D3 have a better near-wall resolution ( $\Delta y_w^+ \leq 2.5$ ,  $\Delta y_m^+ \leq 15$ ) compared with A3, B3, and E3.

The location of the element interfaces for the bottom half the channel in the wall-normal direction ( $y$ ) for the A and B meshes are as follows,  $y^+ \approx \{25, 100\}$ . For C and D (except D3),  $y^+ \approx \{8, 25, 56, 100\}$ . Finally, for the mesh E,  $y^+ = \{25, 50, 75, 100\}$

The meanflow and rms profiles for B3, C3, D3, and E3 are presented in Figure 2.3. The meanflow for D3, shown in Figure 2.3(a), produces the best agreement with the reference DNS [33] while all the other cases show poorer agreement with the reference. B3 and E3 severely overpredict the wall shear stress while C3 significantly underpredicts  $\tau_w$ . It is important to note the presence of slip in the meanflow for all the cases considered thus far (refer to Table 2.1 and see Figure 2.6). This is a unique feature of the DG solutions that allow the solution to be discontinuous at element interfaces. In the current context, the slip in the meanflow represents the difference between the imposed no-slip boundary condition and computed solution at the channel solid walls.

Consider the rms profiles for the above cases plotted in Figure 2.3(b). Again, the best overall agreement with DNS [33], for all the components of turbulence intensity, is obtained using D3. Similar to the meanflow profile, the remaining cases show poor agreement. And, while the profiles for B3 and E3 are similar, the streamwise component of C3 is dramatically different from the latter two. Again, note the non-zero contributions (even with D3) in the rms quantities at the wall ( $y^+ = 0$ ) that arises naturally in DG due to the weak enforcement of wall boundary conditions. On the rms plot (Figure 2.3(b)), let us focus on the  $u$  component, B3 and E3 produce a larger intercept at  $y^+ = 0$  when compared with C3 and D3.

Returning to the slip in the meanflow, B3, D3, and E3 have a negative value while C3 has a positive slip. Further, the absolute value of slip for B3 and E3 is considerably higher than D3. These results are indicative of an inverse relationship between the magnitude of solution jumps ( see Figure 2.3(b)) and the near-wall resolution ( $\Delta y_w^+$ ) [131]. This view is supported by the large value of slip for A3 that shares a similar near-wall resolution ( $\Delta y_w^+$ ) with B3 and E3. It is well-known that the jumps in the DG solution are related to local resolution [39]. For the channel flow, the results above indicate that the  $y$ -direction resolution plays a dominant role in determining the solution jumps (slip) at the wall [131]. Importantly, the presence of significant slip, for example in D3, does not appear to degrade the solution in the interior (see Figure 2.6 that presents the variation of slip and  $\tau_w$  for various meshes).

Profiles of Reynolds stress, shown in Figure 2.3(a), indicate that D3 again produces the best overall agreement with the reference [33]. Note that the non-zero Reynolds stress contribution at the wall is a result of the use of weak boundary condition enforcement. Further, the largest deviation from the reference Reynolds stress profile, shown in Figure 2.3(a), is observed with B3 and E3. Since both these cases employ a large  $\Delta y_w^+$ , this suggests the



Reynolds stress predictions may be particularly sensitive to  $\Delta y_w^+$ .

Meanwhile, the viscous stress profiles, shown in Figure 2.3(a), with noticeable jumps at ( $y/\delta \approx 0.25$  i.e.  $y^+ \approx 25$ ) for B3 and E3 are indications of the low  $y$ -direction resolution employed for these cases. The relatively smoother profiles, i.e. modest interelement jumps for C3 and D3, that use a better resolution in the wall-normal direction, suggest the resolutions used in these cases is sufficient to reasonably resolve the viscous sublayer. However, the thickness of the viscous sublayer for C3 is very prominent compared with the reference consistent with the low drag predictions. Meanwhile, the viscous stress profiles for B3 and E3 are diminished compared with the reference, consistent with the high  $\tau_w$  obtained for these cases. The good correspondence of D3 with the reference viscous stress and total stress profiles (D6) indicates the overall resolution ( $h$  and  $p$ ) in this case is adequate to reasonably represent the near-wall region.

The ability to obtain reasonable estimates for  $\tau_w$  using  $\Delta y_w^+ \approx 2.3$  (D3 with  $\Delta y_m^+ \approx 13$ ) is noteworthy. Traditional discretizations even with an explicit SGS model require  $\Delta y_w^+ \leq 1.0$  [33, 34]. We believe this can be attributed, in part, to the manner of boundary conditions enforcement [44, 130]. The imposition of the no-slip conditions through the BR flux, allowing solution jumps, is effective in “capturing” part of the boundary layer in the jump at the channel wall where the jumps in the solution are closely related to the local residual (in the interior of the element) [39]. In our experience with other discretizations [33, 34], the strict enforcement of the no-slip wall boundary conditions when employing resolutions that are inadequate to sufficiently represent the viscous wall region may explain the poor  $\tau_w$  predictions observed in traditional discretizations. Here, by contrast, allowing the solution to jump at the boundary models the influence of wall *commensurate* with the local resolution enabling reasonable  $\tau_w$  prediction even with moderate  $\Delta y_w^+$  values.

Finally, we examine the energy spectra in the  $x$ - and  $z$ - directions, shown in Figure 2.3. Consider Figure 2.3 and focus on the streamwise component for any visible trends (the spanwise spectra where all the cases share the same resolution may not adequately highlight any trends present.) Clearly, B3, D3, and E3 that all share the same planar resolution produce a similar shaped spectra but with B3 and E3 (with a larger  $\Delta y_w^+$  values) exhibiting a distinctly higher energy content compared to D3.

Significantly, the effects of using coarse grids are clearly seen in the energy spectra. The pile up of energy, seen at the higher wavenumbers, is mainly a result of the absence of viscous dissipation scales [102]. Unfortunately, very high resolutions (DNS) are needed to adequately resolve these scales in the turbulent channel flow [119]. At finite resolutions, the effects of low resolution are handled by introducing a SGS model often in conjunction with a dealiasing mechanism [29, 104, 117, 147]. Thus far, we have not employed a dealiasing strategy nor have we introduced explicit SGS modeling in any of the simulations. However, the energy spectra (see Figure 2.3) indicate the need for such mechanisms in the cases presented above.

At this point, we shift our attention to the role of numerical dissipation, in DG, starting with an examination of the solutions obtained with C3, C4, and C6 that are plotted in Figure 2.4. The meanflow profile, seen in Figure 2.4(a), for  $p \leq 4$  results in significant underprediction of the wall shear stress. We also notice a lower energy content in the

streamwise energy spectra, an underprediction of the peak value of the Reynolds stress, and a prominent viscous layer Figures 2.4(c), 2.4(e), and 2.4(f), respectively. In particular, note the shift of the Reynolds stress peak away from the wall. These results suggest a strong influence of numerical dissipation on the turbulence. And therefore, the statistics obtained resemble flow at a lower Reynolds number.

Recently, Cockburn [39], using a linear hyperbolic system, related the form of the dissipation term to particular choices of numerical fluxes in discontinuous Galerkin methods. Specifically, for a wave equation, the numerical dissipation introduced by the Lax-Friedrichs flux is related to the speed of propagation and the solution jump [39]. Given this, we can expect the dissipation in the streamwise direction to be higher for the turbulent channel flow since that is the principal direction of the meanflow. Further, at the lower resolutions the jumps are likely to be more significant. It is also well-known that upwind schemes are effective in damping scales at high wavenumbers. Therefore, using a low resolution may not provide sufficient scale separation between the energy containing scales (low wavenumbers) and those susceptible to the upwinding effect (see Figure 2.4(c)). Therefore, all the above factors lead to the resolution in the streamwise direction determining the dissipation properties of the simulation. Fortunately, the increase in resolution through polynomial order and/or mesh refinement dramatically reduces the dissipation introduced through the convective flux (see Figures 2.4 and 2.5(e – f)).

This leads us to the consistently higher energy levels observed in the spectra for A, B, and E when compared with C and D, respectively (refer to Figure 2.5). This may be explained by the lower  $y$ -direction resolution for A and B in the near-wall region compared with C and D. The underresolved viscous wall region results in the energy containing eddies that are not sufficiently influenced by the physical damping due to viscous effects. Thus, the equilibrium that is achieved through an interaction of inertial and viscous effects close to the rigid walls is not faithfully represented. This leads to an artificially high energy content in the resolved scales resulting in overprediction in the wall-shear stress. Furthermore, this imbalance is exacerbated for the B mesh, that by virtue of a higher planar resolution, contains lower dissipation (see Figure 2.5). By contrast, the A mesh benefits from a stabilizing influence of the numerical dissipation leading to an overall better agreement with DNS (see Figure 2.5).

Now, we return to the C mesh with an increased wall-normal direction resolution. This leads to improved prediction of the velocity gradients close to the wall minimizing the overprediction in the  $\tau_w$ . However, the presence of numerical dissipation leads to solutions that are overdiffuse (see Figure 2.4). The dissipative effect that arises naturally in the discretization of the convection term has been interpreted by some as an implicit SGS model in the method known as MILES (Monotonically Integrated LES). [63]. The MILES approach, currently an active area of research, is motivated by the need to reduce the computational expense associated with an explicit SGS model. By contrast, our current goal is to evaluate the efficacy of a VMS model to reduce the resolution requirements. Since the effect of an eddy viscosity SGS model is to enhance dissipation, the resolutions ( $h$  and  $p$ ) chosen, in the context of modeling, should be chosen such that the influence of numerical dissipation is minimized. Thus, the current resolution study provides guidelines for selection of the mesh and polynomial order, to fully exploit the local  $hp$  refinement capabilities of  $\ell$ VMS,

in the context of multi-scale modeling. (Note: although not presented here, channel flow results that exploit the local  $hp$ -refinement capabilities at  $Re_\tau > 100$  with no explicit SGS modeling can be found in a related article [131]).

Now, the simulations discussed so far used 8 elements in the spanwise direction and reasonable solutions were obtained with  $p \geq 3$ , given sufficient  $h$  resolution. With 8 elements across the channel, each element is approximately 50 wall-units in width, which roughly corresponds to half the typical streak spacing [99, 100, 148]. To further explore the influence of spanwise element size, we also performed simulations on a coarse  $4 \times 4 \times 4$  mesh using a range of polynomial orders,  $p = 3$  to 6. In this case, the spanwise element size is approximately 100 wall-units which indicates that both a low- and high-speed streak are contained within one element. Consequently, the elements are larger than the near-wall vortices and our experience with DG in two-dimensional simulations indicates that relatively high-polynomial orders are required to adequately resolve a vortex within a single element. Thus, predictably, these simulations were found to be non-linearly unstable (without exact integration) due to inadequate representation of the viscous dissipation scales. Thus, reaffirming the well-known importance of spanwise resolution in wall-bounded turbulent flows [99, 119]. Therefore, we first explore strategies to address the non-linear stability before proceeding to SGS modeling via VMS [42, 43, 88].

## 2.8 Dealiasing Strategies

We observed the presence of aliasing [29, 104] and SGS effects, clearly seen by the pile up of energy at the high wavenumbers in the energy spectra. Fortunately, the *relatively* high resolution in the cases considered so far ensures that the solutions remain stable. Ideally, in the context of LES, one coarsens the mesh in all three coordinate directions. Further, since the effective number of degrees of freedom are reduced, we can expect a heightening of the effects of aliasing and SGS. Therefore, viable options to counter these effects need to be established.

### 2.8.1 Polynomial Dealiasing (PD)

Recently, Kirby and Karniadakis [117] developed algorithms to successfully reduce aliasing in a DG discretization. They employ over-integration (super-collocation) coupled with a Galerkin projection to dealias the solution. They demonstrate the effectiveness of PD for incompressible channel flow at  $Re_\tau = 395$  using a Galerkin spectral/ $hp$  element method [117]. While this particular approach is new, a common strategy employed for dealiasing in global spectral methods is the  $3/2$ -rule [29]. This approach is widely used to dealias Fourier-spectral simulations that have a quadratic non-linearity such as the convection term in the incompressible Navier-Stokes equations.

Kirby and Karniadakis [117] advocate the use of a super-collocation method for dealiasing. This involves employing a greater number of quadrature points ( $q$ ) than normally required to satisfy accuracy criteria to ensure convergence with smooth solutions. Specifically, they

suggest that for a quadratic non-linearity, one should use a value of  $3L/2$ , similar to the  $3/2$ -rule [29], where  $L = p + 1$  is the number modes used to represent the solution for a given polynomial order ( $p$ ) .

The PD approach of Kirby and Karniadakis [117] involves an *increase* in the computational cost. However, the results obtained by Kirby and Karniadakis [117], using a model one-dimensional Burgers problem, suggests that the increase is required just for the convection term that may potentially offset the cost factor. In fact, for channel flow simulations, the  $3/2$ -rule is applied only in the planes ( $x - z$  plane) [29]. Here, as a first attempt towards dealiasing using this approach [117], we apply a super-collocation approach for both the convection and diffusion terms in all three coordinate directions.

A potential advantage of using polynomial dealiasing is increased accuracy since all the integral evaluations are done using a higher quadrature order. Importantly, PD has no foreseeable adverse impact on the solution. Now, it is important to note that, in VMS, modeling is confined to the smallest resolved scales [42, 88]. As a result, there is no direct mechanism present to remove aliasing errors that equally affect all the resolved scales including the large scales. Importantly, a major feature attributed to the success of prior VMS implementations is the preservation of accuracy of the large resolved scales by having no explicit model acting on them. The authors are not aware of any VMS implementation that has not employed some form of dealiasing. Therefore, preventing the adverse effects of aliasing errors on the large scales is necessary to obtain results that are comparable with prior VMS implementations [89, 90, 123, 129, 133].

## 2.8.2 Spectral Filtering (SF)

The Boyd-Vandeven Spectral Filter (SF) was used by Levin and colleagues [110] in a spectral element method for ocean modeling. They apply filtering on the vorticity and divergence fields to achieve non-linear stability. Here, we apply the same SF to the residual after each TVD-RK substep. The SF is described below.

$$\sigma(i/L, s) = \begin{cases} 1, & \text{if } i < s \\ \frac{1}{2}\text{erfc}(2\sqrt{L}\chi(\theta)(|\theta| - \frac{1}{2})), \theta = \frac{i-s}{L-s} & \text{if } s \leq i \leq L \end{cases} \quad (2.29)$$

and

$$\chi(\theta) = \begin{cases} 1, & \text{if } \theta = \frac{1}{2} \\ \sqrt{-\frac{\log(1-4\Omega^2)}{4\Omega^2}}, \Omega(\theta) = |\theta| - \frac{1}{2} & \text{elsewhere} \end{cases}, \quad (2.30)$$

where  $i$  is a index for the modes ( $0 \leq i \leq L$ ). The spectral shift parameter  $s$  biases the filtering action towards the higher modes (See Levin *et al.* [110] for additional details). The transfer function in modal space can be seen in Figure 2.7 for various polynomial orders. The mechanism by which aliasing errors are managed using this approach is by enhancing dissipation (filtering) in the smallest resolved scales (or high wavenumbers in spectral space). Thus, preventing the energy from accumulating in the smallest scales.

The potential advantages of spectral filtering are

1. Enhancing dissipation at the high wavenumbers improves non-linear stability.
2. The transfer function in three-dimensional can be constructed using a tensor product approach allows for a natural implementation of the spectral filter in the current framework.
3. The spectral shift,  $s$ , reduces the impact of filtering on the large scales that is similar in spirit to the VMS model.
4. This is a computationally efficient option compared with polynomial dealiasing [117].

A potential disadvantage of this approach is reduced accuracy. Also, there is no *a priori* rationale for picking the filter parameters.

### 2.8.3 Numerical Results: Dealiasing Strategies

Let us consider a  $4 \times 4 \times 4$  mesh using  $p = 5$  at  $Re_\tau = 100$  that gives a planar resolution in wall units as  $\Delta x^+ \approx 314$  and  $\Delta z^+ \approx 104$  with a minimum near-wall resolution based on the collocation grid  $\Delta y_w^+ \approx 2.14$  ( $\Delta y_m^+ \approx 25$ ).

Figure 2.8 shows the profiles of meanflow, rms, streamwise and spanwise direction spectra, Reynolds stress, and an overlay of the viscous and total stress profiles for the simulations listed in the top half of Table 2.2. This study evaluates the effectiveness of PD [117] and SF [110] for ensuring non-linear stability. Firstly, using  $s = 3$  (SF3 in Table 2.2), is sufficient to ensure stability for long time computation. Using  $s = 1$  (SF1 in Table 2.2), we introduce filtering on a wider range of scales that results in a greater underprediction of  $\tau_w$  compared with  $s = 3$  (see Figure 2.8). In the super-collocation case, using the same mesh and polynomial order, we increase the quadrature order from  $q = 7$  to  $q = 10$ . Although this is one quadrature order greater than  $3L/2$  for illustrative purposes, we have confirmed that a value of  $3L/2$  is sufficient to ensure non-linear stability.

The meanflow profile for PD, shown in Figure 2.8 results in a slight overprediction of drag compared with the reference [33]. Comparison of the rms profiles, seen in Figure 2.8, show results obtained with PD are in better agreement with the reference compared to the SF solutions. Here, we point out that we compute all our statistics on the collocation grid. Therefore, the spectra for the cases that employ PD span a wider number of wavenumbers. First, we note that the artificial accumulation of energy at the highest wavenumbers is reduced for all the cases considered here (see Figure 2.8(c – d)). Note the good correspondence of the energy spectra for both PD and SF3 in the largest scales i.e. low wavenumbers. Meanwhile, the dissipative effect of spectral filtering is confirmed by the dramatically lower energy in the spectra for SF1 with respect to the other two cases shown in Figure 2.8(c).

Importantly, both approaches are successful in reducing aliasing errors sufficiently and lead to stable computations. However, solutions obtained using PD [117] show improved low-order predictions that suggests a potential advantage when compared to spectral filtering [110]. Meanwhile, the Reynolds stress and total stress, shown in Figure 2.8, for all the cases show reasonable agreement with the reference [33]. Finally, the viscous stress profiles for

cases employing filtering, shown in Figure 2.8, have a noticeably more prominent viscous sublayer compared to super-collocation method. The resemblance of SF1 solutions to C3 and C4 results (see Figure 2.4) suggests a strong dissipative action of spectral filtering.

These results demonstrate the suitability of PD as an effective strategy for enhancing stability whilst simultaneously isolating SGS effects. This is seen by the higher energy content in the spectra, clearly observed in the  $u$  component of  $x$ -direction energy spectra shown in Figure 2.8(a). Meanwhile, even with  $s = 3$ , required to ensure stability, the dissipation introduced by spectral filtering makes the role SGS modeling unclear.

## 2.9 Multi-Scale Modeling Using $\ell$ VMS

We present a discussion of the results obtained with LES subgrid-scale modeling starting with parameter selection for  $\ell$ VMS.

### 2.9.1 Parameter Selection

The improved non-linear stability achieved through PD allows a greater flexibility in the choice of the mesh and polynomial order. Additionally in  $\ell$ VMS, the partition  $L_e$  that separates the resolved scales as large and small is required. This is a crucial parameter that determines the accuracy of VMS simulations [89,90,129,133]. Here, we have demonstrated that a  $4 \times 4$  planar mesh using  $p = 5$  is sufficient to produce results with no obvious adverse effects of numerical dissipation.

Further, the resulting element sizes in viscous wall units in the  $x$ - and  $z$ -directions correspond to well-known length scales of the physical structures in the flow [99, 100, 148]. Plots of near-wall streamwise and spanwise direction velocity correlations for  $Re_\tau = 100$  extracted from a  $8 \times 8 \times 8$  mesh using  $p = 6$  simulation are shown in Figure 2.9. The correlations for all three velocity components are considerably diminished by  $x^+ \approx 400$  and  $z^+ \approx 100$  (mean streak spacing) in the streamwise and spanwise directions, respectively [99, 100, 148]. Here, we draw attention to the sharp drop-off in the correlation at  $x^+ \approx 200$  and  $z^+ \approx 50$ .

Recently, Ramakrishnan and Collis [129,133] successfully used these length scales to identify the large scales in their VMS implementation. The numerical discretization in their study employed a Fourier basis in the planar directions that allows a transparent interpretation of modes and the associated physical length scales, leading to a surgical identification of the large and small scales. Analogous to their approach, we select  $L_e = 2$  that constrains the first two modes (constant and linear) in each direction of an individual element to represent the large scales and the remaining modes form the small scales. This ensures that the constant mode that corresponds to the individual element size is in the large scale space. Meanwhile, the linear mode that divides the element is representative of the length scales where the  $x$ - and  $z$ - direction velocity correlations show a sharp drop-off (see Figure 2.9). Thus, using a  $4 \times 4 \times 4$  mesh at  $Re_\tau = 100$ , we largely ensure that length scales

$\Delta x^+ \geq 200$  and  $\Delta z^+ \geq 50$  that relate to the near-wall coherent structures form the large scales.

Finally, the elements in the wall-normal direction are stretched such that the first element size in the wall-normal direction is  $\Delta y_m^+ \approx 25$ . This length scale matches the diameter of a typical near-wall structure [99, 100, 148]. Ramakrishnan and Collis [133] apply scale separation in just the planar directions in lieu of all three coordinate direction introduced in the original implementation by Hughes *et al.* [90]. Results of similar quality obtained by the two approaches suggest that scale separation in the wall-normal direction does not greatly influence the solution. Here, we follow Hughes *et al.* [90] that likely results in a larger small scale space than that obtained by Ramakrishnan and Collis [133]. Finally, we observe that with  $L_e = 2$  in the near-wall region, we ensure that  $\Delta y_m^+ \approx 25$  corresponding to the constant mode, related to the size of the coherent structures, lies in the large scale space.

### 2.9.2 Low Reynolds Number: $Re_\tau = 100$

A comparison of the results obtained using a combination of  $\ell$ VMS and PD is presented in Figures 2.10. The simulation parameters and results are found in the lower half of Table 2.2. Here, we study the effects of including a VMS model and present a direct comparison to a traditional constant coefficient Smagorinsky model [147]. We also comment on the role of numerical dissipation and local  $hp$ -refinement in the context of SGS modeling in  $\ell$ VMS.

First, we focus on the uniform  $p = 5$  case ( $\ell$ VMS1 in Table 2.2). The various turbulence statistics obtained using  $\ell$ VMS1, shown in Figure 2.10, are in better agreement with the reference [33] compared to DNS1 from Figure 2.8. The improvements are most noticeable when comparing the meanflow, spanwise component of the rms, and streamwise energy spectra (compare and contrast plots (a), (b), and (c), respectively of Figure 2.8 and Figure 2.10).

As an illustration of the efficacy of multi-scale modeling, consider setting the partition to  $L_e = 0$  ( $\ell$ VMS4 in Table 2.2) such that all resolved scales are in the small-scales space leading to constant coefficient Smagorinsky model [147]. The meanflow profile, seen in Figure 2.10(a), is representative of the dissipative effect obtained with all the turbulence statistics using  $\ell$ VMS4. Thus, the superior performance of the multi-scale modeling paradigm compared with traditional approaches that introduce modeling on all the resolved scales, observed in prior VMS implementations [89, 90, 133], is demonstrated for a DG spatial discretization as well. We also note in passing that the dissipation introduced by the multi-scale model is clearly less than that observed with SF3 even with  $L_e = 2$  (see Figure 2.8).

Although the results obtained with  $p = 5$  are good, the peak of the Reynolds stress profile, shown in Figure 2.10(e), is still overestimated by  $\ell$ VMS1. As an efficient means of improving the solution, we exploit the  $p$ -refinement capability of  $\ell$ VMS to *locally* increase the near-wall polynomial order from  $p = 5$  to  $p = 6$  such that the polynomial order variation across the channel solid walls is  $p = \{6, 5, 5, 6\}$  ( $\ell$ VMS3 in Table 2.2). The meanflow pro-

file is virtually unchanged from the  $p = 5$  case, however, we see a dramatic improvement in the turbulence intensities and the stress profiles (see plots (b), (e), and (f), respectively of Figure 2.10). In particular, the Reynolds stress profile for  $\ell\text{VMS3}$ , seen in Figure 2.10(e), is virtually indistinguishable from the DNS [33]. A close examination of the rms components also reveals a noticeably lower intercept for  $u_{rms}$  and  $w_{rms}$  at the wall ( $y^+ = 0$ ) for  $\ell\text{VMS3}$ . Although not perceivable in the Figure 2.10(a), a significant reduction in the meanflow slip is recorded in Table 2.2 between  $\ell\text{VMS1}$  and  $\ell\text{VMS3}$ . In the same table, note the lower value of slip for  $\ell\text{VMS1}$  compared to DNS1. These results indicate that while modeling can reduce the slip i.e. solution jumps, the reduction is not as dramatic as that accompanied by resolution increase (see Figure 2.6).

Let us now examine the effect of reducing the polynomial order in the interior of the channel such that  $p = \{5, 4, 4, 5\}$  ( $\ell\text{VMS2}$  in Table 2.2). The meanflow profile, seen in Figure 2.10(a), indicates that the drag is underpredicted. Meanwhile, the remaining statistics show reasonable agreement with the reference and  $\ell\text{VMS1}$ , especially in the near-wall region where they share the same resolution. It is likely that de-refining ( $h$  and  $p$ ) in all three directions leads to a stronger interaction of the model dissipation with the numerical dissipation in the spatial discretization. This suggests that using  $p = 5$  with the current mesh still represents a marginal resolution with respect to numerical dissipation. For a simple channel flow, with well-established guidelines for the selection of the mesh, using a marginal resolution may still result in reasonable results. However, in general flows (see Figure 2.2) where mesh selection is not as well-defined, poor mesh selection could lead to turbulence fluctuations being excessively suppressed altering the unsteady dynamics of the flow. Here, we counter the effects of low mesh ( $h$ ) resolution with polynomial enrichment, as seen with  $\ell\text{VMS5}$ . This feature of the DG spatial discretization can be exploited to greatly simplify mesh design, especially for complex geometries. Ideally, using DG, one aims to exploit both  $h$ - and  $p$ -refinement capabilities simultaneously to improve solution quality efficiently.

Before we proceed, let us consider the dramatic improvement in turbulence seen with local  $hp$ -refinement. It is important to note that a local  $p$ -refinement leads to a simultaneous increase in resolution in *all* three coordinate directions. In  $\ell\text{VMS}$ , an increase in resolution not only leads to a better representation of the solution (near-wall region), but also reduces the impact of the unresolved scales on the largest resolved scales by introducing a greater scale separation [129, 132]. Here, we recall the mechanism and the assumptions of that form the basis of multi-scale modeling [42, 88]. Firstly, the multi-scale model focusses on reducing the SGS effects on the smallest resolved where these effects are most pronounced by enhancing dissipation via a eddy-viscosity model [42, 88] (see Figure 2.10(c) and (d)). Thereby, the non-linear interactions between all the resolved scales (large and small) in a statistical sense are improved. With sufficient scale separation between the unresolved scales and resolved large scales, the indirect effect of modeling introduced through non-linear interactions among the resolved scales is sufficient to ensure good predictions. This is a key assumption in the modeling strategy of VMS [42, 88] that is better satisfied with increased resolution. Further, the interference of numerical dissipation, inherent in DG, with multi-scale model is minimized. It is for *all* these reasons that we see a dramatic improvement in the turbulence statistics, in  $\ell\text{VMS}$ , with a local increase of just one polynomial order from  $p = 5$  to  $p = 6$  ( $\ell\text{VMS1}$  and  $\ell\text{VMS3}$  in Table 2.2; also, see Figure 2.10).



At this stage, We provide a demonstration of the effectiveness of  $hp$ -refinement in lowering numerical dissipation in the context of  $\ell$ VMS. Consider an increase in the number of elements in the streamwise direction from 4 to 6 resulting a  $6 \times 4 \times 4$  mesh using  $p = \{6, 5, 5, 6\}$ . This gives a streamwise extent for each element as  $\Delta x^+ \approx 209$  (refer to Table 2.3 for details). For the current mesh, we need to employ the generalized partition selection parameter within each element. As a consequence, we choose  $Le_x = 1$  that corresponds to the important length scale in the streamwise direction while we retain  $Le_y = Le_z = 2$  as before (see Sections 2.4 and 2.9.1 for details).

A comparison of the results obtained with DNS2 and  $\ell$ VMS5 (refer to Table 2.3), both of which employ PD [117], is shown in Figure 2.11. Without modeling, the lower numerical dissipation (compared with DNS1 in Table 2.2) leads to significant overprediction in the wall shear stress (see Figure 2.11(a)). The peaks of both the spanwise component of the turbulence intensity and the Reynolds stress, shown in plots (b) and (e), respectively of Figure 2.11, are significantly overestimated. In fact, the location of the Reynolds stress peak is also shifted towards the wall. Contrast this with the results obtained using C3 and C4 earlier that tend to underpredict the magnitude of the peak and tend to shift the location away from the wall (refer to Figure 2.4(e)). Similarly, a comparison of the viscous stress profiles (see Figures 2.11(f) and 2.4(f)) confirm the lower levels of the numerical dissipation for the current case. This is further supported by the higher energy content in the streamwise energy spectra compared to the reference [33].

Now, the introduction of the VMS model clearly has a beneficial effect on all the turbulence statistics shown in Figure 2.11. In particular, VMS modeling leads to a meanflow profile and streamwise energy spectra that are indistinguishable from the reference DNS [33]. Meanwhile, the rms, Reynolds stress, viscous, and total stress profiles all show improved agreement with the reference that is especially noticeable in the near-wall region ( $y^+ \leq 50$ ). Importantly, at these resolutions ( $\Delta x^+ \approx 200$ ), the role of SGS modeling, in the context of  $\ell$ VMS, is transparent.

Thus, using a simple channel flow, we have established the role of VMS modeling within a DG spatial discretization using  $\ell$ VMS. Further, we have exploited the local refinement capabilities of  $\ell$ VMS for more accurate and efficient modeling of wall-bounded turbulence. In doing so, we have developed resolution guidelines for wall-bounded turbulence using  $\ell$ VMS. We test the robustness of the guidelines developed here by application to a flow at a higher Reynolds number in the following section.

### 2.9.3 Moderate Reynolds Number: $Re_\tau = 395$

We study the performance of  $\ell$ VMS at a higher Reynolds number, namely,  $Re_\tau = 395$ . The domain size is chosen as  $(\pi, 2, \pi/2)$  in the usual notation. This domain size is smaller than that employed with the DNS [119], however, the size is selected such that the turbulence structures are adequately decorrelated. A mesh is employed such that the relative resolutions in viscous wall units are similar to the  $Re_\tau = 100$  case above, also, this affords the use of similar polynomial orders ( $p = 5$  and  $p = 6$ ). For the current domain, the mesh is chosen to be  $6 \times 8 \times 6$  that gives  $\Delta x^+ \approx 207$ ,  $\Delta y_m^+ \approx 24$ , and  $\Delta z^+ \approx 103$ . Exploiting

the local  $p$ -refinement capabilities of the DG, we use a polynomial distribution from the lower to the upper solid wall as  $p = \{6, 6, 5, 5, 5, 5, 6, 6\}$ . The locations of the interelement boundary interfaces in the wall-normal direction for the lower half of the channel are  $y^+ \approx \{24, 83, 206, 395\}$ . Given the similarity in the relative resolutions, the partition parameters are identical to the  $Re_\tau = 100$  case with a  $6 \times 4 \times 4$  mesh (refer to Table 2.4).

Before we describe the cases at  $Re_\tau = 395$ , we briefly return to the  $Re_\tau = 100$  cases presented in Figure 2.11. There, we observe that the improvement of the solution in the near-wall region associated with the introduction of a multi-scale model ( $\ell$ VMS5) is clear, the differences with the no-model case (DNS2) beyond  $y^+ > 50$  are less significant (see Figure 2.11(a – b) and Figure 2.11(e – f)). This is significant for the higher Reynolds numbers since the viscous effects are confined to a region close to the wall. Therefore, to explore the utility of including a model in the interior of the channel, we confine multi-scale modeling to the near-wall to a region spanning  $y^+ \approx 83$  from both the rigid walls. This represents a hybrid between VMS (below  $y^+ < 83$ ) and DNS ( $y^+ > 83$  upto  $y^+ = 395$ ) in physical space ( $\ell$ VMS7 in Table 2.4). This is achieved by selecting a partition  $L_e$  to include all the resolved scales in the large scale space where we use  $p = 5$ . This effectively turns “off” the model in the core of the channel. We compare the results obtained using  $\ell$ VMS7 with  $\ell$ VMS6 that employs a model throughout the channel and DNS3 that has no active model. The results summary for all three cases is found in Table 2.4.

The results obtained can be seen in Figure 2.12. As expected, DNS3 yields results that closely resemble DNS2 that shares a similar relative resolution, particularly in the near-wall region. The meanflow profile, with an extended logarithmic region, clearly underpredicts the wall shear stress. And although turbulence intensities,  $u_{rms}$  and  $v_{rms}$ , appear reasonable,  $w_{rms}$  clearly has a more pronounced peak than the reference [119]. Similarly, the streamwise energy spectra and the Reynolds stress, shown in plots (c) and (e), respectively of Figure 2.12, also consistently overestimate the DNS [119].

As expected, the introduction of a multi-scale model using  $\ell$ VMS6 appropriately accounts for the inadequacies in the DNS3 solution, shown in Figure 2.12, leading to better agreement with the reference [119]. As usual, these improvements are most clearly observed in the meanflow profile,  $w_{rms}$ , the streamwise energy spectra, and the Reynolds stress shown in plots (a), (b), (c), and (e), respectively of Figure 2.12. Thus, the resolution and parameter guidelines developed at the lower Reynolds number is found to be equally applicable here.

Interestingly, a comparison of the results obtained using  $\ell$ VMS6 and  $\ell$ VMS7 show that they are virtually indistinguishable from each other. This is consistent with our observation even at the lower Reynolds number that the current multi-scale model has minimal impact away from the near-wall region ( $y^+ \geq 50$ ). Thus, exploiting the unique ability of  $\ell$ VMS that allows model parameters to be specified locally on each element, we are able to pursue surgical modeling of the channel flow. Also, in this case, we have eliminated the computational cost associated with an explicit model in the channel interior. This feature of  $\ell$ VMS holds promise for accurate and efficient modeling in flows involving complex geometries.

## 2.10 Conclusions

We have implemented and studied the performance of multi-scale modeling in a DG spatial discretization that we term the Local Variational Multi-Scale ( $\ell$ VMS) method using turbulent channel flow.

A spatial resolution study reveals that at particularly low resolutions the solutions are dominated by numerical dissipation and aliasing errors. For the channel flow, the streamwise direction is found to influence the dissipation in the scheme and spanwise resolution is confirmed to be crucial for non-linear stability. Thus, preliminary resolution guidelines for minimizing these effects are established. Additionally, the weak imposition of wall boundary conditions enforcements is found to allow reasonable wall shear stress predictions even with  $\Delta y_w^+ \approx 2.0$ , thereby mitigating near-wall resolution requirements.

We studied the viability of both spectral filtering [110] and polynomial dealiasing [117] as means of ensuring non-linear stability. While both approaches minimize aliasing, polynomial dealiasing [117] is found to be more suitable for SGS modeling.

Finally, a multi-scale model is introduced that is found to appropriately account for SGS effects and guidelines for the resolution (mesh and polynomial orders) and partition selection for obtaining quality solutions for wall-bounded turbulence using  $\ell$ VMS are developed. In doing so, we demonstrate the efficacy of the local properties of  $\ell$ VMS for effective turbulence prediction. To be more explicit, we exploit the ability to locally vary the fidelity ( $h$  and  $p$ ) and model ( $L_e$ ) for improved efficiency and accuracy.

Overall, we have successfully merged a DG spatial discretization and multi-scale modeling in  $\ell$ VMS. As a result, we obtain a flexible method that holds promise for effective turbulence simulation in complex geometries.

## 2.11 Acknowledgements

Sandia is a multiprogram laboratory operated by Sandia Corporation, a Lockheed Martin Company, for the United States Department of Energy under contract DE-AC04-94AL85000. The first author was partially supported by the Texas Advanced Technology Program under Grant 003604-0011-2001. The second author acknowledges the support of Sandia-DOE LDRD project “A Mathematical Framework for Multiscale Science and Engineering: the Variational Multiscale Method and Interscale Transfer Operators.” Computations at Rice University were performed on an 82 processor Pentium IV Beowulf cluster that was purchased with the aid of NSF MRI grant 0116289-2001.

Case	$p$	$\Delta y_w^+$	Ndof	Slip	$\tau_w$	$u_\tau$
A3	3	4.35	8,192	-5.4e-01	1.08	1.04
A4	4	2.96	16,000	-3.0e-02	1.00	1.00
A5	5	2.14	27,648	1.8e-01	0.98	0.99
A6	6	1.62	43,904	9.0e-02	0.98	0.99
B3	3	4.35	16,384	-7.9e-01	1.31	1.14
B4	4	2.96	32,000	-4.5e-01	1.21	1.10
B6	6	1.62	87,808	1.4e-01	1.05	1.03
C2	2	2.25	6,912	-2.0e-02	0.68	0.82
C3	3	1.40	16,384	1.0e-02	0.80	0.89
C4	4	0.95	32,000	2.0e-03	0.86	0.93
C6	6	0.52	87,808	-2.0e-04	0.95	0.98
D2	2	2.25	13,824	-4.3e-02	0.80	0.89
D3 <sup>†</sup>	3	2.33	32,768	-4.0e-02	0.96	0.98
D4	4	0.95	64,000	6.0e-03	0.98	0.99
D6	6	0.52	175,616	-2.0e-04	0.97	0.98
E3	3	4.32	32,768	-6.9e-01	1.26	1.12

**Table 2.1.** Simulation parameters and results for spatial resolution study at  $Re_\tau = 100$ . The planar element size in wall units for the various mesh topologies: A and C ( $\Delta x^+ \approx 314$ ,  $\Delta z^+ \approx 52.3$ ); B, D, and E ( $\Delta x^+ \approx 157$ ,  $\Delta z^+ \approx 52.3$ ). The minimum height of the element (at the channel walls) in the wall-normal direction for the various mesh topologies: A, B, and E ( $\Delta y_m^+ \approx 25$ ); C and D ( $\Delta y_m^+ \approx 8$ ); D<sup>†</sup> ( $\Delta y_m^+ \approx 15$ ).

Dealiasing	$p$	$q$	$s$	$L_e$	Slip	$\tau_w$	$u_\tau$
SF1	5	7	1	-	1.3e-01	0.85	0.92
SF3	5	7	3	-	1.6e-01	0.87	0.93
DNS1	5	10	-	-	2.0e-01	0.96	0.98
Model	$p$	$q$	$s$	$L_e$	Slip	$\tau_w$	$u_\tau$
$\ell$ VMS1	5	10	-	2	1.8e-01	0.91	0.96
$\ell$ VMS2	{5, 4}	{9, 8}	-	2	1.3e-01	0.87	0.93
$\ell$ VMS3	{6, 5}	{11, 9}	-	2	4.5e-02	0.90	0.95
$\ell$ VMS4*	5	9	-	0	-7.9e-02	0.73	0.86

**Table 2.2.** Simulation parameters and result summary for a  $4 \times 4 \times 4$  using  $p = 5$  to compare spectral filtering against dealiasing  $Re_\tau = 100$ . The element size in wall units for this mesh topology is  $\Delta x^+ \approx 314$  and  $\Delta z^+ \approx 104.3$  in the streamwise and spanwise directions, respectively. The minimum wall-normal direction resolution based on the standard collocation grid is  $\Delta y_w^+ \approx 2.14$  ( $\Delta y_m^+ \approx 25$ ). \*With  $L_e = 0$ ,  $\ell$ VMS simplifies to a traditional Smagorinsky model.

Model	$(L_{e_x}, L_{e_y}, L_{e_z})$	Slip	$\tau_w$	$u_\tau$	Ndof
DNS2	-	1.2e-01	1.01	1.00	26,832
$\ell$ VMS5	(1, 2, 2)	7.3e-02	0.94	0.97	26,832

**Table 2.3.** Simulation parameters and result summary for a  $6 \times 4 \times 4$  using  $p = \{6, 5, 5, 6\}$  at  $Re_\tau = 100$  to evaluate the effectiveness of the  $\ell$ VMS model. The element size in wall units for this mesh topology is  $\Delta x^+ \approx 209$  and  $\Delta z^+ \approx 104.3$  in the streamwise and spanwise directions, respectively. The minimum wall-normal direction resolution based on the standard collocation grid is  $\Delta y_w^+ \approx 1.62$  ( $\Delta y_m^+ \approx 25$ ). All the cases employ polynomial dealiasing where we use  $q = \{11, 9, 9, 11\}$

Model	$(L_{e_x}, L_{e_y}, L_{e_z})$	Slip	$\tau_w$	$u_\tau$	Ndof
DNS3	-	1.3e-01	1.04	1.02	80,496
$\ell$ VMS6	(1, 2, 2)	9.6e-02	0.96	0.98	80,496
$\ell$ VMS7 <sup>†</sup>	(1, 2, 2)	9.9e-02	0.96	0.98	80,496

**Table 2.4.** Simulation parameters and result summary for a  $6 \times 8 \times 6$  using  $p = \{6, 6, 5, 5, 5, 5, 6, 6\}$  at  $Re_\tau = 395$  to evaluate the effectiveness of the  $\ell$ VMS model. The element size in wall units for this mesh topology is  $\Delta x^+ \approx 206$  and  $\Delta z^+ \approx 103.4$  in the streamwise and spanwise directions, respectively. The minimum wall-normal direction resolution based on the standard collocation grid is  $\Delta y_w^+ \approx 1.62$  ( $\Delta y_m^+ \approx 24$ ). <sup>†</sup> refers to a hybrid case where the VMS model is active just in the portion of the channel where we employ  $p = 6$ . All the cases employ polynomial dealiasing where we use  $q = \{11, 11, 9, 9, 9, 9, 11, 11\}$ .

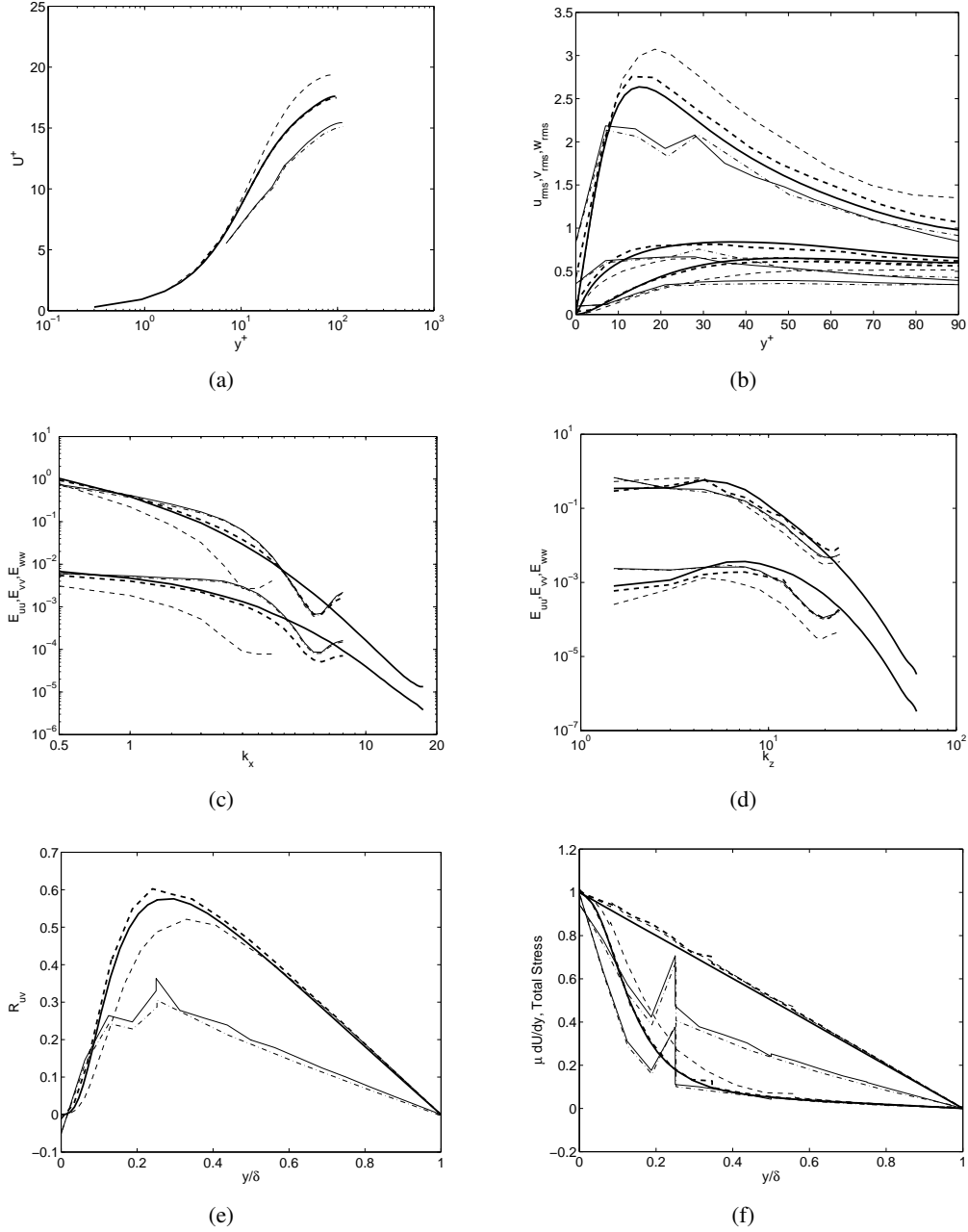


**Figure 2.3.** Profiles of turbulence quantities for  $Re_\tau = 100$  computed with different mesh topologies using  $p = 3$  (refer to Table 2.1). (a) Meanflow. (b) Turbulence intensities. (c) One-dimensional spectra - Streamwise ( $x$ ) direction. (d) One-dimensional spectra - Spanwise ( $z$ ) direction. (e) Reynolds stress. (f) Viscous and total stress: — DNS [33]; --- B3; ---- C3; -.- D3; — E3. Note: the reference for viscous and total stress profiles for all the  $Re_\tau = 100$  results presented in this article use the solution obtained with D6.

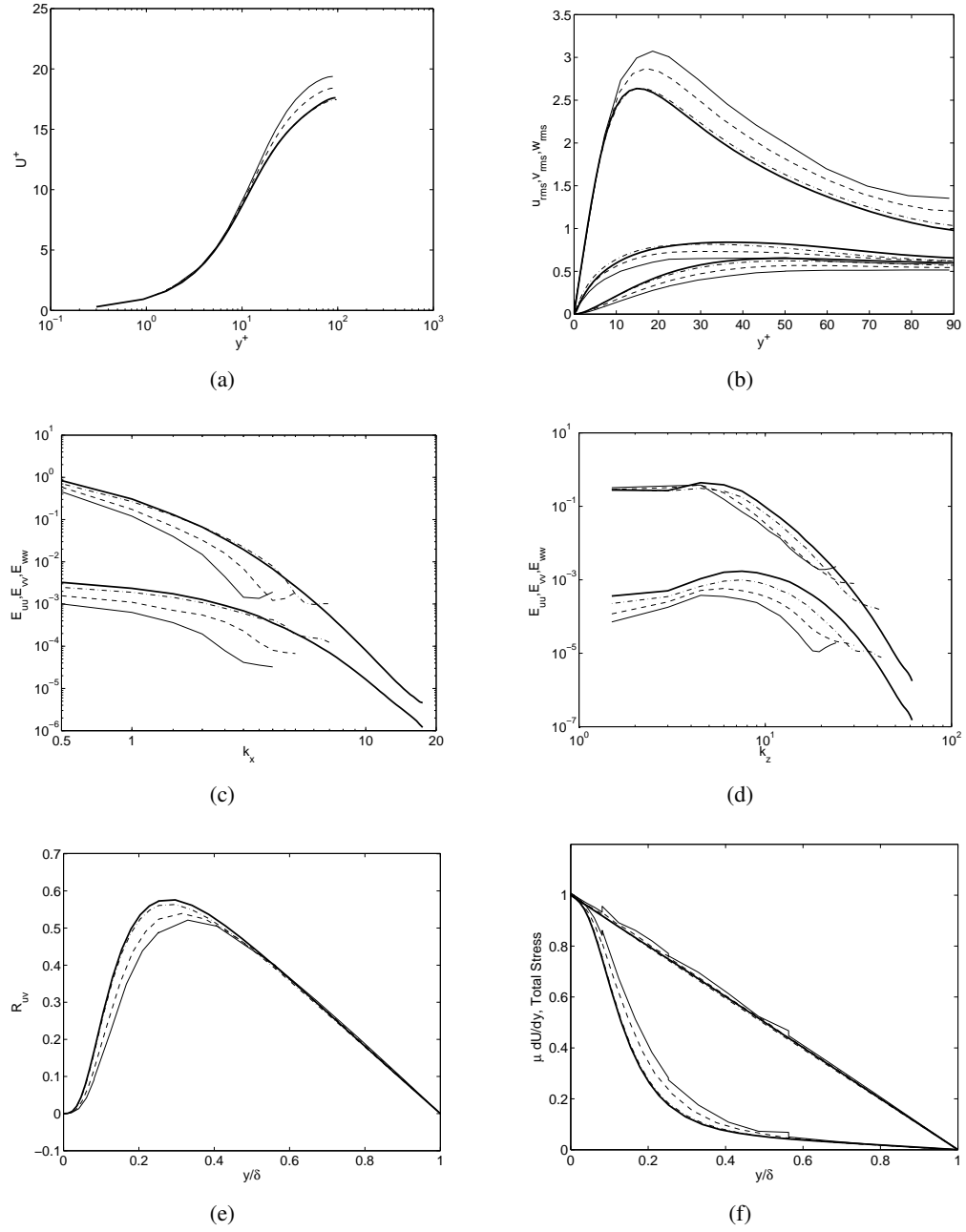


**Figure 2.4.** Profiles of turbulence quantities for  $Re_\tau = 100$  computed with a  $4 \times 8 \times 8$  mesh using different polynomial orders (refer to Table 2.1). (a) Meanflow. (b) Turbulence intensities. (c) One-dimensional spectra – Streamwise ( $x$ ) direction. (d) One-dimensional spectra – Spanwise ( $z$ ) direction. (e) Reynolds stress. (f) Viscous and total stress: — DNS [33]; — C3; - - - C4; - · - C6.

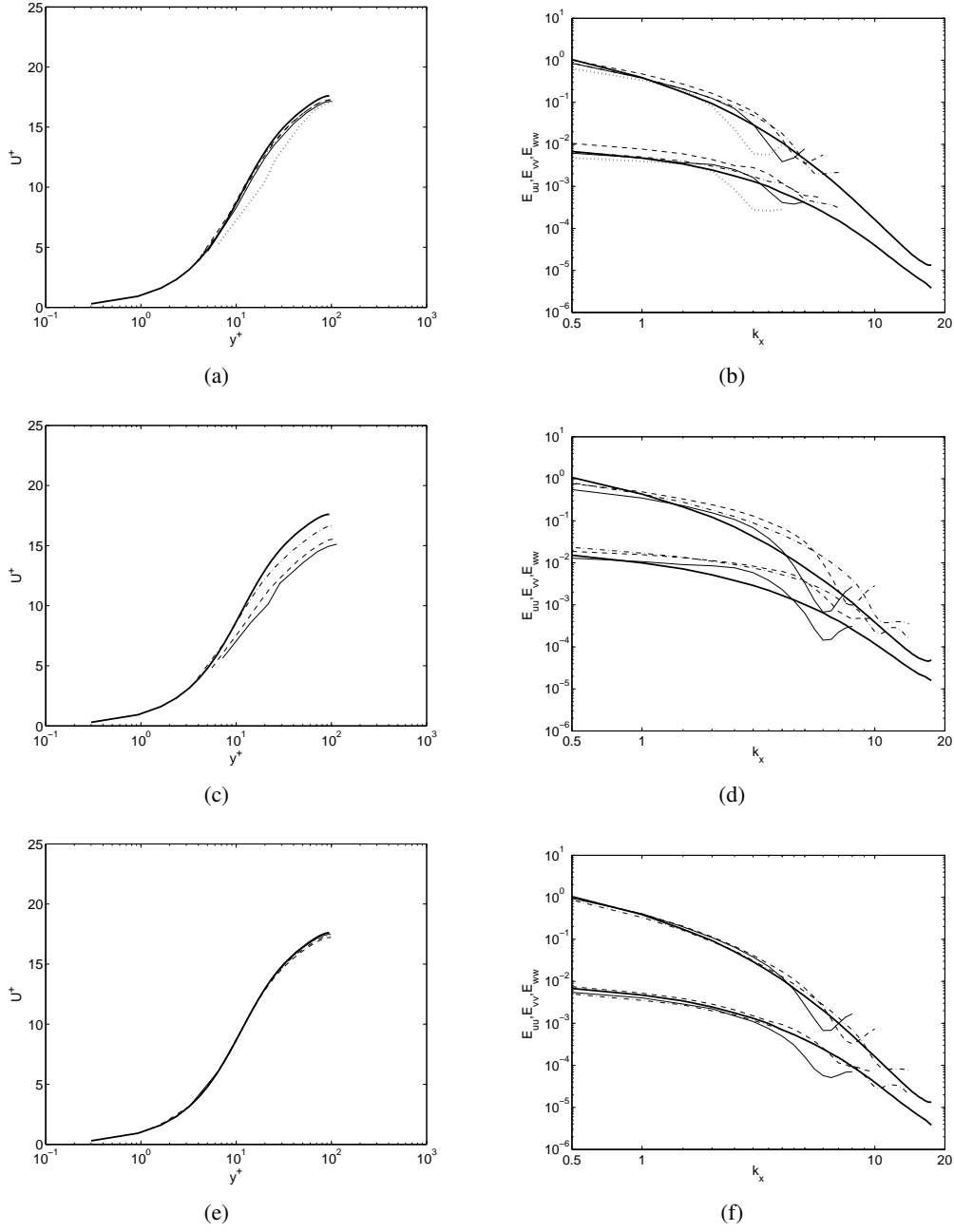


**Figure 2.5.** Profiles of meanflow and one-dimensional streamwise energy spectra, respectively, for different mesh topologies using various polynomial orders (refer to Table 2.1). (a) and (b)  $4 \times 4 \times 8$ : — DNS [33]; ..... A3; — A4; ---- A5; -.- A6. (c) and (d)  $8 \times 4 \times 8$  { (e) and (f)  $8 \times 8 \times 8$  }: — DNS [33]; — B3{D6}; ---- B4{D4}; -.- B6{D6}.



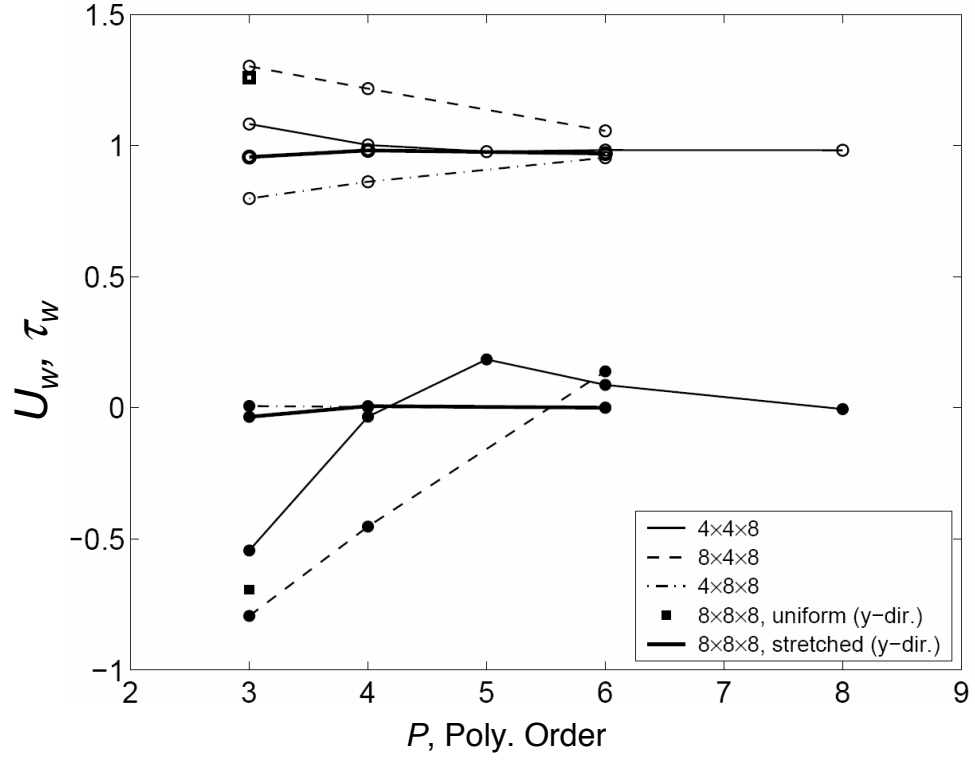


**Figure 2.6.** Wall shear stress and average streamwise velocity slip (at the wall) variation with polynomial orders for different meshes at  $Re_\tau = 100$ . The filled symbols ( $\bullet$ ,  $\blacksquare$ ) are planar averaged streamwise velocity slip at the channel walls ( $U_w$ , slip) while the open symbols ( $\circ$ ,  $\square$ ) are the time-averaged wall shear stress ( $\tau_w$ ).

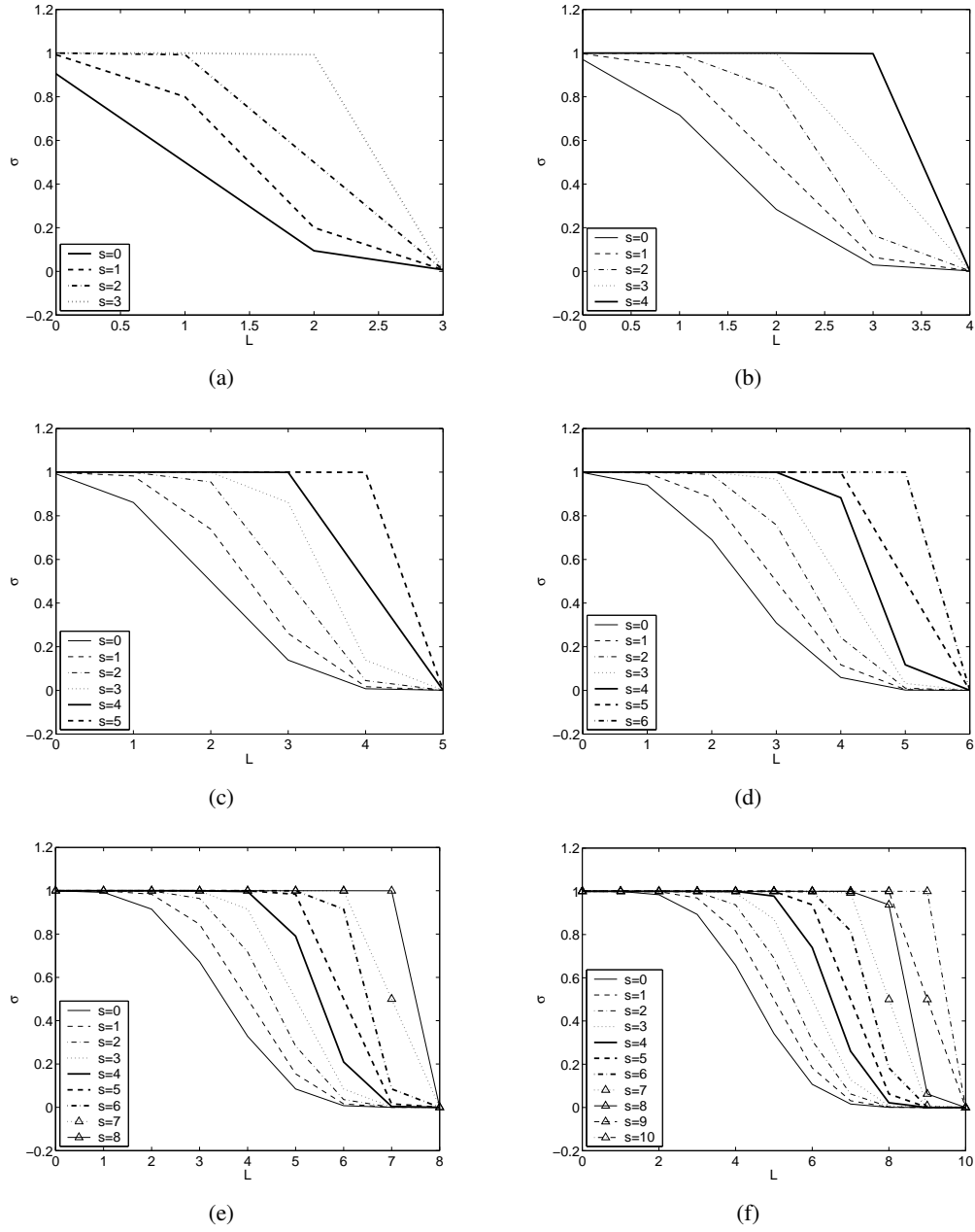


**Figure 2.7.** Spectral filter transfer functions for different polynomial orders. (a)  $p = 3$ ; (b)  $p = 4$ ; (c)  $p = 5$ ; (d)  $p = 6$ ; (e)  $p = 8$ ; (f)  $p = 10$  where  $s$  is the spectral shift parameter.

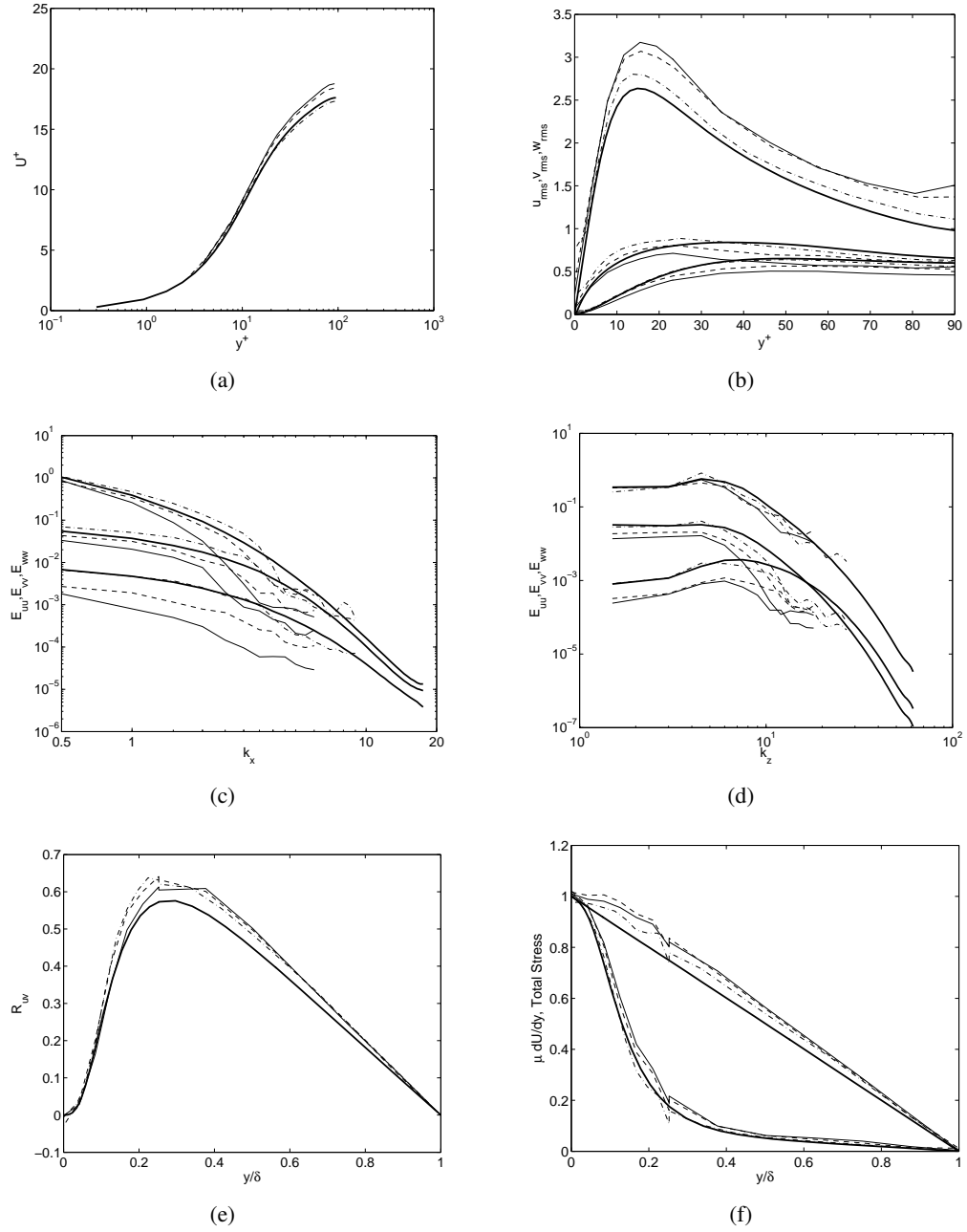
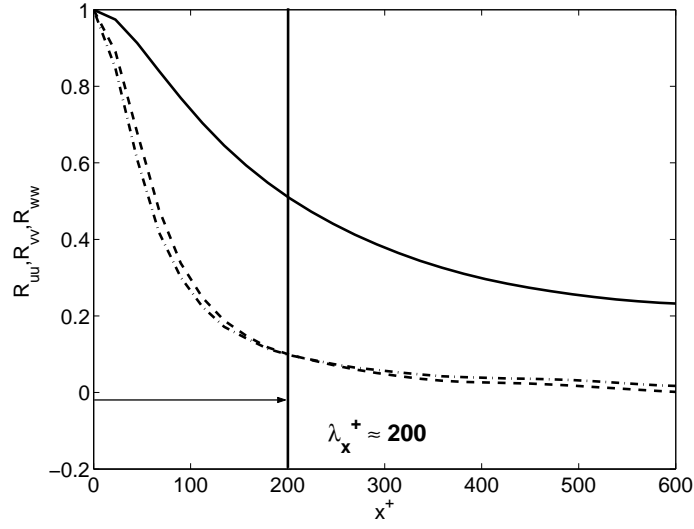
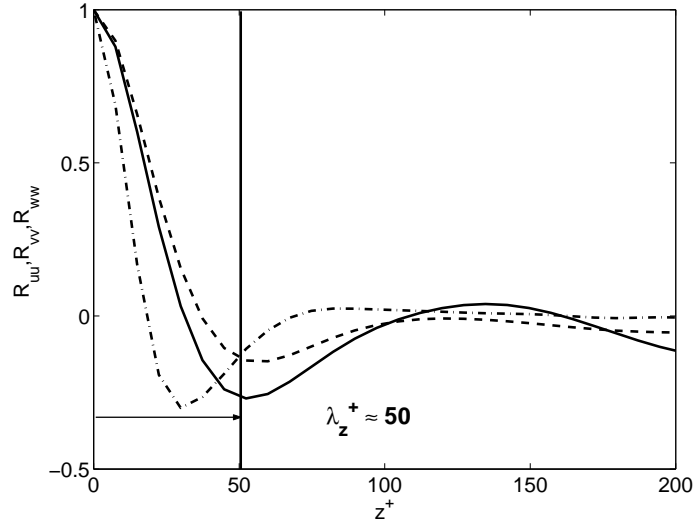


**Figure 2.8.** Meanflow and rms profiles for  $Re_\tau = 100$  computed with a  $4 \times 4 \times 4$  mesh using  $p = 5$  at  $Re_\tau = 100$  with SF [110] and PD [117] (refer to Table 2.2): — DNS [33]; — SF1; ---- SF3; —·— DNS1.



(a)



(b)

**Figure 2.9.** Important length scales for partition selection ( $L_e$ ) in  $\ell$ VMS for the turbulent channel flow [129]. Velocity correlation obtained from a  $8 \times 8 \times 8$  mesh using  $p = 6$  for  $Re_\tau = 100$  at  $y^+ \approx 10$ : (a) Streamwise direction, (b) Spanwise direction.

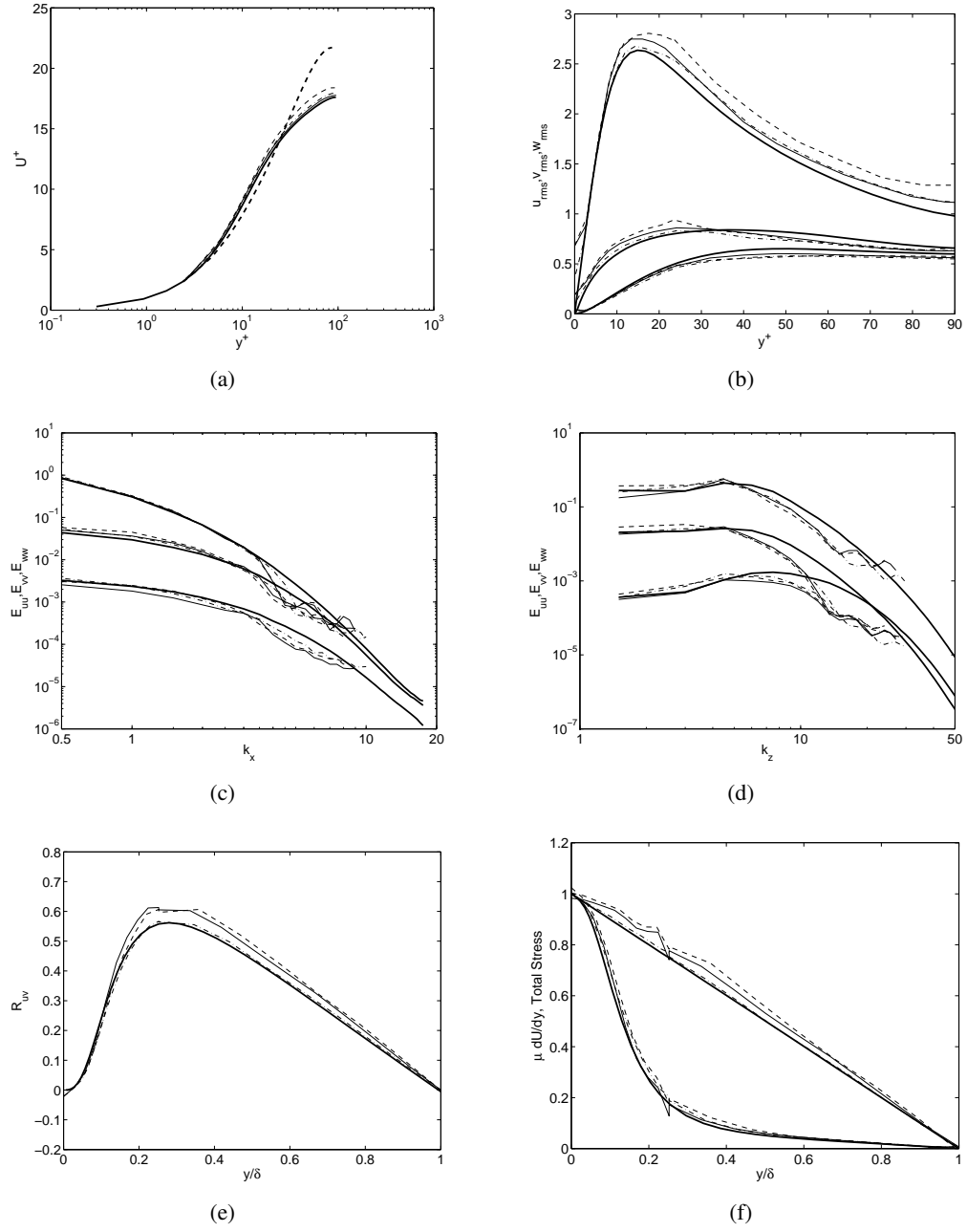


**Figure 2.10.** Turbulence statistics for  $Re_\tau = 100$  computed with a  $4 \times 4 \times 4$  mesh with different polynomial distributions and models (refer to Table 2.2): — DNS [33]; —  $\ell$ VMS1; ----  $\ell$ VMS2; —·—  $\ell$ VMS3; ····  $\ell$ VMS4.

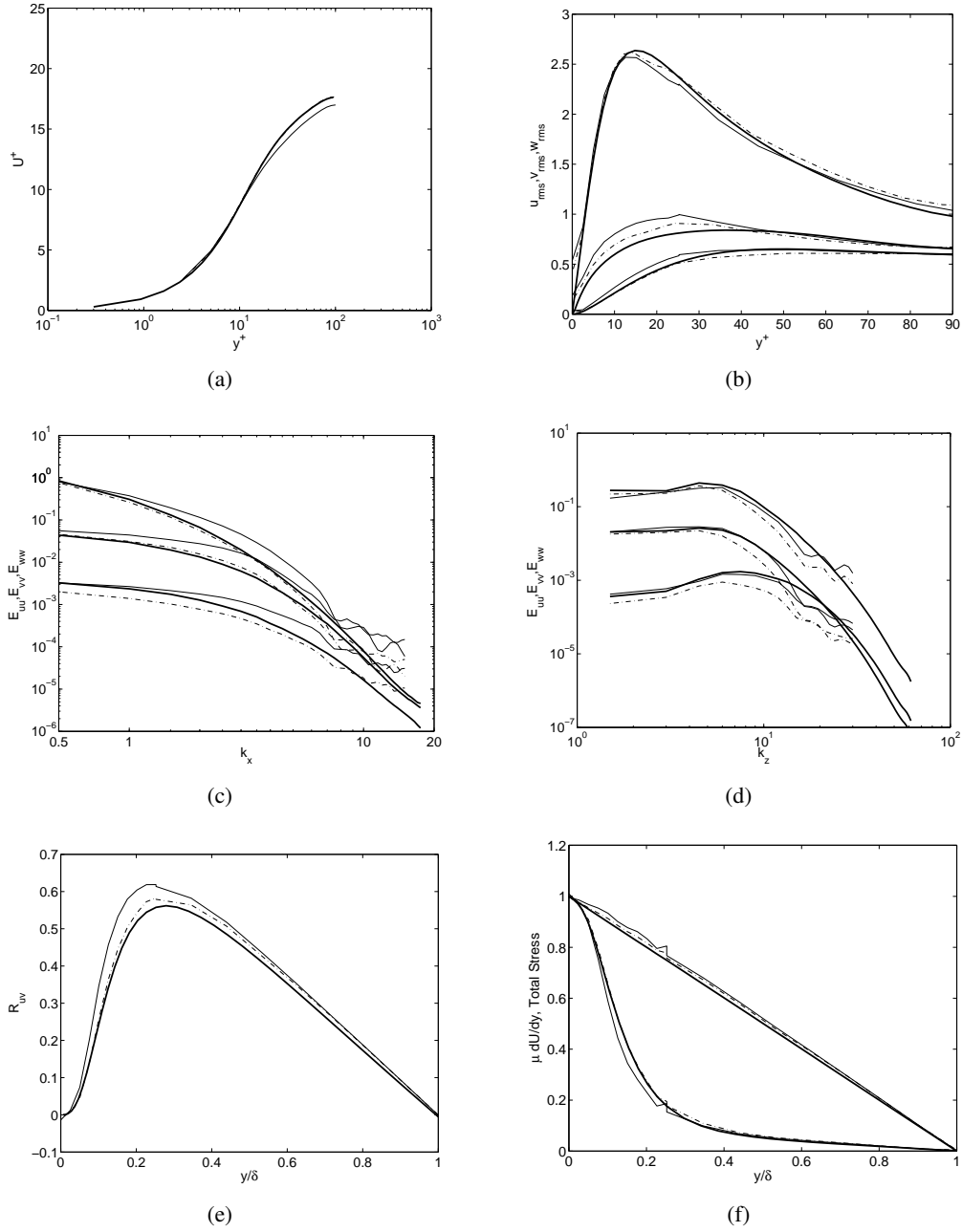


**Figure 2.11.** Turbulence statistics for  $Re_\tau = 100$  computed with a  $6 \times 4 \times 4$  mesh using  $p = \{6, 5, 5, 6\}$  from the bottom to the top wall (refer to Table 2.3): — DNS [33]; — DNS2; - -  $\ell$ VMS5.

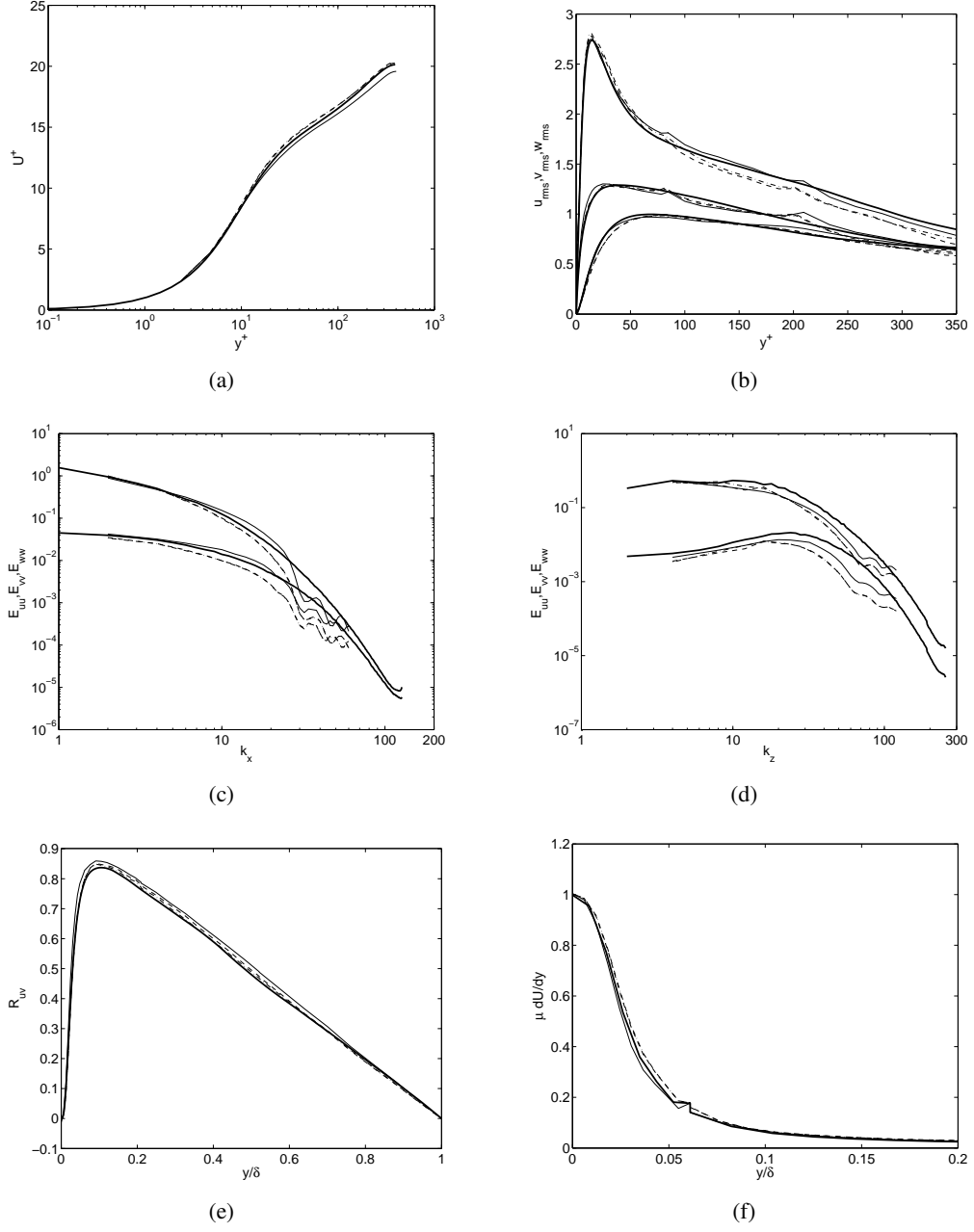


**Figure 2.12.** Turbulence statistics for  $Re_\tau = 395$  computed with a  $6 \times 8 \times 6$  mesh using  $p = \{6, 6, 5, 5, 5, 5, 6, 6\}$  from the bottom to the top wall (refer to Table 2.4): — DNS [119]; — DNS3; - -  $\ell$ VMS6; - - -  $\ell$ VMS7. For plot (f), the reference DNS is a higher resolution solution obtained with the current DG discretization [130].

This page intentionally left blank.



## Chapter 3

# A Multiscale Discontinuous Galerkin Method with the Computational Structure of a Continuous Galerkin Method

**Principle Authors:** Thomas J.R. Hughes<sup>1</sup>, Guglielmo Scovazzi, Pavel B. Bochev, and Annalisa Buffa<sup>2</sup>

Proliferation of degrees-of-freedom has plagued discontinuous Galerkin methodology from its inception over thirty years ago. This paper develops a new computational formulation that combines the advantages of discontinuous Galerkin methods with the data structure of their continuous Galerkin counterparts. The new method uses local, element-wise problems to project a continuous finite element space into a given discontinuous space, and then applies a discontinuous Galerkin formulation. The projection leads to parameterization of the discontinuous degrees-of-freedom by their continuous counterparts and has a variational multiscale interpretation. This significantly reduces the computational burden and, at the same time, little or no degradation of the solution occurs. In fact, the new method produces improved solutions compared with the traditional discontinuous Galerkin method in some situations.

### 3.1 Introduction

The discontinuous Galerkin (DG) method was developed for problems of neutron transport over thirty years ago by Reed and Hill [135]. Early works of note include Lesaint and Raviart [109], Johnson, Nävert and Pitkäranta [95] who, in the context of advection-dominated processes, synthesized DG with SUPG [26] and performed a complete mathematical analysis, and Johnson and Pitkäranta [96], who proved that the DG formulation for pure advection problems enjoys good stability properties, similar to the ones proved for SUPG. The interest in DG developed very slowly but has accelerated significantly in recent years. The compendium of papers in [40] provides a valuable summary of the current state-of-the-art and introduction to the literature. Recent literature on DG methods includes [3, 4, 16, 32, 48–51, 60, 70, 71, 77, 78, 113, 125, 128, 156, 157].

---

<sup>1</sup>Institute for Computational Engineering and Sciences, The University of Texas at Austin, Austin, TX 78712

<sup>2</sup>IMATI - Consiglio Nazionale delle Ricerche, Pavia, Italy

The DG method is felt to have advantages of robustness over the classical continuous Galerkin (CG) method, especially for first-order differential operators associated with hyperbolic equations, and better conditioning of resultant linear equation systems leading to improved iterative performance. There is also an opportunity to link DG with the numerical fluxes (i.e., solutions of the one-dimensional Riemann problem) used in finite volume methods and develop higher-order accurate procedures for wave-propagation. These attributes have led to numerous applications in fluids where the CG method has often proved inadequate. There has also been recent interest in applying DG to elliptic problems so that advective-diffusive phenomena can be modeled. For a review of work in this area, see Arnold *et al.* [7]. Recent studies include Brezzi *et al.* [23], Dawson [47], and Hughes, Masud and Wan [87]. There has been very little work in structural mechanics so far but interest is beginning to grow. See for example, Engel *et al.* [58], and Brezzi and Marini [24].

Despite the increased interest in DG methods, there are shortcomings that limit their practical utility. Foremost among these is the size of the DG equation system for interpolations of linear and higher order. By virtue of the fact that the trial functions are completely discontinuous, there is no sharing of degrees-of-freedom at element boundaries. Consequently, the size of the solution space “explodes.” For example, assuming about seven linear tetrahedral elements per node, the DG system involves approximately 28 times the number of unknowns of the corresponding CG system (see Hughes *et al.* [82]). Storage and solution cost are, obviously, adversely affected, which seems the main reason for the small industrial impact the DG method has had so far. In addition, it has been observed that the vaunted robustness of the DG method is somewhat exaggerated. Simple, one-dimensional examples of pure advection and pure diffusion were shown to give rise to spurious oscillations in Hughes *et al.* [82].

There are two perspectives on the proposed new method. One is to assume a given, continuous finite element space, and then associate to it a completely discontinuous space by releasing all continuity constraints at element interfaces. This viewpoint is somewhat restrictive but is applicable to most situations of engineering interest and therefore is adopted in this paper. Another, more general, view is to start with an arbitrary discontinuous finite element space and then construct a continuous representation from it. This viewpoint will be developed in a forthcoming work of the authors. Once the spaces are defined, a global DG formulation is applied to the discontinuous space. The unique feature of our formulation is the use of local, element-wise problems, to define the discontinuous field in terms of the degrees-of-freedom of the continuous field. The local problems employ weakly imposed boundary conditions and the solutions are still discontinuous but they are parameterized by the degrees-of-freedom of the much smaller continuous space. The global problem has the equation size and structure of a CG method but it is indeed a DG method. The local problems serve to project the solution into a reduced-dimension manifold that expresses the partial-differential structure of the problem considered. This aspect is seen to be related to methods used in wave propagation problems, relying on numerical fluxes inspired by local Riemann solutions, but here the local problems are solved numerically using simple basis functions. The interesting result is that the new method is at least as accurate and robust as the global DG method, and, at the same time, the storage and computational effort are dramatically reduced. As may be obvious from the description, the method has a multiscale interpretation. For this reason, we refer to it as the multiscale DG

method (MDG).

The new method is demonstrated on simple test cases of advection-diffusion. However, the ideas are quite general and may be applied to arbitrary partial-differential equation systems. Section 3.2 is devoted to the introduction of the advection-diffusion problem, to prepare the ground for the global DG formulation presented in Section 3.3. Three variants of the discretization of the Laplace operator are considered: the symmetric, neutral, and skew-symmetric forms. The local problem is described in Section 3.4. The weak formulation is similar to the one used for the global problem, but an additional stabilization term is required. Numerical results are presented in Section 3.5, and conclusions are drawn in Section 3.6.

## 3.2 Advection-Diffusion Equation

This section describes the boundary-value problem for the linear advection-diffusion equation and introduces definitions and notations needed for the DG formulation presented subsequently.

### 3.2.1 Strong form of the problem

Let  $\Omega$  be a bounded domain in  $\mathbb{R}^{n_d}$ , where  $n_d$  is the number of space dimensions, let  $\mathbf{a}$  be a smooth, solenoidal, velocity vector field defined on  $\overline{\Omega}$ , and let  $\kappa$  be a positive, constant, diffusivity coefficient. Consider the following partition of the boundary  $\Gamma = \partial\Omega$ :

$$\Gamma^- = \{x \in \Gamma : \mathbf{a}(x) \cdot \mathbf{n}(x) \leq 0\} \quad (3.1)$$

$$\Gamma^+ = \{x \in \Gamma : \mathbf{a}(x) \cdot \mathbf{n}(x) > 0\} \quad (3.2)$$

where  $\mathbf{n}$  is the outward unit normal with respect to  $\Gamma$ .  $\Gamma^-$  is referred to as the inflow boundary and  $\Gamma^+$  as the outflow boundary. Another partition is given by  $\Gamma = \overline{\Gamma_h} \cup \overline{\Gamma_g}$ ,  $\Gamma_h \cap \Gamma_g = \emptyset$ , and thus

$$\Gamma_g^\mp = \Gamma_g \cap \Gamma^\mp \quad (3.3)$$

$$\Gamma_h^\mp = \Gamma_h \cap \Gamma^\mp \quad (3.4)$$

The setup is illustrated in Figure 3.1. The strong form of the boundary-value problem is:

Find  $\phi : \overline{\Omega} \rightarrow \mathbb{R}$ , such that for all  $f : \Omega \rightarrow \mathbb{R}$ ,  $g : \Gamma \rightarrow \mathbb{R}$ , and  $h : \Gamma \rightarrow \mathbb{R}$ ,

$$\mathbf{a} \cdot \nabla \phi - \kappa \Delta \phi = f \quad \text{in } \Omega \quad (3.5)$$

$$\phi = g \quad \text{on } \Gamma_g \quad (3.6)$$

$$(-\mathbf{a} \phi \chi_{\Gamma_h^-} + \kappa \nabla \phi) \cdot \mathbf{n} = h \quad \text{on } \Gamma_h \quad (3.7)$$

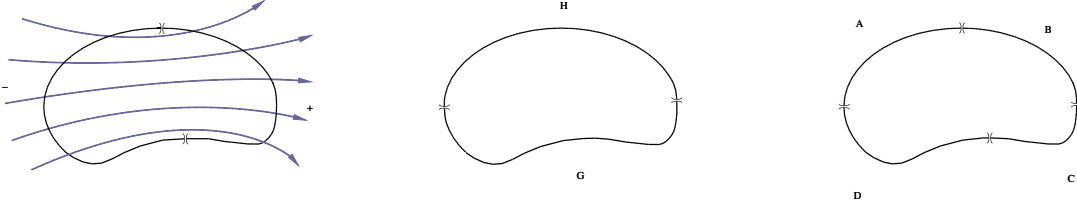


**Figure 3.1.** Boundary partitions.

where  $\chi_{\Gamma_h^-}$  is the characteristic function of the set  $\Gamma_h^-$ . The meaning of the boundary condition on  $\Gamma_h$  is that the total flux (advective plus diffusive) is imposed on the boundary  $\Gamma_h^-$  and the diffusive flux is specified on the boundary  $\Gamma_h^+$ . For further insight into these boundary conditions, see Hughes, Franca and Hulbert [84].

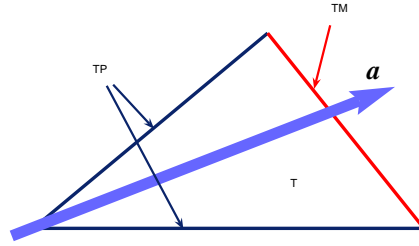


**Figure 3.2.** Schematic of the inflow and outflow boundaries for an element with respect to the convective field  $\mathbf{a}$ .

### 3.2.2 Definitions and notations for the discontinuous Galerkin method

Let  $\mathcal{T}_h$  be a regular family of elements  $T$  generating a partition of  $\Omega$ . For example,  $T$  can be thought of as triangles/tetrahedra, or quadrilaterals/hexahedra, in two/three dimensions, respectively. Let  $h_T$  denote the diameter of  $T$  and  $h = \max_{T \in \mathcal{T}_h} h_T$ . Let  $\mathcal{E}_h$  be the set of element edges (including edges on the boundary  $\Gamma$ ) and  $\mathcal{E}_h^o$  be the set of internal edges (excluding edges on the boundary  $\Gamma$ ). It follows that

$$\mathcal{E}_h = \mathcal{E}_h^o \cup \Gamma \quad (3.8)$$

It is also helpful to define inflow and outflow partitions of the element boundary  $\Gamma_T = \partial T$  (see Fig. 3.2):

$$\Gamma_T^- = \{x \in \Gamma_T : \mathbf{a}(x) \cdot \mathbf{n}(x) \leq 0\} \quad (3.9)$$

$$\Gamma_T^+ = \{x \in \Gamma_T : \mathbf{a}(x) \cdot \mathbf{n}(x) > 0\} \quad (3.10)$$

In order to derive a DG formulation, jumps and averages of scalar and vector functions have to be defined on  $\mathcal{E}_h$ . We shall employ the Brezzi conventions for this purpose. For an interior edge  $e \in \mathcal{E}_h^o$ , let  $T^+$  and  $T^-$  be the two elements sharing it, and let  $\mathbf{n}^+$  and  $\mathbf{n}^-$  be their respective outward-pointing unit normals (see Fig. 3.3). Accordingly, let  $\varphi$  be a scalar field, and  $\varphi^\pm := \varphi|_{T^\pm}$ . For  $e \in \mathcal{E}_h^o$ :

$$\langle \varphi \rangle := \frac{1}{2}(\varphi^+ + \varphi^-) \quad (3.11)$$

$$[[\varphi]] := \varphi^+ \mathbf{n}^+ + \varphi^- \mathbf{n}^- \quad (3.12)$$

Analogously, if  $\boldsymbol{\tau}$  is a vector field,

$$\langle \boldsymbol{\tau} \rangle := \frac{1}{2}(\boldsymbol{\tau}^+ + \boldsymbol{\tau}^-) \quad (3.13)$$

$$[[\boldsymbol{\tau}]] := \boldsymbol{\tau}^+ \cdot \mathbf{n}^+ + \boldsymbol{\tau}^- \cdot \mathbf{n}^- \quad (3.14)$$

Notice that, by definition of “ $[[ \cdot ]]$ ”, the jump of a scalar quantity is a vector and the jump of a vector quantity is a scalar. Definitions (3.12) and (3.14) do not depend on the ordering of the elements. It is important to specialize the previous formulas to the edges on the boundary  $\Gamma$ :

$$[[\varphi]] = \varphi \mathbf{n}, \quad \langle \boldsymbol{\tau} \rangle = \boldsymbol{\tau}, \quad \forall e \in \Gamma \quad (3.15)$$

It will not be necessary to define  $\langle \varphi \rangle$  and  $[[\boldsymbol{\tau}]]$  on the boundary  $\Gamma$ , because they are never utilized. Noting that

$$\begin{aligned} [[\varphi \boldsymbol{\tau}]] &= \varphi^+ \boldsymbol{\tau}^+ \cdot \mathbf{n}^+ + \varphi^- \boldsymbol{\tau}^- \cdot \mathbf{n}^- \\ &= \frac{1}{2} (2\varphi^+ \boldsymbol{\tau}^+ \cdot \mathbf{n}^+ + 2\varphi^- \boldsymbol{\tau}^- \cdot \mathbf{n}^-) \\ &= \frac{\varphi^+ + \varphi^-}{2} (\boldsymbol{\tau}^+ \cdot \mathbf{n}^+ + \boldsymbol{\tau}^- \cdot \mathbf{n}^-) + \frac{\boldsymbol{\tau}^+ + \boldsymbol{\tau}^-}{2} \cdot (\varphi^+ \mathbf{n}^+ + \varphi^- \mathbf{n}^-) \\ &= \langle \varphi \rangle [[\boldsymbol{\tau}]] + \langle \boldsymbol{\tau} \rangle \cdot [[\varphi]] \end{aligned} \quad (3.16)$$

and accounting for (3.15), it follows that

$$\sum_{T \in \mathcal{T}_h} \int_{\partial T} \boldsymbol{\tau} \cdot \mathbf{n} \varphi = \sum_{e \in \mathcal{E}_h} \int_e \langle \boldsymbol{\tau} \rangle \cdot [[\varphi]] + \sum_{e \in \mathcal{E}_h^o} \int_e [[\boldsymbol{\tau}]] \langle \varphi \rangle \quad (3.17)$$

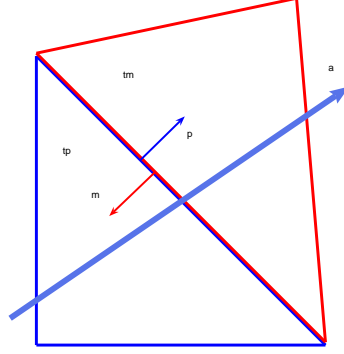


**Figure 3.3.** Schematic of the normals and  $+/-$  regions with respect to an edge.

Another important identity is

$$\begin{aligned}
 \llbracket \varphi \boldsymbol{\tau} \rrbracket &= \varphi^+ \boldsymbol{\tau}^+ \cdot \mathbf{n}^+ + \varphi^- \boldsymbol{\tau}^- \cdot \mathbf{n}^- \\
 &= \varphi^+ \boldsymbol{\tau}^+ \cdot \mathbf{n}^+ + \varphi^\pm \boldsymbol{\tau}^\mp \cdot \mathbf{n}^- + \varphi^\pm \boldsymbol{\tau}^\mp \cdot \mathbf{n}^+ + \varphi^- \boldsymbol{\tau}^- \cdot \mathbf{n}^- \\
 &= \varphi^\pm \llbracket \boldsymbol{\tau} \rrbracket + \llbracket \varphi \rrbracket \cdot \boldsymbol{\tau}^\mp
 \end{aligned} \tag{3.18}$$

which implies

$$\sum_{T \in \mathcal{T}_h} \int_{\partial T} \boldsymbol{\tau} \cdot \mathbf{n} \varphi = \sum_{e \in \mathcal{E}_h^o} \left( \int_e \varphi^\pm \llbracket \boldsymbol{\tau} \rrbracket + \int_e \llbracket \varphi \rrbracket \cdot \boldsymbol{\tau}^\mp \right) + \sum_{e \in \Gamma} \int_e \varphi \boldsymbol{\tau} \cdot \mathbf{n} \tag{3.19}$$

This last result will be used in the sequel to recover the Euler-Lagrange forms of variational problems.

Following the perspective on the new method adopted in Section 3.1 we first introduce the *continuous* finite element space

$$\overline{V}_h^k = \{v \in H^1(\Omega) : v|_T \in \mathcal{P}^k(T), \quad \forall T \in \mathcal{T}_h\} \tag{3.20}$$

where  $\mathcal{P}^k$  is the space of polynomials of degree less than or equal to  $k$ , and then associate with it the *discontinuous* approximation space

$$V_h^k = \{v \in L^2(\Omega) : v|_T \in \mathcal{P}^k(T), \quad \forall T \in \mathcal{T}_h\}. \tag{3.21}$$

According to the interpretation in Section 3.1 we will view  $V_h^k$  as being obtained from  $\overline{V}_h^k$  by releasing interelement continuity constraints.

### 3.3 Global Weak Formulation

In this section a global DG method is presented which will serve as a framework for the solution of the advection-diffusion problem. Skew-symmetric, neutral, and symmetric versions of the DG method are considered. They will be integrated into the global formulation by introducing a switch  $s$ , taking the values +1, 0, and -1, respectively. The symmetric version is the only one which yields a symmetric discretization of the Laplace operator and is the only one that is adjoint consistent, following the terminology of Arnold *et al.* [7].

#### 3.3.1 Conservative formulation

One of the most important design requirements for DG formulations is conservation. In the present formulation a new approach is taken to enforce conservation of the total flux  $\sigma := \mathbf{a}\phi_h - \kappa \nabla \phi_h$ . The global DG formulation reads:

Find  $\phi_h \in V_h^k$  such that,  $\forall \mu_h \in V_h^k$ ,

$$\begin{aligned}
0 = & \sum_{T \in \mathcal{T}_h} \left( - \int_T \nabla \mu_h \cdot (\mathbf{a}\phi_h - \kappa \nabla \phi_h) - \int_T \mu_h f \right) \\
& + \sum_{e \in \Gamma_g} \left( \int_e \mu_h \left( \mathbf{a}(\chi_{\Gamma_g^-} g + \chi_{\Gamma_g^+} \phi_h) - \kappa \nabla \phi_h \right) \cdot \mathbf{n} + \int_e \left( \frac{\epsilon \kappa}{h_\perp} \mu_h + s \kappa \nabla \mu_h \cdot \mathbf{n} \right) (\phi_h - g) \right) \\
& + \sum_{e \in \Gamma_h} \int_e \mu_h \left( (\mathbf{a}\phi_h) \chi_{\Gamma_h^+} \cdot \mathbf{n} - h \right) \\
& + \sum_{e \in \mathcal{E}_h^o} \left( \int_e ([\mu_h] \cdot (\mathbf{a}\phi_h^- - \kappa \nabla \phi_h^-) + s \kappa \nabla \mu_h^- \cdot [\phi_h]) + \int_e \frac{\epsilon \kappa}{h_\perp} [\mu_h] \cdot [\phi_h] \right) \quad (3.22)
\end{aligned}$$

The following definition will be used:

$$h_\perp = \frac{\text{meas}(T^+) + \text{meas}(T^-)}{2 \text{meas}(e)} \quad (3.23)$$

where  $T^-/T^+$  are, respectively, the upwind/downwind elements with respect to the edge  $e$ . Roughly speaking,  $h_\perp$  is a length scale in the direction perpendicular to the edge  $e$ , close to the length of the segment joining the barycenters of  $T^-$  and  $T^+$  (see Fig. 3.4). The selection of the value of the non-dimensional parameter  $\epsilon$  will be described subsequently.

#### Remark

The effect of the parameter  $s$  has been extensively studied in the discontinuous Galerkin literature (see Arnold *et al.* [7], Baumann and Oden [13], and Hughes *et al.* [82]). The symmetric formulation (i.e.,  $s = -1$ ) is adjoint-consistent, guaranteeing optimal  $L_2$ -convergence

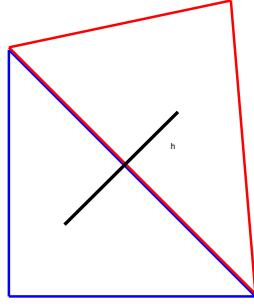


**Figure 3.4.** Definition of  $h_{\perp}$  for two adjacent triangular elements.

rates in the diffusive limit. Ostensibly, the skew formulation (i.e.,  $s = +1$ ) has superior stability properties but the  $\epsilon$ -terms can be used to improve the stability behavior of the neutral (i.e.,  $s = 0$ ) and symmetric formulations.

### 3.3.1.1 Conservation properties

In many applications global and/or local conservation is important. Our DG formulation (3.22) possesses exactly the same global conservation as a continuous Galerkin method. To extract a statement of conservation, consider the case  $\Gamma_g = \emptyset$  and set the weighting function  $\mu_h$  in (3.22) equal to one throughout  $\Omega$ . It is easily seen that the finite element solution  $\phi_h$  satisfies

$$\int_{\Omega} f + \int_{\Gamma_{h-}} h^- + \int_{\Gamma_{h+}} (-\mathbf{a} \cdot \mathbf{n} \phi_h + h^+) = 0. \quad (3.24)$$

which is identical with the conservation statement of a standard Galerkin method; see [79].

To extract a local conservation statement, consider for simplicity an element  $T$  that does not have edges on the boundary  $\Gamma$  and a weight function  $\mu_h$  that equals one on  $T$  and zero on all other elements. Then, (3.22) reduces to

$$-\int_T f + \sum_{e \in \partial T} \left( \int_e (\mathbf{a} \phi_h^- - \kappa \nabla \phi_h^-) \cdot \mathbf{n} + \int_e \frac{\epsilon \kappa}{h_{\perp}} \llbracket \phi_h \rrbracket \cdot \mathbf{n} \right) = 0, \quad (3.25)$$

where we have used that for the given choice of  $\mu_h$  the jump  $\llbracket \mu_h \rrbracket$  is simply the outer normal  $\mathbf{n}$  to  $\partial T$ . Without the stabilization term (3.25) specializes to

$$-\int_T f + \sum_{e \in \partial T} \int_e (\mathbf{a} \phi_h^- - \kappa \nabla \phi_h^-) \cdot \mathbf{n} = 0, \quad (3.26)$$

i.e., the DG method (3.22) is locally conservative. When  $\epsilon > 0$  local conservation is exact to order  $O(\epsilon)$ . This situation is typical of all DG methods that employ interior penalty



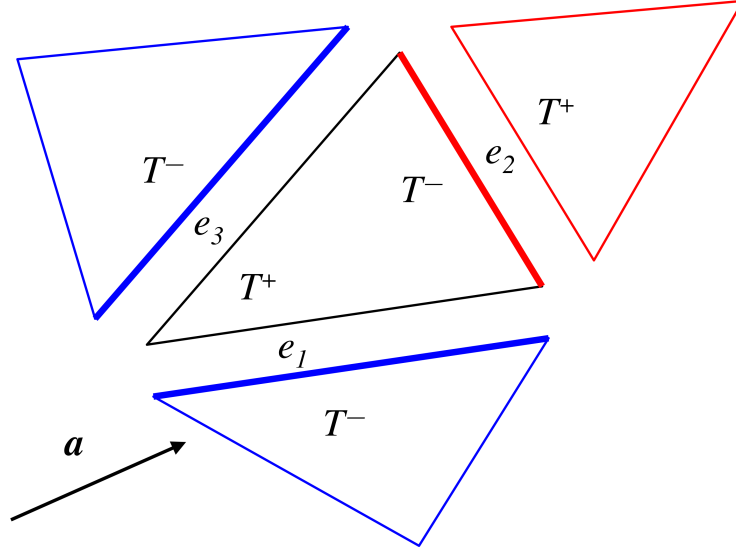


**Figure 3.5.** Local conservation of flux: inflow fluxes from the contiguous upwind elements (blue) are balanced by the outflow flux on the outflow boundary of the element (red).

terms for stabilization. Then the strong local conservation is weakened in the sense that the element conservation law involves terms from *all* surrounding elements, contributed by the last term in (3.25). This is reminiscent of what occurs in CG methods, the  $\epsilon$ -terms here enforcing a weak continuity. It should be noted however, that local conservation is a topological property, while stability and convergence are metric properties, and so, the weakened local conservation does not imply inferior convergence or stability of the DG scheme.

As a final note, we point out that in most DG formulations advective fluxes are *upwinded* while diffusive fluxes are *centered*. This leads to conservation of fluxes that are not located at the same place. A unique property of our DG formulation is the upwinding of the total flux. This results in locally conservative fluxes that are computed entirely in one place. To clarify this important distinction let us assume that  $T$  and  $\mathbf{a}$  are in the configuration shown in Fig. 3.5 and that the edges of  $T$  are numbered counterclockwise starting from the bottom edge. Let  $\phi_h^T$  denote the value of  $\phi_h$  on  $T$  and  $\phi_h^C$  denote the value of this function on the contiguous elements. Then, the conserved flux is given by

$$\mathbf{a}\phi_h^- - \kappa\nabla\phi_h^- = \begin{cases} \mathbf{a}\phi_h^C - \kappa\nabla\phi_h^C & \text{on } e_1 \cup e_3 \\ \mathbf{a}\phi_h^T - \kappa\nabla\phi_h^T & \text{on } e_2 \end{cases} \quad (3.27)$$

From this it is clear that in our formulation the *outflow* fluxes on the outflow boundary of the element in question are balanced by the *inflow* fluxes from the *contiguous* upwind elements; see Fig. 3.5. This consistent upwinding of the flux is reminiscent of the consistent weighting of the residual in a stabilized method [26, 81, 84].

### 3.3.1.2 Euler-Lagrange equations

To understand (3.22), it is instructive to derive the Euler-Lagrange equations by means of an integration-by-parts. Use of (3.17) with  $\boldsymbol{\tau} = \kappa \nabla \phi_h$  and (3.19) with  $\boldsymbol{\tau} = \mathbf{a} \phi_h$  yields:

$$\begin{aligned}
0 = & \sum_{T \in \mathcal{T}_h} \int_T \mu_h (\nabla \cdot (\mathbf{a} \phi_h - \kappa \nabla \phi_h) - f) \\
& + \sum_{e \in \Gamma_g} \int_e \left( \frac{\epsilon \kappa}{h_\perp} \mu_h + s \kappa \nabla \mu_h \cdot \mathbf{n} - \mu_h \mathbf{a} \chi_{\Gamma_g^-} \right) (\phi_h - g) \\
& + \sum_{e \in \Gamma_h} \int_e \mu_h \left( (-\mathbf{a} \phi_h \chi_{\Gamma_h^-} + \kappa \nabla \phi_h) \cdot \mathbf{n} - h \right) \\
& + \sum_{e \in \mathcal{E}_h^o} \left( \int_e (-\mu_h^+ [\mathbf{a} \phi_h - \kappa \nabla \phi_h] + s \kappa \nabla \mu_h^- \cdot [\phi_h]) + \int_e \frac{\epsilon \kappa}{h_\perp} [\mu_h] \cdot [\phi_h] \right) \quad (3.28)
\end{aligned}$$

#### Remarks

1. The first sum weakly enforces satisfaction of the advection-diffusion equation on each element domain  $T$ .
2. The terms multiplied by the parameter  $\epsilon$  serve the purpose of eliminating a kernel in the discrete diffusive operator, in the limit  $\mathbf{a} \rightarrow \mathbf{0}$ .
3. In the second sum, Dirichlet boundary conditions are weakly enforced by weighting their residual  $\phi_h - g$  by the total flux at the inflow and the diffusive flux at the outflow. In the advection-dominated limit, the outflow boundary condition is significantly relaxed, whereas when diffusion dominates, it converges toward strong satisfaction everywhere.
4. In the third sum, Neumann conditions are imposed according to the same rationale as for the Dirichlet conditions. The total flux  $\mathbf{a} \phi_h - \kappa \nabla \phi_h$  is imposed at the inflow, while only the diffusive flux is specified at the outflow.
5. The first term in the last sum weakly enforces continuity of the total flux across internal element interfaces. It represents an upwind total flux, since the jump of the fluxes upwind and downwind of an edge are weighted by the downwind test function  $\mu_h^+$ . The total flux is conserved and upwind.
6. The terms involving  $[\phi_h]$  weakly enforce the continuity of  $\phi_h$  across element interfaces.

### 3.4 Local Weak Formulations

#### 3.4.1 Local problem for the trial solution

The discontinuous field  $\phi_h \in V_h^k$  is linked to a continuous field  $\bar{\phi}_h \in \bar{V}_h^k$  by the following local (i.e., element-by-element) DG problem:

Find  $\phi_h \in V_h^k(T)$  such that,  $\forall v \in V_h^k(T)$ :

$$\begin{aligned} 0 = & - \int_T \nabla v \cdot (\mathbf{a}\phi_h - \kappa \nabla \phi_h) - \int_T v f + \epsilon \int_{\Gamma_T} \frac{\tilde{\kappa}}{h_\perp} v (\phi_h - \bar{\phi}_h) \\ & + \int_{\Gamma_T^+} v \phi_h \mathbf{a} \cdot \mathbf{n} + \int_{\Gamma_T^-} v \bar{\phi}_h \mathbf{a} \cdot \mathbf{n} \\ & + \int_{\Gamma_T} s \kappa \nabla v \cdot \mathbf{n} (\phi_h - \bar{\phi}_h) - \int_{\Gamma_T} \kappa \nabla \phi_h \cdot \mathbf{n} v \end{aligned} \quad (3.29)$$

where

$$\tilde{\kappa} = \kappa + \delta \chi_{\Gamma_T^+} h_\perp \mathbf{a} \cdot \mathbf{n} \quad (3.30)$$

and  $V_h^k(T) = \mathcal{P}^k(T)$ . The parameter  $\delta$  eliminates a kernel which can occur in the limit  $\kappa \rightarrow 0$  in isolated circumstances. Further discussion will be presented subsequently. The Euler-Lagrange equations are:

$$\begin{aligned} 0 = & \int_T v (\nabla \cdot (\mathbf{a}\phi_h - \kappa \nabla \phi_h) - f) + \epsilon \int_{\Gamma_T} \frac{\tilde{\kappa}}{h_\perp} v (\phi_h - \bar{\phi}_h) \\ & + \int_{\Gamma_T^-} v \mathbf{a} \cdot \mathbf{n} (\bar{\phi}_h - \phi_h) - \int_{\Gamma_T} s \kappa \nabla v \cdot \mathbf{n} (\bar{\phi}_h - \phi_h) \end{aligned} \quad (3.31)$$

Equation (3.29) can be succinctly expressed as:

Find  $\phi_h \in V_h^k(T)$  such that,  $\forall v \in V_h^k(T)$ :

$$B(v, \phi_h) = F(v; f, \bar{\phi}_h) \quad (3.32)$$

where

$$\begin{aligned} B(v, \phi_h) = & - \int_T \nabla v \cdot (\mathbf{a}\phi_h - \kappa \nabla \phi_h) - \int_{\Gamma_T} v \kappa \nabla \phi_h \cdot \mathbf{n} \\ & + \int_{\Gamma_T} \left( \frac{\epsilon \tilde{\kappa}}{h_\perp} v + \left( s \kappa \nabla v + v \chi_{\Gamma_T^+} \mathbf{a} \right) \cdot \mathbf{n} \right) \phi_h \end{aligned} \quad (3.33)$$

$$F(v; f, \bar{\phi}_h) = \int_T v f + B_\Gamma(v, \bar{\phi}_h) \quad (3.34)$$

and

$$B_\Gamma(v, \bar{\phi}_h) = \int_{\Gamma_T} \left( \frac{\epsilon \tilde{\kappa}}{h_\perp} v + \left( s \kappa \nabla v - v \chi_{\Gamma_T^-} \mathbf{a} \right) \cdot \mathbf{n} \right) \bar{\phi}_h \quad (3.35)$$

$B(\cdot, \cdot)$  and  $B_\Gamma(\cdot, \cdot)$  are bilinear forms and  $F(\cdot; \cdot, \cdot)$  is linear with respect to its first argument and affine with respect to its second and third arguments. Let  $n_{en}$  denote the number of element nodes and let  $\{\psi_j\}_1^{n_{en}}$  denote the nodal basis for the element in question. The basis functions associated with the element boundary nodes are denoted  $\{\bar{\psi}_j\}_1^{\bar{n}_{en}}$ . Obviously, these are a subset of  $\{\psi_j\}_1^{n_{en}}$ . We write

$$v = \sum_{j=1}^{n_{en}} v_j \psi_j \quad (3.36)$$

$$\phi_h = \sum_{j=1}^{n_{en}} \Phi_j \psi_j \quad (3.37)$$

$$\bar{\phi}_h = \sum_{j=1}^{\bar{n}_{en}} \bar{\Phi}_j \bar{\psi}_j \quad (3.38)$$

$$f = \sum_{j=1}^{n_{en}} f_j \psi_j \quad (3.39)$$

where  $v_j$ ,  $\Phi_j$ , and  $\bar{\Phi}_j$ , and  $f_j$  denote nodal values. The interpretation is that  $\phi_h$  is the discontinuous solution and  $\bar{\phi}_h$  is the continuous solution in which degrees-of-freedom are shared on element boundaries. Substitution into (3.32) yields a local algebraic problem:

$$\mathbf{S} \bar{\Phi} = \bar{\mathbf{S}}_\Gamma \bar{\Phi} + \mathbf{M} \mathbf{f} \quad (3.40)$$

$$S_{ij} = B(\psi_i, \psi_j) \quad (3.41)$$

$$(\bar{S}_\Gamma)_{ij} = B_\Gamma(\psi_i, \bar{\psi}_j) \quad (3.42)$$

$$M_{ij} = \int_T \psi_i \psi_j \quad (3.43)$$

where  $\bar{\Phi} = [\bar{\Phi}_1, \bar{\Phi}_2, \dots, \bar{\Phi}_{\bar{n}_{en}}]^t$ ,  $\Phi = [\Phi_1, \Phi_2, \dots, \Phi_{n_{en}}]^t$ , and  $\mathbf{f} = [f_1, f_2, \dots, f_{n_{en}}]^t$ . Provided  $\mathbf{S}$  is invertible, it is possible to express  $\Phi$  in terms of  $\bar{\Phi}$  and  $\mathbf{f}$ :

$$\Phi = \mathbf{T}_{\phi_h \bar{\phi}_h}^h \bar{\Phi} + \mathbf{T}_{\phi_h f}^h \mathbf{f} \quad (3.44)$$

where  $\mathbf{T}_{\phi_h \bar{\phi}_h}^h = \mathbf{S}^{-1} \bar{\mathbf{S}}_\Gamma$  and  $\mathbf{T}_{\phi_h f}^h = \mathbf{S}^{-1} \mathbf{M}$ . This mapping enables us to eliminate local degrees-of-freedom in favor of global degrees-of-freedom. See Figure 3.6.

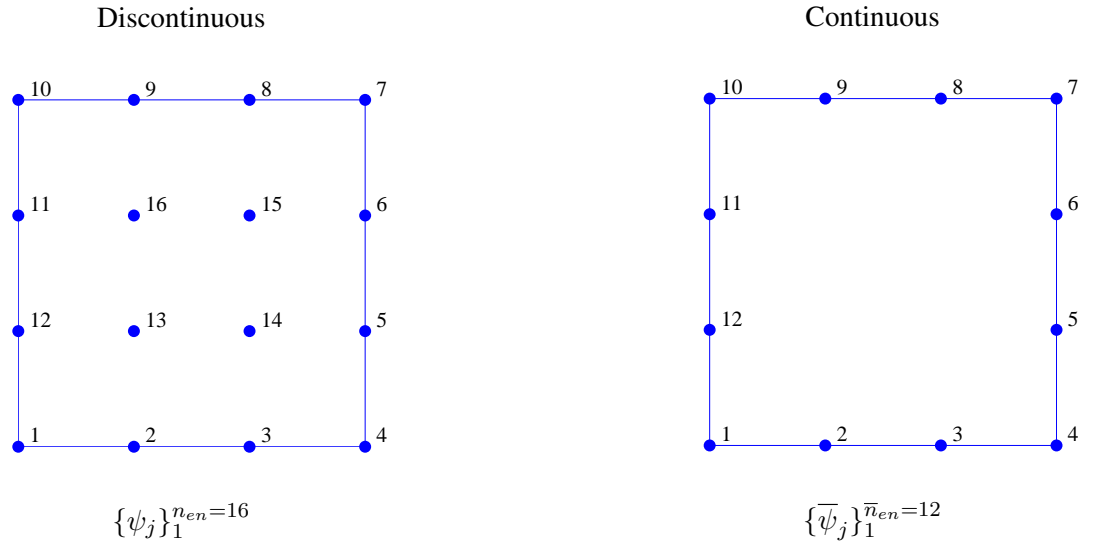


**Figure 3.6.** Schematic illustration of the basis functions in the local problem. On the left is a 16-node bicubic quadrilateral element. Its boundary nodes are identified on the right. The corresponding basis functions satisfy  $\bar{\psi}_j = \psi_j$ ,  $j = 1, 2, \dots, 12$ . The internal degrees-of-freedom, corresponding to  $\psi_{13}, \psi_{14}, \psi_{15}, \psi_{16}$ , are eliminated by the solution of the local problem. Only the unique, shared, boundary degrees-of-freedom are retained in the global problem.

### 3.4.1.1 Multiscale interpretation

Let  $\phi_h = \bar{\phi}_h + \phi'_h$ . We think of  $\bar{\phi}_h \in \bar{V}_h^k$  as the coarse-scale component of the solution, and  $\phi'_h \in V_h^k$  as the fine-scale component. By virtue of the fact that  $\bar{\phi}_h$  is continuous,  $\phi'_h$  may be thought of as the discontinuous part of the solution. Thus, the local problem can be stated as:

Find  $\phi'_h \in V_h^k(T)$  such that,  $\forall v \in V_h^k(T)$ :

$$B(v, \phi'_h) = R(v; f, \bar{\phi}_h) \quad (3.45)$$

where

$$\begin{aligned} R(v; f, \bar{\phi}_h) &= F(v; f, \bar{\phi}_h) - B(v, \bar{\phi}_h) \\ &= \int_T (\nabla v \cdot (\mathbf{a} \bar{\phi}_h - \kappa \nabla \bar{\phi}_h) + v f) - \int_{\Gamma_T} v (\mathbf{a} \bar{\phi}_h - \kappa \nabla \bar{\phi}_h) \cdot \mathbf{n} \\ &= - \int_T v (\mathbf{a} \cdot \nabla \bar{\phi}_h - \kappa \Delta \bar{\phi}_h - f) \end{aligned} \quad (3.46)$$

is the residual of the coarse-scale solution. Comparing (3.46) with (3.33) and (3.34), it is immediately realized that the local problem for the discontinuous correction  $\phi'_h$  corresponds to a local DG method with weakly-enforced homogeneous Dirichlet boundary conditions, driven by the residual. The relationship with the multiscale analysis presented in Hughes [81] and Hughes *et al.* [83] is then evident.

The local algebraic problem becomes

$$\mathbf{S} \Phi' = \bar{\mathbf{S}}_\Gamma \bar{\Phi} - \bar{\mathbf{S}} \bar{\Phi} + \mathbf{M} f \quad (3.47)$$

where

$$\bar{S}_{ij} = B(\psi_i, \bar{\psi}_j) \quad (3.48)$$

leading to

$$\Phi' = \mathbf{T}_{\phi'_h \bar{\phi}_h}^h \bar{\Phi} + \mathbf{T}_{\phi_h f}^h f \quad (3.49)$$

in which

$$\mathbf{T}_{\phi'_h \bar{\phi}_h}^h = \mathbf{T}_{\phi_h \bar{\phi}_h}^h - \mathbf{S}^{-1} \bar{\mathbf{S}} \quad (3.50)$$

#### Remark

If there are no element internal degrees-of-freedom, that is if  $\bar{\psi}_j = \psi_j, \forall j$ , which is typically the case for low-order elements, then  $\bar{\mathbf{S}} = \mathbf{S}$ .

### 3.4.2 Local problem for the weighting function

The discontinuous weighting function  $\mu_h \in V_h^k$  is also linked to the continuous weighting function  $\bar{\mu}_h \in \bar{V}_h^k$  as follows:

*Find  $\mu_h \in V_h^k(T)$  such that,  $\forall v \in V_h^k(T)$ :*

$$B(v, \mu_h) = F(v; 0, \bar{\mu}_h) \quad (3.51)$$

The multiscale version is given by

*Find  $\mu'_h \in V_h^k(T)$  such that,  $\forall v \in V_h^k(T)$ :*

$$B(v, \mu'_h) = R(v; 0, \bar{\mu}_h) \quad (3.52)$$

#### Remarks

1. The introduction of the local problems is seen to eliminate the fine-scale degrees-of-freedom in favor of the coarse-scale degrees-of-freedom. The combination of the local and global weak formulations defines the new MDG method.
2. The present approach has some similarities to the variational multiscale method [81, 83] and the residual-free bubble (RFB) method [22, 25]. There are many variants of these procedures. Perhaps the one which is the closest to the present work is the discontinuous residual-free bubble (DRFB) method of Sangalli [138]. As is typical in RFB methods, Sangalli begins with the standard weak form. Both the finite element and bubble spaces are normally assumed to be conforming but, inspired by [25], in which a discontinuous approximation of the exact bubble is shown to work well in the advection-dominated limit, Sangalli proposes a discontinuous Galerkin formulation of the local problem. There are three ostensible differences between DRFB and the present approach: (1) The global formulation in DRFB derives from the *continuous* Galerkin method, whereas ours derives from the *discontinuous* Galerkin method; (2) DRFB focuses only on the advection-dominated case and does not deal with some of the issues concerning the local problem that we considered, namely, the diffusion-dominated regime, and transition regime where both advective and diffusive mechanisms are important; and (3) the treatment of the weighting function in equation (3.52) has a substantial effect in the present approach but has no effect whatsoever in the RFB method. Despite these differences, the similarities are intriguing and warrant further investigation.

### 3.5 Numerical Results

#### 3.5.1 One-dimensional advection-diffusion

We assume the advective velocity,  $a$ , is positive and constant, and the force,  $f$  is constant. The exact solution of the strong form (3.7) is easily derived:

$$\phi(x) = \phi_0 + (\phi_L - \phi_0) \frac{1 - e^{Pe_L \frac{x}{L}}}{1 - e^{Pe_L}} + \frac{2\mathcal{F}}{Pe_L} \left( \frac{x}{L} - \frac{1 - e^{Pe_L \frac{x}{L}}}{1 - e^{Pe_L}} \right) \quad (3.53)$$

where  $\phi_0$  and  $\phi_L$  are Dirichlet boundary conditions imposed at  $x = 0$  and  $x = L$ ,  $Pe_L = aL/\kappa$  is the Péclet number, and  $\mathcal{F} = fL^2/(2\kappa)$  is the source. In the limit  $Pe_L \rightarrow 0$ , (3.53) yields:

$$\phi(x) = \phi_0 + (\phi_L - \phi_0 + \mathcal{F}) \frac{x}{L} - \mathcal{F} \left( \frac{x}{L} \right)^2 \quad (3.54)$$

##### 3.5.1.1 Weak formulation

It is now worthwhile to recast (3.22) for the case at hand because many simplifications arise.

Find  $\phi_h \in V_h^k([x_e, x_{e+1}])$ ,  $e \in \{1, 2, \dots, n_{el}\}$ , such that,  $\forall \mu_h \in V_h^k([x_e, x_{e+1}])$ :

$$\begin{aligned} 0 = & - \sum_{e=1}^{n_{el}} \int_{x_e}^{x_{e+1}} (\partial_x \mu_h (a\phi_h - \kappa \partial_x \phi_h) + \mu_h f) \\ & + \sum_{e=2}^{n_{el}} \left\{ (-\mu_h^+ + \mu_h^-)(a\phi_h^- - \kappa \partial_x \phi_h^-) + \left( s \kappa \partial_x \mu_h^- + \epsilon \frac{\kappa}{h_\perp} (-\mu_h^+ + \mu_h^-) \right) (-\phi_h^+ + \phi_h^-) \right\}_{x=x_e} \\ & + \left\{ +\mu_h a\phi_h + \epsilon \frac{\kappa}{h_\perp} \mu_h (\phi_h - \phi_L) + s \kappa \partial_x \mu_h (\phi_h - \phi_L) - \kappa \partial_x \phi_h \mu_h \right\}_{x=L} \\ & + \left\{ -\mu_h a\phi_0 + \epsilon \frac{\kappa}{h_\perp} \mu_h (\phi_h - \phi_0) - s \kappa \partial_x \mu_h (\phi_h - \phi_0) + \kappa \partial_x \phi_h \mu_h \right\}_{x=0} \end{aligned} \quad (3.55)$$

where the notation  $\{\eta\}_{x=\tilde{x}}$  stands for  $\eta$  evaluated at  $\tilde{x}$ ,  $e \in \{1, 2, \dots, n_{np}\}$  are the nodes of the mesh, and  $\{x_e | e = 2, \dots, n_{np} - 1 = n_{el}\}$  is the set of interior nodes.

##### 3.5.1.2 Local problem for the trial solution

The local problem reads:

$$B(v, \phi_h) = F(v; f, \bar{\phi}_h) \quad (3.56)$$



with

$$\begin{aligned}
 B(v, \phi_h) = & - \int_{x_e}^{x_{e+1}} \partial_x v (a\phi_h - \kappa \partial_x \phi_h) \\
 & + \left\{ v a\phi_h + \epsilon \frac{\tilde{\kappa}}{h_\perp} v \phi_h + s \kappa \partial_x v \phi_h - \kappa \partial_x \phi_h v \right\}_{x=x_{e+1}} \\
 & + \left\{ \epsilon \frac{\tilde{\kappa}}{h_\perp} v \phi_h - s \kappa \partial_x v \phi_h + \kappa \partial_x \phi_h v \right\}_{x=x_e}
 \end{aligned} \tag{3.57}$$

$$F(v; f, \bar{\phi}_h) = \int_T v f + B_\Gamma(v, \bar{\phi}_h) \tag{3.58}$$

$$\begin{aligned}
 B_\Gamma(v, \bar{\phi}_h) = & + \left\{ \epsilon \frac{\tilde{\kappa}}{h_\perp} v \bar{\phi}_h + s \kappa \partial_x v \bar{\phi}_h \right\}_{x=x_{e+1}} \\
 & + \left\{ -v a\bar{\phi}_h + \epsilon \frac{\tilde{\kappa}}{h_\perp} v \bar{\phi}_h - s \kappa \partial_x v \bar{\phi}_h \right\}_{x=x_e}
 \end{aligned} \tag{3.59}$$

Piecewise linear interpolation is assumed. Let

$$\Phi = \begin{bmatrix} \phi_h^l \\ \phi_h^r \end{bmatrix}, \quad \bar{\Phi} = \begin{bmatrix} \bar{\phi}_h^l \\ \bar{\phi}_h^r \end{bmatrix}, \quad \mathbf{f} = \begin{bmatrix} f^l \\ f^r \end{bmatrix} \tag{3.60}$$

where the superscripts  $l$  and  $r$  stand for the left and right nodal values. Straightforward calculations yield

$$\mathbf{T}_{\phi_h \bar{\phi}_h}^h = \frac{1}{\Delta} \begin{bmatrix} t_{11} & t_{12} \\ t_{21} & t_{22} \end{bmatrix} \tag{3.61}$$

with

$$\Delta = (Pe_h)^2(1 + \delta\epsilon) + (s + \epsilon)(1 + \delta\epsilon)Pe_h + \epsilon/2(2s + \epsilon) \tag{3.62}$$

$$t_{11} = (Pe_h)^2(1 + 2\delta\epsilon) + (s(2 + \delta\epsilon) + \epsilon/2(3 + 2\delta\epsilon))Pe_h + \epsilon/2(2s + \epsilon) \tag{3.63}$$

$$t_{12} = -Pe_h(Pe_h\delta\epsilon + s + \epsilon/2) \tag{3.64}$$

$$t_{21} = Pe_h(Pe_h\delta\epsilon + s + \epsilon/2) \tag{3.65}$$

$$t_{22} = \epsilon((Pe_h)^2\delta + Pe_h(1/2 + \delta(s + \epsilon)) + s + \epsilon/2) \tag{3.66}$$

$$Pe_h = \frac{ah}{2\kappa} \tag{3.67}$$

and

$$\mathbf{T}_{\phi_h f}^h = \frac{h^2}{12\kappa\Delta} \begin{bmatrix} Pe_h(1 + \delta\epsilon) + 3s + 2\epsilon & -Pe_h(1 - 2\delta\epsilon) + 3s + \epsilon \\ 3Pe_h + 3s + \epsilon & 3Pe_h + 3s + 2\epsilon \end{bmatrix} \tag{3.68}$$

	$s = +1$	$s = 0$	$s = -1$
$\Delta$	$Pe_h(Pe_h + 1) + \epsilon(Pe_h + 1) + \epsilon^2/2$	$(Pe_h)^2 + (Pe_h + \epsilon)^2$	$Pe_h(Pe_h - 1) + \epsilon(Pe_h - 1) + \epsilon^2/2$
$\Delta > 0?$	always for $\epsilon > 0$	always for $\epsilon > 0$	for $\epsilon > 1 - Pe_h + \sqrt{1 - Pe_h^2}$ and $\epsilon < 1 - Pe_h - \sqrt{1 - Pe_h^2}$

**Table 3.1.** Analysis of the sign of the determinant  $\Delta$  for  $\delta = 0$ .

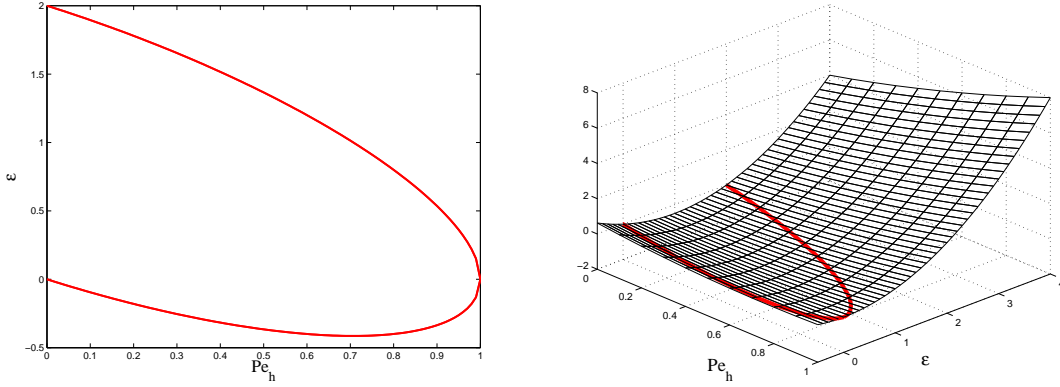


**Figure 3.7.** Locus of  $\Delta = 0$  for  $s = -1$  and  $\delta = 0$  on the  $Pe_h, \epsilon$ -plane (left) and on an elevation plot of the function  $\Delta$ . It is seen that  $\epsilon > 2$  prevents the determinant from vanishing for all Péclet numbers.

Special care has to be taken because, for  $s = -1$ , the determinant,  $\Delta$ , can vanish for certain combinations of  $Pe_h$  and  $\epsilon$ . An analysis of the sign of the determinant is presented in Table 3.1. The locus of  $\Delta = 0$  in the  $Pe_h, \epsilon$ -plane is shown in Figure 3.7, together with an elevation plot of the function  $\Delta(Pe_h, \epsilon)$ . In the multiscale version,  $\mathbf{T}_{\phi_h' \bar{\phi}_h}^h = \mathbf{T}_{\phi_h \bar{\phi}_h}^h - \mathbf{I}_{2 \times 2}$ .

### 3.5.1.3 Limit behavior

Taking limits,  $Pe_h \rightarrow 0$  and  $\infty$ , we have:

$$\lim_{Pe_h \rightarrow 0} \mathbf{T}_{\phi_h \bar{\phi}_h}^h = \begin{bmatrix} 1 & 0 \\ 0 & 1 \end{bmatrix} \quad (3.69)$$

$$\lim_{Pe_h \rightarrow \infty} \mathbf{T}_{\phi_h \bar{\phi}_h}^h = \frac{1}{1 + \delta\epsilon} \begin{bmatrix} 1 + 2\delta\epsilon & -2\delta\epsilon \\ 1 & \delta\epsilon \end{bmatrix} \quad (3.70)$$

$$\lim_{Pe_h \rightarrow 0} \mathbf{T}_{\phi_h f}^h = \frac{h}{6\kappa\epsilon(2s + \epsilon)} \begin{bmatrix} 3s + 2\epsilon & 3s + \epsilon \\ 3s + \epsilon & 3s + 2\epsilon \end{bmatrix} \quad (3.71)$$

$$\lim_{Pe_h \rightarrow \infty} \mathbf{T}_{\phi_h f}^h = \mathbf{0}_{2 \times 2} \quad (3.72)$$

From (3.69) it is seen that, if  $f = 0$ ,  $\phi_h \rightarrow \bar{\phi}_h$  in the diffusive limit, while from (3.70) it is seen that, in the advective limit, full upwinding is performed up to the perturbation of the parameter  $\delta$ , that is  $\phi_h|_{[x_e, x_{e+1}]} \rightarrow \bar{\phi}_h(x_e)\chi|_{[x_e, x_{e+1}]}$ , for  $a$  positive. Notice also that, due to the fact that in the diffusive limit  $\mathbf{T}_{\phi_h f}^h$  does not vanish, the continuous solution,  $\bar{\phi}_h$ , will not in general be equal to the discontinuous solution,  $\phi_h$ , when  $f$  is present. The behavior of the method is schematically illustrated in Figure 3.8.

Note that, in the advective limit,  $Pe_h \rightarrow \infty$ , without the  $\delta$ -term, the transformation  $T_{\phi_h \bar{\phi}_h}$  becomes singular and the global coefficient matrix entries corresponding to the degree-of-freedom  $\bar{\phi}_h^r$  will receive no contribution from the element under consideration. If the node associated with this degree-of-freedom is an outflow node with respect to all elements connected to it, the global coefficient matrix will have a zero row and column corresponding to this degree-of-freedom. Situations where this can occur are schematically illustrated in Figure 3.9. The role of the  $\delta$ -term is to provide stabilization in these circumstances. In all numerical tests, this strategy has proved effective.

### 3.5.1.4 Local problem for the weighting function

Given that the problem of linking  $\mu_h$  to  $\bar{\mu}_h$  is the same as for linking  $\phi_h$  to  $\bar{\phi}_h$ , except  $f = 0$ , the result is

$$\begin{bmatrix} \mu_h^l \\ \mu_h^r \end{bmatrix} = \mathbf{T}_{\mu_h \bar{\mu}_h}^h \begin{bmatrix} \bar{\mu}_h^l \\ \bar{\mu}_h^r \end{bmatrix} \quad (3.73)$$

or

$$\begin{bmatrix} \mu_h^l \\ \mu_h^r \end{bmatrix} = \mathbf{T}_{\mu_h' \bar{\mu}_h}^h \begin{bmatrix} \bar{\mu}_h^l \\ \bar{\mu}_h^r \end{bmatrix} \quad (3.74)$$

with  $\mathbf{T}_{\mu_h \bar{\mu}_h}^h = \mathbf{T}_{\phi_h \bar{\phi}_h}^h$  and  $\mathbf{T}_{\mu_h' \bar{\mu}_h}^h = \mathbf{T}_{\phi_h' \bar{\phi}_h}^h$ .

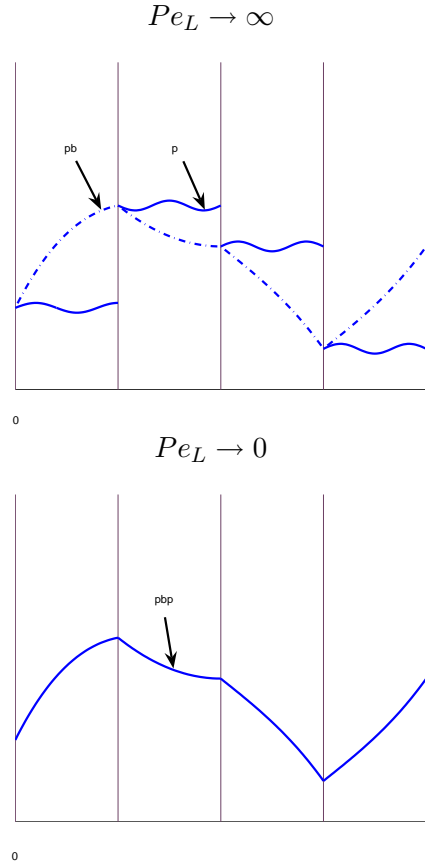


**Figure 3.8.** Schematic of the behavior of the new method. In the advective limit, the solution exhibits upwind influence, whereas in the diffusive limit the solution behaves like the continuous solution although it is not identical to it in the case  $f \neq 0$ .

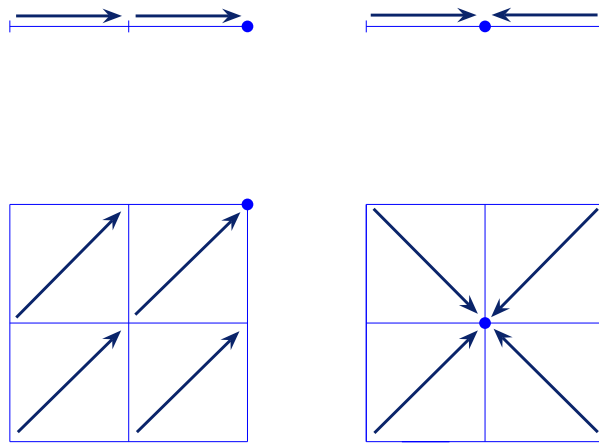


**Figure 3.9.** In the advective limit, outflow and sink nodes are stabilized by the  $\delta$ -term. Strictly speaking, the sink-node cases are precluded by our assumption that  $\mathbf{a}$  is solenoidal. Nevertheless, in numerical calculations  $\mathbf{a}$  will also be a discrete approximation and therefore it will typically not be exactly solenoidal. See Hughes and Wells [91] for a discussion of this issue.

### 3.5.1.5 Numerical results

We compare the continuous and discontinuous representations of the solution for the MDG formulation (i.e.,  $\bar{\phi}_h$  and  $\phi_h$ , resp.) with the solution of the global DG method. We examine the effect of the parameter  $s$  on monotonicity of the solution, and convergence rates. The value  $\epsilon = 2.001$  was used in the calculations. This value is essential for the good behavior of the symmetric case (i.e.,  $s = -1$ ). The parameter  $\delta = 0.01$  was used throughout. Smaller values were not as effective.

In Figures 3.10 and 3.11, results are presented for a fixed, uniform mesh of four elements, and various Péclet numbers. One notices oscillations for the discontinuous representation of the solution,  $\phi_h$ , for skew and neutral cases at intermediate Péclet numbers. The discontinuous solutions for the symmetric case are oscillation-free and monotone for all Péclet numbers. The global DG solution is about the same quality as the discontinuous solution of the MDG method.

In Figure 3.12 and 3.13, results are presented for a fixed Péclet number,  $Pe_L$ , and varying mesh size. The conclusions to be drawn are similar to those of Figures 3.10 and 3.11. In all cases, the continuous representation of the solution for the MDG method,  $\bar{\phi}_h$ , tends to be somewhat better behaved than the discontinuous representation.

$L^2$ -convergence rates for the case  $f = 0$  are presented in Figures 3.14–3.16. The first thing one notices is that in Figures 3.14–3.15, for the skew and neutral versions, the  $L^2$ -convergence rates for the global DG method are first-order. This is to be expected because these methods are not adjoint consistent (see Arnold *et al.* [7]). The symmetric version is adjoint consistent, and so it converges at optimal  $L^2$ -rate, as seen in Figure 3.16. For the present formulation, for *all* values of  $s$ , optimal  $L^2$ -convergence is attained. This is seen to be a consequence of the fact that, in the diffusive limit, the discontinuous solution converges to the continuous solution, which is well-known to attain optimal  $L^2$ -rate of convergence. The local problem has beneficial effect and compensates for the lack of adjoint consistency of the skew and neutral versions.

$L^2$ ,  $H^1$ , and  $L^1$ , convergence rates are presented in Figures 3.17–3.19 for the case  $f = 1$  and the symmetric version. By  $H^1$ -convergence we mean convergence in the “broken”  $H^1$ -seminorm, namely,  $\sum_{T \in \mathcal{T}_h} \int_T |\nabla \cdot|^2$ .

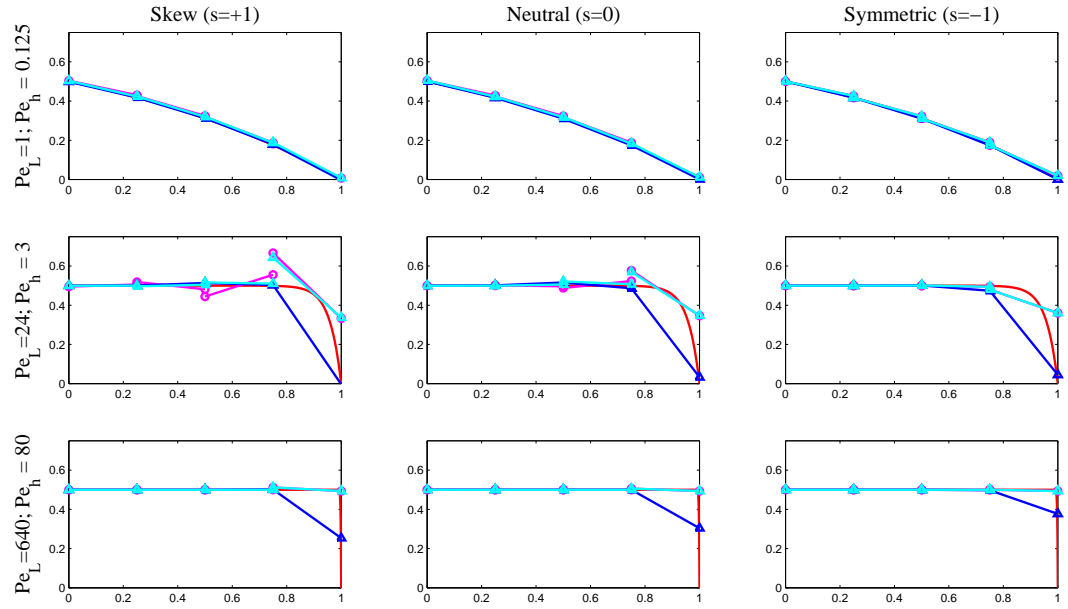


**Figure 3.10.** Solution plots in terms of varying Péclet number, on a uniform mesh of 4 elements, with  $f = 0$ . Red, exact solution; blue, MDG  $\bar{\phi}_h$ ; light blue, MDG  $\phi_h$ ; magenta, global DG solution without local condensation.

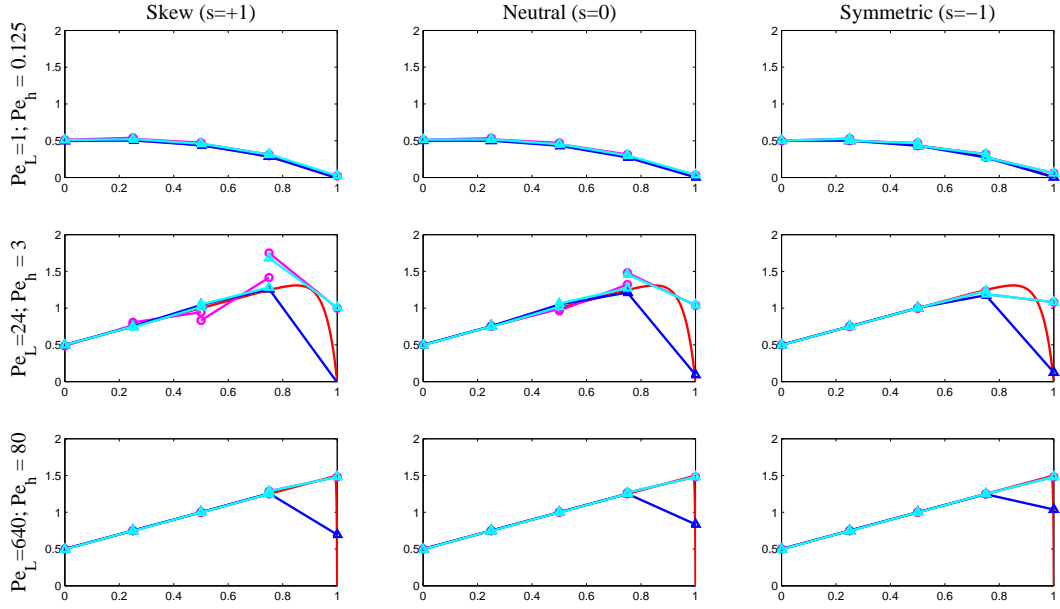


**Figure 3.11.** Solution plots in terms of varying Péclet number, on a uniform mesh of 4 elements, with  $f = 1$ . Red, exact solution; blue, MDG  $\bar{\phi}_h$ ; light blue, MDG  $\phi_h$ ; magenta, global DG solution without local condensation.



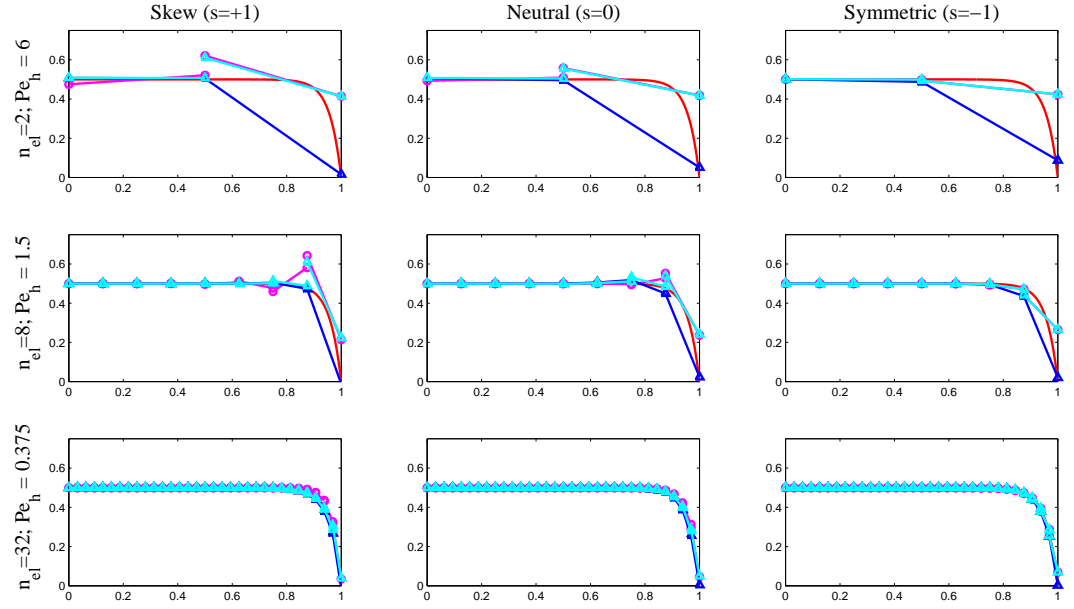


**Figure 3.12.** Solution plots in terms of varying mesh size, on uniform meshes of 2, 8, and 32 elements,  $Pe_L = 24$ , with  $f = 0$ . Red, exact solution; blue, MDG  $\bar{\phi}_h$ ; light blue, MDG  $\phi_h$ ; magenta, global DG solution without local condensation.

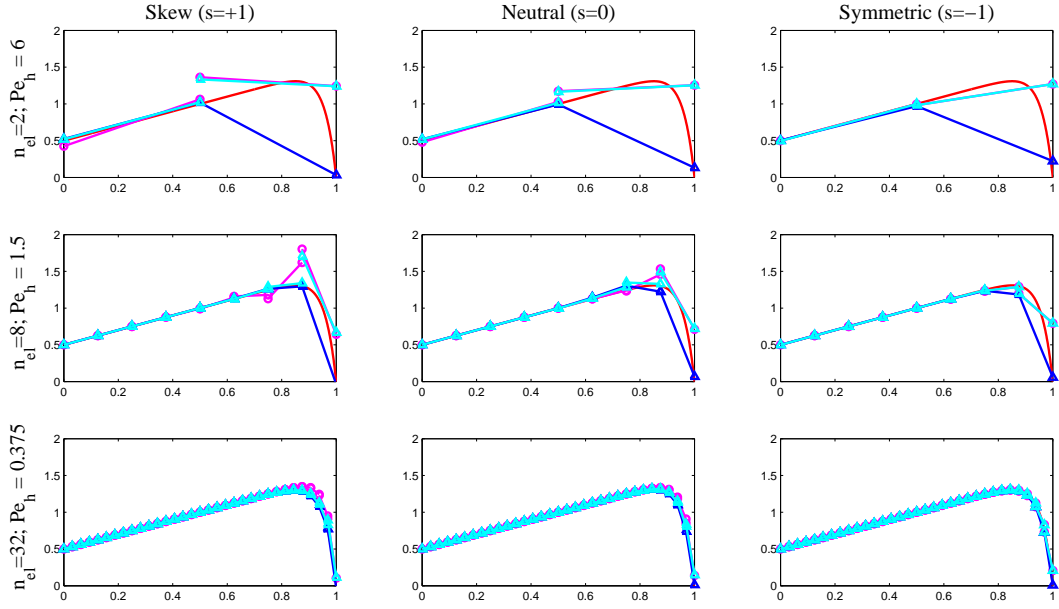


**Figure 3.13.** Solution plots in terms of varying mesh size, on uniform meshes of 2, 8, and 32 elements,  $Pe_L = 24$ , with  $f = 1$ . Red, exact solution; blue, MDG  $\bar{\phi}_h$ ; light blue, MDG  $\phi_h$ ; magenta, global DG solution without local condensation.

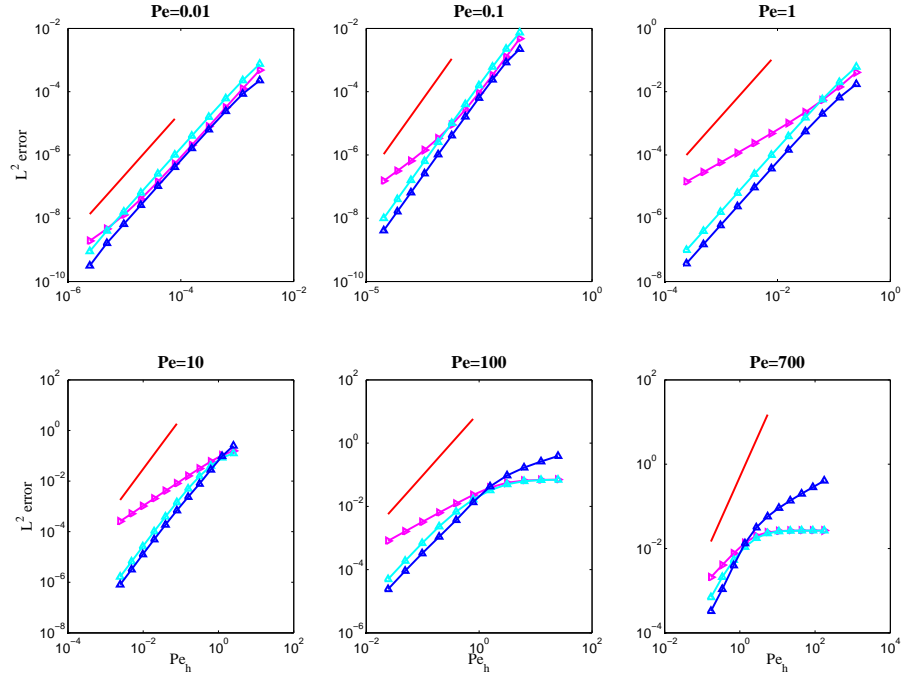


**Figure 3.14.** Convergence rates, skew ( $s = +1$ ) version, with  $f = 0$ . Blue, MDG  $\bar{\phi}_h$ ; light blue, MDG  $\phi_h$ ; magenta, global DG solution without local condensation; red,  $(Pe_h)^2$  slope.

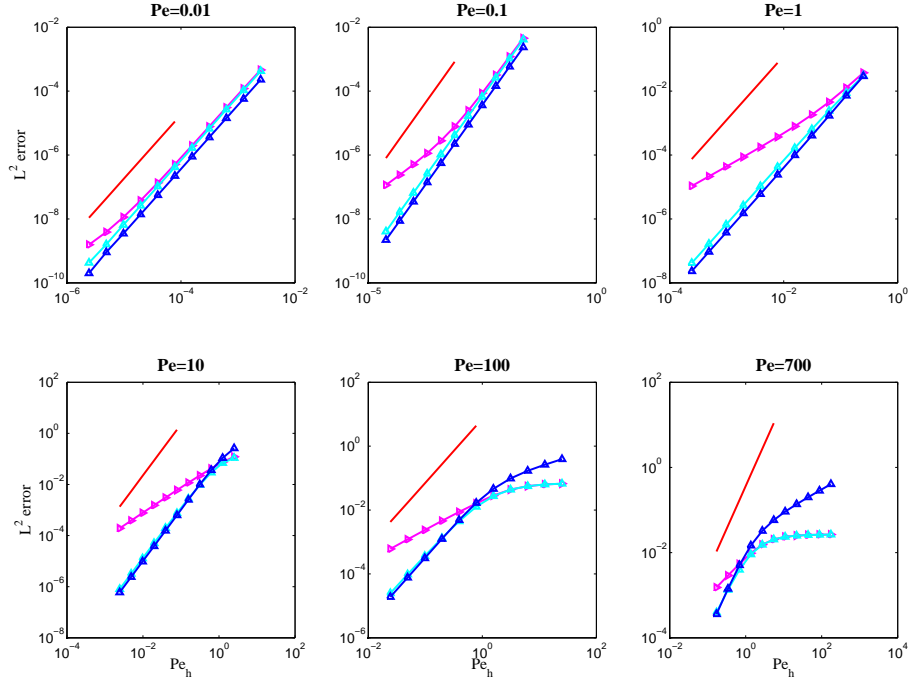


**Figure 3.15.** Convergence rates, neutral ( $s = 0$ ) version, with  $f = 0$ . Blue, MDG  $\bar{\phi}_h$ ; light blue, MDG  $\phi_h$ ; magenta, global DG solution without local condensation; red,  $(Pe_h)^2$  slope.

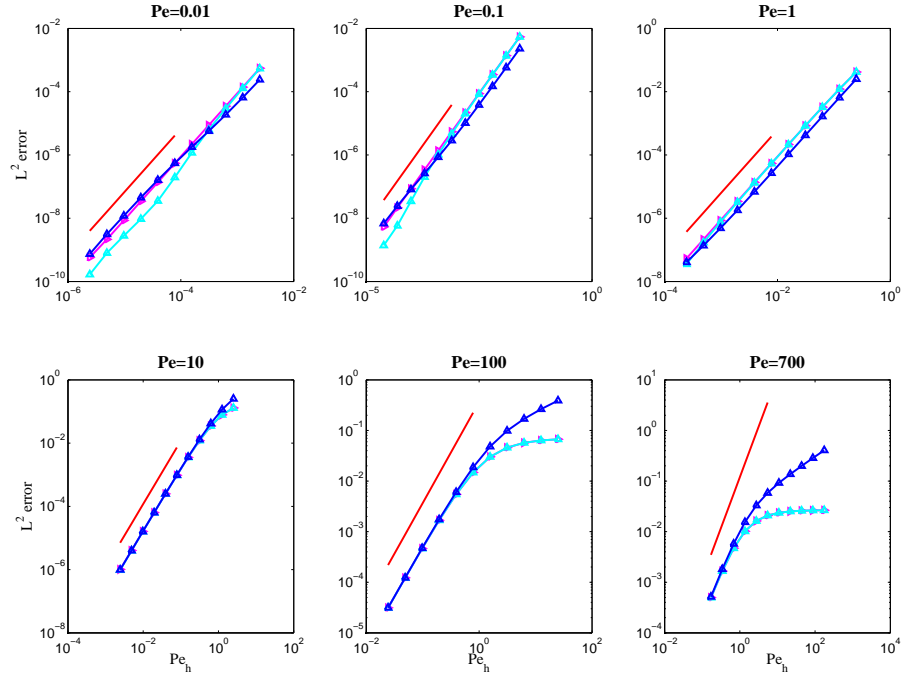


**Figure 3.16.** Convergence rates, symmetric ( $s = -1$ ) version, with  $f = 0$ . Blue, MDG  $\bar{\phi}_h$ ; light blue, MDG  $\phi_h$ ; magenta, global DG solution without local condensation; red,  $(Pe_h)^2$  slope.

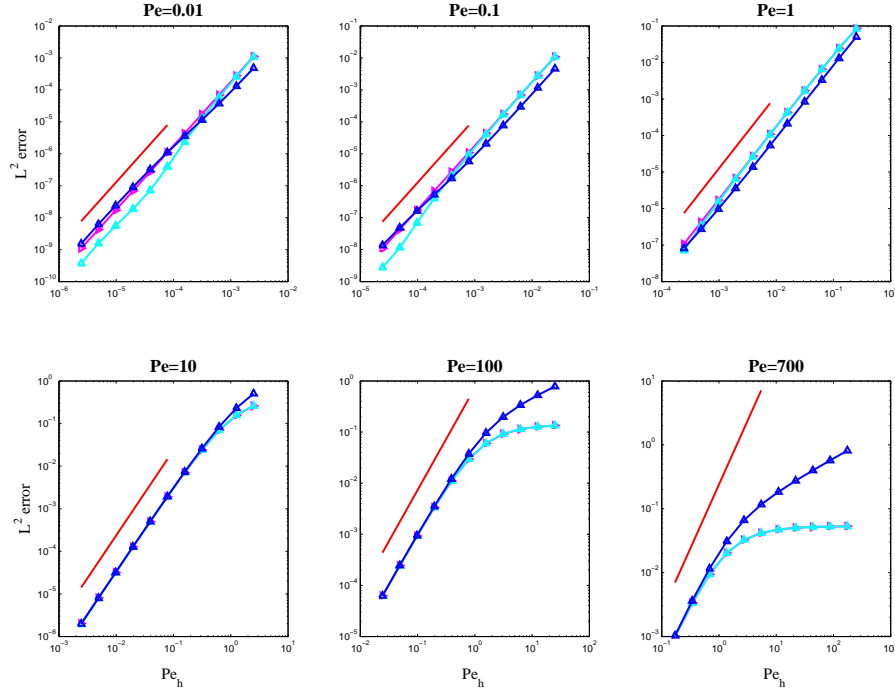


**Figure 3.17.** Convergence rates in the  $L^2$ -norm of the error, symmetric ( $s = -1$ ) version, with  $f = 1$ . Blue, MDG  $\bar{\phi}_h$ ; light blue, MDG  $\phi_h$ ; magenta, global DG solution without local condensation; red,  $(Pe_h)^2$  slope.

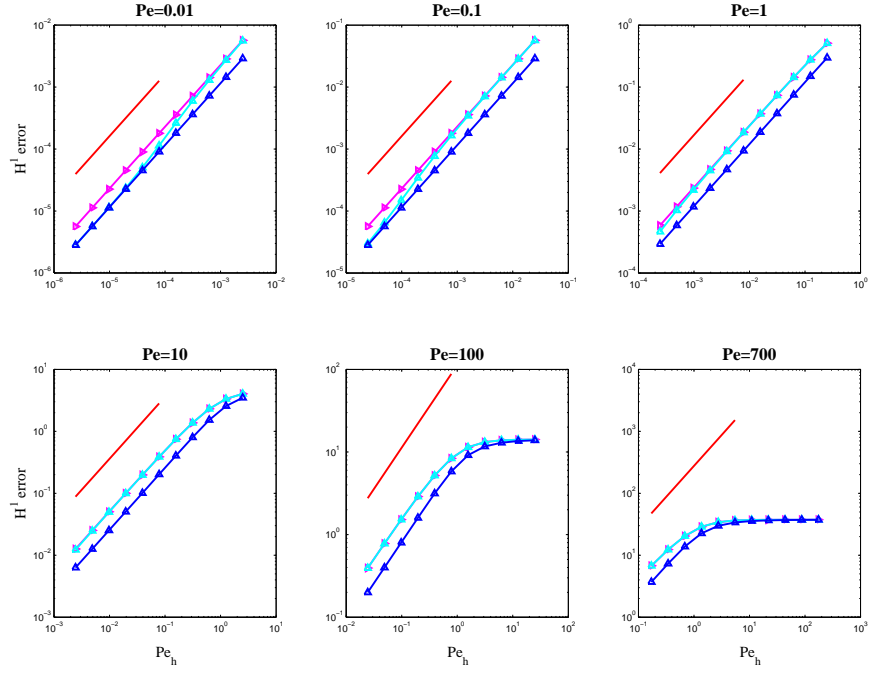


**Figure 3.18.** Convergence rates in the  $H^1$  broken seminorm of the error, symmetric ( $s = -1$ ) version, with  $f = 1$ . Blue, MDG  $\bar{\phi}_h$ ; light blue, MDG  $\phi_h$ ; magenta, global DG solution without local condensation; red,  $(Pe_h)^1$  slope.

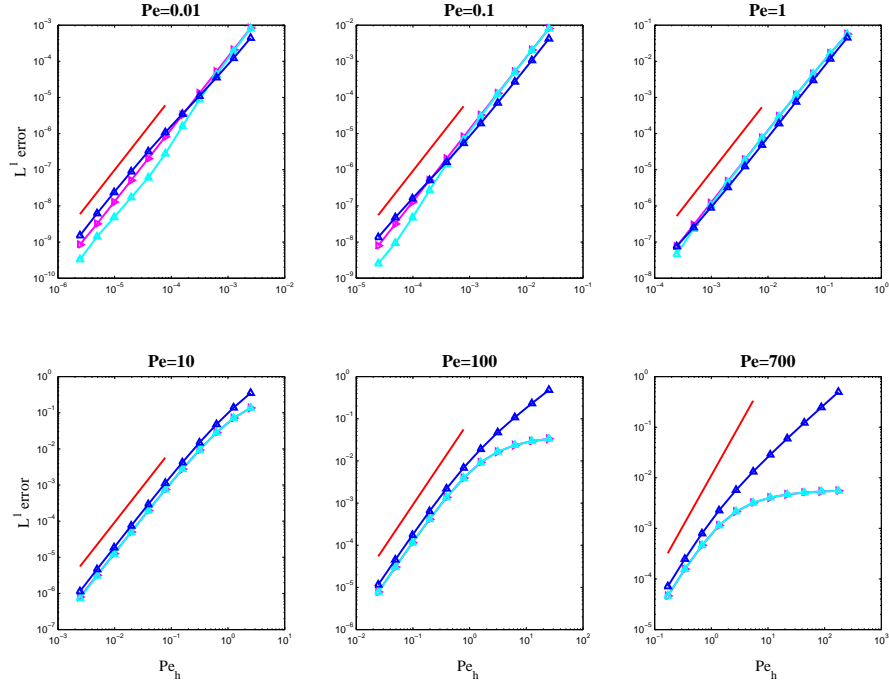


**Figure 3.19.** Convergence rates in the  $L^1$ -norm of the error, symmetric ( $s = -1$ ) version, with  $f = 1$ . Blue, MDG  $\bar{\phi}_h$ ; light blue, MDG  $\phi_h$ ; magenta, global DG solution without local condensation; red,  $(Pe_h)^2$  slope.



### 3.5.2 Two-dimensional advection equation

Two-dimensional simulations were performed to test the robustness and accuracy of the MDG method in the advection-dominated limit,  $\kappa \rightarrow 0$ . Comparisons are again made with the global DG method. Bilinear quadrilateral elements are employed resulting in the number of equations for the global DG method being approximately four times that for the MDG method. The symmetric version of the DG method was used ( $s = -1$ ), and the values of  $\varepsilon$  and  $\delta$  were again taken to be 2.001 and 0.01, respectively.

#### 3.5.2.1 Advection skew to the mesh

The first problem is a robustness test. The domain of the problem is  $\Omega = [0, L] \times [0, L]$  with  $L = 1$ . Dirichlet boundary conditions are set as follows:

$$g = \begin{cases} 1 & \text{if } y = 0 \\ 1 & \text{if } x = 0 \text{ and } y \leq L/5 \\ 0 & \text{otherwise} \end{cases} \quad (3.75)$$

The boundary conditions are enforced weakly for both the global and multiscale DG methods. The advective velocity  $\mathbf{a}$  is constant and forms an angle  $\theta$  with the  $x$ -axis. Three configurations are considered:  $\theta = 30^\circ$ ,  $\theta = 45^\circ$  and  $\theta = 60^\circ$  degrees.

Numerical results for a  $30 \times 30$  mesh are presented in Figures 3.20–3.25. Note that the continuous representation of the solution,  $\bar{\phi}_h$ , is slightly better behaved than the discontinuous representation,  $\phi_h$ , in that oscillations about the internal layer are somewhat less for the former. Comparison of the MDG solution with the global DG solution reveals that the multiscale method is similar in accuracy to the global method. The main attribute of both methods is that there are no spurious oscillations in the vicinity of the outflow boundary conditions. This is an advantage attributable to weakly enforced outflow boundary conditions, and one not shared by strong enforcement (see Brooks and Hughes [26]). However, weak enforcement of inflow Dirichlet boundary conditions offers no similar advantage over strong enforcement. Both the global and multiscale DG methods give rise to oscillations at the inflow discontinuity that attenuates somewhat in the interior of the domain. These oscillations are caused by the  $L^2$ -projection structure of DG methods for data perpendicular to characteristics, such as the inflow boundary condition in the present problem. It is conceivable that, by appropriately restructuring the local problem, more monotone behavior might have been obtained but this was not pursued in the present study.

#### 3.5.2.2 Rotating flow

This problem is an accuracy test. Classical upwind procedures exhibit excessive crosswind diffusion on this problem (see Brooks and Hughes [26]). The domain is again  $\Omega = [0, L] \times$

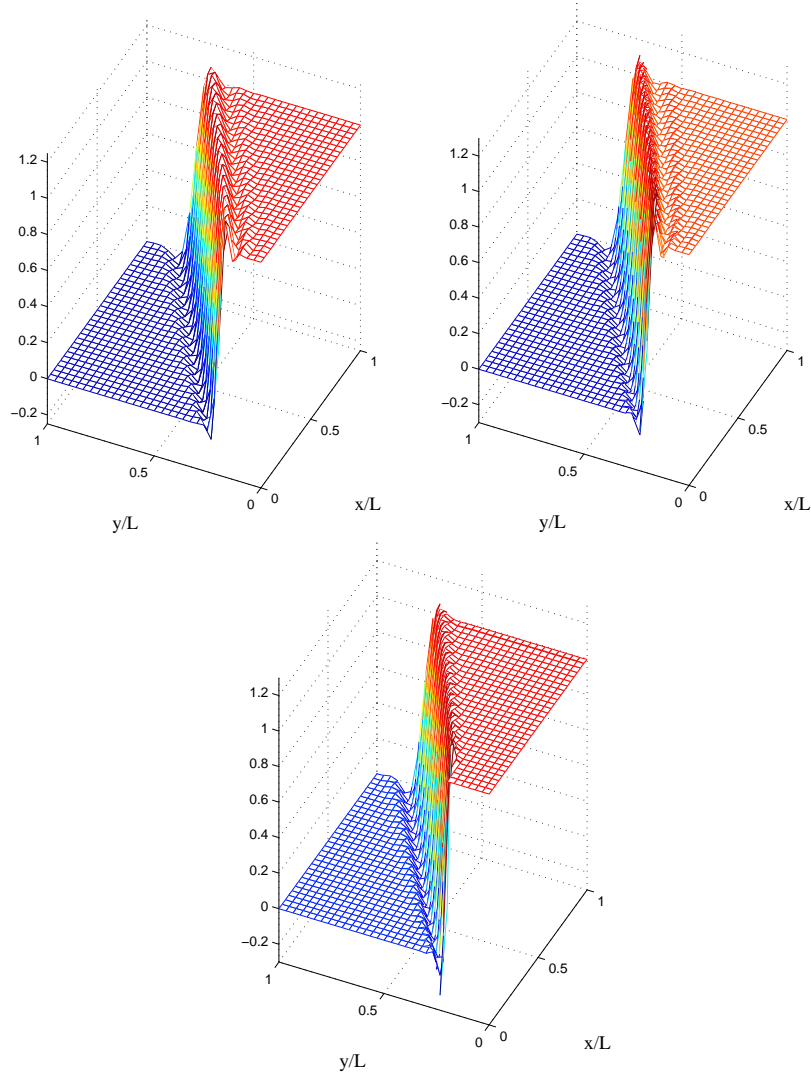


**Figure 3.20.** Advection skew to the mesh,  $\theta = 30^\circ$ . Left, continuous representation of the MDG solution,  $\bar{\phi}_h$ ; center, discontinuous representation,  $\phi_h$ ; right, solution of the global DG method without local condensation.

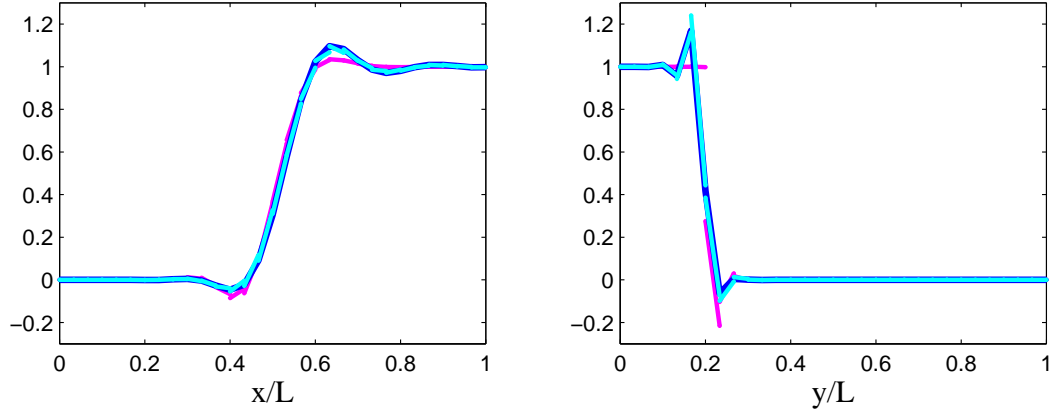


**Figure 3.21.** Advection skew to the mesh,  $\theta = 30^\circ$ . Left, solution at  $y/L = .5$ ; right, solution at  $x/L = 0$ . Blue, MDG  $\bar{\phi}_h$ ; light blue, MDG  $\phi_h$ ; magenta, global DG solution without local condensation.

$[0, L]$  with  $L = 1$ . The two velocity components are:

$$a_x = y - 1/2 \quad (3.76)$$

$$a_y = 1/2 - x \quad (3.77)$$

The solution is prescribed along the slit  $x = L/2$ ,  $y \in [0, L/2]$ , as follows:

$$\bar{\phi}(1/2, y) = \sin^2(2\pi y/L) \quad (3.78)$$

Numerical results on a  $30 \times 30$  mesh are shown in Figure 3.26. There is little to differentiate between the  $\bar{\phi}_h$  and  $\phi_h$  in this case. Both representations are very accurate and there is no appearance of crosswind diffusion.

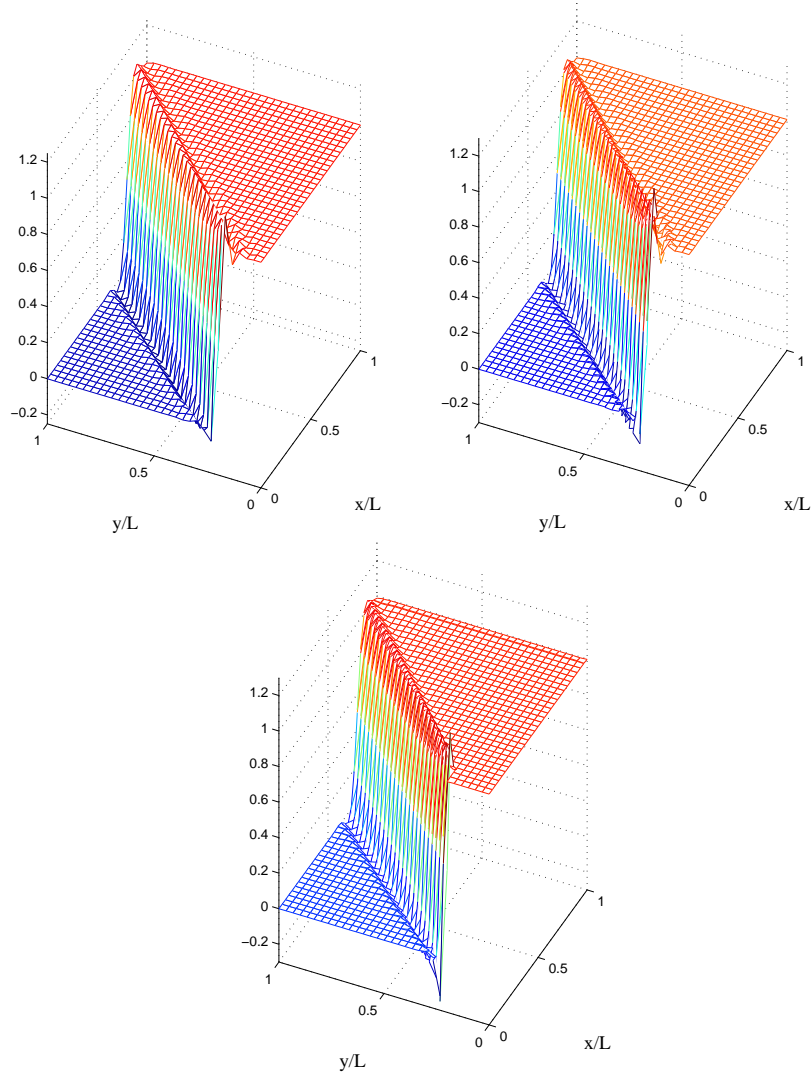


**Figure 3.22.** Advection skew to the mesh,  $\theta = 45^\circ$ . Left, continuous representation of the MDG solution,  $\bar{\phi}_h$ ; center, discontinuous representation,  $\phi_h$ ; right, solution of the global DG method without local condensation.

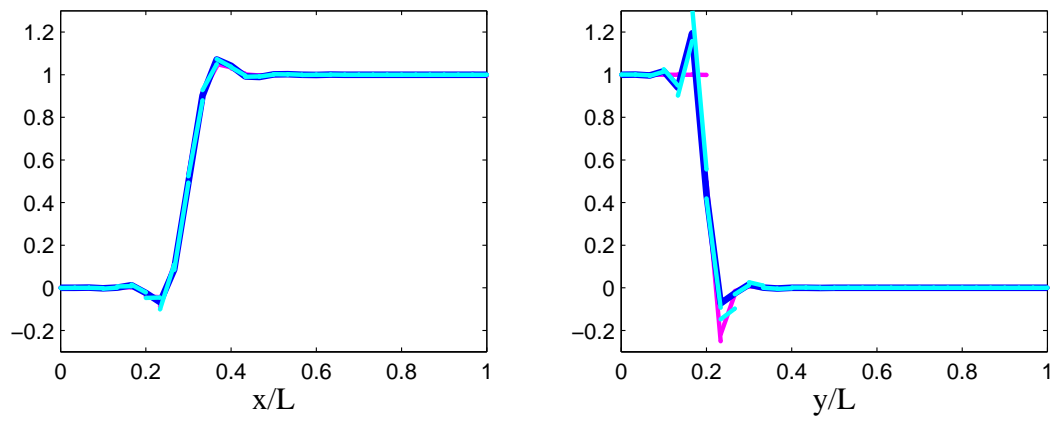


**Figure 3.23.** Advection skew to the mesh,  $\theta = 45^\circ$ . Left, solution at  $y/L = .5$ ; right, solution at  $x/L = 0$ . Blue, MDG  $\bar{\phi}_h$ ; light blue, MDG  $\phi_h$ ; magenta, global DG solution without local condensation.

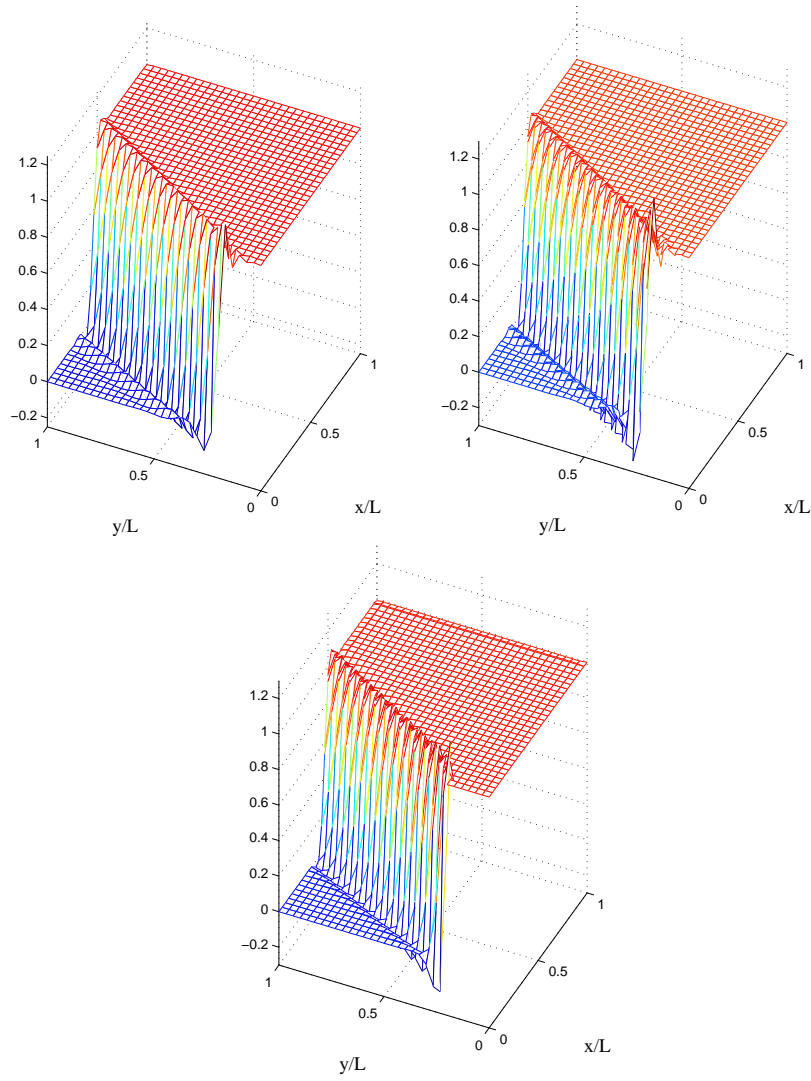


**Figure 3.24.** Advection skew to the mesh,  $\theta = 60^\circ$ . Left, continuous representation of the MDG solution,  $\bar{\phi}_h$ ; center, discontinuous representation,  $\phi_h$ ; right, solution of the global DG method without local condensation.

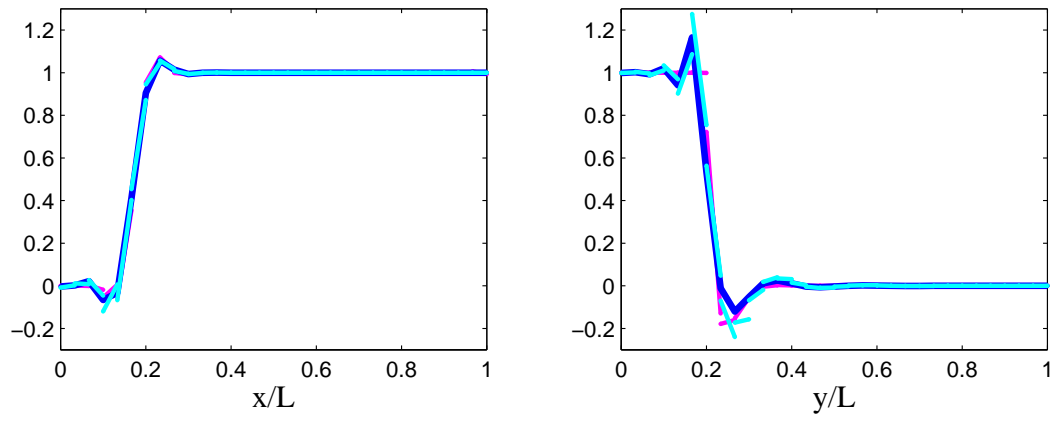


**Figure 3.25.** Advection skew to the mesh,  $\theta = 60^\circ$ . Left, solution at  $y/L = .5$ ; right, solution at  $x/L = 0$ . Blue, MDG  $\bar{\phi}_h$ ; light blue, MDG  $\phi_h$ ; magenta, global DG solution without local condensation.

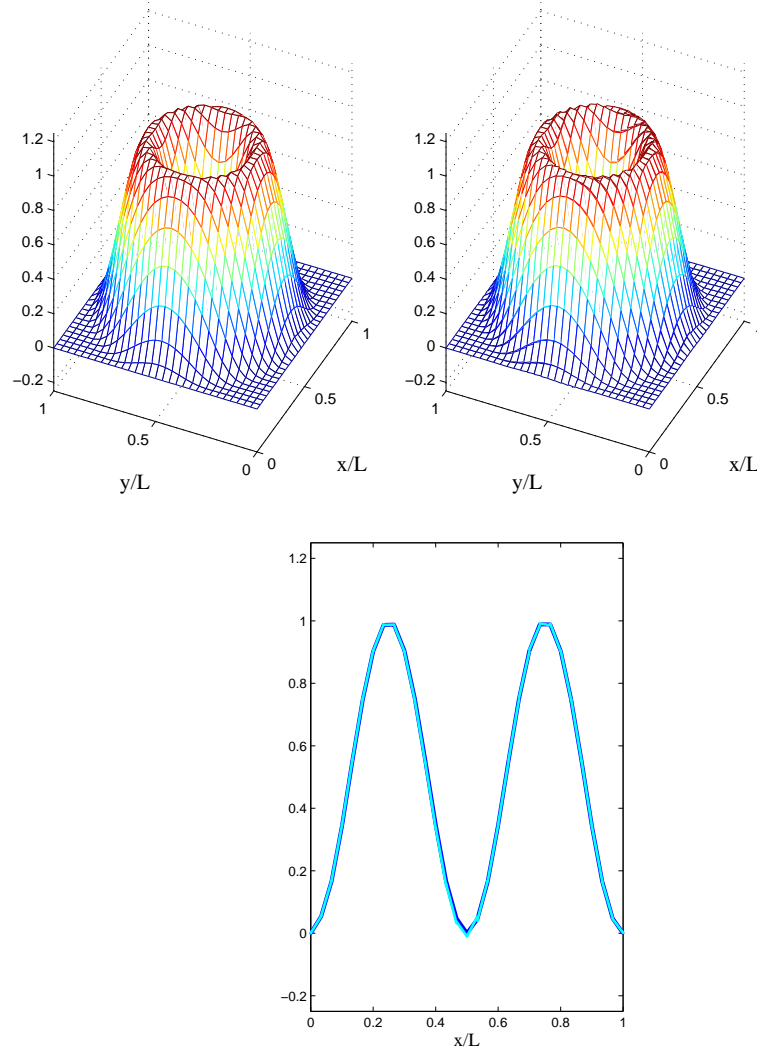


**Figure 3.26.** Rotating flow. Left, continuous representation of the MDG solution,  $\bar{\phi}_h$ ; center, discontinuous representation  $\phi_h$ ; right, solution at  $y/L = .5$ , in which the continuous and discontinuous solutions are seen to overlap.



### 3.6 Conclusions and Future Directions

The objective of the present work was to develop a discontinuous Galerkin method with the reduced computational cost of a corresponding continuous Galerkin method. The method developed achieves this objective and, at the same time, at least attains, and even somewhat improves upon, the performance of the associated continuous Galerkin method. This represents a solution to a fundamental and long-standing problem in discontinuous-Galerkin technology, namely, restraining the proliferation of degrees-of-freedom. Having accomplished this, there is still room for improvement. The discontinuous Galerkin method is certainly more robust than the continuous Galerkin method but, in itself, is not sufficiently robust for many industrial applications. Its improved stability exists primarily along characteristics but not perpendicular to characteristics. The “advection skew to the mesh” problem is illustrative of this fact. There are no oscillations present in the vicinity of the outflow Dirichlet boundary conditions but the internal layer gives rise to transverse oscillations. This deficiency is also present in SUPG (see Brooks and Hughes [26]), and it has long been recognized that additional mechanisms are necessary to produce sufficiently smooth solutions for industrial purposes. In the context of SUPG, this has motivated the development of “discontinuity capturing operators.” See Hughes, Mallet and Mizukami [86] and Hughes and Mallet [85] for the initial conceptions. Numerous improved variants have been developed subsequently by other researchers (see, e.g., [28, 52–55, 59, 64, 141]). Within the framework of the multiscale discontinuous Galerkin method, the local problem provides a vehicle for incorporating desired features. There seems to be a potential connection here with ideas from wave propagation methods based on solutions of the Riemann problem. This would appear to be a fruitful direction for further research, especially in the context of complex nonlinear problems. Other research challenges involve the mathematical basis of the multiscale discontinuous Galerkin method. Its structure is somewhat non-traditional in that solutions involve two distinct representations: the coarse-scale, continuous representation,  $\bar{\phi}_h$ , and the coarse-scale plus fine-scale discontinuous representation,  $\phi_h = \bar{\phi}_h + \phi'_h$ . In addition, the multiscale method requires stabilization terms to control the solution at outflow and sink nodes in the advection-dominated limit. This raises additional mathematical questions.

### Acknowledgement

The authors would like to thank Giancarlo Sangalli for helpful remarks. The work of T. J. R. Hughes and G. Scovazzi was supported by Sandia Contract No. A0340.0 with the University of Texas at Austin. This support is gratefully acknowledged.

This page intentionally left blank.

## Chapter 4

# A Multiscale Discontinuous Galerkin Method

**Principle Authors:** Pavel Bochev, Thomas J. R. Hughes<sup>1</sup>, and Guglielmo Scovazzi

We propose a new class of Discontinuous Galerkin (DG) methods based on variational multiscale ideas. Our approach begins with an additive decomposition of the discontinuous finite element space into continuous (coarse) and discontinuous (fine) components. Variational multiscale analysis is used to define an interscale transfer operator that associates coarse and fine scale functions. Composition of this operator with a donor DG method yields a new formulation that combines the advantages of DG methods with the attractive and more efficient computational structure of a continuous Galerkin method. The new class of DG methods is illustrated for a scalar advection-diffusion problem.

### 4.1 Introduction

Discontinuous Galerkin (DG) methods offer several important computational advantages over their continuous Galerkin counterparts. For instance, DG methods are particularly well-suited for application of  $h$  and  $p$ -adaptivity strategies. DG methods are also felt to have advantages of robustness over conventional Galerkin methods for problems of hyperbolic type [95, 96, 135]. There has also been recent interest in applying DG to elliptic problems so that advective-diffusive phenomena can be modeled; see Brezzi *et al.* [23], Dawson [47], and Hughes, Masud and Wan [87]. For a summary of the current state-of-the-art and introduction to the literature we refer to [7] and [40].

Despite the increased interest in DG methods, there are shortcomings that limit their practical utility. Foremost among these is the size of the DG linear system. Storage and solution cost are, obviously, adversely affected, which seems the main reason for the small industrial impact the DG method has had so far.

In [80] we proposed a new multiscale DG method that has the computational structure of a standard continuous Galerkin method. In this paper we extend this idea to a general multiscale framework for DG methods. Our approach starts with an additive decomposition of a given discontinuous finite element space into continuous (coarse) and discontinuous (fine) components. Then, variational multiscale analysis is used to define an interscale transfer operator that associates coarse and fine scale functions. Composition of this operator with

---

<sup>1</sup>Institute for Computational Engineering and Sciences, The University of Texas at Austin, Austin, TX 78712

a donor DG method yields a new formulation that combines the advantages of DG methods with the attractive and more efficient computational structure of a continuous Galerkin method. Variational multiscale analysis leads to a natural definition of local, elementwise problems that allow for an efficient computation of the interscale operator.

## 4.2 Notation

Throughout this paper  $\Omega$  will denote an open bounded region in  $\mathbb{R}^n$ ,  $n = 2, 3$  with a polyhedral boundary  $\partial\Omega$ . We recall the standard Sobolev spaces  $L^2(\Omega)$  and  $H^1(\Omega)$ . Let  $\mathcal{T}_h$  be a regular partition of  $\Omega$  into finite elements  $K$  that contains only regular nodes [140]. For simplicity, we limit our discussion to two space dimensions. Extension to three dimensions is straightforward.

Every element  $K \in \mathcal{T}_h$  is an image of a reference element  $\hat{K}$  that can be a triangle  $\hat{T}$  or a square  $\hat{Q}$ . The vertices  $\mathbf{v}$  and the edges  $\mathbf{e}$  of  $K$  form the sets  $V(K)$  and  $E(K)$ , respectively;  $V(\mathcal{T}_h) = \cup_{K \in \mathcal{T}_h} V(K)$ ,  $E(\mathcal{T}_h) = \cup_{K \in \mathcal{T}_h} E(K)$ ,  $\Gamma_h^0$  is the set of all internal edges and  $\Gamma_h$  is the set of all edges on  $\partial\Omega$ .

**The local space.** The reference space  $S^{p(\hat{K})}(\hat{K})$  on  $\hat{K}$  is defined as follows:

$$S^{p(\hat{K})}(\hat{K}) = \begin{cases} \varphi = \sum_{i,j} a_{ij} \xi_1^i \xi_2^j, & 0 \leq i, j \leq p(\hat{K}); i+j \leq p(\hat{K}) & \text{if } \hat{K} = \hat{T} \\ \varphi = \sum_{i,j} a_{ij} \xi_1^i \xi_2^j, & 0 \leq i, j \leq p(\hat{K}) & \text{if } \hat{K} = \hat{Q} \end{cases} \quad (4.1)$$

The local element spaces  $S^{p(K)}(K)$  are defined by a mapping of the reference space (4.1) to the physical space.

**The discontinuous finite element space.** Given two integers  $0 \leq p_{\min} < p_{\max}$  we consider the following finite element subspace of  $L^2(\Omega)$

$$\Phi_h(\Omega) = \left\{ \varphi_h \in L^2(\Omega) \mid \varphi_h|_K \in S^{p(K)}(K), \ p_{\min} \leq p(K) \leq p_{\max}; \ \forall K \in \mathcal{T}_h \right\}. \quad (4.2)$$

We will assume that  $p_{\min} \geq 1$ . Note that  $\Phi_h(\Omega)$  is a formal union of the local spaces  $S^{p(K)}(K)$ .

**The continuous finite element space.** The additive decomposition of  $\Phi_h(\Omega)$  is induced by a finite element subspace  $\bar{\Phi}_h(\Omega)$  of  $H^1(\Omega)$ , defined with respect to the same partition  $\mathcal{T}_h$  of  $\Omega$  into finite elements. The space  $\bar{\Phi}_h(\Omega)$  can be defined in many possible ways. However, to ensure  $H^1$  conformity, functions in this space are constrained to be continuous across element interfaces; see [36]. Here, for simplicity we consider a minimal choice of  $\bar{\Phi}_h(\Omega)$  given by (see Fig. 4.2)

$$\bar{\Phi}_h(\Omega) = \left\{ \bar{\varphi}_h \in H^1(\Omega) \mid \bar{\varphi}_h|_K \in S^1(K) \right\}. \quad (4.3)$$

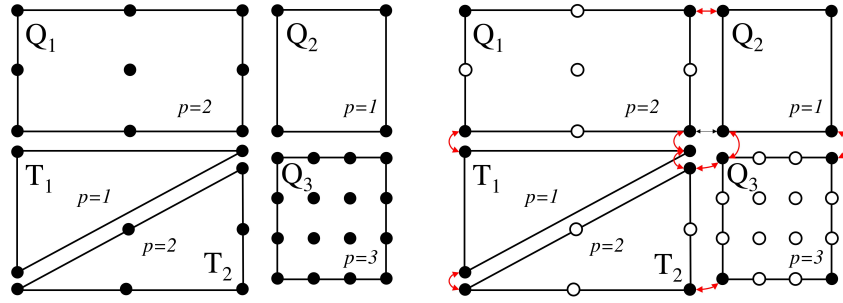


**Figure 4.1.** The space  $\Phi_h(\Omega)$  (left) and the corresponding minimal  $C^0$  space  $\bar{\Phi}_h(\Omega)$  (right).

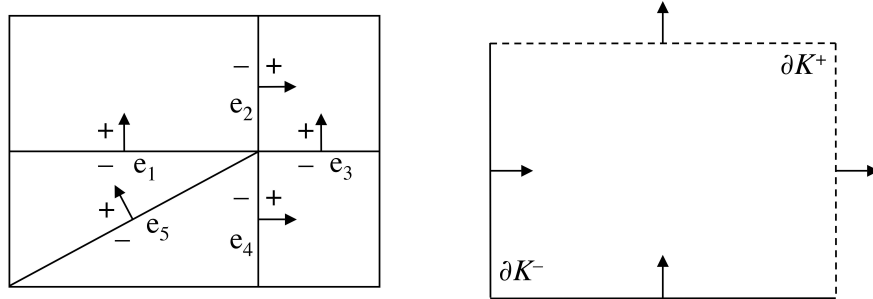


**Figure 4.2.** Orientation of internal edges in  $\mathcal{T}_h$  and  $+/ -$  elements with respect to an edge (left). Partition of element boundary into  $\partial^+ K$  and  $\partial^- K$  (right).

In  $\bar{\Phi}_h(\Omega)$  we consider a nodal basis  $\{\bar{V}_{\bar{\mathbf{v}}}\}$ ;  $\bar{\mathbf{v}} \in V(\mathcal{T}_h)$  such that  $\bar{V}_{\bar{\mathbf{v}}_i}(\bar{\mathbf{v}}_j) = \delta_{ij}$ . The basis functions have local supports given by  $\text{supp}(\bar{V}_{\bar{\mathbf{v}}}) = \cup_{\bar{\mathbf{v}} \in V(K)} K$ . For  $K \in \text{supp}(\bar{V}_{\bar{\mathbf{v}}})$ ,  $\bar{V}_{\bar{\mathbf{v}}}|_K = V_{\mathbf{v}}$  where  $\mathbf{v} \in V(K)$  is the local vertex that corresponds to the global vertex  $\bar{\mathbf{v}} \in V(\mathcal{T}_h)$ . Owing to the assumption  $p_{\min} \geq 1$  the space  $\bar{\Phi}_h(\Omega)$  is contained in  $\Phi_h(\Omega)$ . While the actual choice of  $\bar{\Phi}_h(\Omega)$  and the resulting decomposition will have an impact on the accuracy of the multiscale DG, it will not affect formulation of the overall framework.

**Orientations, jumps and averages.** We briefly review the relevant notation following the Brezzi conventions. We assume that all edges in  $E(\mathcal{T}_h)$  are endowed by orientation. A convenient way to orient an edge is to pick a normal direction to that edge; see Fig. 4.2. An element can be oriented by selecting one of the two possible normal directions to its boundary  $\partial K$ . Without loss of generality, all elements are oriented by using the outward normal.

An internal edge  $\mathbf{e} \in \Gamma_h^0$  is shared by exactly two elements. The outward normal on one of these elements will coincide with the normal used to orient  $\mathbf{e}$ ; we call this element  $K^-$ . The outward normal on the other element will have the opposite direction to the normal on  $\mathbf{e}$ ; we call this element  $K^+$ ; see Fig. 4.2. Edge orientation also induces partition of the boundary of an internal element into  $\partial^+ K$ , consisting of all edges whose normal direction

coincides with the outer normal on  $\partial K$  and  $\partial^- K$ , consisting of all edges  $e$  whose normal direction is opposite to the outer normal on  $\partial K$ .

Let  $\varphi$  be a scalar field, and  $\varphi^\pm := \varphi|_{K^\pm}$ . For  $e \in \Gamma_h^0$  we define the *average* and the *jump* as  $\langle \varphi \rangle := \frac{1}{2}(\varphi^+ + \varphi^-)$  and  $[[\varphi]] := \varphi^+ \mathbf{n}^+ + \varphi^- \mathbf{n}^-$ , respectively. Analogously, if  $\mathbf{u}$  is a vector field,  $\langle \mathbf{u} \rangle := \frac{1}{2}(\mathbf{u}^+ + \mathbf{u}^-)$  and  $[[\mathbf{u}]] := \mathbf{u}^+ \cdot \mathbf{n}^+ + \mathbf{u}^- \cdot \mathbf{n}^-$ . Note that, by definition of “ $[[ \cdot ]]$ ”, the jump of a scalar quantity is a vector and the jump of a vector quantity is a scalar. For edges belonging to  $\Gamma_h$ ,  $[[\varphi]] = \varphi \mathbf{n}$  and  $\langle \mathbf{u} \rangle = \mathbf{u}$ . It will not be necessary to define  $\langle \varphi \rangle$  and  $[[\mathbf{u}]]$  on the boundary  $\Gamma$ , because they are never utilized.

### 4.3 Multiscale Discontinuous Galerkin Method

We consider an abstract linear boundary value problem

$$\mathcal{L}(\mathbf{x}, D)\varphi = f \text{ in } \Omega \quad \text{and} \quad \mathcal{R}(\mathbf{x}, D)\varphi = g \text{ on } \Gamma. \quad (4.4)$$

The multiscale DG framework for problem (4.4) has two basic components. The first is a *donor* DG formulation for (4.4): *find  $\varphi_h \in \Phi_h(\Omega)$  such that*

$$B_{DG}(\varphi_h; \psi_h) = F_{DG}(\psi_h) \quad \forall \psi_h \in \Phi_h(\Omega). \quad (4.5)$$

In (4.5),  $B_{DG}(\cdot; \cdot)$  is a continuous bilinear form  $\Phi_h(\Omega) \times \Phi_h(\Omega) \mapsto \mathbb{R}$  and  $F_{DG}(\cdot)$  is a bounded linear functional  $\Phi_h(\Omega) \mapsto \mathbb{R}$ . We assume that (4.5) has a unique solution  $\varphi_h$  that depends continuously on the data and converges (in a suitable norm) to all sufficiently smooth solutions  $\varphi$  of (4.4). The second component is an interscale transfer (or expansion) operator

$$T : \overline{\Phi}_h(\Omega) \mapsto \Phi_h(\Omega). \quad (4.6)$$

We assume that  $T$  is a bounded linear operator, however, it is not required to be surjective, or invertible. Thus, in general  $T(\overline{\Phi}_h(\Omega))$  will be a proper subspace of the discontinuous space  $\Phi_h(\Omega)$ .

We define the Multiscale DG (MDG) method by a composition of the donor DG scheme with the interscale transfer operator  $T$ : *find  $\overline{\varphi}_h \in \overline{\Phi}_h(\Omega)$  such that*

$$B_{DG}(T\overline{\varphi}_h; T\overline{\psi}_h) = F_{DG}(T\overline{\psi}_h) \quad \forall \overline{\psi}_h \in \overline{\Phi}_h(\Omega). \quad (4.7)$$

Substitution of discontinuous test and trial functions in the donor DG method by  $T\overline{\psi}_h$  and  $T\overline{\varphi}_h$  reduces the number of degrees-of-freedom in the MDG formulation to that of a standard Galerkin method posed on  $\overline{\Phi}_h(\Omega)$ . Since  $T(\overline{\Phi}_h(\Omega)) \subset \Phi_h(\Omega)$ , (4.7) occupies a middle ground between a DG and a CG method for (4.4).

#### 4.3.1 Definition of the interscale operator

The definition of the interscale operator  $T$  is key to a robust, efficient and accurate MDG method. For instance, it is desirable to compute  $T$  locally on each element. To discuss

definition of this operator assume that

$$B_{DG}(\varphi_h; \psi_h) = \sum_{K \in \mathcal{T}_h} B_K(\varphi_h; \psi_h) + \sum_{\mathbf{e} \in \Gamma_h} B_\Gamma(\varphi_h; \psi_h) + \sum_{\mathbf{e} \in \Gamma_h^0} B_{\mathbf{e}}(\{\varphi_h^-, \varphi_h^+\}; \{\psi_h^-, \psi_h^+\}) \quad (4.8)$$

where  $B_K(\cdot; \cdot)$  is a bilinear *local* element form defined for every  $K \in \mathcal{T}_h$ ,  $B_\Gamma(\cdot; \cdot)$  is a bilinear form defined on  $\mathbf{e} \in \Gamma_h$ , and  $B_{\mathbf{e}}(\{\cdot\}; \{\cdot\})$  is an *edge* bilinear form defined for  $\mathbf{e} \in \Gamma_h^0$ .

To define  $T$  we proceed to formally split functions  $\varphi_h \in \Phi_h(\Omega)$  into a continuous (“coarse” scale) part  $\bar{\varphi}_h \in \bar{\Phi}_h(\Omega)$  and a discontinuous (“fine” scale) component  $\varphi'_h \in \Phi_h(\Omega)$ , viz.  $\varphi_h = \bar{\varphi}_h + \varphi'_h$ . Then, (4.5) takes the following form:

$$\begin{aligned} B_{DG}(\bar{\varphi}_h; \bar{\psi}_h) + B_{DG}(\varphi'_h; \bar{\psi}_h) &= F_{DG}(\bar{\psi}_h) \quad \forall \bar{\varphi}_h \in \bar{\Phi}_h(\Omega) \\ B_{DG}(\varphi'_h; \psi'_h) + B_{DG}(\bar{\varphi}_h; \psi'_h) &= F_{DG}(\psi'_h) \quad \forall \psi'_h \in \Phi_h(\Omega) \end{aligned} \quad (4.9)$$

The first line in (4.9) is the coarse scale equation. The second line is the fine scale equation that will be used to define  $T$ . Treating the coarse scale function as data we write this equation as: *find*  $\varphi'_h \in \Phi_h(\Omega)$  *such that*

$$B_{DG}(\varphi'_h; \psi'_h) = F_{DG}(\psi'_h) - B_{DG}(\bar{\varphi}_h; \psi'_h) \quad \forall \psi'_h \in \Phi_h(\Omega). \quad (4.10)$$

We restrict (4.10) to an element  $K$  by choosing test functions  $\psi'_h \in S^{p(K)}(K)$  that vanish outside of this element. With the above selection of a test function,  $(\psi'_h)^+ = \chi(\partial^- K)\psi'_h$  and  $(\psi'_h)^- = \chi(\partial^+ K)\psi'_h$  where  $\chi(\cdot)$  is the characteristic function. Using these identities and that  $(\bar{\varphi}_h)^+ = (\bar{\varphi}_h)^- = \bar{\varphi}_h$ , for a  $C^0$  function, the restricted fine scale problem can be expressed as follows: *find*  $\varphi'_h \in S^{p(K)}(K)$  *such that*

$$\begin{aligned} &B_K(\varphi'_h; \psi'_h) + B_\Gamma(\varphi'_h; \psi'_h) + \sum_{\mathbf{e} \in E(K)} B_{\mathbf{e}}(\{(\varphi'_h)^-, (\varphi'_h)^+\}; \{\chi(\partial^+ K)\psi'_h, \chi(\partial^- K)\psi'_h\}) \\ &= F_{DG}(\psi'_h) - B_K(\bar{\varphi}_h; \psi'_h) - B_\Gamma(\bar{\varphi}_h; \psi'_h) \\ &\quad - \sum_{\mathbf{e} \in E(K)} B_{\mathbf{e}}(\{\bar{\varphi}_h, \bar{\varphi}_h\}; \{\chi(\partial^+ K)\psi'_h, \chi(\partial^- K)\psi'_h\}) \quad \forall \psi'_h \in S^{p(K)}(K). \end{aligned} \quad (4.11)$$

Problem (4.11) relates fine scales to the coarse scales, but remains coupled to the contiguous elements through the numerical flux terms in (4.11). Therefore, it does not meet our criteria for localized computation of the interscale transfer operator  $T$ . However, we make the important observation that our goal is not to solve the DG problem (4.9) but rather use it to define a local computation procedure for  $T$  that maps  $\bar{\varphi}_h$  into the local space  $S^{p(K)}(K)$ . We note that this objective is reminiscent of other applications of variational multiscale analysis in which the fine scale problem is used for *estimation* rather than *approximation* of the unresolved solution component. This process can be accomplished by a modification of the numerical flux inherited from the donor DG formulation, or by using a new flux defined only in terms of the local function  $\varphi'_h \in S^{p(K)}(K)$ . Let  $B'_{\mathbf{e}}(\{\cdot\}; \{\cdot\})$  be the new numerical flux. The local fine scale problem obtained from (4.11) is: *find*  $\varphi'_h \in S^{p(K)}(K)$  *such that*

$$\begin{aligned} &B_K(\varphi'_h; \psi'_h) + B_\Gamma(\varphi'_h; \psi'_h) + \sum_{\mathbf{e} \in E(K)} B'_{\mathbf{e}}(\{\varphi'_h\}; \{\psi'_h\}) \\ &= F_{DG}(\psi'_h) - B_K(\bar{\varphi}_h; \psi'_h) - B_\Gamma(\bar{\varphi}_h; \psi'_h) \\ &\quad - \sum_{\mathbf{e} \in E(K)} B_{\mathbf{e}}(\{\bar{\varphi}_h, \bar{\varphi}_h\}; \{\chi(\partial^+ K)\psi'_h, \chi(\partial^- K)\psi'_h\}) \quad \forall \psi'_h \in S^{p(K)}(K). \end{aligned} \quad (4.12)$$

Problem (4.12) is a local equation that can be solved on an element by element basis. This problem defines an operator  $T_K : \bar{\Phi}_h(\Omega) \mapsto S^{p(K)}(K)$  that maps any given  $C^0$  finite element function  $\bar{\varphi}_h$  to a function in the local element space  $S^{p(K)}(K)$ . Therefore,

$$T : \bar{\Phi}_h(\Omega) \mapsto \Phi_h(\Omega); \quad T|_K = T_K \quad \forall K \in \mathcal{T}_h \quad (4.13)$$

defines an interscale transfer operator  $T$  for the MDG method. The abstract variational equation (4.7) and the local problem (4.12) complete the definition of the MDG framework.

## 4.4 Multiscale DG for a scalar advection-diffusion problem

We consider a model advection diffusion problem written in conservative form:

$$\begin{cases} \nabla \cdot (F_a + F_d) = f & \text{in } \Omega; & -(F_a + F_d) \cdot \mathbf{n} = h^- & \text{on } \Gamma_n^- \\ \varphi = g & \text{on } \Gamma_g; & -(F_d) \cdot \mathbf{n} = h^+ & \text{on } \Gamma_n^+ \end{cases} \quad (4.14)$$

where  $F_d = -\kappa \nabla \varphi$  and  $F_a = \mathbf{a} \varphi$  denote diffusive and advective flux, respectively. The total flux is  $F = F_a + F_d$ . The Neumann boundary condition can be written compactly as  $-(\chi(\Gamma_n^-)F_a + F_d) \cdot \mathbf{n} = h$ ; where  $h = \chi(\Gamma_n^-)h^- + \chi(\Gamma_n^+)h^+$ .

### 4.4.1 A donor DG method for the model problem

When dealing with advection-diffusion problems it is profitable to coordinate edge orientations with the advective direction. Given an edge  $\mathbf{e}$  we choose the normal  $\mathbf{n}_e$  for which  $\mathbf{n}_e \cdot \mathbf{a} \geq 0$ . A general weighted residual form of a Discontinuous Galerkin method for (4.14) is given by: *find*  $\varphi \in \Phi_h(\Omega)$  *such that*

$$\begin{aligned} 0 = & \sum_{i=1}^{n_{el}} - \int_{K_i} (F_i \cdot \nabla \psi + f \psi) d\Omega + \int_{\Gamma_n} (\chi(\Gamma_n^+) F_a \cdot \mathbf{n} - h) \psi d\mathbf{l} + \int_{\Gamma_g} (F \cdot \mathbf{n}) \psi d\mathbf{l} + \\ & \int_{\Gamma_g} \epsilon(\varphi - g) W(\psi) d\mathbf{l} + \sum_{\mathbf{e} \in \Gamma_h^0} \int_{\mathbf{e}} (F_b^h(\varphi^+; \varphi^-) \cdot \llbracket \psi \rrbracket + F_c^h(\psi^+; \psi^-) \cdot \llbracket \varphi \rrbracket + \alpha \llbracket \varphi \rrbracket \llbracket \psi \rrbracket) d\mathbf{l} \end{aligned} \quad (4.15)$$

for all  $\psi \in \Phi_h(\Omega)$ . Above,  $W(\psi)$  is a weight function that enforces the Dirichlet boundary condition weakly,

$$F_b^h \stackrel{\text{def}}{=} s_{11} F_a^h + s_{12} F_d^h \quad \text{and} \quad F_c^h \stackrel{\text{def}}{=} s_{21} F_a^h + s_{22} F_d^h \quad (4.16)$$

are numerical models of the total flux across  $\mathbf{e} \in \Gamma_h^0$  and

$$F_a^h \stackrel{\text{def}}{=} F_a^h(\varphi^+, \varphi^-) \quad \text{and} \quad F_d^h \stackrel{\text{def}}{=} F_d^h(\varphi^+, \varphi^-) \quad (4.17)$$

are constitutive relations for the advective and the diffusive fluxes across  $\mathbf{e}$  in terms of the solution states  $\varphi^+$  and  $\varphi^-$  from the two elements that share  $\mathbf{e}$ . The component bilinear forms in (4.8) can be easily identified from (4.15):

$$B_K(\varphi; \psi) = \int_K -F_K \cdot \nabla \psi d\Omega \quad (4.18)$$



**Table 4.1.** Specialization of fluxes and weight function for the donor DG methods.

Function	DG-A	DG-B
$F_b^h(\varphi^+; \varphi^-)$	$F_a(\varphi^-) + \langle F_d(\varphi) \rangle$	$F_a(\varphi^-) + F_d(\varphi^-)$
$F_c^h(\psi^+; \psi^-)$	$s \langle F_d(\psi) \rangle$	$s F_d(\psi^-)$
$W(\psi)$	$\psi + s F_d(\psi) \cdot \mathbf{n}$	

$$B_\Gamma(\varphi; \psi) = \int_{\Gamma_n} (\chi(\Gamma_n^+) F_a \cdot \mathbf{n}) \psi \, d\mathbf{l} + \int_{\Gamma_g} (F \cdot \mathbf{n}) \psi \, d\mathbf{l} + \epsilon \int_{\Gamma_g} \varphi W(\psi) \, d\mathbf{l} \quad (4.19)$$

$$B_e(\{\varphi^+; \varphi^-\}; \{\psi^+; \psi^-\}) = \int_e (F_b^h(\varphi^+; \varphi^-) \llbracket \psi \rrbracket + F_c^h(\psi^+; \psi^-) \llbracket \varphi \rrbracket + \alpha \llbracket \varphi \rrbracket \llbracket \psi \rrbracket) \, d\mathbf{l}. \quad (4.20)$$

A particular donor DG method is obtained from (4.15) by specification of  $\epsilon$ ,  $\alpha$ , the numerical fluxes in (4.16)-(4.17) for the internal edges  $\Gamma_h^0$ , and the weight function  $W(\psi)$ .

We set  $\epsilon = \alpha = \delta \kappa / h_\perp$ , where  $\delta > 0$  is non-dimensional parameter and  $h_\perp = (\text{meas}(K^+) + \text{meas}(K^-)) / (2 \text{meas}(e))$ . Roughly speaking,  $h_\perp$  is a length scale in the direction perpendicular to the edge  $e$ , close to the length of the segment joining the barycenters of  $K^-$  and  $K^+$ .

A standard choice for  $F_a^h$  is the upwinded advective flux  $F_a^h(\psi^+; \psi^-) = F_a(\psi^-) = \mathbf{a} \varphi^-$ . Possible choices for the numerical diffusive flux are the averaged flux  $F_d^h(\psi^+; \psi^-) = \langle F_d(\psi) \rangle = -\frac{1}{2} (\kappa \nabla \psi^+ + \kappa \nabla \psi^-)$  or the upwinded flux  $F_d^h(\psi^+; \psi^-) = F_d(\psi^-) = -\kappa \nabla \psi^-$ . To define  $F_b^h$  and  $F_c^h$  we set  $s_{11} = s_{12} = 1$ ,  $s_{21} = 0$  and  $s_{22} = s \in \{-1, 0, +1\}$  in (4.16). This leads to two different donor DG methods: DG-A which uses averaged diffusive flux, and DG-B which uses the upwinded version of that flux; see [80]. Flux and weight function definitions for the two methods are summarized in Table 4.1.

The effect of the parameter  $s$  has been extensively studied in the discontinuous Galerkin literature (see Arnold *et al.* [7], Baumann and Oden [13], and Hughes *et al.* [82]). The symmetric formulation ( $s = -1$ ) is adjoint-consistent, guaranteeing optimal  $L_2$ -convergence rates in the diffusive limit. Ostensibly, the skew formulation ( $s = +1$ ) has superior stability properties but the  $\epsilon$  and  $\alpha$ -terms can be used to improve the stability behavior of the neutral (i.e.,  $s = 0$ ) and symmetric formulations. For more details about the implementation of the donor DG and numerical results we refer to [80].

For DG-B the numerical flux  $F_b^h$  is simply the upwinded total flux  $F(\varphi^-)$ . DG-A and DG-B have the same element form  $B_K(\cdot; \cdot)$  (given by (4.18)) and the same boundary form:

$$B_\Gamma(\varphi; \psi) = \int_{\Gamma_n} (\chi(\Gamma_n^+) F_a \cdot \mathbf{n}) \psi \, d\mathbf{l} + \int_{\Gamma_g} (F \cdot \mathbf{n}) \psi \, d\mathbf{l} + \epsilon \int_{\Gamma_g} \underbrace{\varphi (\psi - s \kappa \nabla \psi \cdot \mathbf{n})}_{W(\psi)} \, d\mathbf{l} \quad (4.21)$$

The internal edge form for DG-A is

$$B_e(\{\varphi^+; \varphi^-\}; \{\psi^+; \psi^-\}) = \int_e \alpha \llbracket \varphi \rrbracket \llbracket \psi \rrbracket \, d\mathbf{l} + \int_e \left( \underbrace{(\mathbf{a} \varphi^- - (\kappa \nabla \varphi^+ + \kappa \nabla \varphi^-) / 2)}_{F_b^h} \cdot \llbracket \psi \rrbracket - \underbrace{s (\kappa \nabla \psi^+ + \kappa \nabla \psi^-) / 2}_{F_c^h} \cdot \llbracket \varphi \rrbracket \right) \, d\mathbf{l} \quad (4.22)$$

while for DG-B this form is given by

$$B_e(\{\varphi^+; \varphi^-\}; \{\psi^+; \psi^-\}) = \int_e \alpha \llbracket \varphi \rrbracket \llbracket \psi \rrbracket d\mathbf{l} + \int_e \left( \underbrace{(\mathbf{a}\varphi^- - \kappa \nabla \varphi^-) \cdot \llbracket \psi \rrbracket}_{F_b^h} - \underbrace{s\kappa \nabla \psi^- \cdot \llbracket \varphi \rrbracket}_{F_c^h} \right) d\mathbf{l}. \quad (4.23)$$

#### 4.4.2 The interscale operator

We develop a consistent approach that reduces the edge form  $B_e(\{\cdot\}; \{\cdot\})$  in the donor DG method to a form defined in terms of the local (fine scale) variable  $\varphi'$  and test function  $\psi'$ . In doing so we aim to preserve as much as possible from the structure of the donor DG method in the local problem.

For this purpose we redefine the calculation of the jump, the average and the states  $\varphi^\pm, \psi^\pm$  as follows: given  $\psi \in S^{p(K)}(K)$  its states are defined by

$$\psi^+ = \chi(\partial^- K)\psi \quad \text{and} \quad \psi^- = \chi(\partial^+ K)\psi \quad (4.24)$$

its jump is the vector

$$\llbracket \psi \rrbracket = \mathbf{n}_K \psi, \quad (4.25)$$

and its average is the function itself:

$$\langle \psi \rangle = \psi. \quad (4.26)$$

The rules in (4.24)-(4.26) have the following interpretation. To compute the states and the jump of  $\psi$ , extend by zero to a function  $\psi_0 \in L^2(\Omega)$ . Then  $\llbracket \psi_0 \rrbracket = \mathbf{n}^+ \chi(\partial^- K)\psi_0 + \mathbf{n}^- \chi(\partial^+ K)\psi_0 = \mathbf{n}_K \psi_0$ . Definition (4.26) can be motivated by noting that for affine elements  $\psi$  can be trivially extended to a function  $\psi_\infty \in C^\infty(\Omega)$  for which  $\langle \psi_\infty \rangle = \frac{1}{2}(\psi_\infty + \psi_\infty) = \psi_\infty$  giving (4.26). The local definitions of the numerical fluxes obtained through (4.24)-(4.26) are summarized in Table 4.2.

**Table 4.2.** Specialization of fluxes for the local problem.

Function	DG-A	DG-B
$F_b^h(\varphi)$	$F_a(\chi(\partial^+ K)\varphi) + F_d(\varphi)$	$F_a(\chi(\partial^+ K)\varphi) + F_d(\chi(\partial^+ K)\varphi)$
$F_c^h(\psi)$	$sF_d(\psi)$	$sF_d(\chi(\partial^+ K)\psi)$

##### 4.4.2.1 Local problem for DG-A

The localized edge form for DG-A method is

$$B'_e(\{\varphi\}; \{\psi\}) = \int_e \left( \underbrace{(\mathbf{a}\chi(\partial^+ K)\varphi - \kappa \nabla \varphi) \cdot \mathbf{n}_K \psi}_{F_b^h} - \underbrace{s\kappa \nabla \psi \cdot \mathbf{n}_K \varphi}_{F_c^h} + \alpha \varphi \psi \right) d\mathbf{l}. \quad (4.27)$$

The last two terms can be combined into a single weight function  $W_\alpha(\psi) = \alpha\psi - s\kappa \nabla \psi \cdot \mathbf{n}_K$ . Thus, the local problem obtained from DG-A is: given a  $\bar{\varphi} \in \bar{\Phi}_h(\Omega)$  find  $\varphi' \in$

$S^{p(K)}(K)$  such that

$$\begin{aligned} & B_K(\varphi'; \psi') + B_\Gamma(\varphi'; \psi') + \sum_{\mathbf{e} \in \partial K} \int_{\mathbf{e}} \left( (\mathbf{a}\chi(\partial^+ K)\varphi' - \kappa\nabla\varphi') \cdot \mathbf{n}_K \psi' + \varphi' W_\alpha(\psi') \right) d\mathbf{l} \\ & = F_{DG}(\psi') - B_K(\bar{\varphi}; \psi') - B_\Gamma(\bar{\varphi}; \psi') \\ & \quad - \sum_{\mathbf{e} \in \partial K} B_{\mathbf{e}}(\{\bar{\varphi}, \bar{\varphi}\}; \{\chi(\partial^+ K)\psi', \chi(\partial^- K)\psi'\}) \quad \forall \psi' \in S^{p(K)}(K). \end{aligned} \quad (4.28)$$

**Remark 4.4.1** *This local problem is identical to the one used in [80].*

#### 4.4.2.2 Local problem for DG-B

For DG-B we have the localized edge form:

$$B'_{\mathbf{e}}(\{\varphi\}; \{\psi\}) = \int_{\mathbf{e}} \left( \underbrace{\chi(\partial^+ K)(\mathbf{a}\varphi - \kappa\nabla\varphi)}_{F_b^h} \cdot \mathbf{n}_K \psi - \underbrace{s\chi(\partial^+ K)\kappa\nabla\psi}_{F_c^h} \cdot \mathbf{n}_K \varphi + \alpha\varphi\psi \right) d\mathbf{l}. \quad (4.29)$$

The last two terms can be combined into the weight function  $W_\alpha^-(\psi) = \alpha\psi - s\chi(\partial^+ K)\nabla\psi \cdot \mathbf{n}_K$ , which is an "upwinded" version of  $W_\alpha(\psi)$ . The local problem is: given a  $\bar{\varphi} \in \bar{\Phi}_h(\Omega)$  find  $\varphi' \in S^{p(K)}(K)$  such that

$$\begin{aligned} & B_K(\varphi'; \psi') + B_\Gamma(\varphi'; \psi') + \sum_{\mathbf{e} \in \partial K} \int_{\mathbf{e}} \left( \chi(\partial^+ K)(\mathbf{a}\varphi' - \kappa\nabla\varphi') \cdot \mathbf{n}_K \psi' + \varphi' W_\alpha(\psi') \right) d\mathbf{l} \\ & = F_{DG}(\psi') - B_K(\bar{\varphi}; \psi') - B_\Gamma(\bar{\varphi}; \psi') \\ & \quad - \sum_{\mathbf{e} \in \partial K} B_{\mathbf{e}}(\{\bar{\varphi}, \bar{\varphi}\}; \{\chi(\partial^+ K)\psi', \chi(\partial^- K)\psi'\}) \quad \forall \psi' \in S^{p(K)}(K). \end{aligned} \quad (4.30)$$

## 4.5 Conclusions

In this work we extended the DG method developed in [80] to a general framework for multiscale DG methods that have the computational structure of continuous Galerkin methods. This represents a solution to a fundamental and long-standing problem in discontinuous-Galerkin technology, namely, restraining the proliferation of degrees-of-freedom. Numerical results reported in [80] indicate that for a scalar advection-diffusion equation the new method at least attains, and even somewhat improves upon, the performance of the associated continuous Galerkin method. Within the framework of the multiscale discontinuous Galerkin method, the local problem provides a vehicle for incorporating the necessary stabilization features such as discontinuity capturing and upwinding. There seems to be a potential connection here with ideas from wave propagation methods based on solutions of the Riemann problem, which is worth exploring in more detail.

The MDG formulation can be also viewed as an approach that enables uncoupling of *storage* locations of the data from the *computational* locations where this data is used. For

example, one can envision a situation where information is stored at the nodes and then mapped to flux and circulation degrees-of-freedom by the operator  $T$ . Such an extension of MDG appears to be a fruitful direction for further research.

## Acknowledgement

The authors would like to thank Giancarlo Sangalli and the anonymous referees for helpful remarks. The work of T. J. R. Hughes was supported by Sandia Contract No. A0340.0 with the University of Texas at Austin. This support is gratefully acknowledged.

## Chapter 5

# Force Flux and the Peridynamic Stress Tensor

**Principle Authors: Richard B. Lehoucq and Stewart A. Silling**

The peridynamic model is a framework for continuum mechanics based on the idea that pairs of particles exert forces on each other across a finite distance. The equation of motion in the peridynamic model is an integro-differential equation. In this paper, a notion of a peridynamic stress tensor derived from nonlocal interactions is defined. At any point in the body, this stress tensor is obtained from the forces within peridynamic bonds that geometrically go through the point. The peridynamic equation of motion can be expressed in terms of this stress tensor, and the result is formally identical to the Cauchy equation of motion in the classical model, even though the classical model is a local theory. We also establish that this stress tensor field is unique in a certain function space compatible with finite element approximations.

### 5.1 Introduction

The peridynamic model [143] is an alternative theory of continuum mechanics based on integral, rather than differential, equations. The purpose of peridynamics is to provide a more general framework than the classical theory for problems involving discontinuities or other singularities in the deformation. The integral equations express a nonlocal force model that describes long-range material interaction. In this context, nonlocal means that particles separated by a finite distance may exert nonzero forces upon each other. This nonlocality is in contrast to the local force model intrinsic with classical continuum mechanics.

In the peridynamic model, the ideas of “force per unit area” and a stress tensor are not used. The goal of our paper is to define the *force flux* and the *peridynamic stress tensor* so establishing a closer connection between this and the classical view of continuum mechanics. We demonstrate that the peridynamic equation of motion

$$\rho(\mathbf{x})\ddot{\mathbf{u}}(\mathbf{x}, t) = \int_{\mathcal{R}} \hat{\mathbf{f}}(\mathbf{u}(\mathbf{x}', t) - \mathbf{u}(\mathbf{x}, t), \mathbf{x}' - \mathbf{x}, \mathbf{x}) dV_{\mathbf{x}'} + \mathbf{b}(\mathbf{x}, t) \quad (5.1)$$

when expressed in terms of the peridynamic stress tensor, is formally identical to the classical equation of motion, which is a partial differential equation. Our paper shows that the peridynamic stress tensor implicitly defines a formal Green’s function for the differential

equation

$$\nabla \cdot \boldsymbol{\nu}(\mathbf{x}) = \int_{\mathcal{R}} \hat{\mathbf{f}}(\mathbf{u}(\mathbf{x}', t) - \mathbf{u}(\mathbf{x}, t), \mathbf{x}' - \mathbf{x}, \mathbf{x}) dV_{\mathbf{x}'} . \quad (5.2)$$

Moreover, we show that a unique stress tensor field exists, satisfying an energy principle, within a certain function space compatible with finite element approximations.

The basic relation in the peridynamic model is the equation of motion (5.1) where  $\mathbf{x}$  is a point in the reference configuration of a region  $\mathcal{R}$ ,  $\mathbf{u}$  is the displacement field,  $\mathbf{b}$  is a prescribed body force density field,  $\rho$  is the reference density field, and  $t \geq 0$  is the time. The vector-valued function  $\hat{\mathbf{f}}$  is called the *pairwise force function*, whose value is the force density (with dimensions force/volume<sup>2</sup>) that any point  $\mathbf{x}'$  exerts on  $\mathbf{x}$ . The pairwise force function depends upon

$$\boldsymbol{\eta} = \mathbf{u}(\mathbf{x}', t) - \mathbf{u}(\mathbf{x}, t), \quad \boldsymbol{\xi} = \mathbf{x}' - \mathbf{x},$$

the relative displacement and position vector between  $\mathbf{x}$  and  $\mathbf{x}'$ , respectively, as well as  $\mathbf{x}$  if the body is nonhomogeneous. Balance of linear and angular momenta places the following requirements on  $\hat{\mathbf{f}}$ :

$$\hat{\mathbf{f}}(-\boldsymbol{\eta}, -\boldsymbol{\xi}, \mathbf{x} + \boldsymbol{\xi}) = -\hat{\mathbf{f}}(\boldsymbol{\eta}, \boldsymbol{\xi}, \mathbf{x}), \quad (\boldsymbol{\xi} + \boldsymbol{\eta}) \times \hat{\mathbf{f}}(\boldsymbol{\eta}, \boldsymbol{\xi}, \mathbf{x}) = \mathbf{0} \quad (5.3)$$

for all  $\boldsymbol{\eta}$ , all  $\boldsymbol{\xi}$ , and all  $\mathbf{x} \in \mathcal{R}$ . The function  $\hat{\mathbf{f}}$  contains all constitutive information about the material. It is often convenient, although not an essential feature of the theory, to assume that if  $\mathbf{x}$  and  $\mathbf{x}'$  are separated in the reference configuration by a distance greater than some number  $\delta > 0$  then the particles do not interact:

$$|\boldsymbol{\xi}| > \delta \implies \hat{\mathbf{f}}(\boldsymbol{\eta}, \boldsymbol{\xi}, \mathbf{x}) = \mathbf{0}. \quad (5.4)$$

The number  $\delta$ , if it exists for a particular material, is called the *horizon*.

## 5.2 Peridynamic Stress Tensor

**Definition 5.2.1** Let a peridynamic region  $\mathcal{R}$  be given with pairwise force function  $\hat{\mathbf{f}}$ , and let  $\mathbf{u}$  be the displacement field on  $\mathcal{R}$ . For a given  $t \geq 0$ , define a vector valued function  $\mathbf{f} : \mathbb{R}^3 \times \mathbb{R}^3 \rightarrow \mathbb{R}^3$  by

$$\mathbf{f}(\mathbf{p}, \mathbf{q}) = \begin{cases} \hat{\mathbf{f}}(\mathbf{u}(\mathbf{p}, t) - \mathbf{u}(\mathbf{q}, t), \mathbf{p} - \mathbf{q}, \mathbf{q}) & \text{if } \mathbf{p}, \mathbf{q} \in \mathcal{R} \\ \mathbf{0} & \text{otherwise.} \end{cases}$$

Thus  $\mathbf{f}$  is the force density per unit volume squared that  $\mathbf{p}$  exerts on  $\mathbf{q}$ , and  $\mathbf{f}$  is called the *pairwise force density*. We remark that the constitutive model is supplied by  $\hat{\mathbf{f}}$ , in contrast to  $\mathbf{f}$ .

Define a set  $\mathcal{I}$  consisting of ordered pairs of vectors in which the vectors equal each other:

$$\mathcal{I} = \{(\mathbf{p}, \mathbf{q}) \in \mathbb{R}^3 \times \mathbb{R}^3 \mid \mathbf{p} = \mathbf{q}\}. \quad (5.5)$$

The first of (5.3) and (5.2.1) imply that

$$\mathbf{f}(\mathbf{q}, \mathbf{p}) = -\mathbf{f}(\mathbf{p}, \mathbf{q}) \quad \forall \mathbf{q}, \mathbf{p} \in \mathbb{R}^3. \quad (5.6)$$

This further implies that  $\mathbf{f} = \mathbf{0}$  on  $\mathcal{I}$ .

We assume, throughout this section, that  $\mathbf{f}(\mathbf{x}', \mathbf{x})$  is Riemann-integrable. This assumption does *not* imply that  $\mathbf{f}(\mathbf{p}, \mathbf{q})$  is bounded as  $|\mathbf{p} - \mathbf{q}| \rightarrow 0$ . The example in the last section of this paper illustrates a material in which  $\mathbf{f}$  is unbounded in this sense.

In the remainder of this paper,  $\mathcal{S}$  denotes the unit sphere, and  $d\Omega_{\mathbf{m}}$  denotes a differential solid angle on  $\mathcal{S}$  in the direction of any unit vector  $\mathbf{m}$ .

**Definition 5.2.2** *Let a deformation with displacement field  $\mathbf{u}$  on a region  $\mathcal{R}$  be given, and let  $\mathbf{f}$  be the corresponding pairwise force density. Define the peridynamic stress tensor at any  $\mathbf{x} \in \mathbb{R}^3$  by*

$$\boldsymbol{\nu}(\mathbf{x}) = \frac{1}{2} \int_{\mathcal{S}} \int_0^\infty \int_0^\infty (y+z)^2 \mathbf{f}(\mathbf{x} + y\mathbf{m}, \mathbf{x} - z\mathbf{m}) \otimes \mathbf{m} \, dz \, dy \, d\Omega_{\mathbf{m}}. \quad (5.7)$$

Definition 5.2.1 implies that

$$\mathbf{f}(\mathbf{x} + y\mathbf{m}, \mathbf{x} - z\mathbf{m}) = \hat{\mathbf{f}}(\mathbf{u}(\mathbf{x} + y\mathbf{m}) - \mathbf{u}(\mathbf{x} - z\mathbf{m}), (y+z)\mathbf{m}, \mathbf{x} - z\mathbf{m})$$

where we suppressed  $t$  for brevity.

The following result demonstrates a relationship between the peridynamic stress tensor and the pairwise force density.

**Theorem 5.2.3** *Let a deformation with displacement field  $\mathbf{u}$  on a region  $\mathcal{R}$  be given, let  $\mathbf{f}$  be the corresponding pairwise force density, and let  $\boldsymbol{\nu}$  be given by Definition 5.2.2. If  $\mathbf{f}$  is continuously differentiable on  $\mathbb{R}^3 \times \mathbb{R}^3 - \mathcal{I}$  and if*

$$\mathbf{f}(\mathbf{p}, \mathbf{q}) = o(|\mathbf{p} - \mathbf{q}|^{-2}) \quad \text{as } |\mathbf{p} - \mathbf{q}| \rightarrow \infty, \quad (5.8)$$

then

$$\nabla \cdot \boldsymbol{\nu}(\mathbf{x}) = \int_{\mathcal{R}} \mathbf{f}(\mathbf{x}', \mathbf{x}) \, dV_{\mathbf{x}'} \quad \forall \mathbf{x} \in \mathbb{R}^3. \quad (5.9)$$

**Proof.** To make the notation more concise, define a vector-valued function  $\mathbf{g}$  by

$$\mathbf{g}(\mathbf{m}, y, z) = \mathbf{f}(\mathbf{x} + y\mathbf{m}, \mathbf{x} - z\mathbf{m}) \quad (5.10)$$

so that Definition 5.2.2 may be rewritten in terms of components in an orthonormal coordinate system as

$$\nu_{ij}(\mathbf{x}) = \frac{1}{2} \int_{\mathcal{S}} \int_0^\infty \int_0^\infty (y+z)^2 g_i(\mathbf{m}, y, z) m_j \, dz \, dy \, d\Omega_{\mathbf{m}}. \quad (5.11)$$

Note for later use that (5.6) implies that

$$\mathbf{g}(-\mathbf{m}, z, y) = -\mathbf{g}(\mathbf{m}, y, z). \quad (5.12)$$

Observe from (5.10) and the chain rule that

$$\frac{\partial g_i}{\partial y} = m_j \frac{\partial f_i}{\partial p_j}, \quad \frac{\partial g_i}{\partial z} = -m_j \frac{\partial f_i}{\partial q_j}, \quad \frac{\partial g_i}{\partial x_j} = \frac{\partial f_i}{\partial p_j} + \frac{\partial f_i}{\partial q_j}$$

where the  $p_j$  and  $q_j$  refer to the first and second arguments of  $\mathbf{f}$  as indicated in (5.2.1). Therefore,

$$m_j \frac{\partial g_i}{\partial x_j} = \frac{\partial g_i}{\partial y} - \frac{\partial g_i}{\partial z}. \quad (5.13)$$

By directly differentiating (5.11) and using (5.13),

$$\frac{\partial \nu_{ij}}{\partial x_j} = \frac{1}{2} \int_S \int_0^\infty \int_0^\infty (y+z)^2 \left( \frac{\partial g_i}{\partial y} - \frac{\partial g_i}{\partial z} \right) dz dy d\Omega_{\mathbf{m}}. \quad (5.14)$$

Integration by parts leads to

$$\begin{aligned} \int_0^\infty (y+z)^2 \frac{\partial g_i}{\partial y} dy &= \int_0^\infty \frac{\partial}{\partial y} ((y+z)^2 g_i) dy - 2 \int_0^\infty (y+z) g_i dy \\ &= -z^2 g_i(\mathbf{m}, 0, z) - 2 \int_0^\infty (y+z) g_i dy \end{aligned} \quad (5.15)$$

where (5.8) has been used to drop the term arising from the upper limit of integration, *i.e.*,  $g_i(\mathbf{m}, \infty, z) = 0$ . Similarly,

$$\int_0^\infty (y+z)^2 \frac{\partial g_i}{\partial z} dz = -y^2 g_i(\mathbf{m}, y, 0) - 2 \int_0^\infty (y+z) g_i dz \quad (5.16)$$

Combining (5.14), (5.15), and (5.16), yields

$$\begin{aligned} \frac{\partial \nu_{ij}}{\partial x_j} &= \frac{1}{2} \int_S \left( - \int_0^\infty z^2 g_i(\mathbf{m}, 0, z) dz + \int_0^\infty y^2 g_i(\mathbf{m}, y, 0) dy \right) d\Omega_{\mathbf{m}} \\ &= \frac{1}{2} \int_S \left( \int_0^\infty z^2 g_i(-\mathbf{m}, z, 0) dz + \int_0^\infty y^2 g_i(\mathbf{m}, y, 0) dy \right) d\Omega_{\mathbf{m}} \\ &= \int_S \int_0^\infty y^2 g_i(\mathbf{m}, y, 0) dy d\Omega_{\mathbf{m}} \end{aligned} \quad (5.17)$$

where we have used the changes of variables  $z \leftrightarrow y$ ,  $\mathbf{m} \leftrightarrow -\mathbf{m}$ , and (5.12). Recognizing (5.17) as a volume integral, and replacing  $g_i$  with  $f_i$ , we have that

$$\frac{\partial \nu_{ij}}{\partial x_j} = \int_S \int_0^\infty f_i(\mathbf{x} + y\mathbf{m}, \mathbf{x}) (y^2 dy d\Omega_{\mathbf{m}}) = \int_{\mathcal{R}} f_i(\mathbf{x}', \mathbf{x}) dV_{\mathbf{x}'},$$

and our result is established. ■



**Remark 5.2.4** *The condition (5.8) on the decay of  $\mathbf{f}$  is automatically satisfied by any material with a finite horizon.*

**Remark 5.2.5** *The hypothesis and proof of Theorem 5.2.3 do not restrict the particular constitutive model that gives rise to the interparticle forces. In fact, it is not even necessary to assume that the material has a pairwise force function. For example, the force between any  $\mathbf{p}$  and  $\mathbf{q}$  could be influenced by multibody interactions. (In this case, Definition 5.2.1 would have to be modified.)*

Theorem 5.2.3 allows us to rewrite the peridynamic equation of motion (5.1) as

$$\rho(\mathbf{x})\ddot{\mathbf{u}}(\mathbf{x}, t) = \nabla \cdot \boldsymbol{\nu}(\mathbf{x}, t) + \mathbf{b}(\mathbf{x}, t),$$

which is formally identical to the equation of motion in the classical theory. The stress tensor  $\boldsymbol{\nu}$  is the analogue of the Piola stress tensor in the classical theory.

To investigate the conditions under which  $\boldsymbol{\nu}$  is symmetric, recall from the requirement of balance of angular momentum (second of (5.3)) that  $\mathbf{f}$  is always parallel to the *deformed* bond direction  $\hat{\mathbf{m}} = (\boldsymbol{\xi} + \boldsymbol{\eta})/|\boldsymbol{\xi} + \boldsymbol{\eta}|$ . Therefore, the integrand in Definition 5.2.2 is symmetric when  $\hat{\mathbf{m}} = \mathbf{m}$ , which occurs if  $\mathbf{u} \equiv \mathbf{0}$ . So,  $\boldsymbol{\nu}$  is symmetric if the deformed configuration and the reference configuration are the same. Otherwise,  $\boldsymbol{\nu}$  is in general nonsymmetric (this is also true of the classical Piola stress tensor). In the classical model, the Piola stress tensor  $\mathbf{S}$  can be transformed to a Cauchy stress tensor  $\mathbf{T}$  through the relation  $\mathbf{T} = \mathbf{S}\mathbf{F}^T/(\det \mathbf{F})$ , where  $\mathbf{F}$  is the deformation gradient tensor. However, in the peridynamic model, it is not assumed that  $\mathbf{u}$  is continuously differentiable, so we cannot in general define a deformation gradient tensor. Therefore, although  $\boldsymbol{\nu}$  is analogous to the Piola stress tensor  $\mathbf{S}$ , it is not possible in general to transform  $\boldsymbol{\nu}$  into a Cauchy stress tensor.

### 5.3 Behavior of the Peridynamic Stress Tensor on a Boundary

Many deformations of practical interest involve  $\mathbf{f}$  that fails to be continuously differentiable on  $\partial\mathcal{R}$  as required by Theorem 5.2.3. The following demonstrates that the basic conclusion of Theorem 5.2.3 continues to hold even in this case.

**Theorem 5.3.1** *Suppose that all conditions of Theorem 5.2.3 are met except that  $\mathbf{f}$  is required to satisfy only the weaker condition that it be continuously differentiable on  $(\mathbb{R}^3 - \partial\mathcal{R}) \times (\mathbb{R}^3 - \partial\mathcal{R}) - \mathcal{I}$  rather than on  $\mathbb{R}^3 \times \mathbb{R}^3 - \mathcal{I}$ . Then*

$$\nabla \cdot \boldsymbol{\nu}(\mathbf{x}) = \int_{\mathcal{R}} \mathbf{f}(\mathbf{x}', \mathbf{x}) dV_{\mathbf{x}'} \quad \forall \mathbf{x} \in \mathbb{R}^3 - \partial\mathcal{R}. \quad (5.18)$$

**Proof.** Assume, temporarily, that  $\mathcal{R}$  is convex. Consider  $\mathbf{x} \in \mathcal{R} - \partial\mathcal{R}$ . For this  $\mathbf{x}$ , let  $\ell(\mathbf{m})$  denote the distance from  $\mathbf{x}$  to  $\partial\mathcal{R}$  along the direction  $\mathbf{m}$ . The exterior of  $\mathcal{R}$  contributes

nothing to the integral in Definition 5.2.2, so the limits of integration may be changed as follows:

$$\boldsymbol{\nu}(\mathbf{x}) = \frac{1}{2} \int_S \int_0^{\ell(\mathbf{m})} \int_0^{\ell(-\mathbf{m})} (y+z)^2 \mathbf{f}(\mathbf{x} + y\mathbf{m}, \mathbf{x} - z\mathbf{m}) \otimes \mathbf{m} \, dz \, dy \, d\Omega_{\mathbf{m}}.$$

Upon differentiating to obtain the divergence as in (5.14), the Leibniz rule causes new terms to appear due to the possibly finite limits of integration over  $y$  and  $z$ :

$$\begin{aligned} \frac{\partial \nu_{ij}}{\partial x_j} &= \frac{1}{2} \int_S \left\{ \int_0^{\ell(\mathbf{m})} \int_0^{\ell(-\mathbf{m})} (y+z)^2 \left( \frac{\partial g_i}{\partial y} - \frac{\partial g_i}{\partial z} \right) \, dz \, dy \right. \\ &\quad + \int_0^{\ell(\mathbf{m})} (y + \ell(-\mathbf{m}))^2 g_i(\mathbf{m}, y, \ell(-\mathbf{m})) \, dy \\ &\quad \left. - \int_0^{\ell(-\mathbf{m})} (\ell(\mathbf{m}) + z)^2 g_i(\mathbf{m}, \ell(\mathbf{m}), z) \, dz \right\} d\Omega_{\mathbf{m}}. \end{aligned} \quad (5.19)$$

The integration by parts in (5.15) also involves new terms because of the new limits of integration, for example,

$$\begin{aligned} \int_0^{\ell(\mathbf{m})} (y+z)^2 \frac{\partial g_i}{\partial y} \, dy &= \int_0^{\ell(\mathbf{m})} \frac{\partial}{\partial y} ((y+z)^2 g_i) \, dy - 2 \int_0^{\ell(\mathbf{m})} (y+z) g_i \, dy \\ &= (\ell(\mathbf{m}) + z)^2 g_i(\mathbf{m}, \ell(\mathbf{m}), z) - z^2 g_i(\mathbf{m}, 0, z) \\ &\quad - 2 \int_0^{\ell(\mathbf{m})} (y+z) g_i \, dy. \end{aligned} \quad (5.20)$$

Combining (5.19), (5.20), and the analogue of (5.19) for the integral over  $\partial g_i / \partial z$  shows that the new terms arising from the boundary cancel each other out. So, the remainder of the proof is the same as for Theorem 5.2.3. The case of  $\mathbf{x}$  in the exterior of  $\mathcal{R}$  is handled similarly, establishing the result (5.18). Any finite number of discontinuities in  $\mathbf{g}$  along a direction  $\mathbf{m}$  can be treated in the same way as shown above by defining  $\{\ell_1(\mathbf{m}), \ell_2(\mathbf{m}), \dots\}$  at the locations of the discontinuities. Therefore, the conclusion holds for the case of non-convex  $\mathcal{R}$  as well as convex. ■

**Remark 5.3.2** *Under the conditions of Theorem 5.3.1,  $\boldsymbol{\nu}$  may fail to be differentiable on  $\partial\mathcal{R}$ . However, if we restrict the domain of  $\boldsymbol{\nu}$  to  $\mathcal{R} + \partial\mathcal{R}$ , then the result (5.18) holds on this closed set. This is a familiar situation in the classical theory of continuum mechanics, in which a stress tensor field may be differentiable on  $\mathcal{R}$ , yet fail to be differentiable on  $\mathbb{R}^3$ .*

**Remark 5.3.3** *The peridynamic stress tensor  $\boldsymbol{\nu}$  may be non-null in the exterior of nonconvex  $\mathcal{R}$ , but  $\nabla \cdot \boldsymbol{\nu} = \mathbf{0}$  in this exterior according to (5.18).*

**Remark 5.3.4** *The same explanation of Remark 5.2.5 can be used to show that Theorem 5.3.1 does not require  $\mathbf{f}$  to be a pairwise force function.*

We now address the behavior of the peridynamic stress tensor near  $\partial\mathcal{R}$  and the exterior of  $\mathcal{R}$ .

**Definition 5.3.5** Let  $\mathcal{B}$  be a closed, bounded, region in  $\mathbb{R}^3$  of non-zero volume, and let  $\bar{\mathcal{B}}$  denotes the convex hull of  $\mathcal{B}$ .

The following result provides a boundary condition for the differential equation (5.2).

**Theorem 5.3.6** Let  $\mathbf{f}$  be the pairwise force density resulting from a given displacement field  $\mathbf{u}$  on  $\mathcal{B}$ , and let  $\boldsymbol{\nu}$  be given by Definition 5.2.2. If  $\mathbf{n}(\mathbf{x})$  denotes the outward-directed unit normal to  $\partial\mathcal{B}$  at any  $\mathbf{x} \in \partial\mathcal{B}$ , then

$$\boldsymbol{\nu}(\mathbf{x})\mathbf{n}(\mathbf{x}) = \mathbf{0} \quad \forall \mathbf{x} \in \partial\bar{\mathcal{B}}.$$

**Proof.** Consider any  $\mathbf{x} \in \partial\bar{\mathcal{B}}$ . Use Definition 5.2.2 in component form to obtain

$$\nu_{ij}n_j = \frac{1}{2} \int_{\mathcal{S}} \int_0^\infty \int_0^\infty (y+z)^2 f_i(\mathbf{x} + y\mathbf{m}, \mathbf{x} - z\mathbf{m}) m_j n_j \, dz \, dy \, d\Omega_{\mathbf{m}}. \quad (5.21)$$

Since  $\bar{\mathcal{B}}$  is convex, any line segment whose endpoints are both in  $\bar{\mathcal{B}}$  is contained entirely in  $\bar{\mathcal{B}}$ . In the integrand in (5.21), suppose  $\mathbf{m} \cdot \mathbf{n} > 0$ . Then, because  $\mathbf{n}$  is an outward-directed unit normal, for sufficiently small  $\Delta y > 0$ , the point  $\mathbf{x} + \Delta y \mathbf{m}$  is in the exterior of  $\bar{\mathcal{B}}$ . Therefore, because of the convexity of  $\bar{\mathcal{B}}$ , the entire half-line  $\{\mathbf{x} + y\mathbf{m} \mid y > 0\}$  is in the exterior of  $\bar{\mathcal{B}}$ ; establishing that the integrand in (5.21) vanishes for  $\mathbf{m} \cdot \mathbf{n} > 0$ . Similarly, it vanishes for  $\mathbf{m} \cdot \mathbf{n} < 0$ . The only remaining case is  $\mathbf{m} \cdot \mathbf{n} = 0$ , but since  $m_j n_j$  appears in the integrand, in this case the integrand also vanishes. Hence the integrand vanishes for all  $\mathbf{m}$  and our result is established. ■

**Remark 5.3.7** If  $\mathcal{B}$  is not convex, then  $\boldsymbol{\nu}$  can be non-null at points in  $\bar{\mathcal{B}} - \mathcal{B}$ , even though no material is present there. But  $\boldsymbol{\nu}$  must vanish in the exterior of  $\bar{\mathcal{B}}$ .

**Remark 5.3.8** Theorem 5.3.6 does not require that  $\mathbf{f}$  be continuously differentiable.

Theorem 5.3.6 implies that the peridynamic stress tensor  $\boldsymbol{\nu}$  implicitly defines a formal Green's function for the boundary value problem

$$\begin{aligned} \nabla \cdot \boldsymbol{\nu}(\mathbf{x}) &= \int_{\bar{\mathcal{B}}} \mathbf{f}(\mathbf{x}', \mathbf{x}) \, dV_{\mathbf{x}'} & \mathbf{x} \in \bar{\mathcal{B}} \\ \boldsymbol{\nu}(\mathbf{x})\mathbf{n}(\mathbf{x}) &= \mathbf{0} & \mathbf{x} \in \partial\bar{\mathcal{B}}. \end{aligned} \quad (5.22)$$

## 5.4 Variational Interpretation of the Peridynamic Stress Tensor

Sections 5.2 and 5.3 presented a classical interpretation of the peridynamic stress tensor. This section establishes existence and uniqueness results for  $\boldsymbol{\nu}$  in a variational sense. Such

an interpretation allows us to identify function spaces associated with  $\boldsymbol{\nu}$  and  $\mathbf{f}$  so providing more general conditions than possible with a classical interpretation.

Define

$$\mathbf{F}(\mathbf{x}) = \int_{\mathcal{B}} \mathbf{f}(\mathbf{x}', \mathbf{x}) dV_{\mathbf{x}'} \quad \forall \mathbf{x} \in \mathcal{B}.$$

Let an orthonormal coordinate system be given, and let  $\boldsymbol{\nu}$  be given by Definition 5.2.2. Define three vector fields  $\boldsymbol{\nu}_1, \boldsymbol{\nu}_2, \boldsymbol{\nu}_3$  through

$$(\boldsymbol{\nu}_1)_1 = \nu_{11}, \quad (\boldsymbol{\nu}_1)_2 = \nu_{12}, \quad \dots, \quad (5.23)$$

thus the components of each  $\boldsymbol{\nu}_i$  are  $\nu_{i1}, \nu_{i2}, \nu_{i3}$ .

The balance of linear momentum (first of (5.3)) implies that the mean value of  $F_i = F_i(\mathbf{x})$  over  $\mathcal{B}$  is zero, so that we may choose

$$F_i \in L_0^2(\mathcal{B}) \equiv \{ \psi \mid \psi \in L^2(\mathcal{B}), \int_{\mathcal{B}} \psi = 0 \}$$

where  $L^2(\mathcal{B})$  is the space of square-integrable functions defined on  $\mathcal{B}$  with respect to Lebesgue integration. The notation  $[L^2(\mathcal{B})]^3$ , used below, denotes the space of vector functions defined on  $\mathcal{B} \subset \mathbb{R}^3$ .

We rewrite (5.9) as

$$\int_{\mathcal{B}} \psi (\nabla \cdot \boldsymbol{\nu}_i) dV = \int_{\mathcal{B}} \psi F_i dV, \quad \psi \in L^2(\mathcal{B}).$$

Standard results [136, pp. 586–587] give that

$$\boldsymbol{\nu}_i \in H_0(\text{div}, \mathcal{B}) \equiv \{ \mathbf{w} \mid \mathbf{w} \in [L^2(\mathcal{B})]^3, \nabla \cdot \mathbf{w} \in L^2(\mathcal{B}), \mathbf{w} \cdot \mathbf{n} = 0 \text{ on } \partial\mathcal{B} \}. \quad (5.24)$$

In words, a weak solution of the equation

$$\nabla \cdot \boldsymbol{\nu}_i = F_i, \quad \text{with } \boldsymbol{\nu}_i \cdot \mathbf{n} = 0 \text{ on } \partial\mathcal{B}$$

such that

$$\|\boldsymbol{\nu}_i\|_{H(\text{div}, \mathcal{B})}^2 = \|\boldsymbol{\nu}_i\|_{[L^2(\mathcal{B})]^3}^2 + \|\nabla \cdot \boldsymbol{\nu}_i\|_{L^2(\mathcal{B})}^2 < \infty$$

exists. The solution is unique up to a solenoidal function in  $H_0(\text{div}, \mathcal{B})$ . A unique solution may be specified by the energy principle

$$\inf \frac{1}{2} \int_{\mathcal{B}} |\hat{\mathbf{w}}|^2, \quad \text{subject to } \hat{\mathbf{w}} \in H_0(\text{div}, \mathcal{B}) \quad \text{and} \quad \nabla \cdot \hat{\mathbf{w}} = F_i. \quad (5.25)$$

The energy principle, in effect, selects the (weak) solenoidal function of minimum energy—a unique member of  $H_0(\text{div}, \mathcal{B})$ . This minimization problem is solved by introducing a Lagrange multiplier  $\lambda$ . The optimality system for the associated Lagrangian is: Find  $(\mathbf{w}, \lambda) \in H_0(\text{div}, \mathcal{B}) \times L_0^2(\mathcal{B})$  such that

$$\begin{aligned} (\mathbf{w}, \mathbf{s})_0 + (\nabla \cdot \mathbf{s}, \lambda)_0 &= 0 & \forall \mathbf{s} \in H_0(\text{div}, \mathcal{B}) \\ (\nabla \cdot \mathbf{w}, \psi)_0 &= (F_i, \psi)_0 & \forall \psi \in L_0^2(\mathcal{B}), \end{aligned} \quad (5.26)$$

where

$$(\varphi, \psi)_0 \equiv \int \varphi(\mathbf{x})\psi(\mathbf{x})d\mathbf{x}$$

for  $\varphi, \psi \in L^2(\mathcal{B})$ . The first equation of (5.26) gives that

$$(\mathbf{w}, \mathbf{s})_0 = -(\nabla \cdot \mathbf{s}, \lambda)_0 \quad (5.27)$$

so that  $\lambda$  has a weak derivative. Therefore, applying Green's theorem to the first equation of (5.26), results in

$$(\mathbf{w} - \nabla \lambda, \mathbf{s})_0 = 0 \quad \forall \mathbf{s} \in H_0(\text{div}, \mathcal{B}). \quad (5.28)$$

Selecting  $\mathbf{w} = \boldsymbol{\nu}_i$  and

$$\lambda = \sum_{j=1}^3 \int_0^{x_j} \nu_{ij}(\mathbf{r}) d\mathbf{r}$$

implies that  $\boldsymbol{\nu}_i = \nabla \lambda$ . The second equation of (5.26) is satisfied because of (5.9) so leading to the following result.

**Theorem 5.4.1** *If  $\mathbf{f}$  satisfies the conditions of Theorem 5.3.1 and  $\boldsymbol{\nu}$  is given by Definition 5.2.2, then  $\boldsymbol{\nu}_i$  defined by (5.23) satisfies the energy principle (5.25).*

**Remark 5.4.2** *The proof of Theorem 5.4.1 is a standard argument for the dual formulation of the homogeneous Neumann problem*

$$\begin{aligned} \Delta \lambda(\mathbf{x}) &= F_i(\mathbf{x}), \quad \mathbf{x} \in \mathcal{B} \\ \mathbf{n} \cdot \nabla \lambda(\mathbf{x}) &= 0, \quad \mathbf{x} \in \partial \mathcal{B}, \end{aligned}$$

for example, see [136, pp. 586–588] or [21, p. 43].

**Remark 5.4.3** *Theorem 5.4.1 does not employ the hypothesis that  $\mathbf{f}(\cdot, \cdot)$  is a pairwise force function. See Remark 5.2.5.*

The variational interpretation gives the existence and uniqueness of a peridynamic stress tensor  $\boldsymbol{\nu}$  under substantially more general conditions than Theorem 5.3.1. The force function  $\mathbf{f}$  is only required to be an element of  $L_0^2(\mathcal{B})$  so that differentiability of  $\mathbf{f}$  is not assumed. Moreover, in contrast to Theorem 5.3.6, the boundary condition  $\boldsymbol{\nu} \mathbf{n} = 0$  (in a weak sense) holds on  $\partial \mathcal{B}$  regardless of the convexity of  $\mathcal{B}$ .

The variational interpretation allows us to exploit a relationship with the finite element method. The finite element solution of (5.26) requires a pair of suitable elements for the stress and Lagrange multiplier. The well-known elements of Raviart and Thomas [134] result in a stable finite element method for (5.26). The basis functions for the stress only satisfy continuity of the normal components across elements, and for the Lagrange multiplier are discontinuous across elements. The reader is referred to [21, 136] for more information associated with the stable numerical solution of (5.26).

The tensor  $\boldsymbol{\nu}$  and its finite element approximant  $\boldsymbol{\nu}^h$  are not symmetric, as explained after Theorem 5.2.3. This is in contrast to the classical Hellinger-Reissner mixed formulation of the elasticity equations. The Hellinger-Reissner formulation requires that the stress be an element of  $H_0(\text{div}, \mathcal{B}; \mathbb{S})$  and the displacement in  $L^2(\mathcal{B})$ . The former space is the space of square-integrable symmetric tensors. The recent paper [6] describes the first stable finite discretization of the Hellinger-Reissner mixed formulation in three dimensions. We remark that the common engineering practice assumes a local force model, e.g. Cauchy Stress hypothesis, and a constitutive relation connecting stresses to strains resulting in a displacement based finite element method. The resulting nodal basis functions are continuous across elements.

## 5.5 Peridynamic Force Flux

**Definition 5.5.1** *The peridynamic force flux vector at any  $\mathbf{x}$  in the direction of any unit vector  $\mathbf{n}$  is given by*

$$\boldsymbol{\tau}(\mathbf{x}, \mathbf{n}) = \boldsymbol{\nu}(\mathbf{x})\mathbf{n}.$$

Let  $\mathcal{P}$  be a closed, bounded subregion in the interior of  $\mathcal{B}$ , and assume without loss of generality that  $\mathbf{b} \equiv \mathbf{0}$  on  $\mathcal{B}$ . Let  $\mathbf{L}$  be the total force on  $\mathcal{P}$ . Integrating both sides of (5.1) over  $\mathcal{P}$ ,

$$\int_{\mathcal{P}} \rho \ddot{\mathbf{u}}(\mathbf{x}, t) dV_{\mathbf{x}} = \int_{\mathcal{P}} \int_{\mathcal{B}} \mathbf{f}(\mathbf{x}', \mathbf{x}) dV_{\mathbf{x}'} dV_{\mathbf{x}}.$$

Suppose  $\mathbf{f}$  is such that the conditions of Theorem 5.2.3 are satisfied. Newton's second law applied to the total momentum change within  $\mathcal{P}$  therefore implies, using (5.9) and the divergence theorem,

$$\mathbf{L} = \int_{\mathcal{P}} \int_{\mathcal{B}} \mathbf{f}(\mathbf{x}', \mathbf{x}) dV_{\mathbf{x}'} dV_{\mathbf{x}} = \int_{\mathcal{P}} \nabla \cdot \boldsymbol{\nu}(\mathbf{x}) dV_{\mathbf{x}} = \int_{\partial \mathcal{P}} \boldsymbol{\tau}(\mathbf{x}, \mathbf{n}) dA_{\mathbf{x}} \quad (5.29)$$

where  $\mathbf{n}$  is the outward-directed unit normal vector at any point  $\mathbf{x} \in \partial \mathcal{P}$ . Equation (5.29) shows that the total force on  $\mathcal{P}$  is the surface integral of  $\boldsymbol{\tau}$ . This shows that  $\boldsymbol{\tau}(\mathbf{x}, \mathbf{n})$  is, in this sense, the force per unit area exerted on a surface with normal vector  $\mathbf{n}$  at  $\mathbf{x}$  due to peridynamic interactions.

## 5.6 Mechanical Interpretation of the Force Flux

Definitions 5.2.2 and 5.5.1 yield

$$\boldsymbol{\tau}(\mathbf{x}, \mathbf{n}) = \frac{1}{2} \int_{\mathcal{S}} \int_0^\infty \int_0^\infty (y+z)^2 \mathbf{f}(\mathbf{x} + y\mathbf{m}, \mathbf{x} - z\mathbf{m}) \mathbf{m} \cdot \mathbf{n} dz dy d\Omega_{\mathbf{m}}. \quad (5.30)$$

Let  $\mathbf{y} = \mathbf{x} + y\mathbf{m}$  and  $\mathbf{z} = \mathbf{x} - z\mathbf{m}$ . Consider the differential area  $dA_{\mathbf{y}}$  on a sphere centered at  $\mathbf{z}$  containing  $\mathbf{y}$  that subtends a differential solid angle  $d\Omega$  (Figure 1). Thus

$$dA_{\mathbf{y}} = (y+z)^2 d\Omega.$$

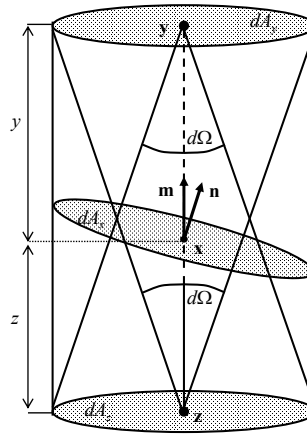


**Figure 5.1.** Interpretation of the force flux at  $\mathbf{x}$  across a plane with unit normal  $\mathbf{n}$ .

The analogous quantity on a sphere centered at  $\mathbf{y}$  containing  $\mathbf{z}$  is identical:

$$dA_{\mathbf{z}} = (y + z)^2 d\Omega.$$

Let  $dA_{\mathbf{x}}$  be the area on a plane with normal vector  $\mathbf{n}$  through  $\mathbf{x}$  that cuts through the cylinder of cross-sectional area  $dA_{\mathbf{y}} = dA_{\mathbf{z}}$  with axis connecting  $\mathbf{y}$  and  $\mathbf{z}$ :

$$dA_{\mathbf{x}} = \frac{(y + z)^2 d\Omega}{\mathbf{m} \cdot \mathbf{n}}$$

where  $\mathbf{m}$  is the unit vector pointing from  $\mathbf{z}$  to  $\mathbf{y}$ . The total force that the volume element  $dA_{\mathbf{y}} dy$  exerts on  $dA_{\mathbf{z}} dz$  is

$$d\mathbf{L} = \mathbf{f}(\mathbf{y}, \mathbf{z}) ((y + z)^2 d\Omega dy) ((y + z)^2 d\Omega dz).$$

Thus, the differential force per unit area on the plane through  $\mathbf{x}$  is

$$\frac{d\mathbf{L}}{dA_{\mathbf{x}}} = \frac{\mathbf{f}(\mathbf{y}, \mathbf{z}) ((y + z)^2 d\Omega)^2 dy dz}{(y + z)^2 d\Omega / \mathbf{m} \cdot \mathbf{n}} = \mathbf{f}(\mathbf{y}, \mathbf{z}) (y + z)^2 (\mathbf{m} \cdot \mathbf{n}) dy dz d\Omega. \quad (5.31)$$

Comparing this with the integrand in (5.30) leads to the physical interpretation of  $\boldsymbol{\tau}$  as the force due to bonds that “go through”  $\mathbf{x}$ , per unit area of a plane with normal  $\mathbf{n}$ . The factor of  $1/2$  appears in (5.30) because the integral sums up both the forces on  $\mathbf{z}$  due to  $\mathbf{y}$  and those on  $\mathbf{y}$  due to  $\mathbf{z}$ , which are of course equal in magnitude.

Our mechanical interpretation of the peridynamics stress is a close descendant of the definition of stress originally introduced in the early days of elasticity. According to Timoshenko [150], *The total stress on an infinitesimal element of a plane taken within a deformed elastic body is defined as the resultant of all the actions of the molecules situated on one side of the plane upon the molecules on the other, the directions of which (actions) intersect the element under consideration.*<sup>1</sup> Replacing *molecule* with peridynamic particle results in a definition that is consistent with our interpretation.

## 5.7 An example

Let  $\mathcal{B}$  be a homogeneous body occupying the half-space  $x_3 \geq 0$ , and let  $\delta > 0$ . Let the pairwise force function be given by

$$\hat{\mathbf{f}}(\boldsymbol{\eta}, \boldsymbol{\xi}) = \frac{\boldsymbol{\xi} + \boldsymbol{\eta}}{|\boldsymbol{\xi} + \boldsymbol{\eta}|^3}, \quad |\boldsymbol{\xi}| \leq \delta \quad (5.32)$$

and (5.4). Physically, this material is mechanically similar to a uniform distribution of gravitational mass, but with a cutoff distance  $\delta$  for interactions. In the reference configuration, *i.e.*,  $\mathbf{u} \equiv \mathbf{0}$ , Definition 5.2.1 and (5.32) yield

$$\mathbf{f}(\mathbf{p}, \mathbf{q}) = \frac{\mathbf{p} - \mathbf{q}}{|\mathbf{p} - \mathbf{q}|^3}, \quad |\mathbf{p} - \mathbf{q}| \leq \delta. \quad (5.33)$$

---

<sup>1</sup>See pages 108–109 of [150]. Timoshenko writes that this definition was due to Saint-Venant and was accepted by Cauchy.



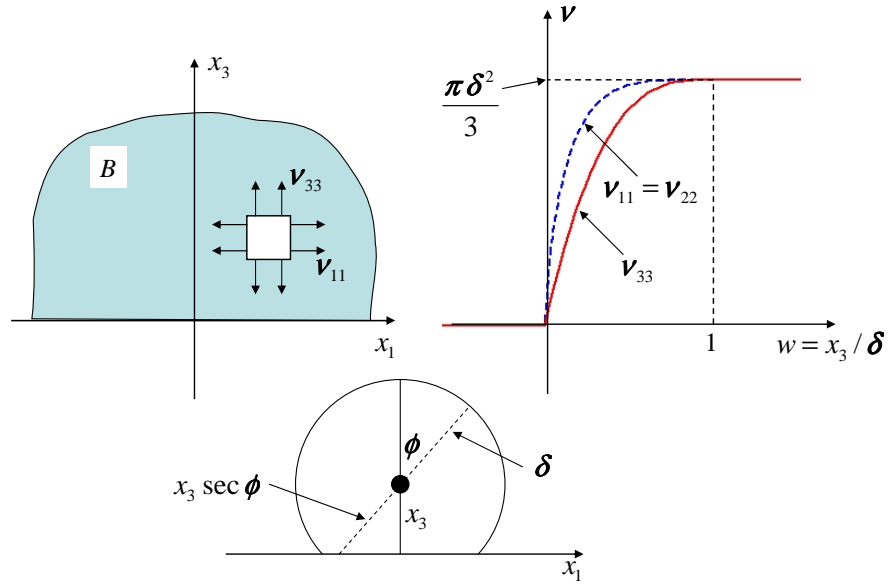


**Figure 5.2.** Peridynamic stress components in a body occupying the upper half-space (Example 1).

At points  $\mathbf{x} \in \mathcal{B}$  sufficiently far the boundary ( $x_3 > \delta$ ), applying (5.33) in Definition 5.2.2 leads to

$$\boldsymbol{\nu}(\mathbf{x}) = \frac{1}{2} \int_{\mathcal{S}} \mathbf{m} \otimes \mathbf{m} \int_0^\delta \int_0^{\delta-y} dz dy d\Omega_{\mathbf{m}}. \quad (5.34)$$

Using the spherical polar angles  $m_1 = \sin \phi \cos \theta$ ,  $m_2 = \sin \phi \sin \theta$ ,  $m_3 = \cos \phi$ , (5.34) may be evaluated as

$$\nu_{ij} = \int_0^{2\pi} \int_0^{\pi/2} m_i m_j \int_0^\delta \int_0^{\delta-y} \sin \phi dz dy d\phi d\theta \quad (5.35)$$

(see Figure 5.2). For points near the boundary ( $0 \leq x_3 < \delta$ ), the limits of integration (5.35) must be altered:

$$\nu_{ij} = \int_0^{2\pi} \int_0^{\pi/2} m_i m_j \int_0^{\min\{\delta, x_3 \sec \phi\}} \int_0^{\delta-y} \sin \phi dz dy d\phi d\theta$$

A straightforward calculation results in the peridynamic stress tensor field components

$$\begin{aligned} \nu_{11} = \nu_{22} &= \frac{\pi \delta^2}{3} \begin{cases} 0 & \text{if } w < 0 \\ \left( -\frac{3w}{2} + 3w^2 - \frac{w^3}{2} - 3w \log w \right) & \text{if } 0 \leq w < 1 \\ 1 & \text{if } 1 \leq w \end{cases} \\ \nu_{33} &= \frac{\pi \delta^2}{3} \begin{cases} 0 & \text{if } w < 0 \\ (1 - (1 - w)^3) & \text{if } 0 \leq w < 1 \\ 1 & \text{if } 1 \leq w \end{cases} \end{aligned} \quad (5.36)$$

$$\nu_{12} = \nu_{21} = \nu_{23} = \nu_{32} = \nu_{31} = \nu_{13} = 0,$$

where  $w = x_3/\delta$ . These components are graphed in Figure 5.2. We also have

$$\nabla \cdot \boldsymbol{\nu} = \begin{pmatrix} 0 \\ 0 \\ \pi(\delta - x_3)^2 \end{pmatrix} \quad 0 \leq x_3 < \delta$$

and zero elsewhere.

Our example illustrates some of the properties of  $\boldsymbol{\nu}$  that have been derived in this paper. These include

1.  $\nabla \cdot \boldsymbol{\nu}$  is continuously differentiable on  $\mathbb{R}^3 - \partial\mathcal{B}$  but not on  $\mathbb{R}^3$  as discussed in Remark 5.3.2,
2.  $\boldsymbol{\nu}\mathbf{n} = \mathbf{0}$  on  $\partial\mathcal{B}$  as shown in Theorem 5.3.6,
3. that  $\mathbf{f}(\mathbf{p}, \mathbf{q})$  need not be bounded as  $|\mathbf{p} - \mathbf{q}| \rightarrow 0$ .

## Chapter 6

# Statistical Coarse-graining of Molecular Dynamics into Peridynamics

**Principle Authors: Richard B. Lehoucq and Stewart A. Silling**

A distinction between molecular dynamics (MD) and classical continuum mechanics (CM) is that the former assumes a nonlocal model of force interaction. This distinction complicates any practical scheme for coarse-graining MD into classical CM, for instance when the finite element method is used for the classical CM discretization. This paper describes a method for representing a collection of atoms at finite temperature as a peridynamic (PD) body. In direct analogy with MD, PD, a continuum theory, uses a nonlocal model of force and avoids the notion of strain germane to classical CM. The PD representation is then homogenized and rescaled to enable a statistical coarse-graining of MD. The coarse-graining avoids the use of a unit cell and the Cauchy-Born rule. In contrast with classical CM, the PD homogenized system of linear springs and masses is shown to have the same dispersion relation as the original spring-mass system. A non-local notion of PD stress is also presented.

### 6.1 Introduction

The recent paper [115] observes that the differential equations of classical linear elasticity break down at length scales up to about 100 angstroms due to the local force assumption. In contrast, the peridynamic (PD) [143] theory of continuum mechanics (CM) is based on *nonlocal* force interactions, and it belongs to the class of microcontinuum theories defined by generalizing the local force assumption to allow force at a distance. However all such theories achieve nonlocality, except for PD, by 1) augmenting the displacement field with supplementary fields (e.g. rotations) to provide information on fine-scale kinematics, 2) using higher order gradients of the displacement field, or 3) averaging the local strains and/or stresses (see [5, 15, 35] for a general discussion and references). In contrast, PD employs an integral operator to *sum* forces and so obviates the need for strain; hence PD is well aligned with MD.

Our coarse graining proceeds in three steps: 1) representation of a collection of interacting atoms at finite temperature as a PD body, 2) homogenization of the PD body, 3) rescaling of the homogenized PD equation of motion to a larger length scale. The coarse-graining avoids the use of a unit cell typical of homogenization approaches [37,62], and any reliance upon the Cauchy-Born rule [57]. For ease of exposition, our coarse graining uses pairwise

force interactions but we remove this restriction at the end of our paper with a PD notion of multibody potentials. We show that the homogenized PD equation of motion for a linear mass-spring model results in the same acoustic and optical phonon dispersion relationships the discrete model. Hence PD reproduces the short-wavelength behavior associated with lattice dynamics, in contrast to classical CM. We also show that a CM notion of stress for the statistical representation of atoms can be defined. The ability to increase the length and time scale in the homogenized and rescaled PD equations provides for multiscale modeling amenable to mathematical analysis by allowing the length scale to vary over the collection of atoms.

MD requires only the current positions of atoms to determine the internal forces on the atoms. In contrast, in CM, the internal forces are not, in general, determined by the current positions of the points alone (an exception to this is a static homogeneous fluid). CM relates internal forces on points in a body to the *deformation* of the body in the macroscopic sense. The current positions must be compared with the positions of the same points in a reference configuration, otherwise concepts such as deformation, stretch, and strain are meaningless. The need to define a reference configuration, which is concept foreign to MD, is one of the fundamental challenges in making the transition to a continuum model for solids.

CM posits a *reference configuration* that may be thought of as the position of the body at  $t = 0$ . The location of a point of the body in the reference configuration is generically called  $\mathbf{x}$ ; any such  $\mathbf{x}$  provides a label for a certain piece of continuous matter. At any time  $t \geq 0$ , the position of the body is given by the map  $\Phi_t$  called the *deformation*, and the deformed image of the body under  $\Phi_t$  is called the *deformed configuration*. The vector  $\Phi_t(\mathbf{x}) - \Phi_0(\mathbf{x}) = \mathbf{u}(\mathbf{x}, t)$  is the *displacement* of  $\mathbf{x}$ .

## 6.2 Peridynamics (PD)

The PD formulation of CM [143] was introduced as a way to model deformation with no assumptions (e.g. continuity, differentiability) on the displacement field, so that discontinuities (e.g. cracks) can be modeled. The PD equation of motion is

$$\rho(\mathbf{x})\ddot{\mathbf{u}} = \int \mathbf{f}(\mathbf{u}' - \mathbf{u}, \mathbf{x}' - \mathbf{x}, \mathbf{x}) dV_{\mathbf{x}'} + \mathbf{b}, \quad (6.1)$$

where  $\mathbf{u} \equiv \mathbf{u}(\mathbf{x}, t)$ ,  $\mathbf{u}' = \mathbf{u}(\mathbf{x}', t)$ ,  $\mathbf{b} \equiv \mathbf{b}(\mathbf{x}, t)$  is a prescribed body force density field,  $\rho$  is mass density in the reference configuration, and  $\mathbf{f}$  is a *pairwise force function* whose value is the force vector (per unit volume squared) that the point  $\mathbf{x}'$  exerts on the point  $\mathbf{x}$ . In (6.1), and throughout this paper, all volume integrals are taken over  $\mathbb{R}^3$ .

All constitutive information about a material is contained in  $\mathbf{f}$ . We assume that there exists a scalar-valued function  $w$  called the *micropotential* such that

$$\mathbf{f}(\boldsymbol{\eta}, \boldsymbol{\xi}, \mathbf{x}) = \nabla_{\boldsymbol{\eta}} w(\boldsymbol{\eta}, \boldsymbol{\xi}, \mathbf{x}), \quad (6.2)$$

where  $\boldsymbol{\xi} = \mathbf{x}' - \mathbf{x}$  and  $\boldsymbol{\eta} = \mathbf{u}' - \mathbf{u}$ , so that  $\boldsymbol{\eta} + \boldsymbol{\xi}$  represents the *current* relative position vector. The concept of a *bond*, denoted by  $\boldsymbol{\xi}$ , that extends over a finite distance is a fundamental

difference between PD and classical CM. The latter is based on the idea of contact forces (interactions between points that are in direct contact with each other).  $\mathbf{f}$  contains a length scale  $\delta$  that represents the cutoff distance (or *horizon*) for interactions (if such a distance is finite).

Balance of linear and angular momenta [143] imply that  $w$  depends only on  $|\boldsymbol{\eta} + \boldsymbol{\xi}|$ ; thus  $w = w_0(|\boldsymbol{\eta} + \boldsymbol{\xi}|, \boldsymbol{\xi}, \mathbf{x})$  for some scalar valued function  $w_0$ . For a PD body at a given time, the strain energy density  $W$  and total strain energy  $U$  are given by

$$W(\mathbf{x}, t) = \frac{1}{2} \int w(\boldsymbol{\eta}, \boldsymbol{\xi}, \mathbf{x}) dV_{\boldsymbol{\xi}}, \quad U(t) = \int W(\mathbf{x}, t) dV_{\mathbf{x}}. \quad (6.3)$$

PD has been implemented in a computational model called EMU [144] that is being applied to a variety of problems across a wide range of length scales, for example [145].

The PD equation of motion (6.1) is an integro-differential equation that can be recast so that it is formally identical to the classical equation of motion. This is accomplished by defining the *PD stress tensor* [107]

$$\boldsymbol{\nu}(\mathbf{x}, t) = \frac{1}{2} \int_{\mathcal{S}} \int_0^\infty \int_0^\infty (y + z)^2 \mathbf{g} \otimes \mathbf{m} dz dy d\Omega_{\mathbf{m}}, \quad (6.4a)$$

$$\mathbf{g} = \mathbf{f}(\mathbf{u}(\mathbf{x} + y\mathbf{m}) - \mathbf{u}(\mathbf{x} - z\mathbf{m}), (y + z)\mathbf{m}, \mathbf{x}) \quad (6.4b)$$

where  $\mathcal{S}$  is the unit sphere,  $d\Omega_{\mathbf{m}}$  is a differential solid angle in the direction of unit vector  $\mathbf{m}$ , and  $\otimes$  indicates the dyadic product of two vectors. The PD stress tensor field is a solution to differential equation

$$\nabla_{\mathbf{x}} \cdot \boldsymbol{\nu}(\mathbf{x}, t) = \int \mathbf{f}(\mathbf{u}' - \mathbf{u}, \mathbf{x}' - \mathbf{x}, \mathbf{x}) dV_{\mathbf{x}'} \quad (6.5)$$

where  $\nabla_{\mathbf{x}} \cdot$  is the divergence operator. The PD stress satisfies  $\boldsymbol{\nu} \cdot \mathbf{n} = 0$  on the convex hull of the body where  $\mathbf{n}$  is the outward unit normal.

Representing the sum of (central) force interactions as the divergence of some stress tensor has an extensive history, see [120]. Irving and Kirkwood [93] derived the stress tensor  $\boldsymbol{\sigma}_V$  due to pairwise force interactions by truncating an infinite series. In a less well known paper, Noll [122] simplified the results of [93] in deriving stress. The PD stress tensor defined above is consistent with these results.

### 6.3 PD Probabilistic Distribution

Consider a set of  $N$  atoms with mass  $m_i$  with positions in a reference configuration  $\{\mathbf{x}_1, \mathbf{x}_2, \dots, \mathbf{x}_N\}$ . Suppose these atoms interact through a pair potential  $v$ . Let  $dV_{\mathbf{x}}$  denote a volume element at a point  $\mathbf{x}$  in the reference configuration. Let  $\mathbf{y} = \boldsymbol{\Phi}_t(\mathbf{x})$ , and at some given  $t \geq 0$ , let  $dV_{\mathbf{y}}$  denote the image of  $dV_{\mathbf{x}}$  under the deformation  $\boldsymbol{\Phi}_t$ . Let  $\Gamma_i(\mathbf{y}, t)$  denote the probability density (per unit volume) of finding atom  $i$  at the point  $\mathbf{y}$  in the deformed configuration

at time  $t$ . We assume there exists a probability density  $\gamma_i$  in the reference configuration, independent of time, such that

$$\Gamma_i(\mathbf{y}, t) dV_{\mathbf{y}} = \gamma_i(\mathbf{x}) dV_{\mathbf{x}}. \quad (6.6)$$

In words, the corresponding probability distribution is conserved: the probability of finding atom  $i$  in  $dV_{\mathbf{y}}$  is independent of time as the volume element deforms under  $\Phi_t$ . (Note that (6.6) is a condition on the mapping  $\Phi_t$ .) The potential energy between volume elements  $dV_{\mathbf{y}}$  and  $dV_{\mathbf{y}'}$  is

$$dU = \sum \sum v(|\mathbf{y}' - \mathbf{y}|) \Gamma_j(\mathbf{y}') \Gamma_i(\mathbf{y}) dV_{\mathbf{y}'} dV_{\mathbf{y}} \quad (6.7)$$

in which the sum  $\sum$  is over the  $N$  atoms. In the (6.7) and the remainder of this paper, double sums do not include  $i = j$ , and for ease of notation denote  $\Gamma_i(\mathbf{y}) = \Gamma_i(\mathbf{y}, t)$ . Define a PD body, in the reference configuration, by

$$\rho(\mathbf{x}) = \sum m_i \gamma_i(\mathbf{x}), \quad (6.8a)$$

$$w(\boldsymbol{\eta}, \boldsymbol{\xi}, \mathbf{x}) = \sum \sum v(|\boldsymbol{\xi} + \boldsymbol{\eta}|) \gamma_j(\mathbf{x} + \boldsymbol{\xi}) \gamma_i(\mathbf{x}), \quad (6.8b)$$

where  $\boldsymbol{\xi} + \boldsymbol{\eta} = \Phi_t(\mathbf{x} + \boldsymbol{\xi}) - \Phi_t(\mathbf{x})$ . As an example, the change of variables  $\mathbf{x}' = \mathbf{x} + \boldsymbol{\xi}$  and  $\mathbf{y}' = \Phi_t(\mathbf{x}')$  gives the  $N$  atom total strain energy (6.3) of (6.8b) as

$$U = \frac{1}{2} \int \int v(|\mathbf{y}' - \mathbf{y}|) \sum \sum \gamma_i(\mathbf{x}') \gamma_j(\mathbf{x}) dV_{\mathbf{x}'} dV_{\mathbf{x}}.$$

Hence, the assumption (6.6) gives the total strain energy as

$$U = \frac{1}{2} \int \int v(|\mathbf{y}' - \mathbf{y}|) \sum \sum \Gamma_i(\mathbf{y}') \Gamma_j(\mathbf{y}) dV_{\mathbf{y}'} dV_{\mathbf{y}}$$

in agreement with (6.7). This result establishes that any deformation of the PD body (6.8) has the correct total strain energy. The special case of atoms with positions  $\mathbf{y}_i(t)$  corresponds to  $\Gamma_i(\mathbf{y}) = \Delta(\mathbf{y} - \mathbf{y}_i(t))$ , where  $\Delta(\cdot)$  is the Dirac delta function. Hence, for an  $N$  atom system,  $U = \frac{1}{2} \sum \sum v(|\mathbf{y}_j - \mathbf{y}_i|)$ . Departures of the  $\gamma_i$  from delta functions encompass probabilistic behavior of atoms at the small scale due to random thermal motions and the inherently chaotic motion of particles in a nonlinear system. It is also possible to identify the  $\gamma_i$  with probabilities arising from quantum mechanical wave functions, *i.e.*,  $\gamma_i = \psi_i^* \psi_i$ .

The purpose of the  $\gamma_i$  is to create a precise connection between the basic kinematical concept in CM, the deformation, and quantities relevant at the small scale. Hence, the PD equation of motion describes the evolution of mass, force and body force densities associated with a probabilistic representation of atoms. The  $\gamma_i$  are not the localization functions considered by Hardy [72] because the  $\gamma_i$ 's are not assumed to be peaked about any location, and they are assumed to satisfy the kinematic constraint (6.6). They are also different from the interpolation functions applied by Kunin [106, pp. 12] to develop of a class of continuous functions with a 1-to-1 correspondence to a discrete lattice.

## 6.4 Homogenization

We have derived a continuum model capable of representing the deformation of a set of atoms whose positions are given by probability distributions. To make this model more useful for traditional CM applications, we *homogenize* the PD fields over space. Let  $\phi$  be a non-negative function on  $\mathbb{R}^3$  such that

$$\phi(\mathbf{q}) = \phi(-\mathbf{q}), \quad \int \phi(\mathbf{q}) dV_{\mathbf{q}} = 1. \quad (6.9)$$

Define a homogenized PD material with micropotential  $w$  by

$$\bar{\rho}(\mathbf{x}) = \int \phi(\mathbf{q}) \rho(\mathbf{x} + \mathbf{q}) dV_{\mathbf{q}} \quad (6.10a)$$

$$\bar{w}(\boldsymbol{\eta}, \boldsymbol{\xi}, \mathbf{x}) = \int \phi(\mathbf{q}) w(\boldsymbol{\eta}, \boldsymbol{\xi}, \mathbf{x} + \mathbf{q}) dV_{\mathbf{q}}. \quad (6.10b)$$

Suppose the body is subjected to a *uniform deformation*, i.e., for some constant tensor  $\mathbf{H}$ ,  $\mathbf{u}(\mathbf{x}, t) = \mathbf{H}\mathbf{x}$  for all  $\mathbf{x}$  and all  $t$ . The total strain energy (6.3) in the homogenized body is

$$\begin{aligned} \bar{U} &= \frac{1}{2} \int \int \int \phi(\mathbf{q}) w(\mathbf{H}\boldsymbol{\xi}, \boldsymbol{\xi}, \mathbf{x} + \mathbf{q}) dV_{\mathbf{q}} dV_{\boldsymbol{\xi}} dV_{\mathbf{x}} \\ &= \frac{1}{2} \int \int w(\mathbf{H}\boldsymbol{\xi}, \boldsymbol{\xi}, \mathbf{z}) dV_{\boldsymbol{\xi}} dV_{\mathbf{z}} = U \end{aligned} \quad (6.11)$$

where the change of variables  $\mathbf{z} = \mathbf{x} + \mathbf{q}$ , and the second of (6.9) were used. This result shows that for any uniform deformation, the total strain energy is invariant under the homogenization.

To illustrate the properties of a homogenized atomic system, we derive acoustic and optical PD phonon dispersion relationships for a 1D linear spring-mass system. For the acoustic relationships, it suffices to consider a 1D lattice with constant spring, mass and spacing  $k$ ,  $m$ , and  $a (= x_{i+1} - x_i)$ . The resulting equation of motion and the strain energy in each spring are given by

$$m\ddot{u}_i = k(u_{i+1} - 2u_i + u_{i-1}), \quad v = \frac{k}{2}(u_{i+1} - u_i)^2. \quad (6.12)$$

Assume continuous and discrete waves  $e^{\iota(\kappa x - \omega t)}$ , where  $\iota = \sqrt{-1}$ ,  $\kappa$  is the wave number, and  $\omega$  is the angular frequency of the wave. Substitution of the discrete wave into (6.12) yields the well-known discrete dispersion relationship

$$\omega_d^2(\kappa) = \frac{2k}{m}(1 - \cos \kappa a). \quad (6.13)$$

Recall that  $\Delta(\cdot)$  is the Dirac delta function, and so the PD density and micropotential are given by

$$\rho(x) = m \sum \Delta(x - x_i), \quad (6.14a)$$

$$w(\eta, \xi, x) = \frac{k}{2} \eta^2 \sum \Delta(x - x_i) \Delta(|\xi| - a), \quad (6.14b)$$

so that homogenizing using (6.10) leads to

$$\bar{\rho}(x) = m \sum \phi(x - x_i), \quad (6.15a)$$

$$\bar{f}(\eta, \xi, x) = k\eta \sum \phi(x - x_i) \Delta(|\xi| - a). \quad (6.15b)$$

Substitution of the continuous wave into the PD equation of motion (6.1) with (6.15) results in

$$m\ddot{u}(x, t) \sum \phi(x - x_i) = k(u(x + a, t) - 2u(x, t) + u(x - a, t)) \sum \phi(x - x_i),$$

where the first of (6.9) has been used. The sums cancel, yielding a continuous dispersion relationship that is identical to (6.13). Hence, we have demonstrated that for this system, the homogenized PD continuum model gives the same dispersion relation as the original lattice.

We now derive the optical phonon dispersion relationships for a one-dimensional diatomic lattice in which the spring constants are all the same, but the masses alternate between  $m_0$  and  $m_1$ . Define separate density and displacement fields  $\rho_\alpha$ ,  $u_\alpha$ ,  $\alpha = 0, 1$ . Let  $x_i^\alpha$  and  $\eta_\alpha = u_{1-\alpha}(x + \xi) - u_\alpha(x)$  denote the positions of the atoms with mass  $m_\alpha$ , and their relative displacement. In an analogous fashion to (6.15), homogenization yields the mass and force densities

$$\bar{\rho}_\alpha = m_\alpha \sum \phi(x - x_i^\alpha), \quad \bar{f}_\alpha = k\eta_\alpha \sum \phi(x - x_i^\alpha) \Delta(|\xi| - a).$$

The assumption  $u_\alpha = A_\alpha e^{i(\kappa x - \omega t)}$ , where  $A_\alpha$  are the amplitudes, results in two coupled homogeneous algebraic equations:

$$m_\alpha A_\alpha \omega^2 = 2k(A_\alpha - A_{1-\alpha} \cos \kappa a), \quad \alpha = 0, 1.$$

This is identical to the secular equation for the original discrete diatomic lattice that leads to the well-known dispersion relations

$$\frac{\omega^2}{k} = \left( \frac{1}{m_0} + \frac{1}{m_1} \right) \pm \sqrt{\left( \frac{1}{m_0} + \frac{1}{m_1} \right)^2 - \frac{4 \sin^2 \kappa a}{m_0 m_1}}.$$

The two roots in this equation correspond to the two branches of the dispersion relation.

Our conclusion is that the PD continuum model with two displacement fields, after homogenization, preserves the dispersion relation of the original system, including both the acoustic and optical branches. In contrast, classical CM results in a linear dispersion curve. (An alternative approach to reproducing the optical branch is to use a single displacement field but include an internal degree of freedom representing the relative displacement within  $m_0$  and  $m_1$  pairs [106].)



## 6.5 Rescaling

The PD equations contain a length scale, or horizon,  $\delta$ , as explained in the discussion following (6.2). Let the micropotentials  $w$ ,  $w'$  correspond to PD materials with horizon  $\delta$ ,  $\delta'$ , respectively, and define the relationship between the two micropotentials as

$$w'(\boldsymbol{\eta}, \boldsymbol{\xi}, \mathbf{x}) = \epsilon^3 w(\epsilon \boldsymbol{\eta}, \epsilon \boldsymbol{\xi}, \mathbf{x}), \quad \epsilon = \frac{\delta}{\delta'} \leq 1. \quad (6.16)$$

Consider a body subjected to a uniform deformation  $\mathbf{H}$ , and let  $\boldsymbol{\xi} = \epsilon \boldsymbol{\xi}'$  so that  $dV_{\boldsymbol{\xi}} = \epsilon^3 dV_{\boldsymbol{\xi}'}$ . Using (6.3) and (6.16), the strain energy density  $W'$  corresponding to  $w'$  is

$$\begin{aligned} W' &= \frac{1}{2} \int w'(\mathbf{H} \boldsymbol{\xi}', \boldsymbol{\xi}', \mathbf{x}) dV_{\boldsymbol{\xi}'} \\ &= \frac{1}{2} \int \epsilon^3 w(\epsilon \mathbf{H} \boldsymbol{\xi}, \epsilon \boldsymbol{\xi}, \mathbf{x}) (\epsilon^{-3} dV_{\boldsymbol{\xi}'}) \\ &= \frac{1}{2} \int_H w(\mathbf{H} \boldsymbol{\xi}, \boldsymbol{\xi}, \mathbf{x}) dV_{\boldsymbol{\xi}} = W. \end{aligned} \quad (6.17)$$

This result shows that under uniform deformation, the strain energy density is invariant under rescaling. Thus, for purposes of macroscopic modeling, the rescaled material model has properties similar to those of the original model. From (6.16), we have that

$$\mathbf{f}' = \nabla_{\boldsymbol{\eta}} w'(\boldsymbol{\eta}, \boldsymbol{\xi}, \mathbf{x}) = \epsilon^4 \nabla_{\boldsymbol{\eta}} w(\epsilon \boldsymbol{\eta}, \epsilon \boldsymbol{\xi}, \mathbf{x}).$$

An immediate conclusion is that rescaled pairwise PD forces are attenuated by  $\epsilon^4 < 1$  when  $\delta' > \delta$ . Moreover, a non-local interaction with respect to the  $\delta$  length scale becomes dramatically insignificant for the larger length scale as the ratio  $\epsilon$  decreases. An important practical implication is that the time step associated with explicit time integration of the rescaled PD equations of motion can be increased, perhaps significantly.

**Peridynamic States.** An extension [146] of the PD model described allows for material models in which the potential due to interactions between an atom at  $\mathbf{y}$  and all other atoms is in general given by  $v(\mathbf{y}_1 - \mathbf{y}, \mathbf{y}_2 - \mathbf{y}, \dots, \mathbf{y}_N - \mathbf{y})$ . In this model, the strain energy density at  $\mathbf{x}$  is expressed as

$$W = \hat{W}(\underline{\mathbf{Y}}), \quad \underline{\mathbf{Y}}\langle \boldsymbol{\xi} \rangle = \Phi_t(\mathbf{x} + \boldsymbol{\xi}) - \Phi_t(\mathbf{x}) \quad (6.18)$$

where  $\underline{\mathbf{Y}}$  is a function called the *deformation state* that maps any bond  $\boldsymbol{\xi}$  into its deformed image. The notation  $\underline{\mathbf{Y}}\langle \boldsymbol{\xi} \rangle$  refers to the value of the function  $\underline{\mathbf{Y}}$  evaluated at the bond vector  $\boldsymbol{\xi}$ . To obtain the bond forces, (6.2) is replaced by

$$\mathbf{f} = \underline{\mathbf{T}}[\mathbf{x}]\langle \boldsymbol{\xi} \rangle - \underline{\mathbf{T}}[\mathbf{x} + \boldsymbol{\xi}]\langle -\boldsymbol{\xi} \rangle, \quad \underline{\mathbf{T}} = \nabla_{\underline{\mathbf{Y}}} W(\underline{\mathbf{Y}})$$

where  $\underline{\mathbf{T}}[\mathbf{x}]$  is the *force state* at  $\mathbf{x}$ , and  $\nabla_{\underline{\mathbf{Y}}} W$  denotes the Frechet derivative of  $W$  with respect to  $\underline{\mathbf{Y}}$ . The essential difference in this generalization is that in (6.18),  $W$  depends not only on the deformation of individual bonds, but on the *collective* deformation of *all* the bonds connected to  $\mathbf{x}$ .

In this generalized, or *state-based*, PD model, the homogenization (6.10b) and rescaling technique (6.16) can be applied if the associated expressions are replaced by

$$\begin{aligned}\bar{W}(\underline{\mathbf{Y}})[\mathbf{x}] &= \int \phi(\mathbf{q}) W(\underline{\mathbf{Y}})[\mathbf{x} + \mathbf{q}] dV_{\mathbf{q}}, \\ W'(\underline{\mathbf{Y}}') &= \epsilon^3 W(\underline{\mathbf{Y}}), \quad \epsilon \underline{\mathbf{Y}}' \langle \underline{\boldsymbol{\xi}}' \rangle = \underline{\mathbf{Y}} \langle \epsilon \underline{\boldsymbol{\xi}} \rangle.\end{aligned}$$

The first equation says that for any deformation state  $\underline{\mathbf{Y}}$ ,  $\bar{W}$  is the volume average of  $W$  weighted by  $\phi$  holding  $\underline{\mathbf{Y}}$  constant. The definition of the PD stress tensor (6.5) still applies, provided (6.4b) is replaced by

$$\mathbf{g} = 2\underline{\mathbf{T}}[\mathbf{x} - z\mathbf{m}] \langle (y + z)\mathbf{m} \rangle.$$

Therefore, (6.5) defines a rigorous stress that can be associated to a multibody potential.

## Chapter 7

# An Atomistic-to-Continuum Coupling Method for Heat Transfer in Solids

**Principle Authors:** Gregory J. Wagner, Reese E. Jones, Jeremy A. Templeton, and Michael L. Parks

In this work, we present a seamless, energy-conserving method to thermally couple atomistic and continuum representations of material. This technique allows a molecular dynamics simulation to be used in localized regions of the computational domain, surrounded and overlaid by a continuum finite element representation. Thermal energy can pass between the two regions in either direction, making larger simulations of nanoscale thermal processes possible. We discuss theoretical developments and numerical implementation details. In addition, we present and analyze a set of representative simulations.

### 7.1 Introduction

As technological advances allow the engineering of devices at ever decreasing length scales, and as ever increasing fidelity is demanded in the computational simulation of these devices, it has become clear that traditional material models based on continuum descriptions of solids can be inadequate at the micro- and nano-scales. Surface effects, grain boundaries, defects, and other deviations from a perfect continuum can have a large effect on material behavior at these scales, and simulation techniques based on descriptions at the atom scale, such as molecular dynamics (MD), have become an important part of the computational toolbox. However, molecular dynamics simulations on even the largest supercomputers are currently limited to systems on the order of a billion atoms [2], large enough for the study of some nano-scale phenomena but still far too small to resolve the micro-to-macroscale interactions that must be captured in the simulation of any real device. The recognition of this limitation on MD has led to the development of several methods for the coupling of atomistic and continuum material descriptions in a single simulation; see [46, 127] for reviews of these methods. The goal of these methods is to allow the use of a continuum-based technique such as finite elements (FE) in parts of the domain where such a description is valid, while using MD near defects or in other regions in which the continuum description breaks down.

To date, most of these atomistic-to-continuum coupling methods have been based on the coupling of the momentum equation (or in the case of quasi-static problems, the equilibrium equation) in the continuum to the equations of motion for the atoms, usually by

combining the Hamiltonians of the two systems [1] or by ensuring that internal forces are properly balanced [101]. Most often, these methods assume that the temperature of the continuum region is in effect zero, and quite a bit of attention has been paid to reducing unwanted internal reflections of waves in the MD lattice at the MD-continuum interface. However, a much more typical scenario for real devices is a temperature that is far above absolute zero. In this case, it is more accurate to recognize lattice waves as energy-carrying phonons, and to think of the surrounding continuum as a thermal bath that maintains the correct balance of incoming and outgoing phonons at the interface at the local temperature.

Some attempts have been made previously to accurately account for the effects of non-zero temperature. Dupuy *et al.* [57] have developed a finite-temperature version of the Quasi-continuum Method that uses a local-harmonic approximation, at a constant temperature, to account for thermal fluctuations of atoms. Rudd and Broughton [137] have developed the coarse-grained molecular dynamics (CGMD) technique for simulations of anharmonic solids at finite temperatures. The bridging scale decomposition method of Wagner and Liu [153] has been extended to finite temperatures by Park *et al.* [126]. However, to our knowledge, no technique exists to couple the thermal fluctuations in the MD region with an energy equation in the continuum to effect true two-way temperature coupling between the MD and continuum regions. In this work, we present a technique for such a coupling, allowing the simulation of nonequilibrium heat transfer between MD and continuum regions of a domain.

Two-way temperature coupling implies that thermal information can pass out of the MD region into the continuum, and that the temperature of the continuum affects the thermal fluctuations of the MD region. The first direction of information flow, from MD to continuum, is important in applications in which phenomena at the atom scale lead to what would be measured in the laboratory as changes in macroscale temperature. Examples of such phenomena include friction [121], laser heating [94], fracture [68], and plastic failure [76], all of which have been studied using MD or even coupled MD-continuum simulations but without a complete treatment of macroscale temperature interactions. By coupling a continuum energy equation to the atom dynamics, we can simulate temperature changes in the continuum, possibly over large distances, that are caused by these atom-scale phenomena.

At the same time, in a coupled simulation any temperature field that is imposed on the continuum should have an effect on the thermal fluctuations of atoms in the MD region. For example, a macroscale temperature gradient on the continuum should lead to a heat flux through an MD region embedded within it. It is important to capture this behavior correctly in a simulation method, because it is known that structures at the atomic scale such as inclusions or grain boundaries can have a large effect on the thermal conductivity of the material [114]. The ability to do two-way temperature coupling allows the nanostructure of the MD region to have the proper effect on the continuum temperature field.

Several previous authors have coupled MD simulations to a continuum energy equation. Ivanov *et al.* [94] have used a two-temperature model to incorporate the effects of the electron temperature on the dynamics of the atomic nuclei in simulations of laser heating of metal films. Schall *et al.* [139] employed a thermostat acting on the atoms in an MD simulation to enforce the correct thermal conductivity in simulations of metals; this

conductivity is otherwise underpredicted by classical MD. Padgett and Brenner [124] used a similar technique to capture the effects of Joule heating in metal nanowires. The principal innovation of the current work is the ability to couple an MD simulation to the temperature field of a continuum that overlaps and surrounds it, such that the two-way coupling of energy between two different domains is effected.

In this work we will use finite elements to solve the heat equation in the continuum. We begin in Section 7.2 by defining the basic problem to be solved and stating the assumptions used. In Sections 7.3 and 7.4, respectively, we derive the forms of the energy equations to be solved in the MD and FE domains; the coupling between the domains follows naturally from our derivation. Time filtering is introduced in Section 7.5 to reduce fluctuations in the temperature field, and in Section 7.6 we present some of the details of the numerical implementation of the method. Example problems are presented in Section 7.7, and we conclude with a discussion in Section 7.8.

## 7.2 Problem Definition

Consider the problem geometry shown in Figure 7.1. A domain  $\Omega$  is discretized with a finite element mesh; the outer boundary of the domain is denoted  $\Gamma$  with outward normal vector  $\mathbf{n}$ . At the same time, an internal portion of the domain  $\Omega_{md}$  is filled by a set of atoms  $\mathcal{A}$ . The remaining portion of the domain in which there are no atoms but only finite elements is denoted  $\Omega_{fem}$ , so that  $\Omega_{md} \cup \Omega_{fem} = \Omega$  and  $\Omega_{md} \cap \Omega_{fem} = \emptyset$ . The boundary between the two subdomains is given by  $\Gamma_{md}$ , with normal vector  $\mathbf{n}_{md}$  oriented into the MD region. Note that the entire domain, including  $\Omega_{md}$ , is discretized with finite elements, so that the atomistic and finite element descriptions co-exist in  $\Omega_{md}$ . In the following, the vector  $\mathbf{X}$  represents the reference coordinates of a given point in  $\Omega$ .

We are concerned with heat transfer problems in which we can assume that the Fourier heat law holds in  $\Omega_{fem}$ , where we will rely on a Galerkin finite element solution. The temperature field  $T(\mathbf{X}, t)$  evolves according to:

$$\rho c_p \dot{T}(\mathbf{X}, t) = \nabla \cdot \kappa \nabla T(\mathbf{X}, t) \quad \text{in } \Omega_{fem} \quad (7.1)$$

where  $\rho$ ,  $c_p$  and  $\kappa$  are the density, specific heat, and thermal conductivity of the material (which we assume to be isotropic). Boundary conditions are specified on  $\Gamma$ , and for generality we assume that  $\Gamma$  can be partitioned into a boundary  $\Gamma_T$  on which temperature is prescribed, and a boundary  $\Gamma_q$  on which heat flux is prescribed:

$$T(\mathbf{X}, t) = \bar{T}(\mathbf{X}, t) \quad \text{on } \Gamma_T \quad (7.2a)$$

$$-\mathbf{n} \cdot \kappa \nabla T(\mathbf{X}, t) = \bar{q}_n(\mathbf{X}, t) \quad \text{on } \Gamma_q \quad (7.2b)$$

Initial conditions will be discussed in a later section, because they must be defined and applied after we have completely described our coupled system.

In  $\Omega_{md}$ , we assume that the heat flow and the corresponding dynamics are too complex, in general, to be described by the Fourier heat law. This region will be treated using classical molecular dynamics, with atomic forces derived from an interatomic potential. Note

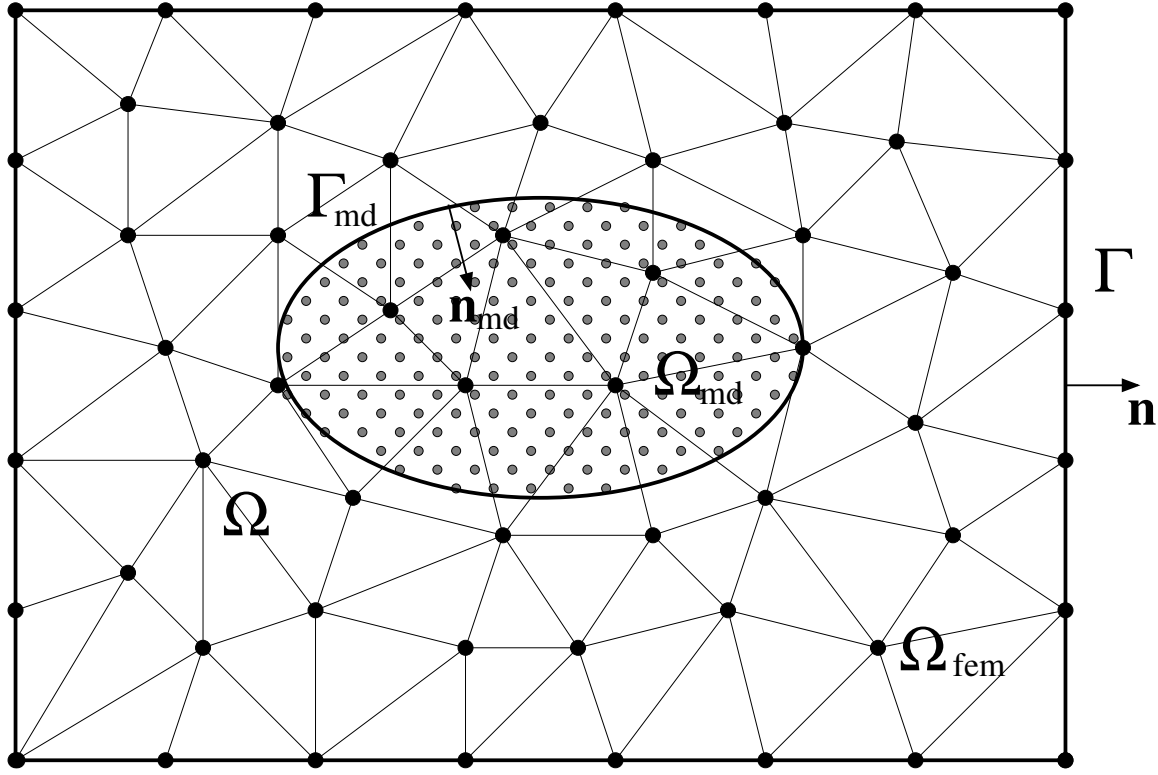


**Figure 7.1.** Coupled domain geometry

that we are considering only phonon heat transport in this region, and that our molecular dynamics cannot represent the electron-mediated heat transfer that dominates in a metal.

For a given atom  $\alpha$ , the equations of motion are given in terms of the atomic position  $\mathbf{x}_\alpha$  and velocity  $\mathbf{v}_\alpha$ :

$$\dot{\mathbf{x}}_\alpha = \mathbf{v}_\alpha \quad (7.3a)$$

$$m_\alpha \dot{\mathbf{v}}_\alpha = \mathbf{f}_\alpha^{md} \equiv -\frac{\partial U^{md}}{\partial \mathbf{x}_\alpha}(\mathbf{x}_\alpha, \mathbf{x}_\beta, \dots) \quad (7.3b)$$

where  $m_\alpha$  is the mass of atom  $\alpha$ , and  $U^{md}(\mathbf{x}_\alpha, \mathbf{x}_\beta, \dots)$  is the interatomic potential energy, which is a function of the positions of all atoms. In Section 7.3, we will discuss implementation details for these molecular dynamics equations and show how they must be augmented to account for heat transfer from the surrounding continuum region.

In our analysis we will make use of integrals over the domain  $\Omega$ , which require special treatment in  $\Omega_{md}$ . We define  $g(\mathbf{X})$  to be an integrable function over  $\Omega$  that takes on values at the atom positions  $\mathbf{X}_\alpha$ . Hence

$$\int_{\Omega} g(\mathbf{X}) dV = \int_{\Omega_{md}} g(\mathbf{X}) dV + \int_{\Omega_{fem}} g(\mathbf{X}) dV \quad (7.4)$$

The particular choice made for the evaluation of  $g(\cdot)$  over  $\Omega_{md}$  lies at the heart of the coupling method because through this means atomistic information is upscaled to the continuum. We define

$$\int_{\Omega_{md}} g(\mathbf{X}) dV \equiv \sum_{\alpha \in \mathcal{A}} g_{\alpha} \Delta V_{\alpha} \quad (7.5)$$

where  $\Delta V_{\alpha}$  is the volume associated with atom  $\alpha$ . In the case where  $g(\mathbf{X})$  corresponds to a continuous function or field,  $g_{\alpha} = g(\mathbf{X}_{\alpha})$  and Eqn. (7.5) is a convenient quadrature; but, where  $g_{\alpha}$  is a quantity, such as atomic velocity, defined only at atoms, Eqn. (7.5) is a means of homogenization.

## 7.3 The Atomistic Temperature Field

### 7.3.1 Nodes-to-atoms reduction operation

For a system of atoms at equilibrium, the system temperature  $T$  can be written [155]:

$$\frac{3}{2} n_a k_B T = \left\langle \sum_{\alpha \in \mathcal{A}} \frac{1}{2} m_{\alpha} |\mathbf{v}_{\alpha}|^2 \right\rangle \quad (7.6)$$

where  $k_B$  is Boltzmann's constant and the angle brackets represent an ensemble or time average. Our primary interest in this work is in non-equilibrium systems, so that (7.6) does not necessarily apply; however, given this expression it is convenient to define a field  $T_{\alpha}$  at the atoms which, when averaged, gives the correct temperature if the system is at equilibrium (and with zero mean velocity):

$$T_{\alpha} \equiv \frac{1}{3k_B} m_{\alpha} |\mathbf{v}_{\alpha}|^2 \quad (7.7)$$

It should be noted that there are lower limits to the applicability of Eqn. (7.6) in terms of number of atoms and the time interval to average over and that other definitions of a local, nonequilibrium temperature exist, see, e.g., [10, 18, 20, 30]. However, the existence of an optimum non-equilibrium temperature measure is still a matter of debate and research, see [31].

The development of a coupled atomistic-to-continuum method requires a relationship between this atomistic temperature field and a continuum field defined on the finite element nodes. We begin by defining an interpolated temperature field  $T^h(\mathbf{X}, t)$ :

$$T^h(\mathbf{X}, t) \equiv \sum_{I \in \mathcal{N}} N_I(\mathbf{X}) \theta_I(t) \quad (7.8)$$

In this expression,  $\mathcal{N}$  is the set of all nodes in the domain,  $\theta_I$  is a temperature degree of freedom defined on node  $I$ , and  $N_I(\mathbf{X})$  is the interpolant associated with node  $I$  evaluated at  $\mathbf{X}$ . Note that because  $\mathbf{X}$  represents the time-independent reference coordinate of a point, all of the time dependence of  $T^h$  is through the degrees of freedom  $\theta_I$ . We will use linear

finite element shape functions as our interpolants in this paper, but many other choices are possible. The superscript on  $T^h$  reflects the fact that the interpolation can be parameterized in terms of some characteristic mesh size  $h$ .

Suppose that we are given a set of atomic temperatures defined as in Eqn. (7.7), along with a set of nodal temperatures  $\theta_I$ . To relate the two temperature definitions to each other, we can minimize the squared difference between  $T^h(\mathbf{X})$  and some temperature field  $T(\mathbf{X})$ . That is, we minimize

$$\int_{\Omega} (T(\mathbf{X}) - T^h(\mathbf{X}))^2 dV \quad (7.9)$$

where integration over the molecular dynamics region of the domain is computed as in (7.5). Taking the variation with respect to  $T_h$  and setting it to zero gives:

$$\int_{\Omega} \delta T^h T^h dV = \int_{\Omega} \delta T^h T dV \quad (7.10)$$

Now assume that  $T$  is a field equal to  $T^h$  in  $\Omega_{fem}$  and  $T_{\alpha}$  at the atom positions in  $\Omega_{md}$ . Explicit use of (7.5) then gives:

$$\int_{\Omega} \delta T^h T^h dV = \sum_{\alpha \in \mathcal{A}} \delta T^h(\mathbf{X}_{\alpha}) T_{\alpha} \Delta V_{\alpha} + \int_{\Omega_{fem}} \delta T^h T^h dV \quad (7.11)$$

The integral over  $\Omega_{fem}$  can be subtracted from both sides. Given Eqn. (7.8) and that the variation  $\delta T^h$  is arbitrary, we can derive an equation true for all  $I$ :

$$\sum_{J \in \mathcal{M}} \left( \sum_{\alpha \in \mathcal{A}} N_{I\alpha} N_{J\alpha} \Delta V_{\alpha} \right) \theta_J = \sum_{\alpha \in \mathcal{A}} N_{I\alpha} \Delta V_{\alpha} T_{\alpha} \quad (7.12)$$

$$N_{I\alpha} \equiv N_I(\mathbf{X}_{\alpha})$$

Here,  $\mathcal{M}$  is the set of all nodes  $J$  for which  $N_J(\mathbf{X}_{\alpha}) \neq 0$  for some atom  $\alpha$ ; i.e. the set of nodes whose shape function supports intersect  $\Omega_{md}$ .

Eqn. (7.12) gives a matrix equation for the nodal temperatures  $\theta_J$ ,  $J \in \mathcal{M}$ . In fact, this is a projection of the atom temperature field into the space of finite element shape functions; we note the similarity between this expression and the projection operation defined in [153] for atom displacements and velocities. In our current work, we find it is unnecessary to compute this projection as defined here; instead, we approximate it using a row-sum lumping of the matrix on the left hand side, leading to:

$$\theta_I = \sum_{\alpha \in \mathcal{A}} \hat{N}_{I\alpha} T_{\alpha} \quad (7.13)$$

$$\hat{N}_{I\alpha} \equiv \frac{N_{I\alpha} \Delta V_{\alpha}}{\sum_{\beta \in \mathcal{A}} N_{I\beta} \Delta V_{\beta}}$$

Specifically, row-sum lumping is a common procedure for approximating a matrix with a diagonal matrix that consists of replacing each row of the matrix with its sum at the diagonal entry, see, e.g., [158, Appendix 8]. Eqn. (7.13) defines an atoms-to-nodes reduction operation rather than a true projection operation, where the coefficients  $\hat{N}_{I\alpha}$  are scaled finite element shape functions.



### 7.3.2 Augmented molecular dynamics force

In order to include the effects of the continuum region on the temperature in  $\Omega_{MD}$ , we augment the force on each atom by a term that is proportional to the velocity of that atom. This form of control is shared by many popular MD thermostat techniques, including the Nose-Hoover [75] and Berendsen [17] thermostats. A similar approach to controlling the energy of an MD simulation has been used by other authors to apply a known heat flux to atoms [92] and to account for coupling between electron and phonon energies in metals [94].

A drag force  $\mathbf{f}_\alpha^\lambda$  is defined and added to the standard molecular dynamics force (cf. Eqn. 7.3b):

$$m_\alpha \dot{\mathbf{v}}_\alpha = \mathbf{f}_\alpha^{md} + \mathbf{f}^\lambda \quad (7.14)$$

where

$$\mathbf{f}^\lambda = -\frac{m_\alpha}{2} \lambda_\alpha \mathbf{v}_\alpha. \quad (7.15)$$

The coefficient  $m_\alpha/2$  is an arbitrary multiplier that will simplify later results. The parameter  $\lambda_\alpha$  may be different for every atom. Since this parameter is used to model interaction with the continuum, a natural choice is to let this function be interpolated from a set of nodal values  $\lambda_I$  defined on the set of nodes  $\mathcal{M}$ :

$$\lambda_\alpha(t) = \sum_{I \in \mathcal{M}} N_{I\alpha} \lambda_I(t) \quad (7.16)$$

The coefficients  $\lambda_I$  can be chosen to enforce conservation of total energy, as derived in the next section.

### 7.3.3 Total energy conservation

The total energy of the combined MD-continuum system can be decomposed between the two regions:

$$E^{tot} = E^{md} + E^{fem} \quad (7.17)$$

The energy of the molecular dynamics region is the sum of the potential and kinetic energies of the atoms:

$$E^{md} = U^{md} + \frac{1}{2} \sum_{\alpha} m_\alpha |\mathbf{v}_\alpha|^2 \quad (7.18)$$

while the energy of the finite element region is given by the thermal energy  $\rho c_p T^h$  integrated over  $\Omega_{fem}$ :

$$E^{fem} = \int_{\Omega_{fem}} \rho c_p T^h(\mathbf{X}, t) dV. \quad (7.19)$$

We will choose the nodal values  $\lambda_I$  such that total energy is conserved throughout the simulation, i.e.  $\dot{E}^{tot} = 0$  if no energy is added to the system at the external boundary. The

rate of change of the MD energy is

$$\begin{aligned}
 \dot{E}^{md} &= \dot{U}^{md} + \sum_{\alpha \in \mathcal{A}} m_{\alpha} (\mathbf{v}_{\alpha} \cdot \dot{\mathbf{v}}_{\alpha}) \\
 &= \sum_{\alpha \in \mathcal{A}} \frac{\partial U^{md}}{\partial \mathbf{x}_{\alpha}} \cdot \dot{\mathbf{x}}_{\alpha} + \sum_{\alpha \in \mathcal{A}} \mathbf{v}_{\alpha} \cdot (\mathbf{f}_{\alpha}^{md} + \mathbf{f}_{\alpha}^{\lambda}) \\
 &= \sum_{\alpha \in \mathcal{A}} \mathbf{v}_{\alpha} \cdot \mathbf{f}_{\alpha}^{\lambda}
 \end{aligned} \tag{7.20a}$$

where we have used Eqns. (7.3b) for the definition of  $\mathbf{f}_{\alpha}^{md}$  and (7.14) for the substitution of  $\dot{\mathbf{v}}_{\alpha}$ .

To compute the rate of change on the finite element system, we use Eqn. (7.1) with the boundary condition  $\bar{q}_n = 0$  on  $\Gamma_q = \Gamma$ . Then:

$$\begin{aligned}
 \dot{E}^{fem} &= \int_{\Omega_{fem}} \rho c_p \dot{T}^h dV \\
 &= \int_{\Omega_{fem}} \nabla \cdot \kappa \nabla T^h dV \\
 &= \int_{\Gamma_{md}} \mathbf{n}_{md} \cdot \kappa \nabla T^h dA
 \end{aligned} \tag{7.21a}$$

The total energy balance is then:

$$\sum_{\alpha \in \mathcal{A}} \mathbf{v}_{\alpha} \cdot \mathbf{f}_{\alpha}^{\lambda} = - \int_{\Gamma_{md}} \mathbf{n}_{md} \cdot \kappa \nabla T^h dA \tag{7.22}$$

Physically, this energy balance suggests that the total work done on the MD system by the additional force  $\mathbf{f}_{\alpha}^{\lambda}$  is equal to the total energy flux out of the FE and into the MD region.

We will choose the nodal values  $\lambda_I$  to satisfy (7.22); however, the solution to this single scalar equation for the  $n_{\mathcal{M}}$  nodes in  $\mathcal{M}$  is clearly non-unique. In order to solve for a set of nodal values, we will “localize” the energy balance by multiplying the summand and integrand by the nodal shape function  $N_I(\mathbf{X})$ :

$$\sum_{\alpha \in \mathcal{A}} N_{I\alpha} \mathbf{v}_{\alpha} \cdot \mathbf{f}_{\alpha}^{\lambda} = - \int_{\Gamma_{md}} N_I \mathbf{n}_{md} \cdot \kappa \nabla T^h dA \tag{7.23}$$

Note that a solution to (7.23) also satisfies (7.22) because of the partition of unity property of the finite element shape functions ( $\sum_I N_I(\mathbf{X}) = 1$ ), as can be seen by summing (7.23) over  $I$ . Although this choice for the localized energy balance is not unique, it will be shown that this form leads to simplifications in the derivation of finite element heat equation.

Substituting Eqns. (7.15) and (7.16) into (7.23), and making use of the definition of atomic temperature (7.7), gives, after some rearrangement:

$$\sum_{J \in \mathcal{M}} \left( \sum_{\alpha \in \mathcal{A}} N_{I\alpha} T_{\alpha} N_{J\alpha} \right) \lambda_J = \frac{2}{3k_B} \int_{\Gamma_{md}} N_I \mathbf{n}_{md} \cdot \kappa \nabla T^h dA \tag{7.24}$$

This system of  $n_{\mathcal{M}}$  equations can be solved for  $\lambda_I$ . The numerical computation of the surface integral on the right-hand side of (7.24) will be discussed in Section 7.6.2.

## 7.4 The Finite Element Heat Equations

In the previous section we related the kinetic energies of the atoms in the MD region to nodal temperatures  $\theta_I$ . However, in our two-way coupled system the nodal temperatures are also affected by the thermodynamics of the continuum FE region, and we must derive a heat equation valid over the entire domain. We begin with Eqn (7.11), from which the reduction operation was derived. Taking the time derivative (note that  $\delta T^h$  is not a function of time) and using the Fourier heat equation (7.1) in  $\Omega_{fem}$  gives

$$\int_{\Omega} \delta T^h \dot{T}^h dV = \sum_{\alpha \in \mathcal{A}} \delta T^h(\mathbf{X}_{\alpha}) \dot{T}_{\alpha} \Delta V_{\alpha} + \int_{\Omega_{fem}} \delta T^h \nabla \cdot \frac{\kappa}{\rho c_p} \nabla T^h dV \quad (7.25)$$

This leads to a matrix equation for the nodal temperatures:

$$\begin{aligned} \sum_{J \in \mathcal{N}} \left( \int_{\Omega} N_I N_J dV \right) \dot{\theta}_J &= \frac{2}{3k_B} \sum_{\alpha \in \mathcal{A}} N_{I\alpha} \Delta V_{\alpha} \mathbf{v}_{\alpha} \cdot (\mathbf{f}_{\alpha}^{md} + \mathbf{f}_{\alpha}^{\lambda}) - \sum_{J \in \mathcal{N}} \left( \int_{\Omega_{fem}} \nabla N_I \cdot \frac{\kappa}{\rho c_p} \nabla N_J dV \right) \theta_J \\ &\quad - \int_{\Gamma_q} N_I \frac{\bar{q}_n}{\rho c_p} dA + \sum_{J \in \mathcal{N}} \left( \int_{\Gamma_{md}} N_I \mathbf{n}_{md} \cdot \frac{\kappa}{\rho c_p} \nabla N_J dA \right) \theta_J \end{aligned} \quad (7.26)$$

In deriving this equation, we have made use of the atom temperature definition (7.7); the modified atomic equation of motion (7.14); the flux boundary condition (7.2b); the fact that the variation  $\delta T^h$  is zero on  $\Gamma_T$ ; the finite element interpolation for  $T^h$  and  $\delta T^h$  (7.8); and the arbitrariness of the nodal variations  $\delta \theta_I$  (except on  $\Gamma_T$ ).

A further simplification is possible if we make two assumptions: (1) that the atomic volume  $\Delta V_{\alpha}$  is uniform over all atoms, and (2) that the specific heat capacity of the system takes the value given by the Dulong-Petit law for a classical solid [155]:

$$c_p = \frac{3k_B}{\rho \Delta V_{\alpha}} \quad (7.27)$$

This expression is a consequence of the equipartition theorem for a harmonic solid. Using the localized energy balance from Eqn. (7.23), the boundary integral over  $\Gamma_{md}$  can be related to the drag force on the atoms:

$$\sum_{J \in \mathcal{N}} \left( \int_{\Gamma_{md}} N_I \mathbf{n}_{md} \cdot \frac{\kappa}{\rho c_p} \nabla N_J dA \right) \theta_J = -\frac{1}{3k_B} \sum_{\alpha \in \mathcal{A}} N_{I\alpha} \Delta V_{\alpha} \mathbf{v}_{\alpha} \cdot \mathbf{f}_{\alpha}^{\lambda} \quad (7.28)$$

Using this result in Eqn. (7.26) gives:

$$\begin{aligned}
 \sum_{J \in \mathcal{N}} \left( \int_{\Omega} N_I N_J dV \right) \dot{\theta}_J &= \frac{2}{3k_B} \sum_{\alpha \in \mathcal{A}} N_{I\alpha} \Delta V_{\alpha} \mathbf{v}_{\alpha} \cdot \left( \mathbf{f}_{\alpha}^{md} + \frac{1}{2} \mathbf{f}_{\alpha}^{\lambda} \right) \\
 &\quad - \sum_{J \in \mathcal{N}} \left( \int_{\Omega_{fem}} \nabla N_I \cdot \frac{\kappa}{\rho c_p} \nabla N_J dV \right) \theta_J - \int_{\Gamma_q} N_I \frac{\bar{q}_n}{\rho c_p} dA \quad (7.29)
 \end{aligned}$$

It may seem surprising that the boundary integral over  $\Gamma_{md}$  does not completely cancel the  $\mathbf{f}_{\alpha}^{\lambda}$  term on the atoms. Since the boundary integral represents heat flow into the FE-only region while the  $\mathbf{f}_{\alpha}^{\lambda}$  term represents the work done on the MD system, it might be expected that these quantities are equal and opposite. The reason for the discrepancy is that in the combined system heat equation (7.29), the temperature represents the total internal energy (kinetic plus potential) of the continuum, but only the kinetic energy of the MD system. The Dulong-Petit law (7.27) assumes equipartition between kinetic and potential energy modes, so that only half of the energy leaving the FE-only region goes into the kinetic energy of the MD system.

Because the boundary  $\Gamma_{md}$  may cut through the interiors of elements, the integral over  $\Omega_{fem}$  in (7.29) is difficult to compute numerically in the form given if standard Gaussian integration over the elements is to be used. To allow the computation of this integral, we can use expression (7.5) to get

$$\begin{aligned}
 \int_{\Omega_{fem}} \nabla N_I \cdot \frac{\kappa}{\rho c_p} \nabla N_J dV &= \int_{\Omega} \nabla N_I \cdot \frac{\kappa}{\rho c_p} \nabla N_J dV - \sum_{\alpha \in \mathcal{A}} \left( \nabla N_I \cdot \frac{\kappa}{\rho c_p} \nabla N_J \right) \Big|_{\alpha} \Delta V_{\alpha} \quad (7.30)
 \end{aligned}$$

The integral over  $\Omega$  can be computed numerically over the elements using standard Gaussian quadrature. In effect, we use the atoms as a set of quadrature points on which to evaluate the integral on  $\Omega_{md}$ . Note that this is not the same as assuming that the Fourier law is valid in this region; we are simply evaluating the integrand at the atom positions.

With this approximation the final form of the differential equation for the nodal temperatures is

$$\begin{aligned}
 \sum_{J \in \mathcal{N}} \left( \int_{\Omega} N_I N_J dV \right) \dot{\theta}_J &= \sum_{\alpha \in \mathcal{A}} \left( \frac{2}{3k_B} N_{I\alpha} \mathbf{v}_{\alpha} \cdot \left( \mathbf{f}_{\alpha}^{md} + \frac{1}{2} \mathbf{f}_{\alpha}^{\lambda} \right) + \sum_{J \in \mathcal{N}} \left( \nabla N_I \cdot \frac{\kappa}{\rho c_p} \nabla N_J \right) \Big|_{\alpha} \theta_J \right) \Delta V_{\alpha} \\
 &\quad - \sum_{J \in \mathcal{N}} \left( \int_{\Omega} \nabla N_I \cdot \frac{\kappa}{\rho c_p} \nabla N_J dV \right) \theta_J - \int_{\Gamma_q} N_I \frac{\bar{q}_n}{\rho c_p} dA \quad (7.31)
 \end{aligned}$$

Eqn. (7.31) together with the modified momentum equation for the atoms (7.14) and expressions for the drag force (7.15) and nodal drag coefficients  $\lambda_I$  (7.24) define our coupled solution scheme. The atom motions affect the finite element solution through the first term on the right-hand side in (7.31); the finite element solution feeds back into the atomic system through the drag force. Thermal information can therefore flow in both directions.

## 7.5 Time-Filtered Coupling

Simulations using (7.14) and (7.31) as written lead to time fluctuations in the nodal temperature field in  $\Omega_{md}$ . Because they are incompatible with the usual behavior of a continuum that obeys the Fourier heat law, these fluctuations are undesirable if we are trying to couple to a smoothly varying temperature field in the surrounding continuum, or if we want to compare to experimentally measured temperatures. Fluctuations can be reduced by using large elements that effectively average the atomic contributions  $T_\alpha$  to the temperature over a large number of atoms. To reduce the fluctuations even further, especially when geometry or other considerations, such as resolving spatial inhomogeneities, prevent use of very large elements, we can average in time. Since this time average is to be computed “on the fly” and used in the coupling scheme, we must use a one-sided, causal time average based only on the past values of the nodal temperature field.

To accomplish this, we define a time filtering operation as:

$$\langle f(t) \rangle \equiv \int_{-\infty}^t f(t') G(t - t') dt' \quad (7.32)$$

where  $G(t)$  is a kernel function of the form

$$G(t) = \frac{1}{\tau} e^{-t/\tau} \quad (7.33)$$

and  $\tau$  is the time scale of our filtering operation. The filter defined in (7.32) has at least three useful properties. First, it commutes with time differentiation:

$$\frac{d}{dt} \langle f \rangle = \left\langle \frac{df}{dt} \right\rangle \quad (7.34)$$

Second, the time derivative of a filtered function can be rewritten as a simple, first order ODE:

$$\frac{d}{dt} \langle f \rangle = \frac{f - \langle f \rangle}{\tau} \quad (7.35)$$

so that  $\langle f \rangle$  can be obtained by evolving this ODE in time, rather than explicitly calculating the integral in (7.32). Third, the filter is invertible:

$$\langle f(t) \rangle = g(t) \Rightarrow f(t) = g(t) + \tau \frac{dg}{dt}(t) \quad (7.36)$$

The first of these three properties is true for any kernel function  $G(t)$  that goes to zero as  $t$  goes to infinity, but the second and third properties are dependent on our particular choice of  $G(t)$ .

In order to smooth the fluctuations in the nodal temperature field, we can apply the time filtering operation directly to the atomic temperatures in Eqn (7.11), giving:

$$\int_{\Omega} \delta T^h T^h dV = \left\langle \sum_{\alpha \in \mathcal{A}} \delta T^h(\mathbf{X}_{\alpha}) T_{\alpha} \Delta V_{\alpha} \right\rangle + \int_{\Omega_{fem}} \delta T^h T^h dV \quad (7.37)$$

The reduction operation that gives the nodal temperature field in terms of the temperature at the atoms (7.13) becomes

$$\theta_I = \left\langle \sum_{\alpha \in \mathcal{A}} \hat{N}_{I\alpha} T_{\alpha} \right\rangle \quad (7.38)$$

The total energy to be conserved (cf. 7.17) is, in this case,

$$E^{tot} = \langle E^{md} \rangle + E^{fem} \quad (7.39)$$

Following the same procedure as in Sections 7.3.2 and 7.3.3, while applying the filter inversion from (7.36), gives a slightly different expression for the nodal drag force coefficients (cf. 7.24):

$$\sum_{J \in \mathcal{M}} \left( \sum_{\alpha \in \mathcal{A}} N_{I\alpha} T_{\alpha} N_{J\alpha} \right) \lambda_J = \frac{2}{3k_B} \int_{\Gamma_{md}} N_I \mathbf{n}_{md} \cdot \kappa (\nabla T^h + \tau \nabla \dot{T}^h) dA \quad (7.40)$$

The atomic momentum equations (7.14), (7.15), and (7.16) are otherwise unchanged.

Finally, the finite element temperature evolution equation with time filtering becomes

$$\begin{aligned} & \sum_{J \in \mathcal{N}} \left( \int_{\Omega} N_I N_J dV \right) \dot{\theta}_J \\ &= \left\langle \frac{2}{3k_B} \sum_{\alpha \in \mathcal{A}} N_{I\alpha} \mathbf{v}_{\alpha} \cdot \left( \mathbf{f}_{\alpha}^{md} + \frac{1}{2} \mathbf{f}_{\alpha}^{\lambda} \right) \Delta V_{\alpha} \right\rangle + \sum_{J \in \mathcal{N}} \sum_{\alpha \in \mathcal{A}} \left( \nabla N_I \cdot \frac{\kappa}{\rho c_p} \nabla N_J \right) \Big|_{\alpha} \theta_J \Delta V_{\alpha} \\ & \quad - \sum_{J \in \mathcal{N}} \left( \int_{\Omega} \nabla N_I \cdot \frac{\kappa}{\rho c_p} \nabla N_J dV \right) \theta_J - \int_{\Gamma_q} N_I \frac{\bar{q}_n}{\rho c_p} dA \end{aligned} \quad (7.41)$$

The filtered quantity on the right-hand side is computed at nodes using the ODE in Eqn. (7.35); this will be more fully described in Section 7.6.3.

## 7.6 Numerical Implementation Details

### 7.6.1 Computation of interatomic forces

The force  $\mathbf{f}_{\alpha}^{md}$  on each atom is computed in the standard way for a molecular dynamics simulation, i.e. from the derivative of an interatomic potential function with respect to  $\mathbf{x}_{\alpha}$ . In general, this potential depends on interaction between atoms within some specified cutoff radius  $r_c$  of each other. One issue that requires special treatment in our coupled method is the handling of atoms within a distance  $r_c$  of the boundary  $\Gamma_{md}$ . These atoms do

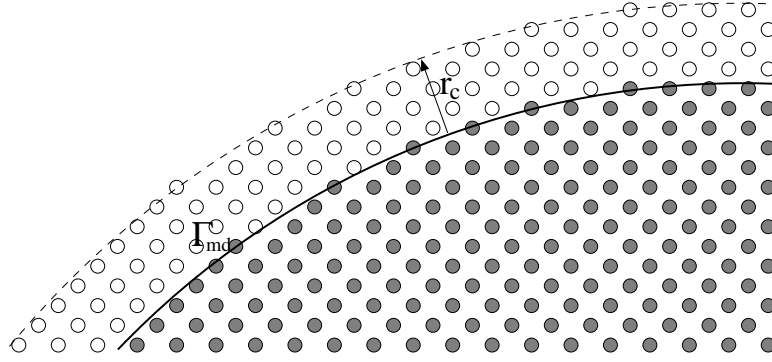


**Figure 7.2.** Ghost atoms (empty circles) near  $\Gamma_{md}$  used to compute interatomic forces.

not have the full complement of neighbors that they would have in a bulk solid, and so, if not treated carefully, these atoms will behave as if they are near a free surface rather than in the interior of the domain.

Our approach to handling these atoms is to store the positions of a number of “ghost atoms” located near the boundary  $\Gamma_{md}$ . In this commonly employed treatment, all atoms in the lattice that are within a distance  $r_c$  outside the boundary are stored as ghost atoms (see Figure 7.2). These atoms are considered to be part of the continuum region and thus have zero displacement, but their positions are used to compute the forces in atoms lying on the interior of  $\Omega_{md}$ .

### 7.6.2 Surface integrals on the MD interface

Akin to the issue of evaluating the domain integral over  $\Omega_{fem}$  in Eqn. (7.30), the integral over surface  $\Gamma_{md}$  on the right-hand side of Eqn. (7.24) may be difficult to compute especially if the surface does not coincide with finite element faces. We have found that an effective approach is to approximate this integral using a combination of the divergence theorem together with projection of derivative fields onto nodal variables. First, note that the integral in question can be rewritten in terms of volume integrals over  $\Omega_{md}$ :

$$\int_{\Gamma_{md}} N_I \mathbf{n}_{md} \cdot \kappa \nabla T^h dA = \int_{\Omega_{md}} N_I \nabla \cdot \kappa \nabla T^h dV + \int_{\Omega_{md}} \nabla N_I \cdot \kappa \nabla T^h dV \quad (7.42)$$

Volume integrals over  $\Omega_{md}$  can be computed through a sum over atoms, as in Eqn. (7.5). The difficulty is that the second derivative of  $T^h$ , in the first integral on the right-hand side, is infinite on element boundaries when finite element shape functions with standard  $C^0$  continuity are used. However, this integral cannot be neglected, nor simply evaluated on element interiors, since the integral over the element boundaries makes a finite contribution to the total value of the expression. The approach we have taken is to approximate this integral by projecting the second derivative of the temperature onto a field  $L(\mathbf{X})$  that is

defined by a nodal interpolation:

$$L(\mathbf{X}) = \sum_{I \in \mathcal{N}} N_I(\mathbf{X}) L_I \approx \nabla \cdot \kappa \nabla T^h \quad (7.43)$$

This leads to an approximation for the values  $L_I$ :

$$\begin{aligned} L_I &= \Delta V_I^{-1} \int_{\Omega} N_I \nabla \cdot \kappa \nabla T^h dV \\ &= -\Delta V_I^{-1} \int_{\Omega} \nabla N_I \cdot \kappa \nabla T^h dV - \Delta V_I^{-1} \int_{\Gamma} N_I \bar{q}_n dA \end{aligned} \quad (7.44)$$

where  $\Delta V_I = \int_{\Omega} \nabla N_I dV$  is a measure of the volume associated with node  $I$ . This expression can be formally derived by using a Galerkin formulation to solve (7.43) and using a lumped diagonal approximation for the mass matrix that multiplies  $L_I$ . In the second line of (7.44), the boundary integral on  $\Gamma$  is zero as long as node  $I$  does not lie on  $\Gamma$ .

With this approximation, the expression for the boundary integral becomes:

$$\begin{aligned} \int_{\Gamma_{md}} N_I \mathbf{n}_{md} \cdot \kappa \nabla T^h dA &= \sum_{J \in \mathcal{N}} \left[ \int_{\Omega_{md}} N_I N_J dV \right] L_J \\ &\quad + \sum_{J \in \mathcal{N}} \left[ \int_{\Omega_{md}} \nabla N_I \cdot \kappa \nabla N_J dV \right] \theta_J \end{aligned} \quad (7.45)$$

Both integrals over  $\Omega_{md}$  are evaluated by summing over the atoms as in (7.5). Note the difference between these integrals and those that appear in Eqn. (7.44); those integrals, including the mass matrix whose inverse is approximated as  $\Delta V_I$ , are over the entire domain  $\Omega$ . The terms in brackets in (7.45) are constant in time and can be computed at the beginning of the simulation. This approximation for the boundary integral term in Eqn. (7.24) can be evaluated in the same way whether the MD/FE boundary coincides with element faces or cuts through element interiors; there is no need to store any discretized representation of the surface.

### 7.6.3 Time Integration

In order to simplify the description of our time integration scheme, we can rewrite the differential equations (7.14) and (7.41) in a more compact form:

$$\dot{\mathbf{x}}_{\alpha} = \mathbf{v}_{\alpha} \quad (7.46a)$$

$$\dot{\mathbf{v}}_{\alpha} = \frac{1}{m_{\alpha}} \mathbf{f}_{\alpha}^{md}(\mathbf{x}_{\beta}) - \frac{1}{2} \mathbf{v}_{\alpha} \lambda_{\alpha}(\mathbf{x}_{\beta}, \mathbf{v}_{\beta}, \dot{\theta}_K, \ddot{\theta}_K) \quad (7.46b)$$

$$\sum_J M_{IJ} \dot{\theta}_J = F_I(\mathbf{x}_{\beta}, \mathbf{v}_{\beta}, \theta_K) \quad (7.46c)$$

where  $\beta \in \mathcal{A}$  and  $K \in \mathcal{N}$ ,  $M_{IJ}$  is the matrix with elements defined by the integral on the left-hand side of (7.41),  $F_I(\mathbf{x}_{\beta}, \mathbf{v}_{\beta}, \theta_K)$  is the right-hand side of (7.41), and

$$\lambda_{\alpha} \equiv \sum_{I \in \mathcal{M}} \hat{N}_{I\alpha} \lambda_I \quad (7.47)$$



Here, the nodal values  $\lambda_I$  are given by the solution to (7.40). In (7.46) we have emphasized the dependence of  $\mathbf{f}_\alpha^{md}$ ,  $\lambda_\alpha$ , and  $F_I$  on the atomic and nodal variables.

For compactness we will drop subscripts  $\alpha$  and  $I$  in the following; subscripts will instead represent the timestep as we integrate from step  $n$  to step  $n+1$ . The integration scheme we use is an explicit predictor-corrector method that is second-order accurate in the displacements. The scheme is based on a modified version of the velocity-Verlet algorithm for  $\mathbf{x}$  and  $\mathbf{v}$  [69], and the Gear predictor-corrector method for  $\theta$  [65]. First, update the atomic velocities to the half time step  $n + \frac{1}{2}$ :

$$\tilde{\mathbf{v}}_{n+1/2} = \mathbf{v}_n \exp\left(-\frac{1}{4}\Delta t \lambda(\mathbf{x}_n, \mathbf{v}_n, \dot{\theta}_n, \ddot{\theta}_n)\right) \quad (7.48a)$$

$$\mathbf{v}_{n+1/2} = \tilde{\mathbf{v}}_{n+1/2} + \frac{1}{2m}\Delta t \mathbf{f}^{md}(\mathbf{x}_n) \quad (7.48b)$$

The exponential term in (7.48a) results from an operator split on (7.46b), and approximating  $\lambda$  as a constant for a half timestep. The positions can then be updated over the entire time step:

$$\mathbf{x}_{n+1} = \mathbf{x}_n + \Delta t \mathbf{v}_{n+1/2} \quad (7.49)$$

The predictor step for the nodal temperature field  $\theta_I$  uses a Taylor expansion about the current state. We find that to retain accuracy when time filtering is used, we need to store derivatives up to the third derivative  $\ddot{\theta}$ :

$$\tilde{\theta}_{n+1} = \theta_n + \Delta t \dot{\theta}_n + \frac{1}{2}\Delta t^2 \ddot{\theta}_n + \frac{1}{6}\Delta t^3 \ddot{\ddot{\theta}}_n \quad (7.50a)$$

$$\dot{\tilde{\theta}}_{n+1} = \dot{\theta}_n + \Delta t \ddot{\theta}_n + \frac{1}{2}\Delta t^2 \ddot{\ddot{\theta}}_n \quad (7.50b)$$

$$\ddot{\tilde{\theta}}_{n+1} = \ddot{\theta}_n + \Delta t \ddot{\ddot{\theta}}_n \quad (7.50c)$$

$$\ddot{\ddot{\tilde{\theta}}}_{n+1} = \ddot{\ddot{\theta}}_n \quad (7.50d)$$

The velocity corrector updates  $\mathbf{v}$  to step  $n+1$ , again using a split operator:

$$\tilde{\mathbf{v}}_{n+1} = \mathbf{v}_{n+1/2} + \frac{1}{2m}\Delta t \mathbf{f}^{md}(\mathbf{x}_{n+1}) \quad (7.51a)$$

$$\mathbf{v}_{n+1} = \tilde{\mathbf{v}}_{n+1} \exp\left(-\frac{1}{4}\Delta t \lambda(\mathbf{x}_{n+1}, \tilde{\mathbf{v}}_{n+1}, \dot{\tilde{\theta}}_n, \ddot{\tilde{\theta}}_n)\right) \quad (7.51b)$$

Finally, temperature is updated to  $n+1$  by computing the correct value of  $\dot{\theta}$  from Eqn.

(7.46c):

$$R \equiv \Delta t (M^{-1} F(\mathbf{x}_{n+1}, \mathbf{v}_{n+1}, \tilde{\theta}_{n+1}) - \dot{\tilde{\theta}}_{n+1}) \quad (7.52a)$$

$$\theta_{n+1} = \tilde{\theta}_{n+1} + \frac{3}{8} R \quad (7.52b)$$

$$\dot{\theta}_{n+1} = \dot{\tilde{\theta}}_{n+1} + \frac{1}{\Delta t} R \quad (7.52c)$$

$$\ddot{\theta}_{n+1} = \ddot{\tilde{\theta}}_{n+1} + \frac{3}{2\Delta t^2} R \quad (7.52d)$$

$$\ddot{\ddot{\theta}}_{n+1} = \ddot{\ddot{\tilde{\theta}}}_{n+1} + \frac{1}{\Delta t^3} R \quad (7.52e)$$

Coefficients on the right-hand side of Eqn (7.52) are obtained from Gear [65].

When time filtering is used, filtered values such as the first term on the right-hand side of (7.41) must be computed. This is done by using the ODE given in (7.35) to update at every time step. For this we use a simple second-order Crank-Nicholson method; the update of the filtered value of a general function  $f$  is the solution to

$$\frac{1}{\Delta t} [\langle f \rangle_{n+1} - \langle f \rangle_n] = \frac{1}{2\tau} [(f_{n+1} - \langle f \rangle_{n+1}) + (f_n - \langle f \rangle_n)] \quad (7.53)$$

This is easily solved for  $\langle f \rangle_{n+1}$ .

#### 7.6.4 Initial Conditions and the Rescaling Thermostat

In most simulations we require that the initial temperature field at time  $t = 0$  in the entire domain be set to some known function. Usually this is a constant value on the domain, although in some cases we desire a spatially varying temperature field. For the finite element temperature field this is simply a matter of setting the nodal values  $\theta_I$  equal to the desired values at  $t = 0$ , but in the MD region we must ensure that the atomic temperatures are consistent with these values, i.e. by Eqn. (7.13) we require:

$$\sum_{\alpha \in \mathcal{A}} \hat{N}_{I\alpha} T_\alpha = \bar{\theta}_I \quad (7.54)$$

where  $\bar{\theta}_I$  are the desired nodal temperatures.

The state of the system at  $t = 0$  must satisfy (7.54) while still reflecting a reasonable distribution of particle velocities and positions; for example, the total energy should be partitioned approximately equally between potential and kinetic energies. For this reason, we cannot simply assign velocities to the atoms at  $t = 0$ , but must allow the simulation to achieve a near-equilibrium distribution while enforcing (7.54), at least on average. One way to achieve this is to evolve the free system dynamics while repeatedly rescaling the atomic velocities by some multiplicative factor  $\xi(\mathbf{x})$ , which we must compute. Since we want to satisfy the constraint at each node, it seems reasonable to expect that  $\xi(\mathbf{x})$  will belong to a function space with a number of degrees of freedom equal to the number of nodes (so that

the number of equations will equal the number of unknowns). We will assume therefore that, like  $\theta$ ,  $\xi$  is a “coarse” scale variable defined by a set of nodal values  $\xi_I$ . We can then obtain  $\xi$  at any atom  $\alpha$  using our finite element shape functions:

$$\xi_\alpha = \sum_I N_{I\alpha} \xi_I. \quad (7.55)$$

The rescaled velocity at atom  $\alpha$  can then be written:

$$\tilde{\mathbf{v}}_\alpha = \xi_\alpha^{1/2} \mathbf{v}_\alpha. \quad (7.56)$$

We use the square root of  $\xi_\alpha$  to scale the velocity so that when we compute the temperature, which is proportional to  $v_\alpha^2$ , the scaling will be linear. After rescaling, the atom velocities satisfy the equation:

$$\sum_I \hat{N}_{I\alpha} \tilde{T}_\alpha = \bar{\theta}_I \quad (7.57)$$

where

$$\begin{aligned} \tilde{T}_\alpha &= \frac{1}{3k_B} m_\alpha |\tilde{\mathbf{v}}_\alpha|^2 \\ &= \xi_\alpha T_\alpha \end{aligned} \quad (7.58)$$

Substituting for the interpolated values of  $\xi_\alpha$  gives a simple matrix equation for the nodal values  $\xi_I$ :

$$\mathbf{M}^\xi \boldsymbol{\xi} = \bar{\boldsymbol{\theta}} \quad (7.59)$$

where

$$M_{IJ}^\xi = \sum_\alpha \hat{N}_{I\alpha} T_\alpha N_{J\alpha} \quad (7.60)$$

Given a set of atomic velocities and an initial temperature field  $\bar{\theta}_I$  at time  $t = 0$ , we can solve for  $\xi_I$ , interpolate to the atoms, and rescale the velocities. The resulting atomic temperature field reduced to the nodes will match the given field. In practice, we find that the best initial condition is obtained by allowing the MD system to run freely for a few picoseconds, while periodically applying the rescaling thermostat derived above. This allows time for the system to achieve equipartition of energy between kinetic and potential energies; this equipartition can be imperfect if the rescaling thermostat is applied to a system that is far from the desired temperature or far from equilibrium.

## 7.7 Examples

We performed a set of representative problems to investigate and illustrate the performance of the proposed coupling algorithm. All simulations used the Lennard-Jones pair potential

$$\phi(r) = 4\varepsilon \left( \left( \frac{\sigma}{r} \right)^{12} - \left( \frac{\sigma}{r} \right)^6 \right) \quad (7.61)$$

for the interatomic interactions with parameters  $\varepsilon/k_B = 119.8 \text{ K}$  and  $\sigma = 3.405 \text{ \AA}$  for solid argon, taken from [151]. Non-periodic atomic boundaries were padded with two unit

cells (four layers) of ghost atoms. An atomic mass of  $m_\alpha = 39.948 \text{ amu}$  was used and the equilibrium, face-centered cubic lattice constant  $\ell = 5.406 \text{ \AA} \approx 1.775\sigma$  at  $30 \text{ K} \approx 0.25\epsilon/k_B$  was calculated using a finite-temperature, zero pressure simulation. The continuum thermal diffusivity  $\frac{\kappa}{\rho c_p} = 50 \text{ \AA}^2/\text{ps}$  was calculated using a thermal conductivity value  $\kappa = 0.5 \text{ W/(mK)}$  estimated from [151] and a heat capacity value  $\rho c_p = 1.1 \text{ MJ/(K m}^3\text{)}$  from Eqn. (7.27). Standard 8-node tri-linear hexahedral elements were employed in the finite element representation of the material.

To initialize the states of the atoms in all of the following simulations, we used the thermostat described in Section 7.6.4 in a thermalization procedure consisting of rescaling every 100 steps for several thousand time steps. We found that a time step of  $0.005 \text{ ps} \approx t_E/172.5$ , was sufficiently accurate and stable to produce the following results. Here,  $t_E \approx 0.4 \sqrt{m_\alpha \sigma^2 / \epsilon}$  is the approximate Einstein vibrational period for the lattice. Note that we use the same time step size for both the MD and continuum equations.

### 7.7.1 One Dimensional Heat Conduction

In this example, a transient, non-equilibrium heat flux simulation was effected using temperature boundary conditions on the ends of a FE grid which subsumed the MD region. The atomic system was  $(20 \times 8 \times 8)\ell$  in size and centered in the overlapping finite element domain of size  $(48 \times 8 \times 8)\ell$ . The domain was discretized using cubical elements; simulations were run with element sizes of  $h = \{8, 4, 2\}\ell$ , resulting in meshes with 6, 48, and 384 elements, respectively. The  $[100]$  crystal directions were aligned with the axes of the computational domain. The problem geometry for the  $h = 4\ell$  case is shown in Figure 7.3.

Periodic boundaries were imposed on the lateral ( $\pm y$  and  $\pm z$ ) faces of the rectangular domain. The temperature of the entire system was initially brought to  $30 \text{ K}$  via rescaling and, immediately following the thermalization stage, the end temperatures were changed to  $40 \text{ K}$  and  $20 \text{ K}$  for the left ( $-x$ ) and right ( $+x$ ) ends, respectively. The longitudinal temperature traces, Figure 7.4, of this essentially one-dimensional problem show good agreement with the corresponding solution of the classical heat conduction equation. For moderately sized MD simulations, including this simple test problem, we do not expect discernible effects of the finite speed of propagation of heat waves and, consequently, the Fourier model in the FE-only regions appears to be sufficiently representative. The work of Volz *et al.* [152] and Ho *et al.* [74] illustrate, for nearly 1D and strictly 2D systems respectively, the potential discrepancies between Fourier behavior and MD simulations, albeit at much higher pressures and temperatures than those investigated here. Using the estimate  $1/\sqrt{3}c_1$  employed in both [152] and [74] for the speed of the “second sound” wave, where  $c_1$  is the speed of the first (transverse) wave, we calculate a thermal wave speed of  $c_2 \approx 700 \text{ m/s}$ . At this velocity a thermal pulse will transit a typical finite element ( $h = 4\ell$ ) in about  $3.2 \text{ ps}$ . Since this transit time is on the order of the filter scale we employ, it is reasonable that our simulations show results that are consistent with a (nearly) infinite speed of heat propagation.

Specifically, we ran simulations using various values of the time filter parameter  $\tau = \{0.05, 0.2, 1.0, 5.0, 10.0, 25.0\} \text{ ps}$ . As a demonstration of the effect of time filtering on

temperature fluctuations, Figure 7.5 shows the root mean square (RMS) fluctuation in time at the center point of the system as a function of  $\tau$  for each mesh size  $h$ . For large values of  $\tau$ , the RMS values are proportional to  $\tau^{-1/2}$ ; this is the expected behavior if the number of phonons being averaged over is proportional to the filter time, since the RMS of  $N$  samples is expected to be inversely proportional to the square root of  $N$ . Likewise, the dependence on the mesh size approximately follows the trend  $h^{-3/2}$ , consistent with averaging over a number of phonons proportional to the element volume. Note that data was only sampled in the range  $t \in [500, 1000] ps$ , where the temperatures have reached a statistical steady-state.

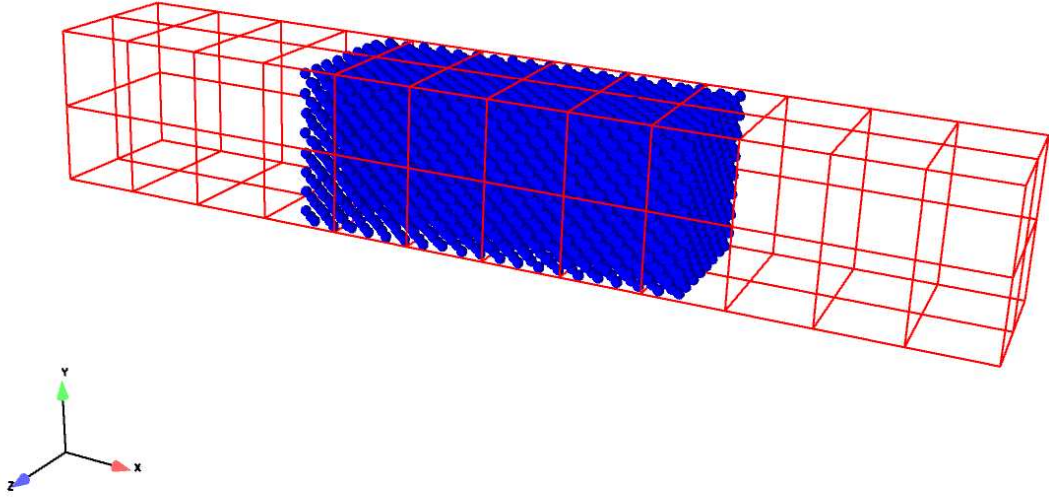


**Figure 7.3.** One dimensional heat conduction: mesh and atomic positions for  $h = 4\ell$

### 7.7.2 Diffusion of an Initial Gaussian Temperature Field

In order to show consistency between a full MD solution and a coupled simulation, we compared two simulations: (a) a “reference” simulation where the computational region  $(32 \times 32 \times 8)\ell$  was completely filled with atoms and the FE grid was only used for data-processing; and (b) a coupled simulation where the MD region  $(16 \times 16 \times 8)\ell$  only partly filled the computational domain (Figure 7.6). In both these simulations an initial (two dimensional) temperature field,  $T(x, y, z) = (20.0 K) \exp(-\sqrt{x^2 + y^2}/(50.0 \text{Å})) +$

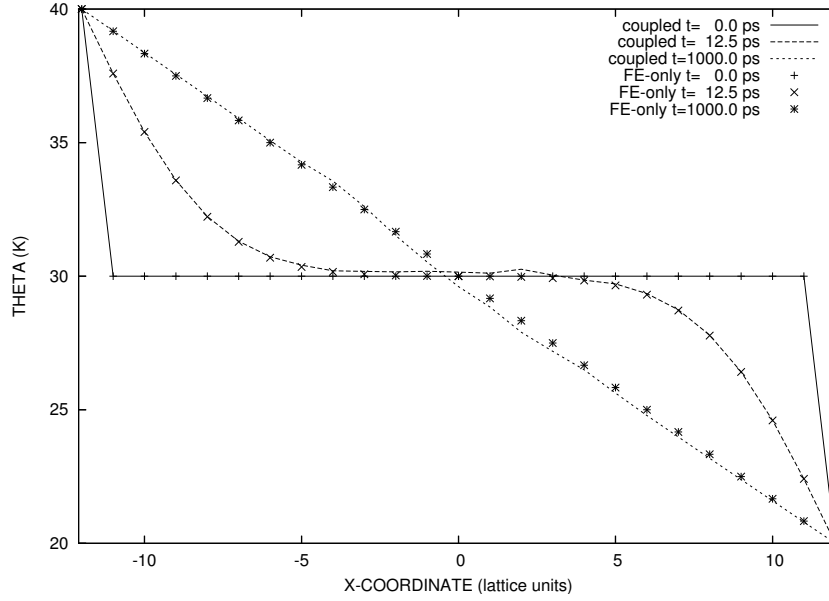


**Figure 7.4.** Temperature profiles for  $h = 2\ell$  and  $\tau = 25 ps$  at  $t = 0.0, 12.5, 1000.0 ps$

(20.0 K), was imposed via the rescaling thermostat and let diffuse with adiabatic conditions on the lateral boundaries and periodic conditions on the top and bottom. In the case of the coupled simulation, we merely left the natural, zero flux boundary conditions in place; for the reference simulation, we imposed zero displacement boundary conditions so that no work would be done on the system and it would behave adiabatically as an NVE ensemble. Also, we used a time filter scale  $\tau = 10.0 ps$  in both simulations, which, in the case of the reference simulation, was merely used to reduce the atomic data to comparable nodal temperatures.

It is clear from the sequence of temperature contours shown in Figure 7.7 that the coupled simulation is quite comparable to the more computationally expensive full MD reference simulation. Figure 7.8 shows the normalized coarse scale energy  $\sum_I \theta_I(t) / \sum_I \theta_I(0)$  for the two systems. Note that this quantity is different from the total energy expressed in Eqn. (7.17), since (7.17) uses kinetic and potential energies of the atoms in the MD region and is exactly conserved by design. Instead, the quantity plotted in Figure 7.8 uses the nodal temperature values everywhere in the domain; this is related to the only the kinetic energy for the atoms, and thus is not exactly conserved. In both systems, this quantity changes slightly early in the simulation; this can be attributed to the fact that the system is initially not in equilibrium and does not have an equilibrium equipartition between potential and kinetic energy. In both systems the integrated energy eventually fluctuates around a constant value; fluctuations are larger in the reference system because it contains many more atoms (131,072 vs. 32,768). The fact that our coupled system reaches a constant energy demonstrates that the method for this problem is stable, and that energy neither grows nor is dissipated by our numerical treatment.

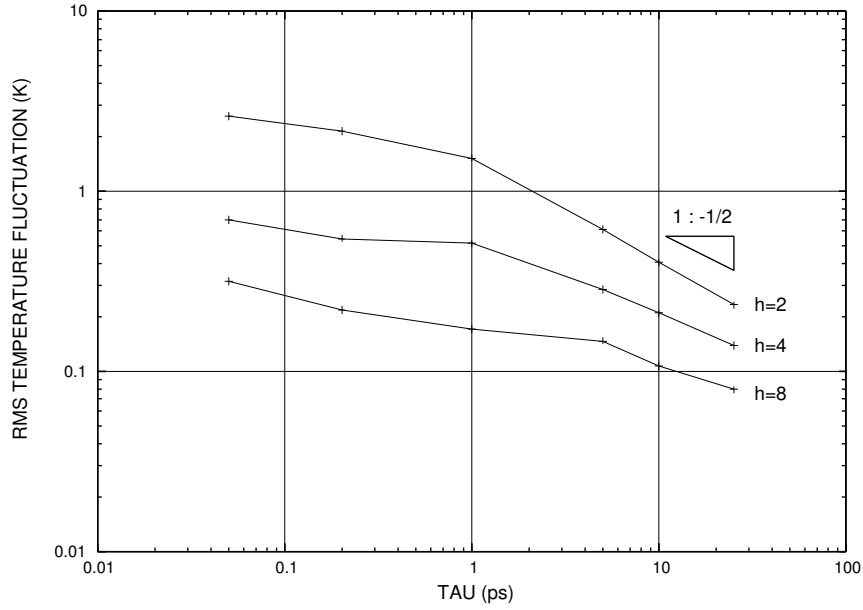


**Figure 7.5.** Root mean square fluctuations of temperature at center of the domain as a function of  $\tau$  for various  $h$

### 7.7.3 Thermal Transport Across an Acoustic Mismatch

In this example, atoms in a two lattice unit wide region in the middle of the a computational domain  $(40 \times 12 \times 12)\ell$  were given atomic masses ten times their nominal value to create an ersatz grain boundary (Figure 7.9). As in the one-dimensional conduction simulation, lateral boundaries were prescribed to be periodic and temperatures were specified on the ends. In this case, the left end was given a temperature of  $50\text{ K}$  and the right end  $10\text{ K}$ . A parameter study was done to show how the MD system size  $(2a \times 12 \times 12)\ell$  affects the calculated temperature profile. As can be seen in Figure 7.10, the MD/FE boundary can be brought within three lattice units of the mismatch boundary with no substantial effect on the steady-state temperature profile. It is interesting to note that the profile is not entirely symmetric, with the low temperature side showing greater deviations across MD system size and an ordering of this difference with  $a$ . Despite this small effect, it is clear that the coupled method was successful in simulating the temperature jump expected at a grain-like boundary.

## 7.8 Discussion and Conclusions

In this work we have presented a seamless, energy-conserving method to couple the temperature fields of atomistic and continuum representations of material. The method allows the use of MD in a localized region of a domain, surrounded and overlaid by a continuum finite element solution. Inside the MD region the dynamics are governed by the detailed

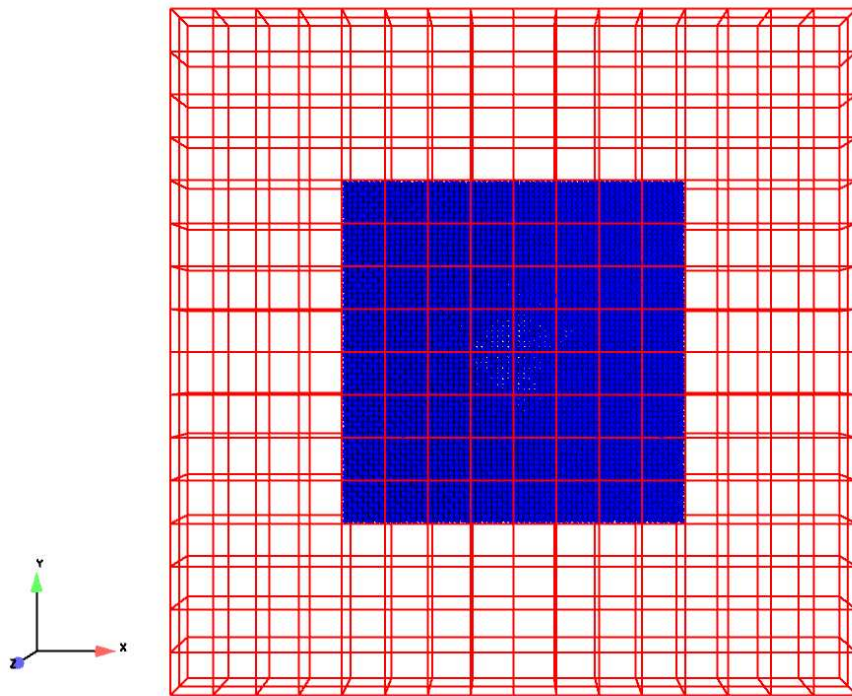


**Figure 7.6.** Mesh and atomic positions for the coupled simulation of the diffusion of an initial Gaussian temperature field

interatomic interactions, while everywhere else the heat transfer is governed by the Fourier heat law. A strength of the method is that computations do not depend on the boundaries of the MD region aligning with finite element faces, so that the shape of the MD region can be arbitrary. This simplifies the task of generating discretized domains; and it allows for the possibility of very simple resizing or rediscritization of both the finite element mesh and the MD lattice, which is one component of an adaptive simulation.

The main motivation for development of this method is to simulate problems in which either heat is generated in a localized region (e.g. laser heating, surface friction) or in which localized microstructures at the atomic scale strongly affect the heat transfer (e.g. thermal transport across grain boundaries or near defects). The example problem presented in Section 7.7.3 is an example of the latter type of application. In both cases the method can allow solution on a much larger domain than would be possible using MD alone, since MD can be used only where necessary to correctly capture the relevant phenomena. However, the method is also useful in smaller problems as a convenient way of applying temperature boundary conditions to non-equilibrium MD simulations. For example, in the example problems presented in both Sections 7.7.1 and 7.7.3 the method was used to fix the temperature on the ends of the domain; this is an attractive alternative to other approaches that may be used, such as applying MD thermostats to regions near the boundaries which typically



creates artificial Kapitza-like temperature jumps.

It should be pointed out that although we have assumed a Fourier heat law applies in the continuum region, this assumption is not required for the method presented. It is straightforward to replace Eqn. (7.1) with a different form, for example, the Maxwell-Cattaneo-Vernotte model typically employed to represent the finite speed of propagation of heat waves, see, e.g., [74, 97, 152]. On the other hand, the method does not provide an *a priori* way of determining what the correct form of the heat law should be in the continuum, nor does it allow for the analytical derivation of coefficients in a heat law. Physical or numerical experiments, or theory, must be used to provide a relation between heat flux and temperature.

A clear direction for the extension of this work is to combine the thermal coupling derived here with coupling of the momentum equations, as has been done previous using related methods, to capture the full thermo-mechanical behavior of a material. Although in the current work we have not been concerned with the elimination of internal wave reflections in the MD region, which has been the subject of previous work, our method does provide a way to capture the thermal information contained in these small-scale waves and allow it to be transported as heat into the continuum. By combining the strengths of MD and continuum simulation methods in this way, we can develop a powerful tool for the simulation of a range of important multi-scale engineering problems.

## Acknowledgments

Sandia is a multiprogram laboratory operated by Sandia Corporation, a Lockheed Martin Company, for the United States Department of Energy under contract DE-AC04-94AL85000. We are grateful for helpful discussions with Rich Lehoucq, Pavel Bochev, Alex Slepoy and Jon Zimmerman in the development of this work and preparation of the manuscript.

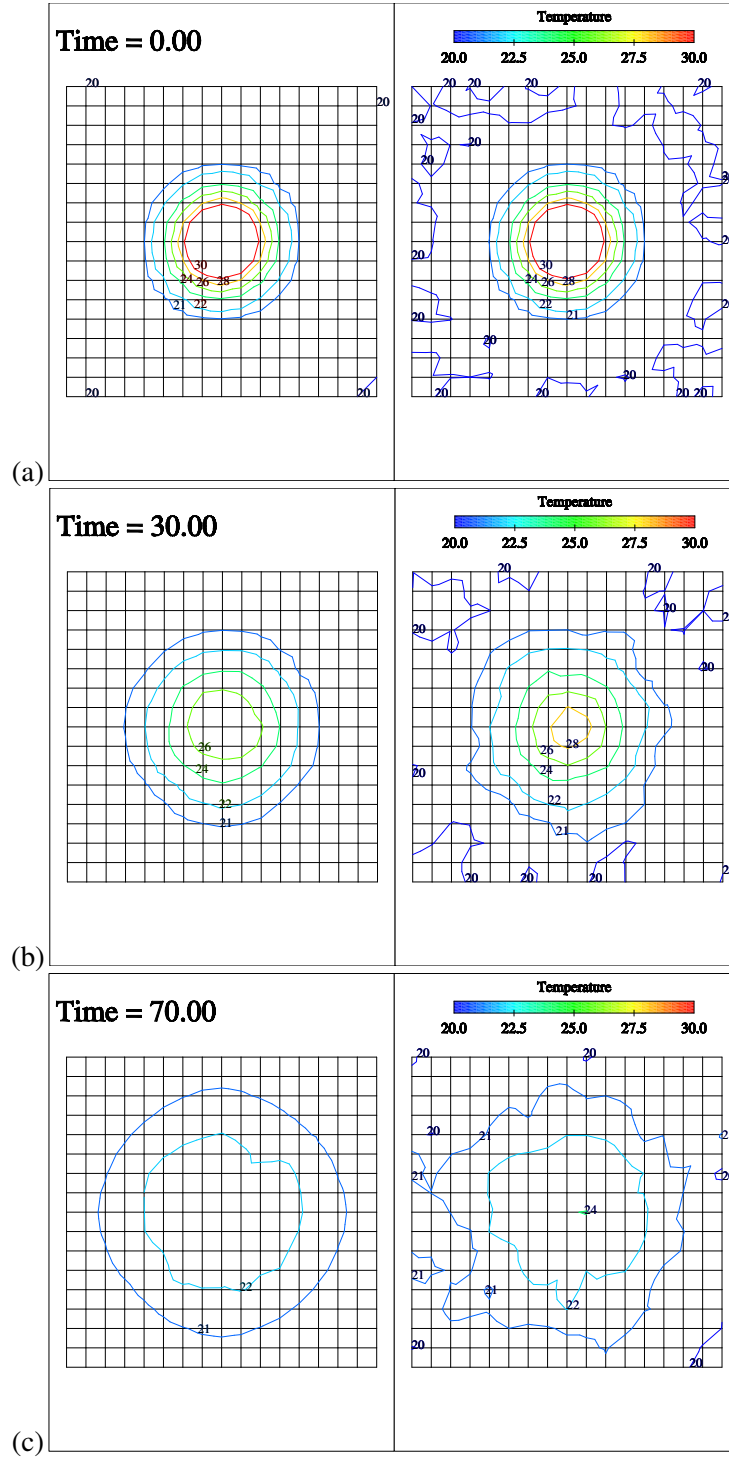


**Figure 7.7.** Comparison of a sequence of temperature contours for the coupled simulation (left) and the reference simulation (right): (a) initial  $t = 0.0$  ps, (b)  $t = 30.0$  ps, and (c)  $t = 70.0$  ps

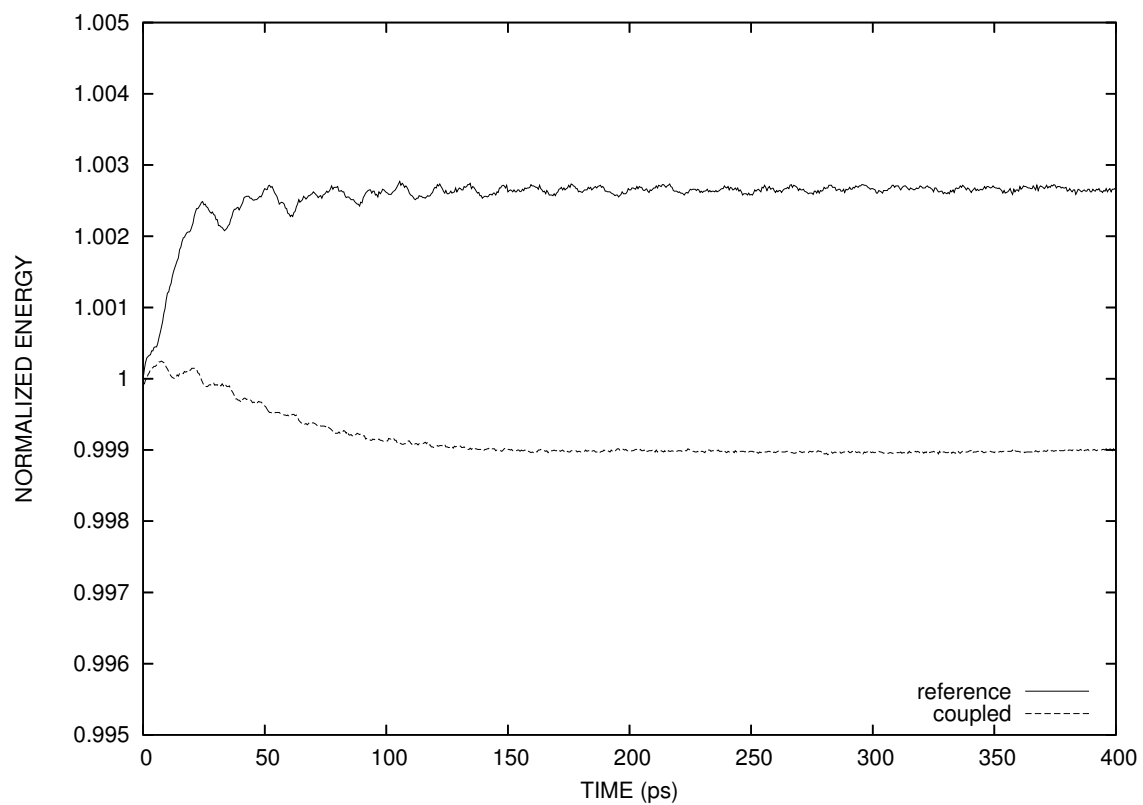


**Figure 7.8.** Comparison of integrated temperature evolution for the diffusion of a Gaussian temperature field

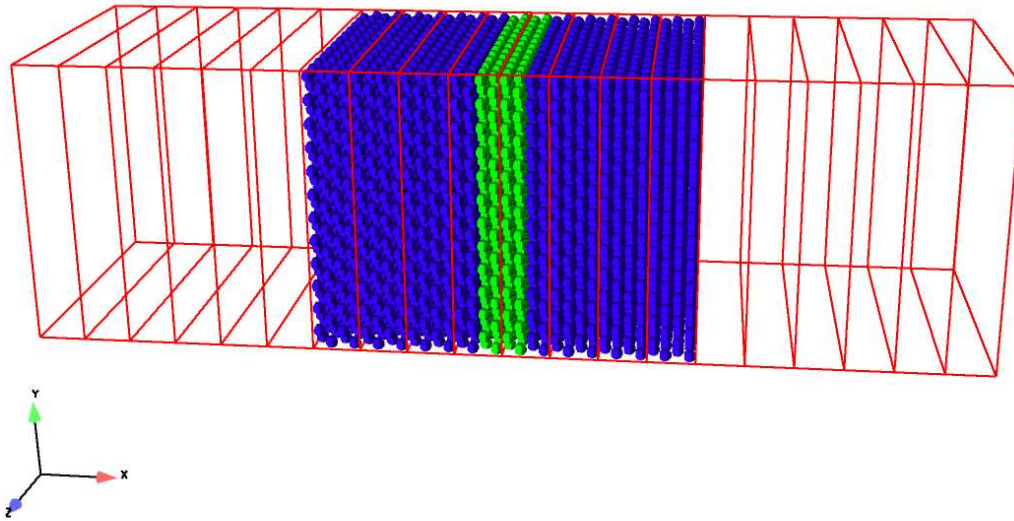


**Figure 7.9.** Mesh and atomic positions for  $a = 8$  showing regions of different atomic mass

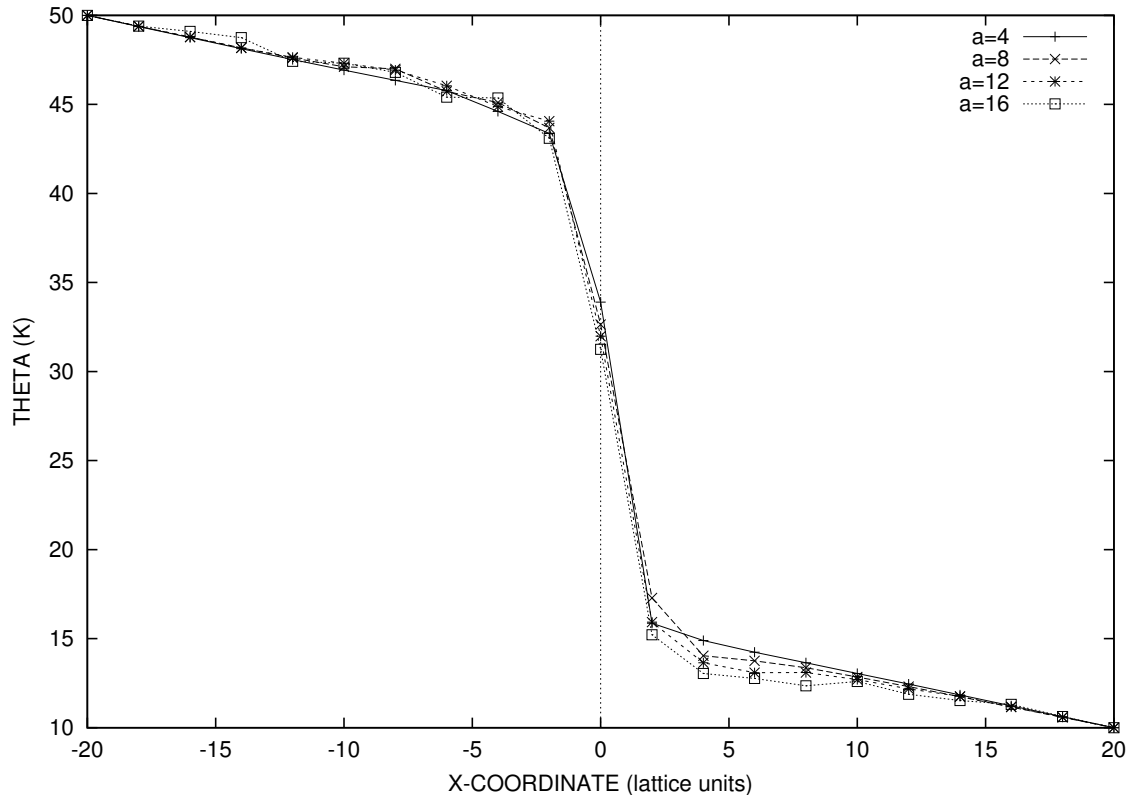


**Figure 7.10.** Temperature profiles for various atomic domain sizes  $a$

This page intentionally left blank.

# References

- [1] F. ABRAHAM, J. BROUGHTON, N. BERNSTEIN, AND E. KAXIRAS, *Spanning the length scales in dynamic simulation*, Computers in Physics, 12 (1998), pp. 538–546.
- [2] F. ABRAHAM, R. WALKUP, H. GAO, M. DUCHAINEAU, T. D. LA RUBIA, AND M. SEAGER, *Simulating materials failure by using up to one billion atoms and the world’s fastest computer: Work-hardening*, Proceedings of the National Academy of Sciences of the United States of America, 99 (2002), pp. 5783–5787.
- [3] S. ADJERID, K. D. DEVINE, J. E. FLAHERTY, AND L. KRIVODONOVA, *A posteriori error estimation for discontinuous Galerkin solutions of hyperbolic problems*, Computer Methods in Applied Mechanics and Engineering, **191**(11-12) (2001), pp. 1097–1112.
- [4] J. ALBERTY AND C. CARSTENSEN, *Discontinuous Galerkin time discretization in elastoplasticity: motivation, numerical algorithms, and applications*, Computer Methods in Applied Mechanics and Engineering, **191**(43) (2002), pp. 4949–4968.
- [5] M. ARNDT AND M. GRIEBEL, *Derivation of higher order gradient continuum models from atomistic models for crystalline solids*, Multiscale Mod. Simul., 4 (2005), pp. 531–562.
- [6] D. N. ARNOLD, G. AWANOU, AND R. WINTHER, *Finite elements for symmetric tensors in three dimension*, Math. Comp., (2007). to appear.
- [7] D. N. ARNOLD, F. BREZZI, B. COCKBURN, AND L. D. MARIN, *Unified analysis of discontinuous Galerkin methods for elliptic problems*, SIAM J. Numer. Anal., 39 (2002), pp. 1749–1779.
- [8] S. ARUNAJATESAN AND N. SINHA, *Unified unsteady RANS-LES simulations of cavity flowfields*, AIAA 2001-0516, (2001).
- [9] H. L. ATKINS, *Continued development of the discontinuous Galerkin method for computational aeroacoustic applications*, AIAA Paper 97-1581, (1997).
- [10] A. BARANYAI, *Temperature of nonequilibrium steady-state systems*, Physical Review E (Statistical Physics, Plasmas, Fluids, and Related Interdisciplinary Topics), 62 (2000), pp. 5989 – 97.
- [11] F. BASSI AND S. REBAY, *A high-order accurate discontinuous finite element method for the numerical solution of the compressible Navier–Stokes equations*, J. Comp. Phys., 131 (1997), pp. 267–279.
- [12] —, *A high order discontinuous Galerkin method for compressible turbulent flows*, in Discontinuous Galerkin Methods: Theory, Computation, and Applications,

- B. Cockburn, G. E. Karniadakis, and C.-W. Shu, eds., no. 11 in *Lecture Notes in Computational Science and Engineering*, Springer, 2000, pp. 77–88.
- [13] C. E. BAUMANN AND J. T. ODEN, *A discontinuous hp finite element method for convection-diffusion problems*, *Computer Methods in Applied Mechanics and Engineering*, **175** (1999), pp. 311–341.
  - [14] C. E. BAUMANN AND J. T. ODEN, *A discontinuous hp finite element method for the Euler and Navier–Stokes equations*, *Inter. J. Num. Meth. Fluids*, 31 (1999), pp. 79–95.
  - [15] Z. P. BAŽANT AND M. JIRÁSEK, *Nonlocal integral formulations of plasticity and damage: Survey of progress*, *Journal of Engineering Mechanics*, 128 (2002), pp. 1119–1149.
  - [16] R. BECKER, P. HANSBO, AND M. G. LARSON, *Energy norm a posteriori error estimation for discontinuous Galerkin methods*, *Computer Methods in Applied Mechanics and Engineering*, **192**(5-6) (2003), pp. 723–733.
  - [17] H. BERENDSEN, J. POSTMA, W. VANGUNSTEREN, A. DINOLA, AND J. HAAK, *Molecular-dynamics with coupling to an external bath*, *Journal of Chemical Physics*, 81 (1984), pp. 3684–3690.
  - [18] E. BERTIN, O. DAUCHOT, AND M. DROZ, *Temperature in nonequilibrium systems with conserved energy*, *Physical Review Letters*, 93 (2004), pp. 230601 – 4.
  - [19] P. BOCHEV, T. J. R. HUGHES, AND G. SCOVAZZI, *A multiscale discontinuous Galerkin method*, in *Large Scale Scientific Computing*, I. Lirkov, S. Margenov, and J. Wasniewski, eds., LNCS 3743, 2005, pp. 84–93.
  - [20] C. BRAGA AND K. P. TRAVIS, *A configurational temperature Nose-Hoover thermostat*, *Journal of Chemical Physics*, 123 (2005), pp. 134101 – 1.
  - [21] F. BREZZI AND M. FORTIN, *Mixed and Hybrid Finite Element Methods*, Springer series in computational mathematics, Springer-Verlag, 1991.
  - [22] F. BREZZI, L. P. FRANCA, T. J. R. HUGHES, AND A. RUSSO,  $b = \int g$ , *Computer Methods in Applied Mechanics and Engineering*, **145** (1997), pp. 329–339.
  - [23] F. BREZZI, G. MANZINI, D. MARINI, P. PIETRA, AND A. RUSSO, *Discontinuous Galerkin approximations for elliptic problems*, *Numerical Methods for Partial Differential Equations*, **16**(4) (2000), pp. 365–378.
  - [24] F. BREZZI AND L. D. MARINI, *A nonconforming element for the Reissner-Mindlin plate*, *Computers and Structures*, **81**(8-11) (2003), pp. 515–522.
  - [25] F. BREZZI AND A. RUSSO, *Choosing bubbles for advection-diffusion problems*, *Mathematical Models and Methods in Applied Sciences*, **4** (1994), pp. 571–587.
  - [26] A. N. BROOKS AND T. J. R. HUGHES, *Streamline upwind/Petrov-Galerkin formulations for convection dominated flows with particular emphasis on the incompressible Navier-Stokes equations*, *Computer Methods in Applied Mechanics and Engineering*, **32** (1982), pp. 199–259.



- [27] G. L. BROWN AND A. ROSHKO, *On density effects and large structure in turbulent mixing layers*, J. Fluid Mech., 64 (1974), pp. 775–816.
- [28] E. BURMAN AND A. ERN, *A nonlinear diffusion and discrete maximum principle for stabilized Galerkin approximations of the convection-diffusion-reaction equation*, Computer Methods in Applied Mechanics and Engineering, **191**(35) (2002), pp. 3833–3855.
- [29] C. CANUTO, M. Y. HUSSAINI, A. QUARTERONI, AND T. A. ZANG, *Spectral Methods in Fluid Dynamics*, Springer-Verlag, 1988, p. 69.
- [30] J. CASAS-VAZQUEZ AND D. JOU, *Nonequilibrium temperature versus local-equilibrium temperature*, Physical Review E (Statistical Physics, Plasmas, Fluids, and Related Interdisciplinary Topics), 49 (1994), pp. 1040 – 8.
- [31] —, *Temperature in non-equilibrium states: a review of open problems and current proposals*, Reports on Progress in Physics, 66 (2003), pp. 1937 – 2023.
- [32] P. CASTILLO, *A superconvergence result for discontinuous Galerkin methods applied to elliptic problems*, Computer Methods in Applied Mechanics and Engineering, **192**(41-42) (2003), pp. 4675–4685.
- [33] Y. CHANG, *Reduced Order Methods for Optimal Control of Turbulence*, PhD thesis, Rice University, Mechanical Engineering and Materials Science, 2000.
- [34] Y. CHANG, S. S. COLLIS, AND S. RAMAKRISHNAN, *Viscous effects in control of near-wall turbulence*, Phys. Fluids, 14 (2002), pp. 4069–4080.
- [35] Y. CHEN, J. D. LEE, AND A. ESKANDARIAN, *Atomistic viewpoint of the applicability of microcontinuum theories*, International Journal of Solids and Structures, 41 (2004), pp. 2085–2097.
- [36] P. CIARLET, *The finite element method for elliptic problems*, Classics in applied mathematics, SIAM, Philadelphia, 2002.
- [37] J. D. CLAYTON AND P. W. CHUNG, *An atomistic-to-continuum framework for nonlinear crystal mechanics based on asymptotic homogenization*, J. Mech. Phys. Solids, 54 (06), p. 16041639.
- [38] B. COCKBURN, ed., *High-order methods for computational applications*, *Lecture Notes in Computational Science and Engineering*, Springer, Berlin, 1999, ch. Discontinuous Galerkin methods for convection-dominated problems, pp. 69–224.
- [39] —, *Discontinuous Galerkin methods*, ZAMM - Journal of Applied Mathematics and Mechanics /Zeitschrift für Angewandte Mathematik und Mechanik, 83 (2003), pp. 731–754.
- [40] B. COCKBURN, G. E. KARNIADAKIS, AND C.-W. SHU (EDS.), *Discontinuous Galerkin Methods: Theory, Computation and Applications*, *Lecture Notes in Computational Science and Engineering*, 11, Springer-Verlag, 2000.

- [41] G. N. COLEMAN, J. KIM, AND R. D. MOSER, *A numerical study of turbulent supersonic isothermal-wall channel flow*, J. Fluid Mech., 305 (1995), pp. 159–83.
- [42] S. S. COLLIS, *Monitoring unresolved scales in multiscale turbulence modeling*, Phys. Fluids, 13 (2001), pp. 1800–1806.
- [43] —, *The DG/VMS method for unified turbulence simulation*, AIAA Paper 2002-3124, (2002).
- [44] —, *Discontinuous Galerkin methods for turbulence simulation*, in Proceedings of the 2002 Center for Turbulence Research Summer Program, 2002, pp. 155–167.
- [45] S. S. COLLIS AND Y. CHANG, *On the use of LES with a dynamic subgrid scale model for the optimal control of wall bounded turbulence*, in Recent Advances in DNS and LES, D. Knight and L. Sakell, eds., Kluwer Academic Publishers, 1999, pp. 99–110.
- [46] W. CURTIN AND R. MILLER, *Atomistic/continuum coupling in computational materials science*, Modelling and Simulation in Materials Science and Engineering, 11 (2003), pp. R33–R68.
- [47] C. DAWSON, *The  $P^{k+1}$ - $S^k$  local discontinuous Galerkin method for elliptic equations*, SIAM Journal on Numerical Analysis, **40**(6) (2003), pp. 2151–2170.
- [48] C. DAWSON AND J. PROFT, *Discontinuous and coupled continuous/discontinuous Galerkin methods for the shallow water equations*, Computer Methods in Applied Mechanics and Engineering, **191**(41-42) (2002), pp. 4721–4746.
- [49] —, *Space-time discontinuous Galerkin finite element method with dynamic grid motion for inviscid compressible flows: II. Efficient flux quadrature*, Computer Methods in Applied Mechanics and Engineering, **191**(41-42) (2002), pp. 4747–4780.
- [50] —, *Coupled discontinuous and continuous Galerkin finite element methods for the depth-integrated shallow water equations*, Computer Methods in Applied Mechanics and Engineering, **193**(3-5) (2003), pp. 289–318.
- [51] —, *Discontinuous/continuous Galerkin methods for coupling the primitive and wave continuity equations of shallow water*, Computer Methods in Applied Mechanics and Engineering, **192**(47-48) (2003), pp. 5123–5145.
- [52] P. A. B. DE SAMPAIO AND A. L. G. A. COUTINHO, *A natural derivation of discontinuity capturing operator for convection-diffusion problems*, Computer Methods in Applied Mechanics and Engineering, **190**(46-47) (2001), pp. 6291–6308.
- [53] E. G. D. DO CARMO AND G. B. ALVAREZ, *A new stabilized finite element formulation for scalar convection-diffusion problems: the streamline and approximate upwind Petrov-Galerkin method*, Computer Methods in Applied Mechanics and Engineering, **192**(31-32) (2003), pp. 3379–3396.
- [54] —, *A new upwind function in stabilized finite element formulations, using linear and quadratic elements for scalar convection-diffusion problems*, Computer Methods in Applied Mechanics and Engineering, **193**(23-26) (2004), pp. 2383–2402.

- [55] G. J. DONG, X. Y. LU, AND L. X. ZHUANG, *Discontinuity-capturing finite element computation of unsteady flow with adaptive unstructured mesh*, Acta Mechanica Sinica, **20**(4) (2004), pp. 347–353.
- [56] M. DUBINER, *Spectral methods on triangles and other domains*, J. Sci. Comp., 6 (1991), p. 345.
- [57] L. M. DUPUY, E. B. TADMOR, R. E. MILLER, AND R. PHILLIPS, *Finite-temperature quasicontinuum: Molecular dynamics without all the atoms*, Phys. Rev. Lett., 95 (2005), p. 060202.
- [58] G. ENGEL, K. GARIKIPATI, T. J. R. HUGHES, M. G. LARSON, L. MAZZEI, AND R. L. TAYLOR, *Continuous/discontinuous finite element approximations of fourth-order elliptic problems in structural and continuum mechanics with applications to thin beams and plates, and strain gradient elasticity*, Computer Methods in Applied Mechanics and Engineering, **191**(34) (2002), pp. 3669–3750.
- [59] C. C. FANG AND T. W. H. SHEU, *Development of an adaptive discontinuity-capturing hyperbolic finite element model*, International Journal of Numerical Methods in Fluids, **44**(9) (2004), pp. 957–973.
- [60] C. FARHAT, I. HARARI, AND U. HETMANIUK, *A discontinuous Galerkin method with Lagrange multipliers for the solution of Helmholtz problems in the mid-frequency regime*, Computer Methods in Applied Mechanics and Engineering, **192**(11-12) (2003), pp. 1389–1419.
- [61] J. H. FERZIGER, *Large eddy simulation*, in Simulation and Modeling of Turbulent Flows, T. B. Gatski, M. Y. Hussaini, and J. L. Lumley, eds., ICASE/LaRC Series in Computational Science and Engineering, Oxford University Press, 1996, ch. 3.
- [62] J. FISH, W. CHEN, AND R. LI, *Generalized mathematical homogenization of atomistic media at finite temperatures in three dimensions*, Comput. Methods Appl. Mech. Engrg., 196 (2007), pp. 908–922.
- [63] C. FUREBY AND F. GRINSTEIN, *Large eddy simulation of high-reynolds-number free and wall-bounded flows*, J. Comp. Phys., 181 (2002), pp. 68–97.
- [64] A. C. GALEAO, R. C. ALMEIDA, AND S. M. C. MALTA, *Finite element analysis of convection dominated reaction-diffusion problems*, Applied Numerical Mathematics, **48**(2) (2004), pp. 205–222.
- [65] C. GEAR, *Numerical Initial Value Problems in Ordinary Differential Equations*, Prentice-Hall, Englewood Cliffs, New Jersey, 1971.
- [66] M. GERMANO, U. PIOMELLI, P. MOIN, AND W. H. CABOT, *A dynamic subgrid-scale eddy viscosity model*, Phys. Fluids A, 3 (1991), pp. 1760–1765.
- [67] S. GHOSAL AND P. MOIN, *The basic equations for the large-eddy simulation of turbulent flows in complex-geometry*, J. Comp. Phys., 118 (1995), pp. 24–37.
- [68] P. GUMBSCH AND R. CANNON, *Atomistic aspects at brittle fracture*, MRS Bulletin, 25 (2000), pp. 15–20.

- [69] J. HAILE, *Molecular Dynamics Simulation: Elementary Methods*, Wiley, New York, 1992.
- [70] P. HANSBO AND M. G. LARSON, *Coupling of continuous and discontinuous Galerkin methods for transport problems*, Computer Methods in Applied Mechanics and Engineering, **191**(29-30) (2002), pp. 3213–3231.
- [71] —, *Discontinuous Galerkin methods for incompressible and nearly incompressible elasticity by Nitsche’s method*, Computer Methods in Applied Mechanics and Engineering, **191**(17-18) (2002), pp. 1895–1908.
- [72] R. J. HARDY, *Formulas for determining local properties in molecular-dynamics simulations: shock waves*, J. Chem. Phys., 76 (1982), pp. 622–628.
- [73] C. HIRSCH, *Numerical Computation of Internal and External Flows, Vol. I: Fundamentals of Numerical Discretization*, Wiley, New York, 1988.
- [74] J.-R. HO, C.-J. TWU, AND C.-C. HWANG, *Molecular-dynamics simulation of thermoelastic waves in a solid induced by a strong impulse energy*, Physical Review B (Condensed Matter and Materials Physics), 64 (2001), pp. 014302 – 10.
- [75] W. HOOVER, *Canonical dynamics - equilibrium phase-space distributions*, Physical Review A, 31 (1985), pp. 1695–1697.
- [76] M. HORSTEMEYER, M. BASKES, AND S. PLIMPTON, *Computational nanoscale plasticity simulations using embedded atom potentials*, Theoretical and Applied Fracture Mechanics, 37 (2001), pp. 49–98.
- [77] P. HOUSTON, I. PERUGIA, AND D. SCHÖTZAU, *Energy norm a posteriori error estimation for mixed discontinuous Galerkin approximations of the Maxwell operator*, Computer Methods in Applied Mechanics and Engineering, **194**(2-5) (2005), pp. 499–510.
- [78] P. HOUSTON, C. SCHWAB, AND E. SÜLI, *Discontinuous hp-finite element methods for advection-diffusion-reaction problems*, SIAM Journal on Numerical Analysis, **39**(6) (2002), pp. 2133–2163.
- [79] T. HUGHES, G. ENGEL, L. MAZZEI, AND M. LARSON, *The continuous Galerkin method is locally conservative*, Journal of Computational Physics, **163**(2) (2000), pp. 467–488.
- [80] T. HUGHES, G. SCOVAZZI, P. BOCHEV, AND A. BUFFA, *A multiscale discontinuous Galerkin method with the computational structure of a continuous Galerkin method*, Comp. Meth. Appl. Mech. Engrg., 195 (2006), pp. 2761–2787.
- [81] T. J. R. HUGHES, *Multiscale phenomena: Green’s functions, the Dirichlet-to-Neumann formulation, subgrid-scale models, bubbles and the origin of stabilized methods*, Computer Methods in Applied Mechanics and Engineering, **127** (1995), pp. 387–401.

- [82] T. J. R. HUGHES, G. ENGEL, L. MAZZEI, AND M. G. LARSON, *A comparison of discontinuous and continuous Galerkin methods based on error estimates, conservation, robustness and efficiency*, in *Discontinuous Galerkin Methods: Theory, Computation and Applications*, B. Cockburn, G. Karniadakis, and C.-W. Shu, eds., Springer-Verlag, 2000.
- [83] T. J. R. HUGHES, G. R. FEIJÓO, L. MAZZEI, AND J.-B. QUINCY, *The Variational Multiscale Method — a paradigm for computational mechanics*, *Computer Methods in Applied Mechanics and Engineering*, **166** (1998), pp. 3–24.
- [84] T. J. R. HUGHES, L. P. FRANCA, AND G. M. HULBERT, *A new finite element formulation for computational fluid dynamics. VIII. The Galerkin/least-squares method for advective-diffusive equations*, *Computer Methods in Applied Mechanics and Engineering*, **73**(2) (1989), pp. 173–189.
- [85] T. J. R. HUGHES AND M. MALLET, *A new finite element method for computational fluid dynamics: III. The generalized streamline operator for multidimensional advection-diffusion systems*, *Computer Methods in Applied Mechanics and Engineering*, **58**(3) (1986), pp. 305–328.
- [86] T. J. R. HUGHES, M. MALLET, AND A. MIZUKAMI, *A new finite element method for computational fluid dynamics: II. Beyond SUPG*, *Computer Methods in Applied Mechanics and Engineering*, **54**(3) (1986), pp. 341–355.
- [87] T. J. R. HUGHES, A. MASUD, AND J. WAN, *A stabilized mixed discontinuous Galerkin method for Darcy flow*, *Computer Methods in Applied Mechanics and Engineering*, **195** (2006), pp. 3347–3381.
- [88] T. J. R. HUGHES, L. MAZZEI, AND K. E. JANSEN, *Large eddy simulation and the variational multiscale method*, *Comp Vis Sci*, **3** (2000), pp. 47–59.
- [89] T. J. R. HUGHES, L. MAZZEI, A. A. OBERAI, AND A. A. WRAY, *The multiscale formulation of large eddy simulation: Decay of homogeneous isotropic turbulence*, *Phys. Fluids*, **13** (2001), pp. 505–512.
- [90] T. J. R. HUGHES, A. A. OBERAI, AND L. MAZZEI, *Large eddy simulation of turbulent channel flows by the variational multiscale method*, *Phys. Fluids*, **13** (2001), pp. 1755–1754.
- [91] T. J. R. HUGHES AND G. N. WELLS, *Conservation properties for the Galerkin and stabilized forms of the advection-diffusion and incompressible Navier-Stokes equations*, *Computer Methods in Applied Mechanics and Engineering*, **194** (2005), pp. 1141–1159.
- [92] T. IKESHOJI AND B. HAFSKJOLD, *Nonequilibrium molecular-dynamics calculation of heat-conduction in liquid and through liquid-gas interface*, *Molecular Physics*, **81** (1994), pp. 251–261.
- [93] J. IRVING AND J. KIRKWOOD, *The statistical mechanical theory of transport processes. IV. the equations of hydrodynamics*, *J. Chem. Phys.*, **18** (1950), pp. 817–829.

- [94] D. IVANOV AND L. ZHIGILEI, *Combined atomistic-continuum modeling of short-pulse laser melting and disintegration of metal films*, Physical Review B, 68 (2003), p. 064114.
- [95] C. JOHNSON, U. NÄVERT, AND J. PITKÄRANTA, *Finite element methods for linear hyperbolic problems*, Computer Methods in Applied Mechanics and Engineering, **45** (1984), pp. 285–312.
- [96] C. JOHNSON AND J. PITKÄRANTA, *An analysis of the discontinuous Galerkin method for a scalar hyperbolic equation*, Mathematics of Computation, **46**(173) (1986), pp. 1–26.
- [97] D. D. JOSEPH AND L. PREZIOSI, *Heat waves*, Reviews of Modern Physics, 61 (1989), pp. 41 – 73.
- [98] G. E. KARNIADAKIS AND S. J. SHERWIN, *Spectral/hp Element Methods for CFD*, Oxford University Press, 1999.
- [99] J. KIM, P. MOIN, AND R. MOSER, *Turbulence statistics in fully developed channel flow at low Reynolds number*, J. Fluid Mech., 177 (1987), pp. 133–166.
- [100] S. J. KLINE, W. C. REYNOLDS, F. A. SCHRAUB, AND P. W. RUNSTADLER, *The structure of turbulent boundary layers*, J. Fluid Mech., (1967).
- [101] J. KNAP AND M. ORTIZ, *An analysis of the quasicontinuum method*, Journal of the Mechanics and Physics of Solids, 49 (2001), pp. 1899–1923.
- [102] A. N. KOLMOGOROV, *The local structure of turbulence in incompressible viscous fluid for very large reynolds number*, Dokl. Akad. Nauk SSSR, 30 (1941), pp. 301–305.
- [103] B. KOOBUS AND C. FARHAT, *A variational multiscale method for the large eddy simulation of compressible turbulent flows on unstructured meshes-applications to vortex shedding*, Computer Methods in Applied Mechanics and Engineering, 193 (2004), pp. 1367–1383.
- [104] A. G. KRAVCHENKO AND P. MOIN, *On the effect of numerical errors in large eddy simulation of turbulent flows*, J. Comp. Phys., 131 (1996), pp. 310–322.
- [105] S. KUMAR AND E. LOTH, *Detached eddy simulations of an iced-airfoil*, AIAA 2001-0678, (2001).
- [106] I. A. KUNIN, *Elastic Media with Microstructure I: One-Dimensional Models*, Berlin: Springer-Verlag, 1982.
- [107] R. B. LEHOUCQ AND S. A. SILLING, *Force flux and the peridynamic stress tensor*, J. Mech. Phys. Solids, (2007). to appear; available online.
- [108] —, *Statistical coarse-graining of molecular dynamics into peridynamics*, Phys. Rev. Lett., (2007). Submitted.

- [109] P. LESAINTE AND P. A. RAVIART, *On a finite element method for solving the neutron transport equation*, in Mathematical Aspects of Finite Elements in Partial Differential Equations, de Boor C., ed., Academic Press, New York, 1974.
- [110] J. G. LEVIN, M. ISKANDARANI, AND D. B. HAIDVOGEL, *A spectral filtering procedure for eddy-resolving simulations with a spectral element ocean model*, J. Comp. Phys., 137 (1997), pp. 130–154.
- [111] D. K. LILLY, *A proposed modification of the Germano subgrid-scale closure method*, Phys. Fluids A, 4 (1992), pp. 633–635.
- [112] D. P. LOCKARD AND H. L. ATKINS, *Efficient implementations of the quadrature-free discontinuous Galerkin method*, AIAA 99-3309, (1999).
- [113] L. MACHIELS, *A posteriori finite element bounds for output functionals of discontinuous Galerkin discretizations of parabolic problems*, Computer Methods in Applied Mechanics and Engineering, **190**(26-27) (2001), pp. 3401–3411.
- [114] A. MAITI, G. MAHAN, AND S. PANTELIDES, *Dynamical simulations of nonequilibrium processes - heat flow and the Kapitza resistance across grain boundaries*, Solid State Communications, 102 (1997), pp. 517–521.
- [115] R. MARANGANTI AND P. SHARMA, *Length scales at which classical elasticity breaks down for various materials*, Phys. Rev. Let., 98 (2007), p. 195504.
- [116] M. P. MARTIN, U. PIOMELLI, AND G. V. CANDLER, *Subgrid-scale models for compressible large-eddy simulations*, Ther. Comp. Fluid Dyn., 13 (2000), pp. 361–376.
- [117] R. M. KIRBY AND G. E. KARNIADAKIS, *De-aliasing on non-uniform grids: algorithms and applications*, J. Comp. Phys., 191 (2003), pp. 249–264.
- [118] P. MOIN AND K. MAHESH, *Direct numerical simulation: A tool in turbulence research*, Ann. Rev. Fluid Mech., 30 (1998), pp. 539–78.
- [119] R. D. MOSER, J. KIM, AND N. N. MANSOUR, *Direct numerical simulation of turbulent channel flow up to  $Re_\tau = 590$* , Phys. Fluids, 11 (1999), p. 943.
- [120] A. I. MURDOCH, *A critique of atomistic definitions of the stress tensor*, J Elasticity, 88 (2007), pp. 113–140.
- [121] M. MUSER, *Towards an atomistic understanding of solid friction by computer simulations*, Computer Physics Communications, 146 (2002), pp. 54–62.
- [122] W. NOLL, *Die herleitung der grundgleichungen der thermomechanik der kontinua aus der statistischen mechanik*, J. Rational Mech. Anal., 4 (1955), pp. 627–646.
- [123] A. A. OBERAI AND T. J. R. HUGHES, *The variational multiscale formulation of LES: Channel flow at  $Re_\tau = 590$* , AIAA 2002-1056, (2002).
- [124] C. PADGETT AND D. BRENNER, *A continuum-atomistic method for incorporating Joule heating into classical molecular dynamics simulations*, Molecular Simulation, 31 (2005), pp. 749–757.

- [125] J. PALANIAPPAN, R. B. HABER, AND R. L. JERRARD, *A spacetime discontinuous Galerkin method for scalar conservation laws*, Computer Methods in Applied Mechanics and Engineering, **193**(33-35) (2004), pp. 3607–3631.
- [126] H. PARK, E. KARPOV, AND W. LIU, *A temperature equation for coupled atomistic/continuum simulations*, Computer Methods in Applied Mechanics and Engineering, **193** (2004), pp. 1713–1732.
- [127] H. PARK AND W. LIU, *An introduction and tutorial on multiple-scale analysis in solids*, Computer Methods in Applied Mechanics and Engineering, **193** (2004), pp. 1733–1772.
- [128] S.-H. PARK AND J. L. TASSOULAS, *A discontinuous Galerkin method for transient analysis of wave propagation in unbounded domains*, Computer Methods in Applied Mechanics and Engineering, **191**(36) (2002), pp. 3983–4011.
- [129] S. RAMAKRISHNAN, *Variational multiscale methods for turbulence control*, master’s thesis, Rice University, 2002. Available electronically at <http://mems.rice.edu/~collis>.
- [130] ———, *Local Variational Multiscale Method for Turbulence Simulation*, PhD thesis, Rice University, 2005.
- [131] S. RAMAKRISHNAN AND S. S. COLLIS, *Multiscale modeling for turbulence simulation in complex geometries*, AIAA Paper 2004-0241, (2004).
- [132] ———, *Partition selection in multi-scale turbulence modeling*, Submitted to Physics of Fluids, (2004).
- [133] ———, *Turbulence control simulations using the variational multiscale method*, AIAA J., **42** (2004), pp. 745–753.
- [134] P. A. RAVIART AND J. M. THOMAS, *A mixed finite element method for second order elliptic problems*, in Mathematical Aspects of Finite Element Methods, I. Galligani and E. Magenes, eds., Springer-Verlag, 1977, pp. 292–315.
- [135] W. H. REED AND T. R. HILL, *Triangular mesh methods for the neutron transport equation*, tech. report, LA-UR-73-479, Los Alamos Scientific Laboratory, 1973.
- [136] J. ROBERT AND J.-M. THOMAS, *Mixed and hybrid methods*, in Finite Element Methods (Part 1), P. Ciarlet and J. Lions, eds., vol. II of HANDBOOK OF NUMERICAL ANALYSIS, Elsevier Science (North-Holland), 1991, pp. 523–640.
- [137] R. RUDD AND J. BROUGHTON, *Coarse-grained molecular dynamics: Nonlinear finite elements and finite temperature*, Physical Review B, **72** (2005), pp. 144104–1–32.
- [138] G. SANGALLI, *A discontinuous residual-free bubble method for advection-diffusion problems*, Journal of Engineering Mathematics, **49** (2004), pp. 149–162.



- [139] J. SCHALL, C. PADGETT, AND D. BRENNER, *Ad hoc continuum-atomistic thermostat for modeling heat flow in molecular dynamics simulations*, Molecular Simulation, 31 (2005), pp. 283–288.
- [140] C. SCHWAB, *p- and hp- finite element methods. Theory and applications in solid and fluid mechanics*, Clarendon Press, Oxford, 1998.
- [141] Y. T. SHIH AND H. C. ELMAN, *Modified streamline diffusion schemes for convection-diffusion problems*, Computer Methods in Applied Mechanics and Engineering, **174**(1-2) (1999), pp. 137–151.
- [142] M. SHUR, P. R. SPALART, M. STRELETS, AND A. TRAVIN, *Detached-eddy simulation of an airfoil at high angle of attack*, in Fourth International Symposium on Engineering Turbulence Modeling and Experiments, Corsica, 24–26 May 1999, W. Rodi and D. Laurence, eds., Elsevier, New York, 1999.
- [143] S. A. SILLING, *Reformulation of elasticity theory for discontinuities and long-range forces*, J. Mech. Phys. Solids, 48 (2000), pp. 175–209.
- [144] S. A. SILLING AND E. ASKARI, *A meshfree method based on the peridynamic model of solid mechanics*, Computer and Structures, 83 (2005), pp. 1526–1535.
- [145] S. A. SILLING AND F. BOBARU, *Peridynamic modeling of membranes and fibers*, Int. J. Non-Linear Mech., 40 (2005), pp. 395–409.
- [146] S. A. SILLING, M. EPTON, O. WECKNER, J. XU, AND E. ASKARI, *Peridynamic states and constitutive modeling*, Journal of Elasticity, (to appear).
- [147] J. SMAGORINSKY, *General circulation experiments with the primitive equations. I. The basic experiment*, Mon. Weather Rev, 91 (1963), pp. 99–165.
- [148] C. R. SMITH AND S. P. METZLER, *The characteristics of low-speed streaks in the near-wall region of a turbulent boundary layer*, J. Fluid Mech., 129 (1983), p. 27.
- [149] M. STRELETS, *Detached eddy simulation of massively separated flows*, AIAA 2001-0879, (2001).
- [150] S. P. TIMOSHENKO, *History of strength of materials*, Dover, 1983. Unabridged and unaltered republication of the 1953 book originally published by McGraw-Hill Book Company, Inc., N.Y.
- [151] K. TRETIKOV AND S. SCANDOLO, *Thermal conductivity of solid argon from molecular dynamics simulations*, Journal of Chemical Physics, 120 (2004), pp. 3765–3769.
- [152] S. VOLZ, J. B. SAULNIER, M. LALLEMAND, B. PERRIN, P. DEPOND, AND M. MARESCAL, *Transient Fourier-law deviation by molecular dynamics in solid argon*, Physical Review B (Condensed Matter), 54 (1996), pp. 340 – 7.
- [153] G. WAGNER AND W. LIU, *Coupling of atomistic and continuum simulations using a bridging scale decomposition*, Journal of Computational Physics, 190 (2003), pp. 249–274.

- [154] G. J. WAGNER, R. E. JONES, J. A. TEMPLETON, AND M. L. PARKS, *An atomistic-to-continuum coupling method for heat transfer in solids*, Comput. Methods Appl. Mech. Engrg., (2007). Submitted.
- [155] J. WEINER, *Statistical Mechanics of Elasticity*, Dover, Mineola, NY, 2nd edition ed., 2002.
- [156] G. N. WELLS, K. GARIKIPATI, AND L. MOLARI, *A discontinuous Galerkin formulation for a strain gradient-dependent damage model*, Computer Methods in Applied Mechanics and Engineering, **193**(33-35) (2004), pp. 3633–3645.
- [157] T. WERDER, K. GERDES, D. SCHÖTZAU, AND C. SCHWAB, *hp-Discontinuous Galerkin time stepping for parabolic problems*, Computer Methods in Applied Mechanics and Engineering, **190**(49-50) (2001), pp. 6685–6708.
- [158] O. C. ZIENKIEWICZ AND R. L. TAYLOR, *The Finite Element Method*, vol. 1, McGraw-Hill, London, 4th ed., 1989.

## DISTRIBUTION:

1	MS 1322	John Aidun, 1435
1	MS 1318	Ken Alvin, 1416
1	MS 1320	Pavel Bochev, 1414
1	MS 1320	E.P. Chen, 8776
1	MS 1320	Scott Collis, 1414
1	MS 1320	Richard Lehoucq, 1414
1	MS 9409	Chris Moen, 8757
1	MS 1320	Michael Parks, 1414
1	MS 1319	Guglielmo Scovazzi, 1431
1	MS 1322	Stewart Silling, 1435
1	MS 1318	David Womble, 1410
1	MS 9409	Reese Jones, 8776
1	MS 1318	Andy Salinger, 1416
1	MS 0316	John Shadid, 1437
1	MS 1318	James Stewart, 1411
1	MS 0378	Randall Summers, 1431
1	MS 9409	Jeremy Templeton, 8757
1	MS 0370	Timothy Trucano, 1411
1	MS 9409	Gregory Wagner, 8757
1	MS 9409	Jonathan Zimmerman, 8776
1	MS 9018	Central Technical Files, 8944 (electronic copy)
1	MS 0899	Technical Library, 9536 (electronic copy)
1	MS 0123	D. Chavez, LDRD Office, 1011





